

https://dspace.org/

Use of Multispectral Satellite Imagery to Monitor the Decant Pond of Tailings Dams

O'Donovan, Christopher Galen

2023-08

University of the Witwatersrand, Johannesburg

https://hdl.handle.net/10539/39945

O'Donovan, Christopher Galen. (2023). Use of Multispectral Satellite Imagery to Monitor the Decant Pond of Tailings Dams. [Master's dissertation, University of the Witwatersrand, Johannesburg]. WIReDSpace. https://hdl.handle.net/10539/39945

Downloaded from a DSpace repository. https://dspace.org/

USE OF MULTISPECTRAL SATELLITE IMAGERY TO MONITOR THE DECANT POND OF TAILINGS DAMS

Christopher Galen O'Donovan

Student Number: 669684

A dissertation submitted to the Faculty of Engineering and the Built Environment, University of the Witwatersrand, Johannesburg, in fulfilment of the requirements for the degree of Master of Science in Engineering.

Supervised by Dr. Luis Alberto Torres-Cruz.

Co-supervised by Prof. Elhadi Adam.

Johannesburg, 2023.

DECLARATION

Candidate's declaration:

I declare that this dissertation is my own unaided work. It is being submitted to the Degree of Master of Science to the University of the Witwatersrand, Johannesburg. It has not been submitted before for any degree or examination to any other University.

Signed by:

Christopher Galen O'Donovan



On the 2nd day of August 2023.

Declaration of works published or presented pertaining to this dissertation:

Publications:

O'Donovan, C.G., Adam, E. & Torres-Cruz, L.A. (2022) Remote sensing of the decant pond of tailings dams: Insights from a South African case study. *Journal of the Southern African Institute of Mining and Metallurgy*. 122 (4), 167–172.

Torres-Cruz, L.A. & O'Donovan, C.G. (2023) Public remotely sensed data raise concerns about history of failed Jagersfontein dam. *Scientific Reports*. 13 (1), 4953. doi:10.1038/s41598-023-31633-5.

Presentations:

O'Donovan, C.G. (2021) Remote sensing of the decant pond of tailings dams: Insights from a South African case study. In: *Proceedings of the Southern African Institute of Mining and Metallurgy's Conference on Global Tailings Standards and Opportunities for the Mine of the Future*. 15 November 2021. Online

ABSTRACT

Tailings dam failures, such as the Jagersfontein failure in the Free State province and the Fundão and Feijão failures in Brazil, have brought into question the ability of the mining industry to operate safely, threatening its social license. To improve the safety of tailings dams, leading indicators of dam safety should be monitored. The location and historical behaviour of the tailings decant pond provides insight into several such leading indicators and can be used as a proxy to flag potential construction issues. This work investigates the use of public multispectral data collected by the Sentinel-2 satellite mission to monitor the supernatant tailings dam decant pond. This is achieved by leveraging the cloud-based Google Earth Engine platform and open-source GIS tools. Sentinel-2 acquires visible and near infrared spectrum data with a spatial resolution of 10 m and a revisit time of 5 days. Pond data is obtained by visual assessment and automated thresholding of Sentinel-2 imagery. Thresholds of near-infrared (NIR) reflectance and the normalised difference water index (NDWI) obtained by a least square error analysis are investigated. Implementation of the method at three South African tailings dams, constituting four decant ponds, illustrates the capabilities and limitations of Sentinel-2 imagery. High spatial resolution (<5 m) multispectral satellite imagery and natural colour aerial orthophotos (<0.25 m) serve as reference data. Visually assessed Sentinel-2 pond data presented a bias towards slight over estimation of the pond area compared to reference data. Other leading indicators did not show systematic bias across all sites. In general, the deviation between Sentinel-2 and the reference measurements was high, indicating that Sentinel-2 imagery should be used with caution for measurements critical to dam safety. Site-specific thresholds of NIR and NDWI indicated that automated thresholding of the NDWI is superior to NIR reflectance alone. It is shown that Sentinel-2 timeseries imagery can be used in tailings dam monitoring to supplement existing construction surveillance frameworks and provide historical pond data in the absence of such information.

ACKNOWLEDGEMENTS

I would like to extend my sincerest thanks to:

Dr. Luis Alberto Torres-Cruz in the School of Civil and Environmental Engineering for his patient and persistent support and motivation throughout the research and writing process.

Prof. Elhadi Adam in the School of Geography, Archaeology and Environmental Studies for his clear and concise guidance in the realm of remote sensing.

Fraser Alexander (Pty) Ltd. for the financial sponsorship that made this project possible.

Planet Labs PBC for research access to PlanetScope imagery.

My family and friends for their kindness and support during this time of self-improvement.

TABLE OF CONTENTS

Declaration ... **ii**

Abstract ... **iv**

Acknowledgements ... **v**

Table of Contents ... **vi**

List of Figures ... **x**

List of Tables ... **xv**

List of Symbols ... **xvii**

List of Acronyms and Nomenclature ... **xviii**

1 Introduction ... **1**

1.1 Background ... **1**

1.2 Justification ... **2**

1.3 Research objectives ... **4**

1.4 Dissertation structure ... **6**

2 Literature Review ... **7**

2.1 Tailings dam failures and trajectory ... **7**

2.2 Importance of the tailings dam pond ... **9**

2.3 Remote sensing of water bodies ... **15**

2.4 Gap in the literature ... **19**

3 Materials and Methods ... **22**

3.1 Investigation sites ... **22**

3.1.1 Elikhulu ... 22

3.1.2 Ergo ... 24

3.1.3 Impala ... 25

3.2 Imagery ... **26**

3.2.1 Introduction ... 26

3.2.2 Temporal domain of the study ... 30

3.2.3 Input data ... 31

3.2.4 Reference data ... 32

3.3 Data acquisition and processing tools 39
3.3.1 Sentinel Hub EO Browser 39
3.3.2 Planet Explorer 40
3.3.3 Google Earth Engine 41
3.3.4 CDNGI Geospatial Portal and SkySat Tasking Dashboard 43
3.3.5 QGIS 44
3.4 Data analysis 46
3.4.1 Image processing 46
3.4.2 Visual image analysis 47
3.4.3 Image threshold analysis 50
3.4.4 Accuracy assessment 57
3.4.5 Imagery temporal separation 61
4 Results and Discussion 62
4.1 Introduction 62
4.2 Data derived by visual assessment 62
4.2.1 Pond area 62
4.2.2 Minimum beach length 74
4.2.3 Pond centroid displacement 80
4.2.4 Minimum beach length versus pond area 86
4.3 Sentinel-2 thresholds and threshold derived data 87
4.3.1 Near infrared (NIR) threshold 87
4.3.2 Normalised difference water index (NDWI) threshold 96
4.3.3 Visual assessment, NIR and NDWI thresholds compared 104
4.3.4 Sentinel-2 threshold versus very high-resolution reference data 106
5 Conclusion 108
5.1 Summary of works 108
5.1.1 Justification and objective 108
5.1.2 Pond data from visual assessment of Sentinel-2 108
5.1.3 Pond delineation by threshold of Sentinel-2 109
5.2 Conclusions 111
5.3 Further work 113

6 References 115

7 Appendix-A: Very High-Resolution Reference Imagery 123

7.1 Elikhulu East 123

7.2 Elikhulu West 127

7.3 Ergo 130

7.4 Impala 132

8 Appendix-B: Sentinel-2 Image Threshold Derivations 134

8.1 Elikhulu East 134

8.1.1 Histogram and transect threshold assessment 134

8.1.2 NIR threshold derived pond area data 137

8.1.3 NDWI threshold derived pond area data 138

8.1.4 Threshold performance versus very high-resolution reference data 139

8.2 Elikhulu West 140

8.2.1 Histogram and transect assessment 140

8.2.2 NIR threshold derived pond area data 143

8.2.3 NDWI threshold derived pond area data 144

8.2.4 Threshold performance versus very high-resolution reference data 145

8.3 Ergo 146

8.3.1 Histogram and transect assessment 146

8.3.2 NIR threshold derived pond area data 149

8.3.3 NDWI threshold derived pond area data 149

8.3.4 Threshold performance versus very high-resolution reference data 150

8.4 Impala 151

8.4.1 Histogram and transect assessment 151

8.4.2 NIR threshold 154

8.4.3 NDWI threshold 154

8.4.4 Threshold performance versus very high-resolution reference data 155

9 Appendix-C: Catalogue of Images 156
9.1 Elikhulu 156
9.2 Ergo 159
9.3 Impala 162
10 Appendix-D: Google Earth Engine Code 165
10.1 Threshold optimisation 165
10.2 Transect 165
10.3 Histogram 165

LIST OF FIGURES

Figure …..……..…….……..... Page

Figure 2-1: Causes of tailings dams failures globally between 1910 and 2021 (Bowker & Chambers, 2021). 8

Figure 2-2: Schematic tailings dam ring dyke construction adapted from Blight (2009:p.19). 9

Figure 2-3: Schematic tailings dam raising methods a) downstream, b) centre line, c) upstream (Blight, 2009:p.282). 10

Figure 2-4: The tailings dam water balance (Blight, 2009:p.384). 11

Figure 2-5: A generalised relationship between distance from deposition and particle size distribution adapted from Blight (2009:p.297). 13

Figure 2-6: The effects of evaporative and sun drying on material consolidation pressure and void ratio (From Blight, 2009 p.325). 14

Figure 2-7: Simple soil behaviour model indicating the different shear characteristics of the same material in loose and dense states (Casagrande, 1979). 14

Figure 2-8: Upstream tailings management, a) good practice and b) poor practice (Martin & McRoberts, 1999). 15

Figure 2-9: The spectral characteristics of: a) electromagnetic energy sources, b) atmospheric transmission and c) common remote sensing systems (Lillesand et al., 2015:p.11)..... 16

Figure 2-10: Timeline and spatial and temporal resolutions of multispectral satellite imagery available to civilians from 1970 to 2021 (Turner et al., 2021). 18

Figure 3-1: Elikhulu SkySat image acquired on 26 April 2022 rendered in natural colour..... 23

Figure 3-2: Ergo SkySat image acquired on 26 April 2022 rendered in natural colour..... 25

Figure 3-3: Impala SkySat image acquired on 6 April 2022 rendered in natural colour. 26

Figure 3-4: Sentinel-2A and 2B normalised spectral responses for the 10 m bands (ESA, 2022). 32

Figure 3-5: An indicative normalised spectral response of the Dove Classic constellation (Planet, 2018). 34

Figure 3-6: An indicative normalised spectral response of the blue, green, red and near infrared bands of the Dove-R and SuperDove instruments (Planet, 2018). 34

Figure 3-7: SkySat imagery and enlargement depicting the finest spatial resolution achieved as well as the detail rendered in the near infrared band. .. 36

Figure 3-8: An indicative normalised spectral response of the SkySat constellation (Planet, 2018). 36

Figure 3-9: Drone survey imagery and enlargement depicting the finest spatial resolution achieved. 37

Figure 3-10: CDNGI aerial imagery and enlargement depicting the finest spatial resolution achieved. 38

Figure 3-11: Sentinel Hub EO Browser user interface. 40

Figure 3-12: Planet Explorer web interface. 41

Figure 3-13: Google Earth Engine JavaScript Code Editor interface. 42

Figure 3-14: CDNGI Geospatial Portal. 43

Figure 3-15: SkySat Tasking Dashboard. 44

Figure 3-16: QGIS 3.28 interface. 45

Figure 3-17: NIR and NDWI colour ramp. 47

Figure 3-18: Example Sentinel-2 visually assessed pond (acquired 2019-01-15). 48

Figure 3-19: Example PlanetScope visually assessed pond area (acquired 2019-01-15). 48

Figure 3-20: Visual representation of pond related tailings dam safety metrics. 49

Figure 3-21: Spectral profiles of various land covers adapted from Lillesand, Kiefer & Chipman (2015:p.17) with Sentinel-2 10 m bands overlayed. 51

Figure 3-22: Schematic histogram of the near infrared reflectance sampled from within the crestline. 52

Figure 3-23: Schematic image of a tailings dam and transect, indicating the pond, beach and crestline. 53

Figure 3-24: Schematic of the interpretation of a transect through a) NIR and b) NDWI imagery data. 54

Figure 3-25: Algorithm for automated calculation of the pond area in an image collection by multiple thresholds and estimation of an optimum threshold[1]. 56

Figure 3-26: Example of the expected relationship between varying threshold values and the sum of square error and the optimum threshold. 57

Figure 3-27: Example of PlanetScope vs S2 (Sentinel-2) NIR threshold derived pond. 60

Figure 3-28: Example of PlanetScope vs S2 (Sentinel-2) NDWI threshold derived pond. 60

Figure 4-1: Pond area with image acquisition time delineated by visual assessment of Sentinel-2. 63

Figure 4-2: Agreement between pond area measurements a) of all pond sizes and b) ponds smaller than 400 $x10^3$ m^2 delineated by visual assessment of Sentinel-2 (S2) and PlanetScope (PS) imagery. 65

Figure 4-3: Ratio of the area obtained by S2 (Sentinel-2) to PS (PlanetScope) versus pond area magnitude. 66

Figure 4-4: Histogram of A_{S2} (Area by Sentinel-2) to A_{PS} (Area by PlanetScope) pond area ratio. 67

Figure 4-5: Temporal separation versus normalised absolute pond area difference. 69

Figure 4-6: Temporal separation over a narrowed domain versus normalised absolute pond area difference. 70

Figure 4-7: A comparison of PlanetScope satellite generation and the mean normalised absolute area difference recorded at each site. 72

Figure 4-8: Summary of pond area by visual assessment of Sentinel-2 (S2) versus very high-resolution reference imagery. 73

Figure 4-9: Minimum beach lengths delineated by visual assessment of S2 (Sentinel-2) and PS (PlanetScope) imagery. 75

Figure 4-10: Agreement between minimum beach lengths determined by visual assessment of Sentinel-2 (S2) and PlanetScope (PS) imagery..... 76

Figure 4-11: Ratio of the minimum beach length obtained by S2 (Sentinel-2) to PS (PlanetScope) versus minimum beach length magnitude..... 77

Figure 4-12: Histogram of the ratio of the MBL (minimum beach length) measured by Sentinel-2 to PlanetScope. 78

Figure 4-13: Summary of minimum beach length by visual assessment of Sentinel-2 (S2) versus very high-resolution reference imagery. 79

Figure 4-14: Pond centroid displacement delineated by visual assessment of Sentinel-2 imagery..... 80

Figure 4-15: Agreement between pond centroid movement by visual assessment of S2 (Sentinel-2) and PS (PlanetScope) imagery..... 81

Figure 4-16: Ratio of the pond centroid displacement obtained by S2 (Sentinel-2) to PS (PlanetScope) versus pond centroid displacement magnitude. 83

Figure 4-17: Histogram of the S2 (Sentinel-2) to PS (PlanetScope) centroid displacement ratio. 83

Figure 4-18: Summary of pond centroid displacement by visual assessment of Sentinel-2 (S2) versus very high-resolution reference imagery. 85

Figure 4-19: Pond area versus minimum beach length delineated by visual assessment of Sentinel-2 imagery..... 86

Figure 4-20: NIR threshold derivation by minimum sum of square errors. 90

Figure 4-21: Pond area by S2 (Sentinel-2) NIR threshold versus visually assessed PS (PlanetScope) imagery. 92

Figure 4-22: Ratio of the area obtained by Sentinel-2 (S2) NIR threshold to PS (PlanetScope) versus pond area magnitude. 93

Figure 4-23: Histogram of the ratio of area obtained by S2 (Sentinel-2) NIR threshold to PS (PlanetScope). 93

Figure 4-24: NDWI threshold derivation by minimum sum of square error. 97

Figure 4-25: Pond area by S2 (Sentinel-2) NDWI threshold versus visually assessed PS (PlanetScope) reference imagery. 100

Figure 4-26: Ratio of the area obtained by Sentinel-2 (S2) NDWI threshold to PS (PlanetScope) versus pond area magnitude. 101

Figure 4-27: Histogram of the ratio of area obtained by S2 (Sentinel-2) NDWI threshold to PS (PlanetScope). 101

Figure 4-28: Pond area by S2 (Sentinel-2) NIR and NDWI thresholds versus visually assessed very high-resolution reference imagery. 106

LIST OF TABLES

Table ……..…….…….……..…….. Page

Table 2-1: Leading indicators of tailings dam safety (Boswell & Sobkowicz, 2018) 20

Table 3-1: Investigation sites and characteristics at time of investigation 22

Table 3-2: Overview of imagery sources and basic properties 30

Table 4-1: Visually assessed Sentinel-2 versus PlanetScope pond area data statistics..... 67

Table 4-2: Sentinel-2 versus very high-resolution reference pond area data statistics..... 73

Table 4-3: Visually assessed Sentinel-2 versus PlanetScope minimum beach length data statistics 78

Table 4-4: Sentinel-2 versus very high-resolution reference minimum beach length data statistics 79

Table 4-5: Visually assessed Sentinel-2 versus PlanetScope minimum beach length data statistics 84

Table 4-6: Sentinel-2 versus very high-resolution reference pond centroid displacement data statistics..... 85

Table 4-7: Sentinel-2 NIR 2019 to 2021 histogram and transect assessment results..... 87

Table 4-8: Sentinel-2 NIR threshold values obtained by training against visually assessed pond area data 91

Table 4-9: Statistics of NIR threshold derived Sentinel-2 pond area data versus PlanetScope reference data 95

Table 4-10: Sentinel-2 NDWI 2019-2021 histogram and transect assessment results..... 96

Table 4-11: NDWI threshold values obtained by training against visually assessed pond areas 99

Table 4-12: Statistics of NDWI threshold derived Sentinel-2 pond area data versus PlanetScope reference data 103

Table 4-13: Comparision of visual assessment, NIR and NDWI statistics 105

Table 4-13: Statistics of threshold derived Sentinel-2 pond area data versus very high-resolution reference data 107

Table 5-1: Sentinel-2 versus PlanetScope summary statistics 109

Table 5-2: Sentinel-2 versus very high-resolution reference data summary statistics 109

Table 5-3: Sentinel-2 NIR and NDWI thresholds 110

Table 5-4: Sentinel-2 versus PlanetScope area data summary statistics 110

Table 5-5: Sentinel-2 versus very high-resolution reference pond area data summary statistics 111

LIST OF SYMBOLS

Pond area (m^2)	A
Minimum beach length (m or km)	MBL
Centroid displacement distance (m)	ΔC
Acquisition time (time since epoch, milliseconds)	T
Shear stress (kPa)	τ
Displacement (mm)	δ
Effective stress (kPa)	σ'
Void ratio	e
Radiance (Watts / steradian / m^2)	L
Reflectance (Ratio)	R
Wavelength (nm or μm)	λ
Sample mean	$\bar{X}$
Sample standard deviation	S
Null hypothesis mean	μ_0
Test statistic	T_0

LIST OF ACRONYMS AND NOMENCLATURE

List of acronyms

API: Application Programming Interface
CDNGI: Chief Directorate of National Geospatial Information (RSA)
ESA: European Space Agency
GDAL: Geospatial Data Abstraction Library
GEE: Google Earth Engine
GIS: Geographic Information System
GSD: Ground Sample (or Sensing) Distance
IDE: Integrated Development Environment
NASA: National Aeronautics and Space Administration (USA)
NDWI: Normalised Difference Water Index
NIR: Near Infrared
PS: PlanetScope
S2: Sentinel-2
SIAC: Sensor Invariant Atmospheric Correction
TSF: Tailings Storage Facility
USGS: United States Geological Survey
UTM: Universal Transverse Mercator

Nomenclature

Acquisition: The data acquired by a remote sensing system at a point in time for a particular geographic location.

Active remote sensing: Remote sensing of objects by transmission of a signal and measuring the response. e.g., Radio detection and ranging (Radar).

Barge: A floating tailings pond decant system.

Constellation: A group of satellites in similar orbits performing the same function.

Decant pond: The supernatant water body atop a tailings dam, usually located around the penstock or decant structure.

Normalised spectral responses: The relative sensitivity of a sensor to different radiation wavelengths.

Passive remote sensing: Remote sensing of objects using reflected or emitted radiation. e.g., aerial photography.

Penstock: A pipe or tower used to decant water from the supernatant pond of a tailings dam. Usually present on ring dyke tailings dams where the pond is centrally located. Common in South Africa.

Pixel: The smallest discrete unit of a digital image.

Reflectance: The ratio of reflected to incident radiance: L_{ref}/L_{inc}. Reported as a value between 0 and 1 for each pixel in a remotely sensed image. Often scaled to a 16bit integer between 0 and 10^4 to reduce memory consumption.

Remote sensing: The act of obtaining information about an object through an analysis of data acquired without coming into direct contact with the object.

Revisit: The time between subsequent satellite passes of a given satellite system or constellation over a particular location where the opportunity for an acquisition exists.

Satellite tasking: To send an instruction to a satellite to record data or acquire an image of an area of interest.

Spatial resolution: The minimum size of an object that can be detected by a remote sensing system. Usually taken as the nominal dimensions of pixels in the sensed image or the ground sample distance. Can be influenced by image postprocessing, such as pan sharpening.

Spectral resolution: The limit to which a remote sensing system can distinguish between different features based on their spectral properties. Usually, a function of the number and width of electromagnetic bands sensed.

Surface reflectance: Radiance data processed to account for incident solar radiation, solar angle and to remove the effects of atmospheric transmission.

Tailings dam: A structure used to retain and store hydraulically deposited tailings slurry.

Tailings: The fine residues that remain after processing ore.

Temporal resolution: The limit to which a remote sensing system can detect changes with time. Usually, inferred from the cadence or revisit time between subsequent image acquisitions.

Threshold: The critical value of a pixel in an image which will determine if the pixel is classified into one group or another.

Top of atmosphere reflectance: Radiance data processed to account for incident solar radiation and solar angle without removing the effects of atmospheric transmission or opacity.

1 INTRODUCTION

1.1 Background

Public earth observation satellites provide rich multispectral imagery at a regular cadence which is used primarily to monitor large scale land surface change. Improvements in the resolution of public earth observation satellites, namely Sentinel-2 (ESA, 2015), may have created the opportunity to now use this data to monitor civil and mining infrastructure.

No one geospatial imaging system provides the best spatial, temporal and spectral resolutions, due to the physical and logistical challenges associated with building such systems. Rather different systems can be designed to fit into resolution niches that provide data for specific purposes (Lillesand et al., 2015; Jensen, 2015). Sentinel-2 has improved upon the spatial and temporal resolution of the Landsat mission, reducing nominal multispectral ground sampling distances from 30 m to 10 m, in the visible and near infrared spectrum, and going from an acquisition cadence at the equator of 8 days with Landsat 8 and 9 in tandem, to 5 days with Sentinel 2A and 2B (ESA, 2015; USGS, 2019, 2022). These improvements make the Sentinel-2 system applicable not only to its primary objective of land surface change monitoring (ESA, 2015), but also to civil and geotechnical engineering (Turner et al., 2021; McAllister et al., 2022).

Tailings are the fine-grained mine waste or residue material that remains after the constituents of value have been extracted from an ore. The material is typically transported hydraulically and discharged as a slurry for permanent, or long-term, containment in tailings dams that are raised concurrently with filling (Blight, 2009). Although there are other types of tailings storage facilities (TSFs) using methods such as in-pit disposal and dry stacking, tailings dams are the most common (Franks et al., 2021). Tailings dam disasters over the last decade, such as the Mount Polley in Canada, the Fundão and Feijão dam failures in Brazil and the recent Jagersfontein and Williamson kimberlite dam failures in Africa, have highlighted the potential dangers associated with similar facilities and have heightened public and regulatory scrutiny of these structures (Roche et al., 2017;

Morrison et al., 2018; Morrison & Gomide, 2019; Morrill et al., 2022; Burger, 2022; UNEP, 2022; Petley, 2022). Accordingly, there is a need to provide practical technologies that can contribute to safer tailings monitoring practices (Atif et al., 2021).

The increasing occurrence of very serious tailings dam failures (Bowker & Chambers, 2015, 2017) and systemic stability issues revealed in public tailings disclosures (Franks et al., 2021) further highlight the importance of tailings dam monitoring systems. The decant pond is a feature of tailings dams that provides insight into the operational state of the dam. The size and location of the decant pond provide insight into several indicators of dam safety (Boswell & Sobkowicz, 2018).

Sentinel-2 is of higher spatial and temporal resolution than other public earth observation satellites (ESA, 2015; USGS, 2019, 2022; Turner et al., 2021). These improvements in spatial resolution will improve the accuracy to which ground surface changes can be measured (Boyle et al., 2014; Fisher et al., 2018). Therefore, this recent addition to the open-access suite of geospatial imagery may have created an opportunity to generate accurate spatial data on the tailings dam decant pond. Furthermore, this imagery could provide such pond data at lower cost, as the imagery is public, with higher temporal cadence than typically achieved by commercial satellite data or terrestrial survey.

1.2 Justification

Increases in the power and scale of mining equipment since the start of the 20th century has propelled mine production forward, yet little improvement has been made in the way of more sophisticated mining strategies (Humphreys, 2020). This together with lowering ore grades and greater production quantities presents a scenario of ever higher volumes of mine waste and an implicit lower capital margin for its disposal, posing a significant challenge to the mining industry (Mudd, 2007, 2010; Bowker & Chambers, 2017). The tragic Jagersfontein tailings dam failure in South Africa and the internationally high profile Mount Polley, Fundão and Feijão tailings dam failures have called into question and highlighted shortcomings in mine waste management practices (ICOLD, 2001; Church of

England, 2021; Morrill et al., 2022; Burger, 2022). With very serious tailings dam disasters increasing in frequency (Bowker & Chambers, 2015, 2017) there is apparently a need to change mine waste disposal practice and better leverage available technology to monitor tailings dam safety (ICOLD, 2001; Roche et al., 2017).

The review of past tailings dam incidents and failures shows that the amount of water in tailings dams plays a critical role in the likelihood and consequences of failure (ICOLD, 2001; Lyu et al., 2019; Bowker & Chambers, 2021). For instance, the proximity of the decant pond to the perimeter wall directly contributed to the failure of the Merriespruit tailings dam in South Africa in 1994 (Blight, 2009; Niekerk & Viljoen, 2005) and the regular proximity of the pond to the crest of the Feijão dam allowed deposition of weak slimes in the structural zone that contributed to the failure (Robertson et al., 2019). Additionally, although the Mount Polley tailings dam failure in Canada was triggered by undetected weak foundation soils, the post failure investigation noted that the catastrophic breach could have been avoided by maintaining a small pond and long beaches of dry tailings between the pond and dam crest (Hoffman, 2015).

A georeferenced outline of the supernatant pond provides data on several leading indicators of dam safety. Such leading indicators being the pond area and minimum dry beach length, or beach freeboard as it is sometimes referred (Boswell & Sobkowicz, 2018). Therefore, timely monitoring of the pond and an understanding of its historical behaviour can enhance the safety of tailings dams.

Satellite imagery is an established tool for tailings dam monitoring and provides several benefits over traditional terrestrial means (Mitchell et al., 2018; Lumbroso et al., 2021). For instance, analysis of multispectral imagery from the Landsat satellite mission disclosed the position of the pond on the Merriespruit tailings dam prior to its failure and informed the investigation into the causes (Blight, 2009; Niekerk & Viljoen, 2005). More recently, investigations into the Fundão and Feijão tailings dam failures used public, Google Earth and Sentinel-2, as well as commercial satellite imagery to assess the behaviour of the tailings dam ponds at the facilities during construction (Morgenstern et al., 2016; Robertson et al.,

2019). A post failure investigation of the Jagersfontein dam failure in the Free State province made use of public satellite and aerial orthophoto imagery to recreate and assess the construction history of the dam leading up to its failure in September 2022 (Torres-Cruz & O'Donovan, 2023).

Public multispectral satellite imagery is used to monitor the surface area and associated volume of natural and artificial surface water bodies (McFeeters, 1996, 2013; Pekel et al., 2016; Huang et al., 2018; Tottrup et al., 2022) and has been used to analyse the environmental devastation following tailings dam disasters (Rana et al., 2021). Given that tailings dam ponds typically have a significantly smaller area than conventional water reservoirs and contain water potentially very high in suspended solids, the accuracy to which these smaller areas can be measured using public multispectral satellite imagery requires careful consideration. Currently there are no investigations into the accuracy of public multispectral satellite imagery as a tool to systematically measure the boundary of tailings dam ponds. This study contributes to filling this gap in the literature.

In this work, the tailings decant pond will be derived from Sentinel-2 imagery using visual assessment and automated thresholding. Sentinel-2 derived pond safety metrics are compared to analogous pond data obtained by visual assessment of higher spatial resolution reference imagery.

The bias and standard deviation of Sentinel-2 measurements compared to measurements obtained by higher spatial resolution reference datasets is investigated.

1.3 Research objectives

Geospatial tailings decant pond data is a valuable resource to tailings dam engineers and stakeholders alike. However, this data is usually only obtained by mine and tailings dam operators and is not openly available.

Public earth observation data has been used to determine the location of the tailings decant pond in post failure investigations of several large tailings dam failures of the past decade. There is, however, no systematic comparison of

tailings pond measurements derived from public earth observation satellites and other higher resolution sources of such pond data.

The objective of this research is to determine the accuracy of tailings decant pond measurements associated with leading indicators of dam safety made using multispectral Sentinel-2 satellite imagery. Such pond data includes the pond area, the minimum beach length and the pond centroid. This is achieved by comparing tailings dam pond measurements made using Sentinel-2 to the same measurements made using higher spatial resolution reference imagery.

A further objective of this research is to develop an algorithm that can determine optimum thresholds of near infrared (NIR) reflectance and the normalised difference water index (NDWI) to generate tailings decant pond data. This objective extends to testing the accuracy of the pond measurements generated by these derived thresholds. The accuracy of the threshold derived data is assessed by comparison of pond areas generated by thresholding of Sentinel-2 imagery to visually assessed pond areas based on the higher spatial resolution reference data.

1.4 Dissertation structure

This dissertation organised into the following chapters:

1. *Literature Review*

A summary of the literature search conducted. The major areas covered are: The characteristics of tailings dams amenable to satellite remote sensing; remote sensing works pertinent to detecting water bodies; and the relevance of remote sensing of the tailings dam decant pond.

2. *Methods and Materials*

The materials and methods chapter presents the sites investigated in this research, the imagery data acquired, and how imagery data was processed and handled to meet the research objective.

3. *Results and Discussion*

The results are presented alongside the discussion in a single chapter. Important findings from analysis of the results are provided and discussed.

4. *Conclusion*

The conclusion provides a summary of the work as a whole and the main findings of the research project.

5. *References*

A complete list of reference in the Harvard (author, date) format.

6. *Appendices*

Data analysed in this project but too lengthy to include in the main text of this work is included in the appendices for the reader's reference. This includes the very high-resolution reference imagery; Sentinel-2 imagery analysis by transect and histogram; complete reproduction of threshold derived pond area data alongside training data; the catalogue of the Sentinel-2 and PlanetScope imagery used in the study; and, finally links to Google Earth Engine scripts are provided.

2 LITERATURE REVIEW

2.1 Tailings dam failures and trajectory

Tailings dams are different to water dams in many respects. Water dams are seen as assets storing an often scarce and valuable commodity. Tailings dams are structures constructed from, and intended to retain, the uneconomical wastes of the extractive industry (ICOLD, 2001). Water dams are typically constructed in a single effort while tailings dams are constructed and operated simultaneously, being raised concurrently with filling. The result is a protracted process requiring the combined effort of successive generations of staff (Blight, 2009:p.453). These factors, among others, impact both attitude towards and the ability to implement good construction practices on tailings dams. Furthermore, mine funding models largely undervalue future environmental and social costs arising due to the mine and its waste products (Roche et al., 2017:p.59).

Causes of tailings dam failures in the World Mine Tailings Failures Database from 1915 – 2021 catalogued by Bowker and Chambers (2021), shown in Figure 2-1, indicates that approximately one third of tailings dam failures can be attributed to overtopping and seepage erosion. Corresponding analysis of tailings dam failure data by Lyu et al. (2019) indicate that as many as half of reported tailings dam failures can be attributed to overtopping and seepage erosion.

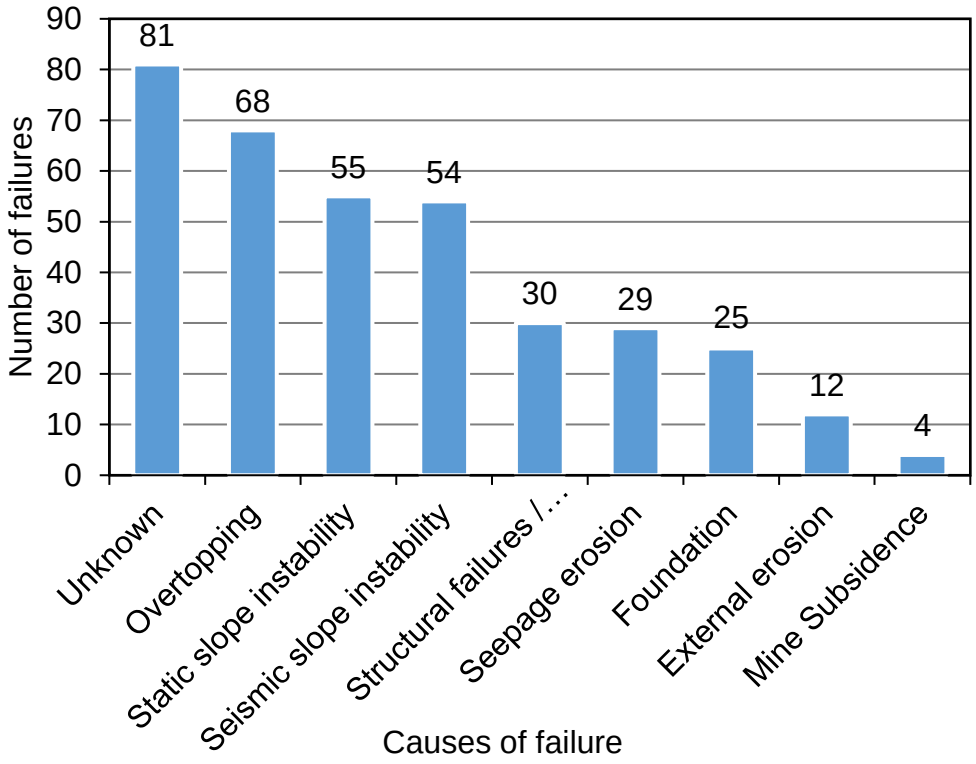


Figure 2-1: Causes of tailings dams failures globally between 1910 and 2021 (Bowker & Chambers, 2021).

Analysis of the tailings dam failure statistics indicates an upward trend in the annual number of very serious tailings dam failures (Bowker & Chambers, 2017). According to the ICOLD Committee on Tailings Dams And Waste Lagoons (1995-2001) (ICOLD, 2001), whose data is incorporated into the database managed by Bowker and Chambers (2021), most tailings dam failures can be attributed to a lack of control of the water balance and a lack of understanding of the features controlling safe operation. The commission concludes that tailings dam failure risk can largely be mitigated by the adequate application of available engineering technology to the design, construction and operation of tailings dam. Such technology includes routine monitoring and safety audits (ICOLD, 2001). Furthermore, the work by Vermeulen (2001) on gold tailings dams in South Africa concludes that the single most important factor in maintaining the stability and serviceability of tailings dams is control of the phreatic surface.

2.2 Importance of the tailings dam pond

Although there are several types of tailings storage facility, such in-pit disposal and dry-stack facilities (Blight, 2009:p.17), by far the most widespread is the tailings dam (Franks et al., 2021). Of the different tailings dams construction methods, the upstream method is currently the most common, both by volume of tailings stored and number of active facilities (Franks et al., 2021). Upstream tailings dam construction is often preferred over centreline and downstream methods, for economic reasons (Vermeulen, 2001; Blight, 2009). In South Africa, the majority of gold tailings dams are operated as perimeter ring dykes raised upstream (Vermeulen, 2001). A schematic representation of a typical ring-dyke tailings dams construction is shown in Figure 2-2 with the different raising methods shown in Figure 2-3 thereafter.

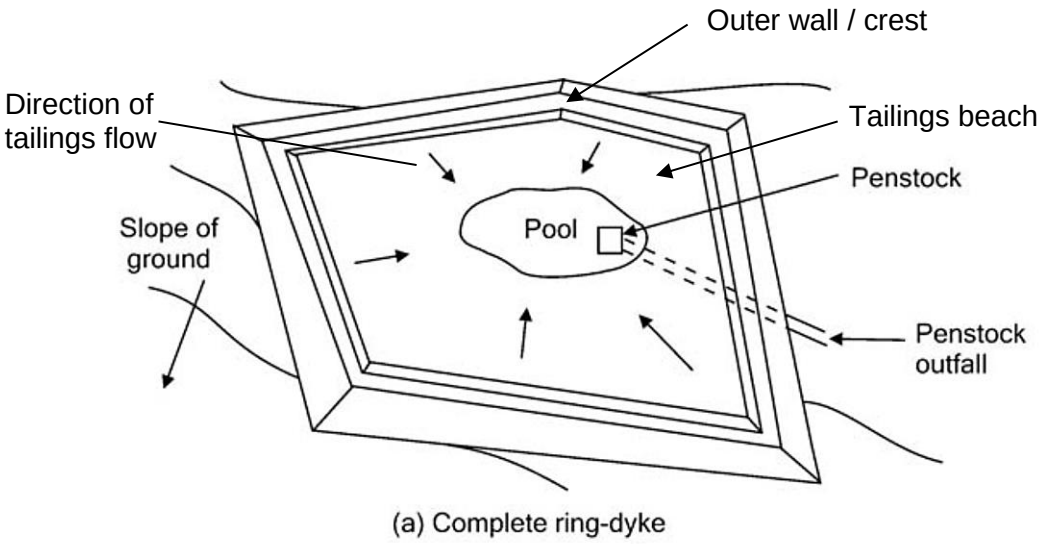


Figure 2-2: Schematic tailings dam ring dyke construction adapted from Blight (2009:p.19).

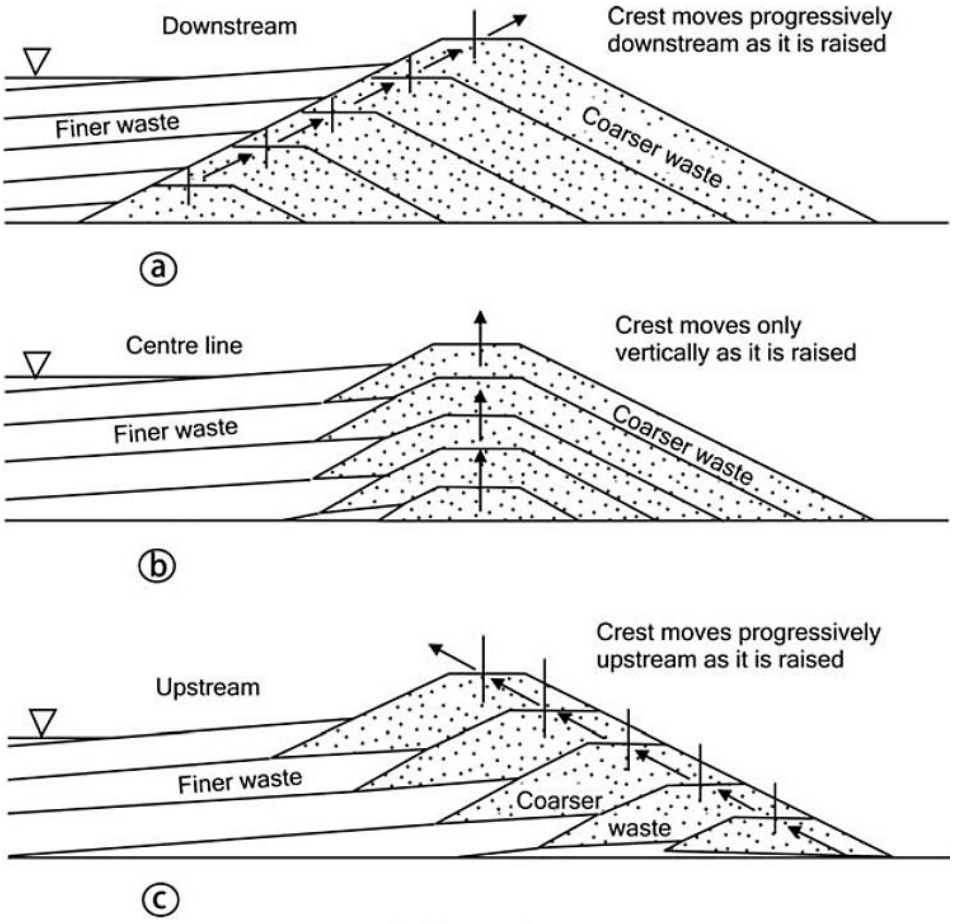


Figure 2-3: Schematic tailings dam raising methods a) downstream, b) centre line, c) upstream (Blight, 2009:p.282).

Tailings dams typically have a pool or pond of supernatant water at the location of the decant structure. The outer wall of the tailings dam, that part responsible for the stability of the structure, should be separated from the tailings pond by a beach of dry tailings per Figure 2-2 (Martin & McRoberts, 1999; Blight, 2009; Fourie et al., 2022). In South Africa, the National Environmental Management: Waste Act requires that the pond on a tailings dam be kept at least 50 m away from the outer wall (Department of Environmental Affairs, 2015). For upstream tailings dams, this may be interpreted as the horizontal distance from the edge of the pond to the location of the crest of the outer wall when at full height.

The water balance on a tailings dam is controlled by input of water from the delivery of slurry and precipitation and by water removed by the decant and under

drain systems. Water is lost to uncollected seepage and evaporation. Water entering the dam that is not removed by the decant system or lost to evaporation will become seepage and contribute to the phreatic surface within the dam, see Figure 2-4. A raised phreatic surface increases pore water pressure, reducing effective stress and so negatively impacts slope stability (Das & Soghan, 2014).

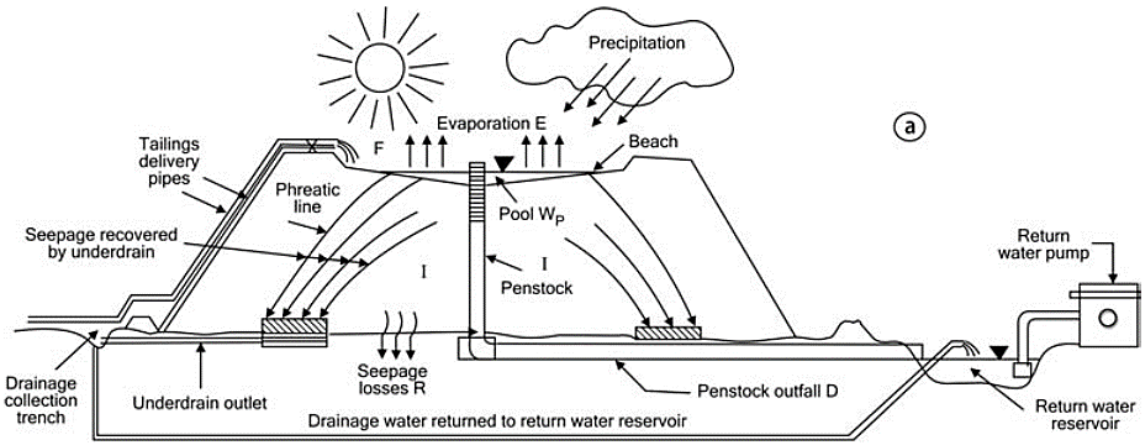


Figure 2-4: The tailings dam water balance (Blight, 2009:p.384).

The failure at Merriespruit in 1994 can be attributed to a runaway failure mechanism initiated by an overtopping event as a result of poor water management at the dam (Blight, 2009:p.468). Furthermore, poor management of the water balance at Mount Polley (including a large body of supernatant water and the absence of long dry beaches) was flagged in the post failure investigation as a factor that allowed the massive loss of impounded material (Hoffman, 2015). The pond surface area serves as an approximation of the volume of water stored in a facility and presents a positive correlation with the volume of tailings runout at failure (Rourke & Luppnow, 2015). The large ponds of water close to the outer wall observed at the Jagersfontein tailings dam prior to its failure indicate deviation from sound engineering practice (Torres-Cruz & O'Donovan, 2023). Notwithstanding tailings dam design considerations, a pond located further from the outer wall of a tailings dam with a smaller area creates a reduced hydrostatic head driving seepage compared to a larger pond in close proximity to the outer

wall (Blight, 2009:p.335). Therefore, a smaller pond located far from the outer wall is preferable and promotes dam safety.

A definition of the boundary of the pond not only provides an indication of the water volume stored on a facility, but it also provides data on the tailings beach length and the location of the pond within a dam. Maintenance of wide tailings beaches benefits dam safety by contributing to the minimum freeboard and creates a spatial buffer between the dam crest and the pond (Boswell & Sobkowicz, 2018; Fourie et al., 2022). Were the pond sizes kept small and minimum beach lengths adhered to prior to the failures at Bafokeng in the North West province and Merriespruit in the Free State, the facilities would not have failed (Blight, 2009:pp.466, 468). Wide tailings beaches also contribute to the structural integrity of tailings dams by separating slimes from sand tailings. The post failure investigation of the Feijão dam breach in Brazil notes that short tailings beaches and the proximity of the pond to the dam crest allowed fine, loose and contractive materials to be deposited in the structural zone of the embankment (Morgenstern et al., 2016).

A long beach promotes tailings facility stability for several reasons. Long beach lengths provide a greater distance between the point of discharge of tailings and the location of the pond. In general, this in turn promotes particle segregation of tailings with the coarser fraction deposited first and finer material deposited later (Blight, 2009:p.297), as illustrated in Figure 2-5. Having the coarser fraction of tailings deposited in the outer region of a tailings dam promotes the drainage of material in this zone which is relied upon for structural integrity of the dam.

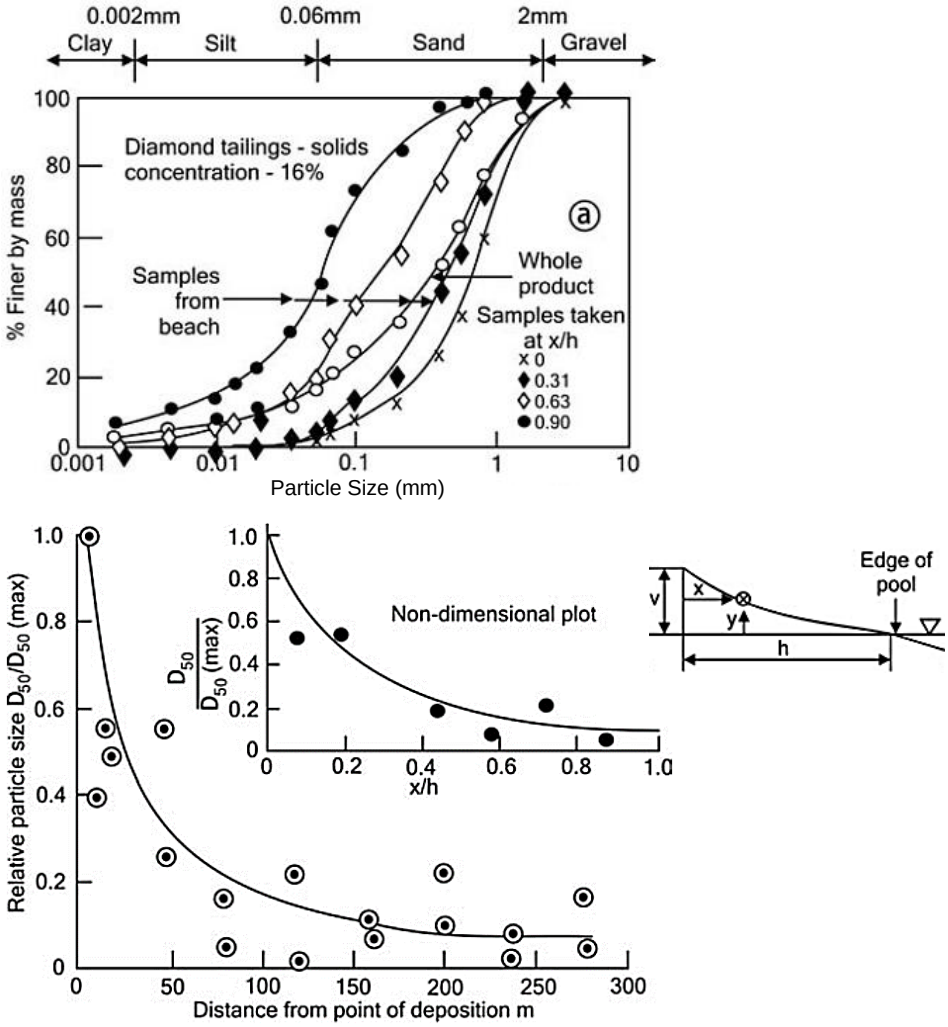


Figure 2-5: A generalised relationship between distance from deposition and particle size distribution adapted from Blight (2009:p.297).

Long beaches expose deposited material to the atmosphere promoting sun drying and evaporation. Sun dried tailings achieves lower void ratios (higher densities) than tailings dried by evaporation alone, both of which achieve significantly lower void ratios than tailings consolidated from a slurry without the effects of evaporation (Blight, 2009:p.325), as illustrated in Figure 2-6. Although not all tailings necessarily exhibit particle segregation on deposition (Vermeulen, 2001), all tailings materials should consolidate more rapidly under the effects of sun drying and desiccation. Materials deposited at a higher density will exhibit a higher peak undrained shear strength, shown schematically in Figure 2-7 (Castro,

1969; Casagrande, 1979; Terzaghi et al., 1996), and will be less susceptible to liquefaction (Jefferies & Been, 2015).

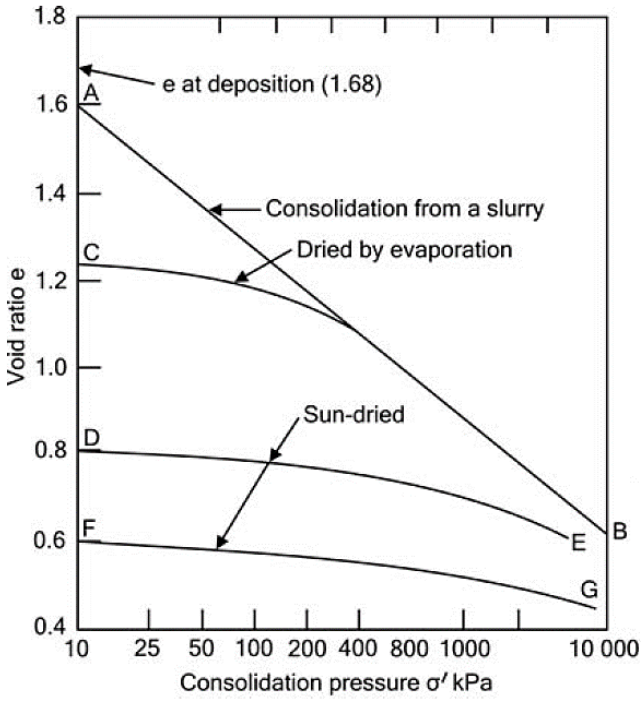


Figure 2-6: The effects of evaporative and sun drying on material consolidation pressure and void ratio (From Blight, 2009 p.325).

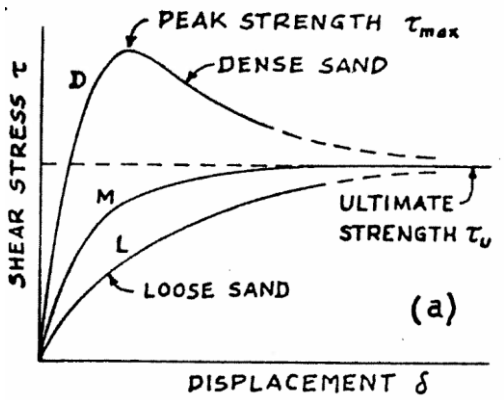


Figure 2-7: Simple soil behaviour model indicating the different shear characteristics of the same material in loose and dense states (Casagrande, 1979).

Good upstream tailings dam management hinges on maintaining a low phreatic surface and a region of denser drained material in the structural zone of the dam (Martin & McRoberts, 1999), as illustrated in Figure 2-8. The location of the phreatic surface and the position of the slimes-sand tailings boundary is dependent on the location of the pond, and therefore amenable to tracking.

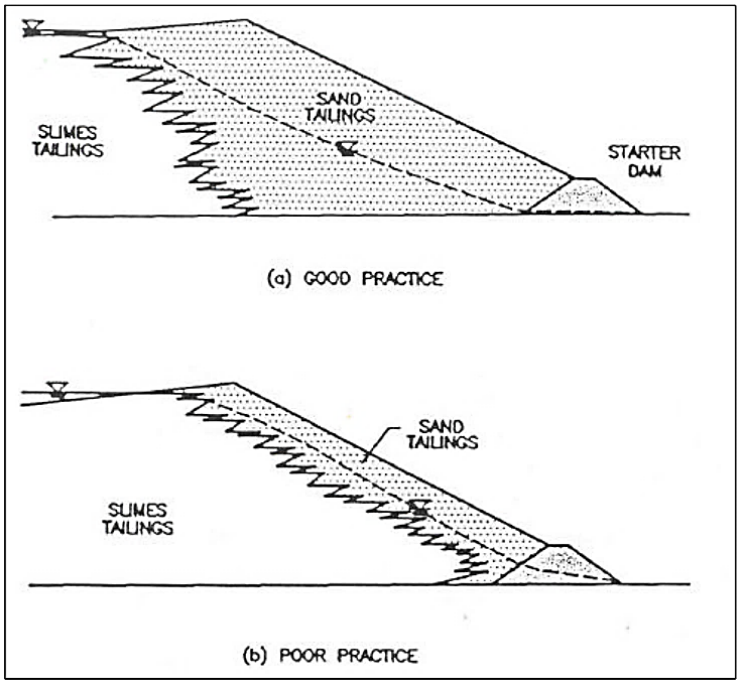


Figure 2-8: Upstream tailings management, a) good practice and b) poor practice (Martin & McRoberts, 1999).

2.3 Remote sensing of water bodies

Remote sensing is broadly defined as the science of obtaining information about an object or phenomenon by an analysis of data acquired without coming into physical contact with that object or system (Lillesand et al., 2015). The field encompasses a broad range of disciplines from photography to radar to aerial surveying and includes spaceborne sensors (i.e. satellites). Remote sensing can be broken down into two broad categories, passive and active. Passive remote sensing entails measuring the reflected or emitted radiation from an object, while active remote sensing entails sending a signal and measuring its return such as radar, sonar, or LiDAR. This work will focus on passive remote sensing using the

visible and near infrared electromagnetic spectrum as detailed in Figure 2-9, encompassing multispectral satellite and aerial orthophoto imagery.

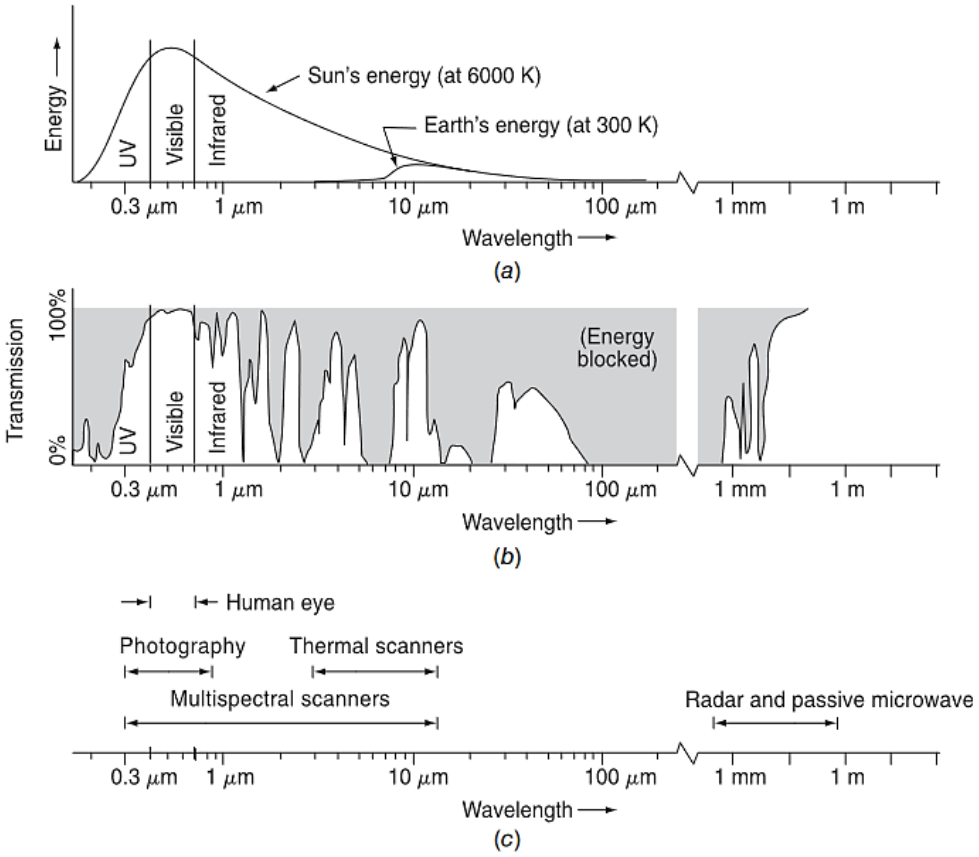


Figure 2-9: The spectral characteristics of: a) electromagnetic energy sources, b) atmospheric transmission and c) common remote sensing systems (Lillesand et al., 2015:p.11).

Numerous remote sensing platforms provide multispectral imagery of the surface of the earth that is accessible to the public. Figure 2-10 provides a summary of the historical and current complement of moderate and high spatial resolution (<30 m) public and commercial optical satellite platforms of interest to the civil engineer. Notable public satellite missions are Landsat-8 and Sentinel-2 (Turner et al., 2021). Landsat-8, part of Landsat Data Continuity Mission, is a multispectral and thermal infrared earth observation satellite operated by NASA and the USGS (USGS, 2010) which has been used to accurately map long-term global surface water changes since the 1980s (Pekel et al., 2016). The Sentinel-2 mission is a constellation of two multispectral imager satellites operated by the

European Space Agency (ESA, 2015) and has been used to provide high cadence and current reservoir and surface water monitoring data (Zupanc et al., 2019; Tottrup et al., 2022). The Landsat-8 imagery platform has a spatial resolution of 30 m in the visible and near infrared spectrum, which can be pansharpened to 15 m, and has a revisit time of 16 days (USGS, 2010; Jensen, 2015:p.75). Sentinel-2 was devised with similar earth observation objectives to Landsat but with the intention of improving return cadence and spatial resolution. To this end, Sentinel-2 is composed of two satellites providing a maximum revisit time of just 5 days with a spatial resolution in the visible and near infrared bands of 10 m (ESA, 2015; Jensen, 2015:p.87). Given the objective of this research to monitor tailings dam ponds, often smaller than 100 m across that can vary rapidly with time, Sentinel-2 was the platform of choice given the improved spatial resolution and higher revisit time.

Very high-resolution satellite platforms provide the opportunity to monitor surface features with a high degree of spatial certainty. Most commercial satellite data presents two major caveats. First the data needs to be procured and so cost is a limiting factor. Secondly commercial satellites generally need to be tasked, which means that competing interests in a region may limit the revisit capability (Turner et al., 2021). PlanetScope is a recent commercial constellation that provides high spatial resolution (<5 m) multispectral imagery with global coverage at a near daily revisit, providing a robust archive of reference imagery for comparison to Sentinel-2 or Landsat 8 (Tottrup et al., 2022). Difficulties posed by monitoring surface water with Sentinel-2 are the limits of the mission's spatial and temporal resolution, both of which are improved over prior public missions (Huang et al., 2018; Turner et al., 2021), cloud obstruction and challenges classifying the large volume of data produced (Tottrup et al., 2022).

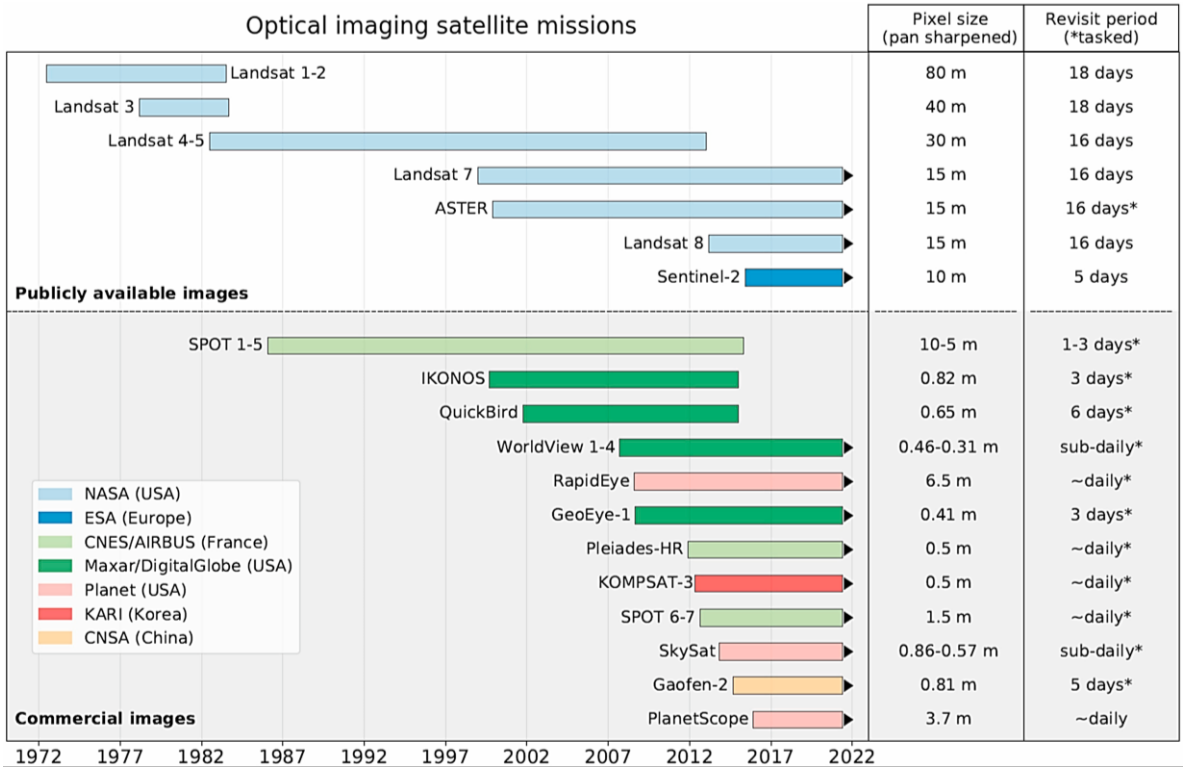


Figure 2-10: Timeline and spatial and temporal resolutions of multispectral satellite imagery available to civilians from 1970 to 2021 (Turner et al., 2021).

There are several techniques to delineate features in satellite imagery. The first and most common method being visual inspection and assessment of the imagery. This technique has been used to generate global statistics on mine activities (Werner et al., 2020) using Google Earth data. Object and pixel based image classification using machine learning can enhance and automate classification of satellite imagery into any number of different categories, aiding data acquisition (Jensen, 2015:p.361). Such techniques require suitable training datasets which pose a challenge where the features requiring classification are not geospatially static, such as moving water surfaces (Bangira et al., 2019). Simple techniques using pixel based thresholds also present an opportunity to classify imagery into binary classes (Otsu, 1979; Huang & Wang, 1995) and detect features such as water boundaries in satellite imagery (Mondejar & Tongco, 2019).

Spectral indexing is a common image processing and enhancement calculation used in optical remote sensing to aid image interpretation. A spectral index

makes use of the reflectance properties of a particular material or surface type to enhance its presence in remotely sensed imagery (Jensen, 2015:p.315). For instance, the normalised difference vegetation index (NDVI) makes use of healthy vegetation's relatively low reflectance in red light and high reflectance in near infrared light to enhance the appearance of vegetation in imagery over other common surface types (Rouse et al., 1973). Similarly, the normalised difference water index (NDWI) is a simple but effective image metric that takes advantage of water's relatively high and low reflectance in the green and near infrared wavelengths respectively. The NDWI uses this property to amplify the parts of a remotely sensed image likely to contain open water, thereby aiding its detection (McFeeters, 1996, 2013). Site-specific thresholding of the NDWI has been shown to be comparable to machine learning techniques to delineate water bodies in multispectral satellite imagery (Bangira et al., 2019; Sekertekin, 2021). Furthermore, thresholding of the NDWI is computationally simpler than machine learning which is important where global scale monitoring systems need to be maintained on a small budget (Zupanc et al., 2019).

2.4 Gap in the literature

Public optical satellite platforms, namely Sentinel-2 and Landsat, are well established tools to monitor water on the surface of the earth (McFeeters, 1996; Pekel et al., 2016; Huang et al., 2018; Tottrup et al., 2022). In the tailings industry satellite imagery was used to determine the pond location prior to failure of Merriespruit dam, setting a precedent in the South African judiciary (Niekerk & Viljoen, 2005; Blight, 2009). Optical satellite imagery data was used to determine the historical location of the pond in post failure investigations of the Fundão and Feijão tailings dams, detailed in the report appendices (Morgenstern et al., 2016; Robertson et al., 2019).

The concept of leading and lagging indicators in the context of tailings dam safety is proposed by Boswell & Sobkowicz (2018). Lagging indicators of dam safety are those measures of performance that can be easily measured but are hard to improve or influence once a change has occurred. An example is the deformation of a slope. Leading indicators on the other hand are typically input oriented, which

may be hard to measure or quantify but can easily improve performance. The leading indicators of tailings dam safety described by Boswell & Sobkowicz (2018) are provided in Table 2-1. The table details where such indicators were present for prominent failures. Interestingly, leading indicators of dam safety amendable to measurement by satellite or aerial imagery were flagged at all failures. These indicators being the beach freeboard, the contained volume of fluid and changes in the water level.

Table 2-1: Leading indicators of tailings dam safety (Boswell & Sobkowicz, 2018)

Historical Tailings Failure, Date / Reference	Buffalo Creek, 1972 Blight et al ('03)	Bafokeng, 1974 Blight et al ('03)	Stava, 1985 Morgenstern (2000)	Merriespruit, 1994 Wagener et al ('97)	Los Frailes, 1998 Alonso & Gens ('06)	Mt. Polley, 2014 Morgenstern et al('15)	Samarco, 2015 Morgenstern et al('16)
Leading Indicator							
Rate of rise	×		×	×	×	×	×
Beach freeboard	×	×	×	×	×	×	×
Height of dam	×	×	×	×	×	×	×
Contained volume of fluid	×	×	×	×	×	×	×
Changes in water level	×	×	×	×	×	×	×
Slope steepening		×			×	×	
Recycle water capacity	×	×	×	×	×	×	×
Foundation geotechnics					×	×	

Public multispectral satellite imagery presents an opportunity to monitor the pond of active tailings dams and track pond behaviour with time (O'Donovan et al., 2022). Geospatial pond data can be used to quantify pond behaviour with time providing insight into the tailings dam water balance, location of the phreatic surface and beach freeboard or minimum beach length. Such information would prove invaluable to stakeholders and communities living in the vicinity of tailings dams, who often have little information regarding the facilities (Roche et al., 2017).

Currently there is no research available on the use of public satellite imagery to proactively monitor leading indicators of tailings dam safety linked the decant pond. To contribute to the common knowledgebase this research aims to determine the accuracy Sentinel-2 measurements of the tailings pond. In addition, research is conducted to assess the viability of using site-specific thresholds to automate pond delineation. If successful this work could, for example, be used to contribute tailings dam safety data to the global database of active tailings dams (GRIDA, 2022).

3 MATERIALS AND METHODS

3.1 Investigation sites

This study considers three active tailings storage facilities in the highveld region of South Africa. The facilities investigated are being raised upstream and are operated using different decant and slurry deposition technologies. One facility uses two compartments and is operated with two separate decant ponds. In total four pond compartments are monitored. The sites are listed in Table 3-1 below. The sites are all operated by the same tailings contractor and were selected to provide a range of pond and facility footprint sizes as well as different ore commodity types and deposition methods. The Elikhulu site was investigated during commissioning and into operation to gain insight into remote sensing during transitions in the construction phase. Different deposition methods and decant systems are also used and the sites are in three different mining locales in South Africa.

Table 3-1: Investigation sites and characteristics at time of investigation

Name	Commodity	Location (decimal degrees)	Deposition Method	Decant System	Construction Stage	No. of Ponds
Elikhulu	Gold	26.489°S 29.084°E	Cyclone	Barge	Commissioning / Operational	2
Ergo	Gold	26.348°S 28.317°E	Cyclone	Barge	Operational	1
Impala	Platinum	25.518°S 27.240°E	Spigot	Penstock	Operational	1

3.1.1 Elikhulu

The Elikhulu Tailings Retreatment plant is a gold reprocessing operation located southwest and adjacent to the town of Evander in the Mpumalanga province. The operation is reclaiming tailings from three mine waste facilities in the vicinity (Pan African Resources, 2017). The Elikhulu Tailings Storage Facility that receives the waste from the reclamation plant was selected for this study (26.489°S; 29.084°E), shown in Figure 3-1. The tailings storage facility is an upstream tailings dam composed of two active compartments, the upper compartment to

the east (referred to hereafter as Elikhulu East) and the lower compartment to the west (referred to hereafter as Elikhulu West). Therefore, Elikhulu has two ponds that require monitoring and the site constitutes two separate compartments in this investigation. The facility is lined with black geomembrane (geoliner) which was apparent during the observed commissioning stage. Geomembranes are widely used in waste management to provide environmental barriers and are often composed of readily available plastics, such as high-density polyethylene (Department of Environmental Affairs, 2013). To stabilise geomembranes against ultraviolet degradation, carbon black is used by manufacturers to absorb deleterious radiation and re-emit this energy safely in long wavelength infrared (Koerner, 2012:p.33). Geomembranes stabilised with carbon black tend to absorb in most wavelengths of incident solar radiation and so the scenario at Elikhulu presents an interesting site characteristic for remote sensing.

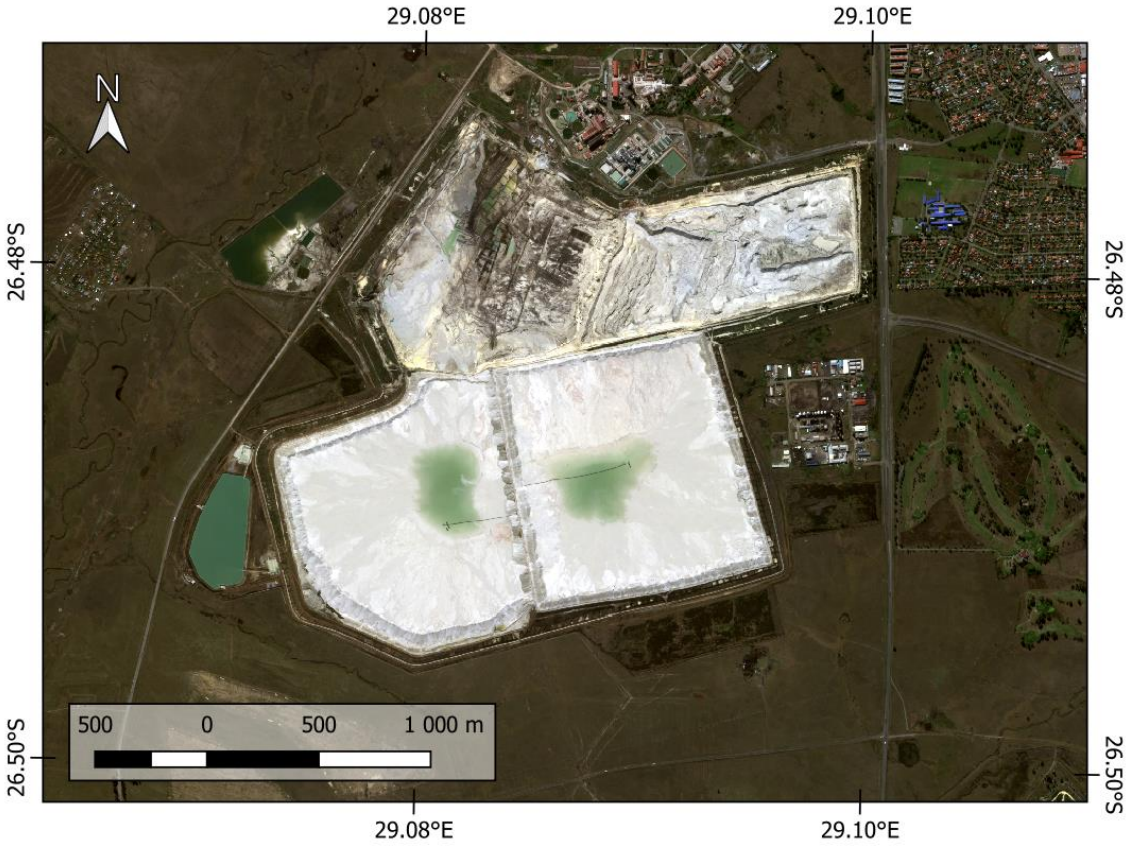


Figure 3-1: Elikhulu SkySat image acquired on 26 April 2022 rendered in natural colour.

The Elikhulu tailings dam site is adjacent to a decommissioned tailings storage facility which is being reclaimed by the operation. The Elikhulu tailings dam facility was commissioned in late 2018 and so this study captures the commissioning of the facility and discharge of tailings into the geomembrane lined basin.

The upper (east) and lower (west) compartment floodable plateau areas are both approximately 1.1 km² in plan area with nominal pond areas of between 10 x10^3 m^2 and 250 x10^3 m^2. Nominal pond widths are between 80 m to 110 m for the east compartment and 190 m to 230 m for the west compartment.

3.1.2 Ergo

The DRD Gold Ergo operation reprocesses tailings from reclaimed mine waste facilities located to the south-east of Johannesburg in the Witwatersrand region of Gauteng. Reprocessed tailings is disposed of at the Ergo Brakpan Tailings Storage Facility, also known as Withok Tailings Dam (26.348°S; 28.317°E) (DRDGOLD Limited, 2022), shown in Figure 3-2. The site will be referred to hereafter as Ergo. The Ergo tailings dam has a floodable plateau area of 3.8 km^2. The pond area ranges between 0.8 km^2 and 2.0 km^2 and has a nominal width of between 800 m and 1 200 m.

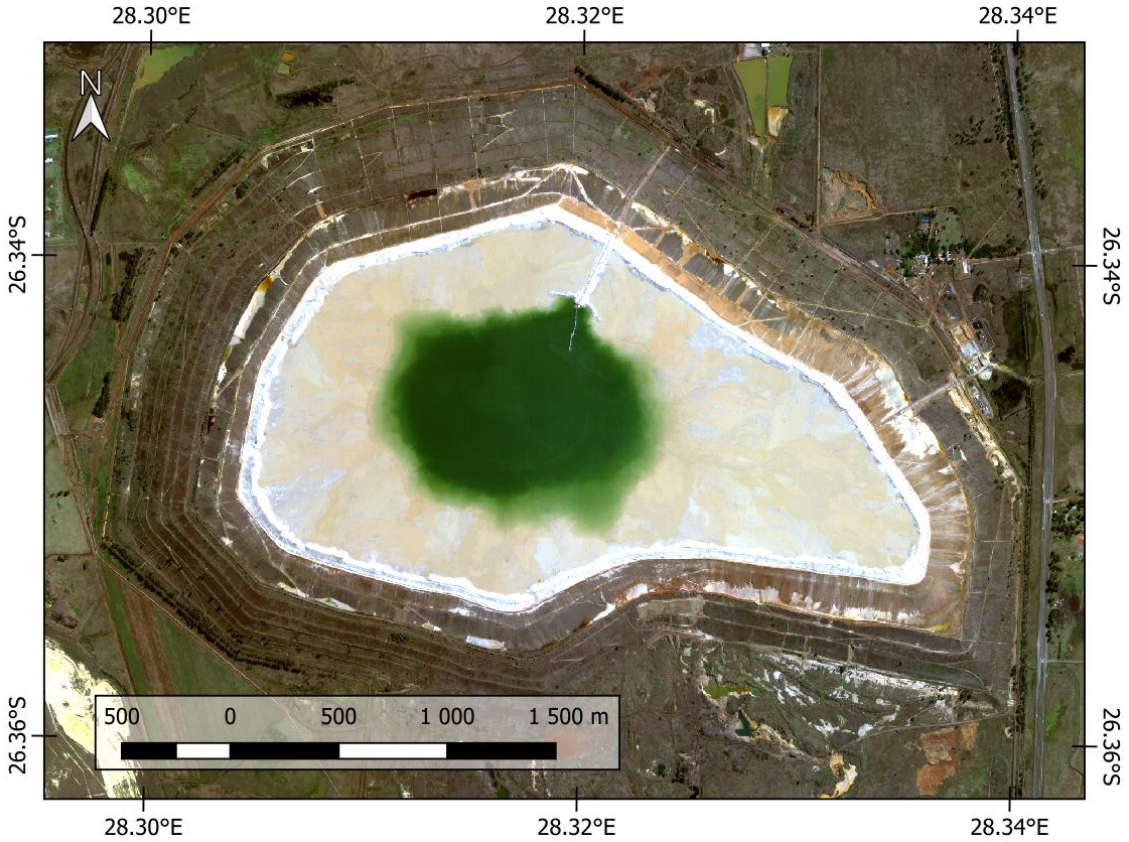


Figure 3-2: Ergo SkySat image acquired on 26 April 2022 rendered in natural colour.

3.1.3 Impala

The Impala Rustenburg platinum mining complex is located on the western limb of the Bushveld complex, a prominent platinum group metal mining area north of the Magaliesberg mountain range. The Impala Rustenburg mining area is located to the north-east of Rustenburg in the Northwest province and comprises multiple shafts and concentrating and smelting plants. The operation disposes of tailings waste material in the Impala Rustenburg Dam 4 (25.518°S; 27.240°E) (Implats, 2022), shown in Figure 3-3.

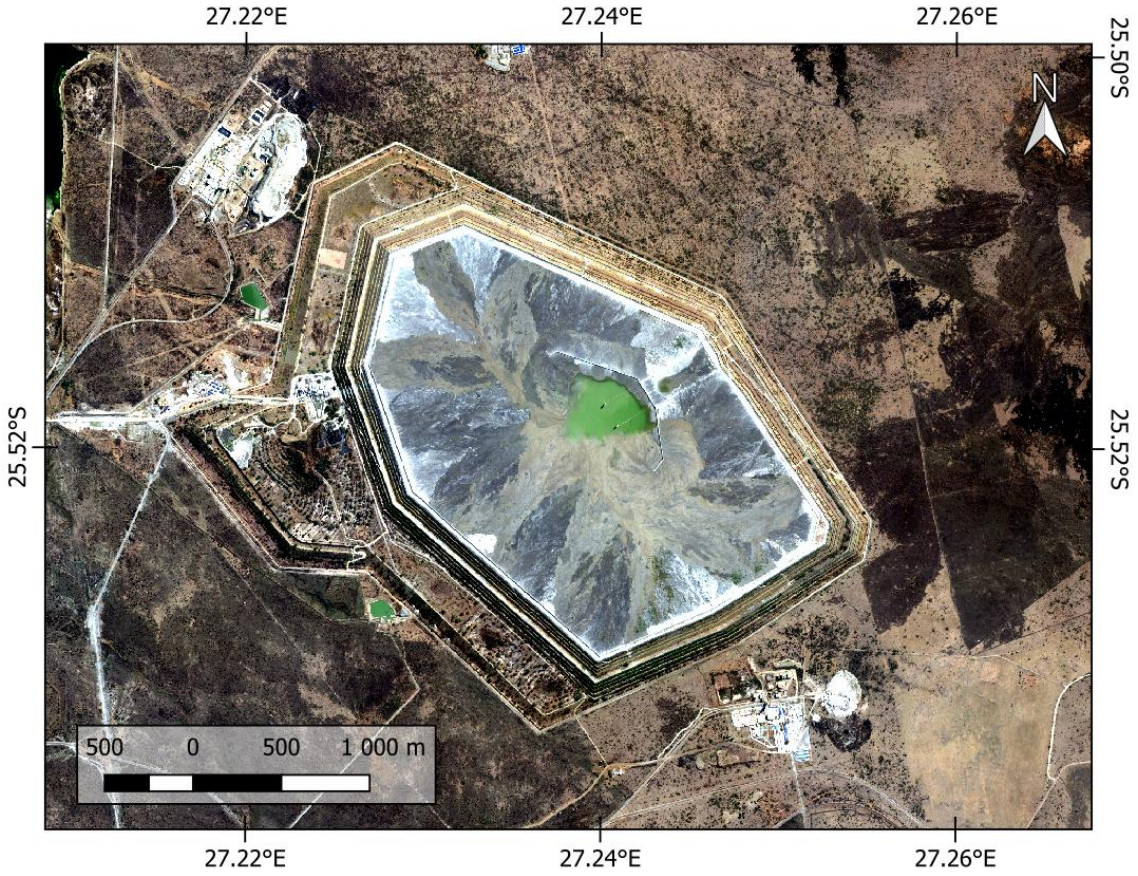


Figure 3-3: Impala SkySat image acquired on 6 April 2022 rendered in natural colour.

The Impala Platinum Rustenburg Dam 4, referred to hereafter as Impala, is a tailings dam with a floodable plateau area of 3.9 km^2, similar to Ergo. The pond is generally kept smaller on the dam, when compared to Ergo, in relation to the floodable area, with an area of between 200 x10^3 to 50 x10^3 m^2 and a nominal width of 300 to 450 m.

3.2 Imagery

3.2.1 Introduction

The spatial resolution of an imaging system is a measure of the smallest object or distance defined by such a system. In digital imagery, defining an object, or determining a distance, entails interpreting relationships between pixels. The nominal size of these pixels in geospatial imagery, also referred to as the ground

sample distance, is associated with the ability of the imagery to resolve objects and the distances between them. In general, finer pixel spacing, or smaller ground sample distances, provide higher spatial resolution. It is generally accepted that higher spatial resolutions provide the ability to define objects and distances with a greater degree of certainty. However, as the quality of geospatial imagery is not only quantified by its pixel density, it is also important to consider other imagery properties over and above the spatial resolution. In the case of earth observation data, each image represents a snapshot of the earth's surface in time. A shorter time between images provides the ability to define temporal changes at a higher resolution with time. This time between images is referred to as the temporal resolution of the imaging system, where shorter cadences between acquisitions represents a higher temporal resolution. Further to spatial and temporal resolutions, electromagnetic energy available to an imaging system may be filtered or separated into bandwidths, or bands for short. This allows the intensity of particular bands to be interpreted independently other wavelengths. Resolving colour, when speaking in terms of the visible light spectrum imagery, and spectral emission or reflectance properties, speaking more generally, requires independent intensities of different bands of light. A higher number of bands and narrower bandwidths provide increased resolving power and classification abilities. This is referred to as spectral resolution. A further property of remote sensing systems is the ability to differentiate between fine changes in the intensity of light within a particular bandwidth, referred to as radiometric resolution. Modern satellite systems must discretise signals into packets of data for digital transmission and the radiometric resolution of an image may be quantified as the bit depth of the pixels in each bands acquired by the system (Lillesand et al., 2015; Jensen, 2015).

It is important to consider the limitations and trade-offs required to achieve certain resolutions, be that spatial, temporal or spectral. An imaging system may provide better temporal resolution by regularly covering wider swaths of ground area using a wider field of view or higher orbit altitude but at the expense of spatial resolution. Furthermore, given that the smaller ground sensing distance associated with greater spatial resolution reduces the area from which light is

gathered by each pixel of a sensor, a higher spatial resolution requires light be sensed from a wider bandwidth, imposing a limitation on the spectral resolution. Furthermore, sensing a narrower bandwidth of light to achieve greater spectral resolution reduces the amount of incident electromagnetic radiation available for a remote sensing system to convert into a digital signal, and so a trade-off exists between spatial and spectral resolutions. At the lower energy parts of the electromagnetic spectrum incident on or emitted from earth, the amount of energy available at the sensor may dictate what ground sensing distance scales are possible (Lillesand et al., 2015; Jensen, 2015).

Imagery in this study is divided into input and reference data. Input data is the imagery being assessed for use in temporal tailings monitoring. Reference data provides comparison for assessment of the accuracy of the input imagery. Sentinel-2 was selected as the input data of this study.

It is good practice to use reference data with a finer spatial resolution than data being evaluated (Olofsson et al., 2014). Given the temporal characteristics of this work, the main reference datasets considered needed to also have high temporal cadence and finer spatial resolution than Sentinel-2 while still providing spectral resolution that matches Sentinel-2. PlanetScope provides high-resolution imagery (<5 m). The imagery was identified to meet the required criteria for use as reference imagery. Moreover, PlanetScope has been used before as reference data in the assessment of Sentinel-2 surface water measurements by Tottrup et al. (2022).

To provide additional reference data over and above PlanetScope, very high-resolution (<1.0 m) images were acquired by tasking multispectral satellite imagery and from aerial and drone visible spectrum orthophoto archives. All satellite imagery provides at least visible and near infrared spectral data, while the aerial and drone imagery provide only visible spectrum data. In practice, the very high spatial resolution of the orthophoto imagery compensates for the lack of near infrared band data by allowing visualisation of fine surface textures such as water surface ripples.

At each site, Sentinel-2 and PlanetScope images were selected pairwise per month for each of the thirty-six months of the main study period, as described in section 3.2.1 below. Images were paired when acquisition of a cloud free image coincided on the same day in the datasets. In the few situations where cloud free imagery could not be obtained from both databases on the same day, a concession was made by first selecting a Sentinel-2 image for the month in question and then finding the nearest PlanetScope image without cloud obstructing the tailings pond. In rare cases where no cloud-free Sentinel-2 image was present in the database for a given month in the study period, imagery at the end of the preceding or start of the following month was considered. Cloud-free imagery was prioritized over minimization of the temporal separation between the input and reference imagery sets. SkySat images were tasked to coincide with the acquisition of a Sentinel-2 image. As the dates of drone and aerial orthophotos could not be tailored for this study, images were paired with the temporally closest Sentinel-2 image.

Very high-resolution satellite and aerial orthophoto imagery represent the best available data on the tailings pond. This data is therefore used in a separate comparison to Sentinel-2 and is collectively referred to as the *very high-resolution reference dataset.* The images are reproduced in Appendix-A. The Sentinel-2 and PlanetScope imagery is not directly reproduced due to the volume of data. The catalogue of images in Appendix-C provides a list of the Sentinel-2 and PlanetScope images used which can be sourced directly from Sentinel-Hub, Google Earth Engine or Planet Labs (see section 3.3 for description of these platforms).

A summary of the datasets used is given in Table 3-2 below.

Table 3-2: Overview of imagery sources and basic properties

Imagery Source *Use*	**Spatial Resolution (m)**	**Spectral Bands Used**	**Revisit**
Sentinel-2 *Input*	10.0	Visible + near infrared	5 days
PlanetScope *Reference*	3.0 to 4.2 Resampled to 3.0	Visible + near infrared	~daily
SkySat *Reference*	0.58 - 0.86 panchromatic 0.76 - 1.0 multispectral Resampled to 0.5	Visible + near infrared	~daily (tasked)
CDNGI *Reference*	0.25	Visible	Ad-hoc
Drone *Reference*	0.10	Visible	Ad-hoc

3.2.2 Temporal domain of the study

The bulk of the investigation uses data acquired within a three-year period, from the start of 2019 to the end of 2021. This date range was chosen to coincide with beginning of the ESA's Sentinel-2 surface reflectance dataset on Google Earth Engine (GEE Data Catalogue, 2022) for the study region at the time of the research. The study and main data collection period ended at the start of 2022, to allow time for interpretation and analysis. This period was used to compare the input Sentinel-2 data with the higher spatial resolution (<5 m) PlanetScope reference imagery. Data was acquired and catalogued to provide evenly distributed data points in time throughout the period.

The very high spatial resolution reference imagery (<1.0 m) acquired by SkySat, the CDNGI and drone survey, is not readily available or evenly distributed in time. This influenced the allowable temporal domain for comparison of Sentinel-2 to this reference data. Access to the very high-resolution satellite tasking platform was available only in 2022. Aerial and drone orthophotos were acquired in 2018, 2020, and 2021 of Ergo, Elikhulu and Impala respectively. Thus, a wider study period with less stringent control over temporal distribution of the data, applies to this class of higher spatial resolution reference imagery (2018-2022).

3.2.3 Input data

The objective of this study is to assess the use of Sentinel-2 to make tailings dam decant pond measurements. Therefore, the input data of this study is imagery acquired by the Sentinel-2 mission (referred to hereafter as Sentinel-2 or S2). Sentinel-2 is a satellite constellation operated by the European Space Agency (ESA). It is currently comprised of two identical satellites (Sentinel-2A and 2B) in the same near polar sun-synchronous orbit but separated by half a phase (180 degrees). This orbit provides a descending node equator crossing time of 10:30 (local solar time), similar to other land monitoring satellite missions, allowing data integration between missions. The mean orbital altitude is 786 km with an imaging swath width of 290 km (ESA, 2015). Imagery data processed to top of atmosphere and surface reflectance is publicly available shortly after acquisition, usually within a few hours, in an archive dating back to June 2015 and March 2017 for top of atmosphere and surface reflectance products respectively (GEE Data Catalogue, 2022). This research makes use of the surface reflectance dataset published by the ESA on Google Earth Engine. Local South African coverage of the dataset begins in late 2018. Where Sentinel-2 images were required for analysis prior to the start of the published surface reflectance dataset (Level 2A), atmospheric correction was performed on the available top of atmosphere dataset (Level 1C) using the Sensor Invariant Atmospheric Correction (SIAC) tool (Yin et al., 2022) implemented on Google Earth Engine. Sentinel-2 operates in the coastal blue, visible, near infrared and shortwave infrared parts of the electromagnetic spectrum. This study makes use of the visible and near infrared bands with spatial resolution of 10 m, shown in Figure 3-4 below.

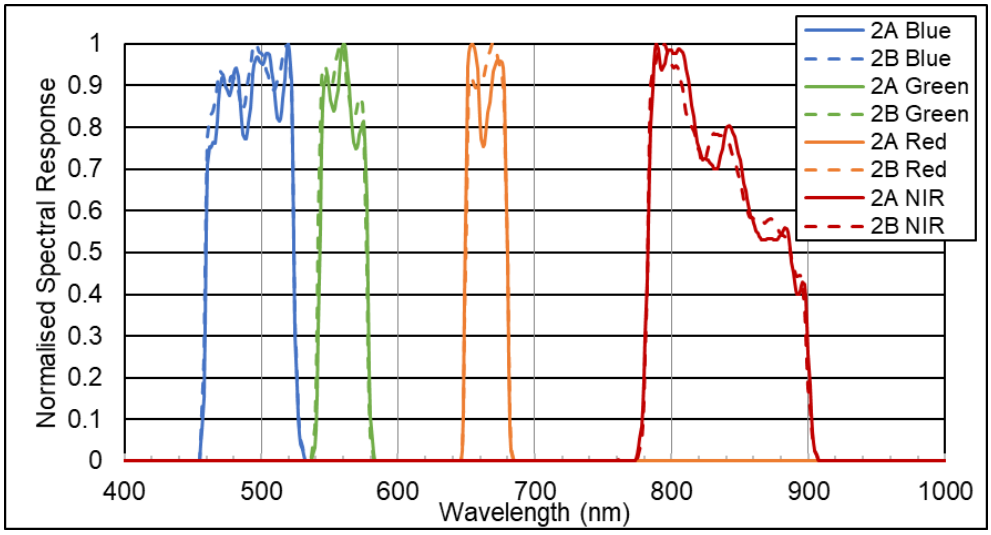


Figure 3-4: Sentinel-2A and 2B normalised spectral responses for the 10 m bands (ESA, 2022).

For comparison to the PlanetScope reference imagery, one Sentinel-2 image was acquired per month for each of the 36 months in the study period. Furthermore, Senintel-2 images were obtained when acquired on the same day as a SkySat image acquisition. Sentinel-2 images were obtained as near in time as practically possible to the available aerial and drone imagery from the CDNGI and surveyor.

3.2.4 Reference data

To assess the accuracy of Sentinel-2 tailings dam decant pond measurements, reference data of higher spatial resolution is required. As the tailings pond can vary rapidly in plan dimensions with time it is important that temporal separation of the input and reference data was minimised. The sources of reference data are discussed in the following sections. All satellite reference data was pre-processed to orthorectified surface reflectance products.

3.2.4.1 PlanetScope

Reference data required high temporal cadence, blue, green, red and near infrared bandwidth acquisition with similar spectral profiles to Sentinel-2 at a finer spatial resolution. To this end, PlanetScope imagery was acquired for comparison to Sentinel-2.

PlanetScope is a commercial constellation of satellites operated by Planet Labs PBC. Access to the data archive was possible through Planet Labs PBC's research access grant which allows download of a maximum of 50 images per month for academic research. PlanetScope satellites use the CubeSat 3U form factor, measuring approximately 10 x 10 x 30 cm before the solar panel array is deployed. The constellation comprises approximately 130 satellites in sun synchronous near polar orbits at altitudes of between 450 and 580 km with equator crossing times of between 9:30 and 11:30 am (local solar time). The constellation has been launched over several years spanning three satellite generations. Given the high number of satellites at multiple different orbit phases, the constellation can provide near daily imagery of every point on earth with a ground sample distance of between 3.0 and 4.2 m. Orthorectified imagery products are resampled to 3.0 m. The constellation is currently made up of three generations of satellites, named Dove Classic (PS2), Dove-R (PS2.SD) and SuperDove (PSB.SD). The Dove Classic satellites, being the first-generation satellite that started image acquisition in July 2014, use a Bayer Array split-frame sensor to capture visible and near infrared spectrum data. The subsequent generation Dove-R and SuperDove satellites began image acquisition in March 2019 and March 2020 respectively. The satellites use an updated 'Butcher Block' imaging system that provides a higher spectral resolution than the earlier Bayer Array and split frame design (Planet, 2022). As the constellation is replenished, older satellites are replaced with newer generations and is therefore in constant flux. The normalised spectral responses of the two sensor classes used in this study are provided in Figure 3-5 and Figure 3-6 below.

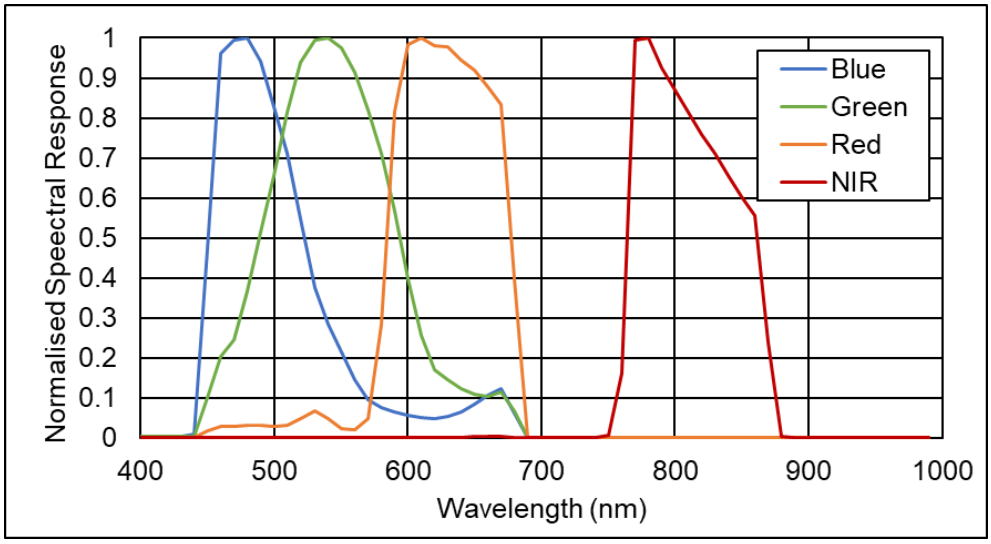


Figure 3-5: An indicative normalised spectral response of the Dove Classic constellation (Planet, 2018).

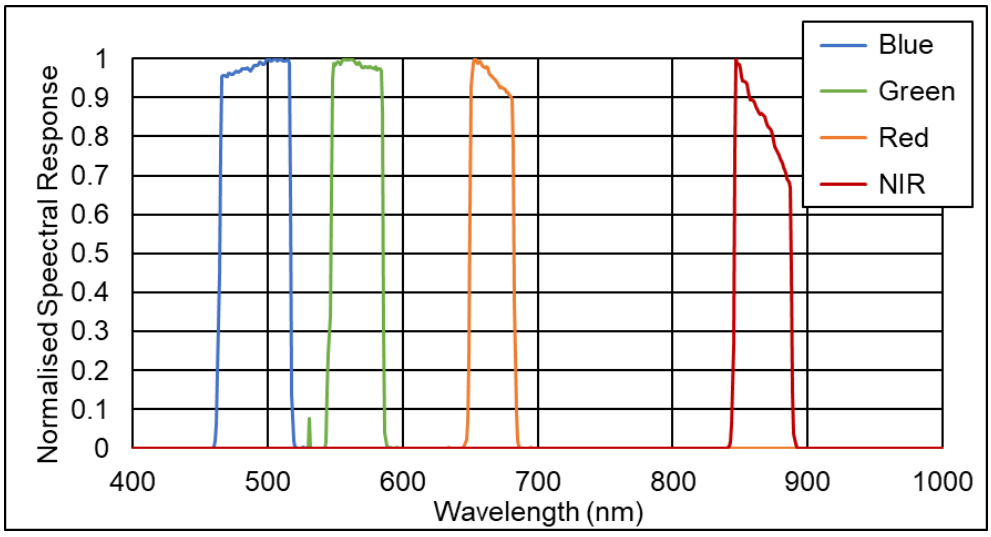


Figure 3-6: An indicative normalised spectral response of the blue, green, red and near infrared bands of the Dove-R and SuperDove instruments (Planet, 2018).

The two imaging systems show different spectral responses in Figure 3-5 and Figure 3-6. The Dove Classic sensor generates significant overlap between visible light bandwidths, seen in Figure 3-5, because of the matrix interpolation required to process imagery into discrete band values at each pixel from the Bayer Array filter. The 'Butcher Block' type sensor of the Dove-R and SuperDove

instruments provides a higher spectral resolution with narrower bandwidths and no overlap between bands as displayed in Figure 3-6. The visible bands are analogous to Sentinel-2. The NIR band of the Dove-R and SuperDove sensors is narrower than and falls within the 10 m NIR band (band 8) of Sentinel-2.

One PlanetScope reference image is paired to each Sentinel-2 image per month for each of the 36 months investigated at each of the study sites. This study used a combination of all Planet sensor types as the constellation could only provide the daily imaging required to pair the images with Sentinel-2 if all sensor types were considered. PlanetScope imagery was visually assessed and not automatically classified to reduce the impact of differences in the spectral responses of the satellites within the constellation. Where possible, the higher spectral resolution sensors aboard the Dove-R and SuperDove platforms were favoured given their similarity to Sentinel-2. Lists of the PlanetScope images and sensor types for each site are provided in Appendix-C.

3.2.4.2 SkySat

SkySat is a constellation of 21 very high spatial resolution multispectral satellite imagers. The constellation is made up of satellites in sun-synchronous orbits and inclined orbits at altitudes of between 600 and 400 km (typically less than 450 km). The equatorial crossing time for the satellites in sun-synchronous orbit is either 10:30 or 13:00 (local solar time) and varies for the satellites in inclined orbits. To achieve a high spatial resolution, the constellation uses imagers equipped with 3.6 m focal length telescopes. The constellation can achieve ground sample distances of less than 0.81 m for multispectral bands. After orthorectification and pan sharpening images are provided at a spatial resolution of 0.5 m (Planet, 2022).

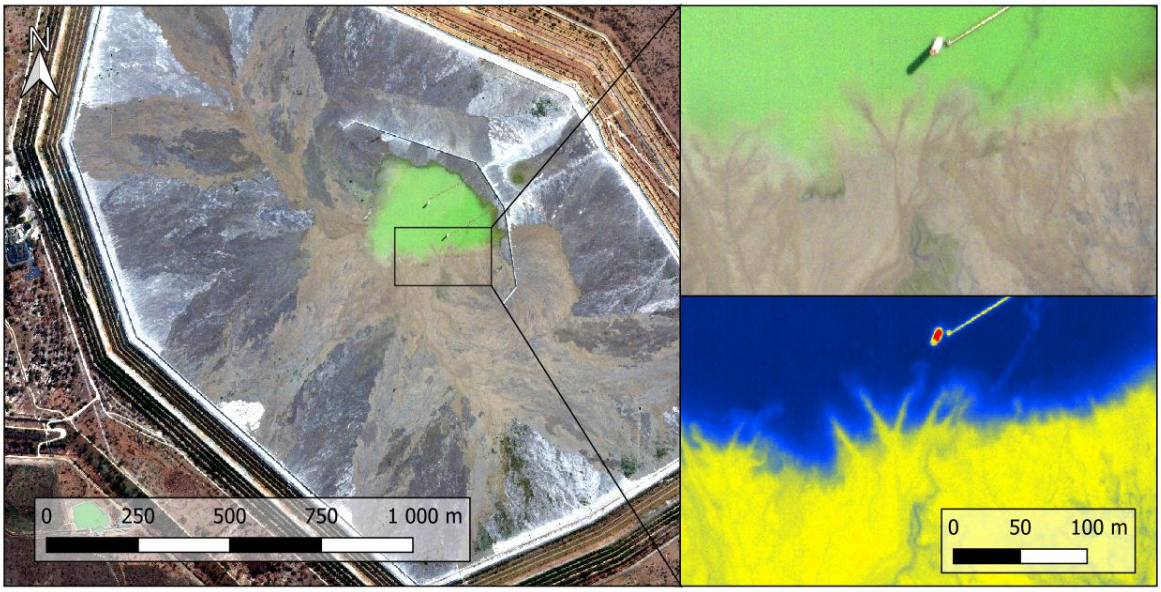


Figure 3-7: SkySat imagery and enlargement depicting the finest spatial resolution achieved as well as the detail rendered in the near infrared band.

The spectral band resolution is shown below, with a pan band (not shown) covering the whole spectral domain of the multispectral bands.

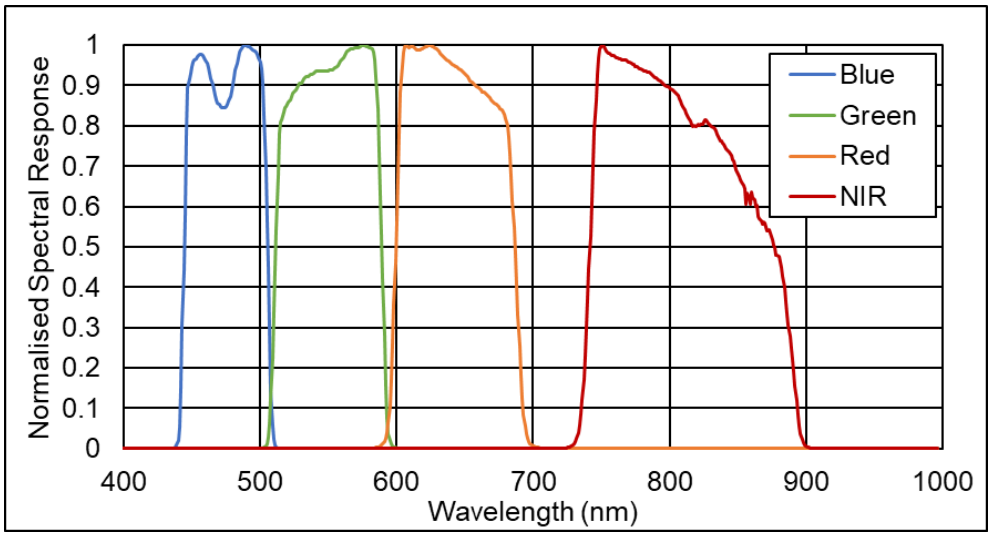


Figure 3-8: An indicative normalised spectral response of the SkySat constellation (Planet, 2018).

Comparing the normalised spectral response curves above, the SkySat sensors do not provide the spectral resolution of Sentinel-2 or the Dove-R and Super Dove sensors. This is likely a trade-off between spatial and spectral resolution. Smaller

areas sensed by each pixel in a finer spatial resolution sensor collect radiant light from a smaller area of the ground surface. Therefore, pixel sensors need to either be more sensitive or capture light from a larger bandwidth to keep the signal to noise ratio within tolerance.

SkySat was chosen as a reference dataset as it allowed interpretation of tailings dams in very high spatial resolution multispectral imagery.

3.2.4.3 Drone and aerial orthophoto imagery

Orthophoto imagery acquired by drone survey was obtained for the Elikhulu study site with a spatial resolution of 10 cm within the visible light spectrum. Aerial (airplane borne camera) photograph imagery was obtained from the CDNGI for the Ergo and Impala sites. The CDNGI aerial photograph images were acquired in visible spectrum with a spatial resolution of 25 cm. Examples of the orthophoto data are shown in Figure 3-9 and Figure 3-10 below. Data is reproduced in Appendix-A for reference.

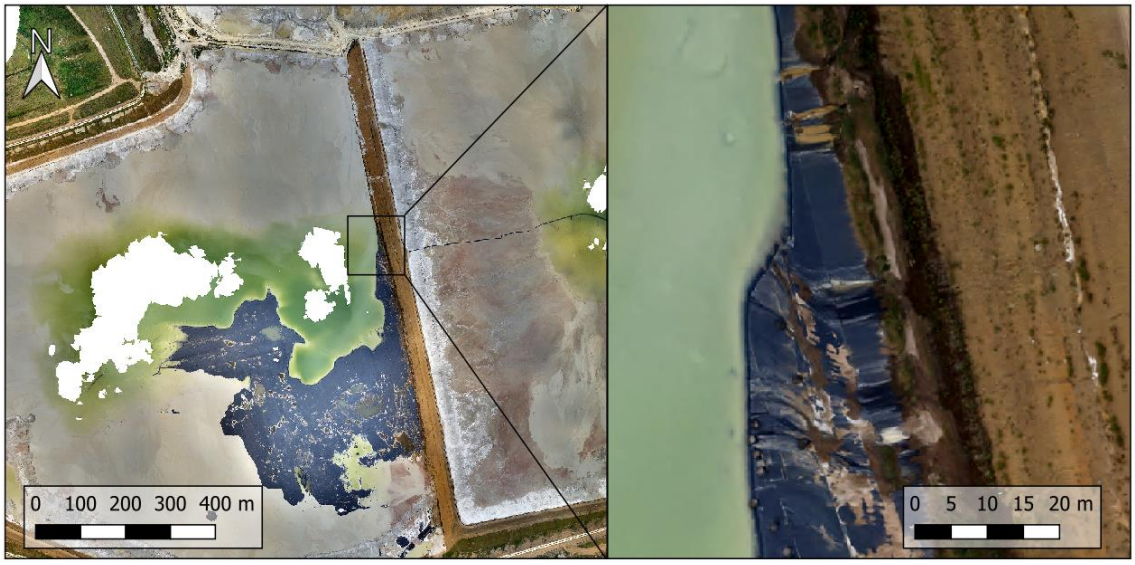


Figure 3-9: Drone survey imagery and enlargement depicting the finest spatial resolution achieved.

Figure 3-9 presents the drone orthophoto that was acquired at Elikhulu on 2 March 2020 with a spatial resolution of 10 cm. The orthophoto is composed of a mosaic of multiple smaller images obtained by a drone flying at a low altitude

carrying a small format digital camera acquiring data in the visible spectrum (DJI, 2022). Areas where no imagery was acquired, such as in the centre of the pond are shown white. The above imagery was used to delineate the tailings pond edge.

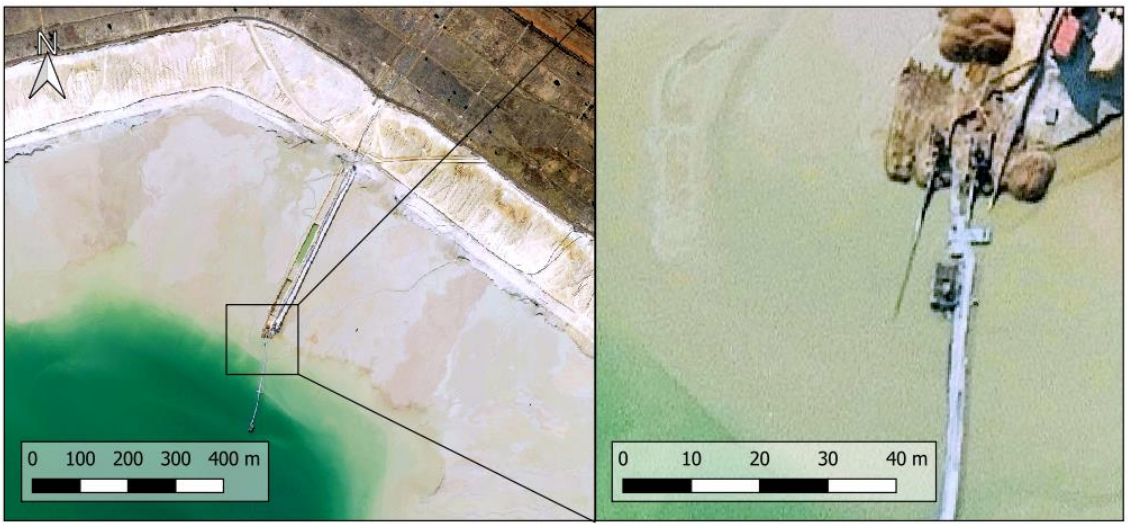


Figure 3-10: CDNGI aerial imagery and enlargement depicting the finest spatial resolution achieved.

Aerial photography is a similar source of orthophoto data to drone imagery, however, images are typically acquired from a higher altitude, using a large or medium format digital camera. This technology allows for a wider swath per image and the use of heavier equipment, typically aboard a light fixed wing aircraft (Jensen, 2015:p.101). As observed with the CDNGI orthophotos, fewer large images were stitched together to create the final mosaic when compared to the drone orthophoto mosaic. The aerial orthophoto imagery has a spatial resolution of 25 cm as shown in Figure 3-10 above. This data was used as reference imagery because of its very high spatial resolution.

3.2.4.4 Alternative reference data

Tachymetric measurement of the pond edge would provide the most robust ground truth data on the tailings pond location. However due to the often low tailings material densities and strengths around the pond (Vermeulen, 2001; Blight, 2009; Santamarina et al., 2019) directly surveying the pond edge is

potentially too dangerous. In engineering practice, very high-resolution aerial and satellite imagery provide the data used to measure the tailings pond edge (Mitchell et al., 2018).

Multispectral and hyperspectral aerial imagery could theoretically be acquired (Jensen, 2015:p.104). Such data was not available for this study. Therefore, the very high-resolution data acquired by SkySat had the advantage of a near infrared band that was not available in the CDNGI or drone aerial orthophotos.

3.3 Data acquisition and processing tools

Data was catalogued, acquired and processed using several web-interface tools and an open-source GIS application. The platforms are described individually in the section that follows.

3.3.1 Sentinel Hub EO Browser

Sentinel Hub EO Browser is a web interface that allows members of the public to interact with a large catalogue of satellite imagery. The catalogue accessible to the public comprises Sentinel-2 and Landsat-8 among others and provides intuitive tools to browse and filter the data. A screenshot of the interface is shown in Figure 3-11.

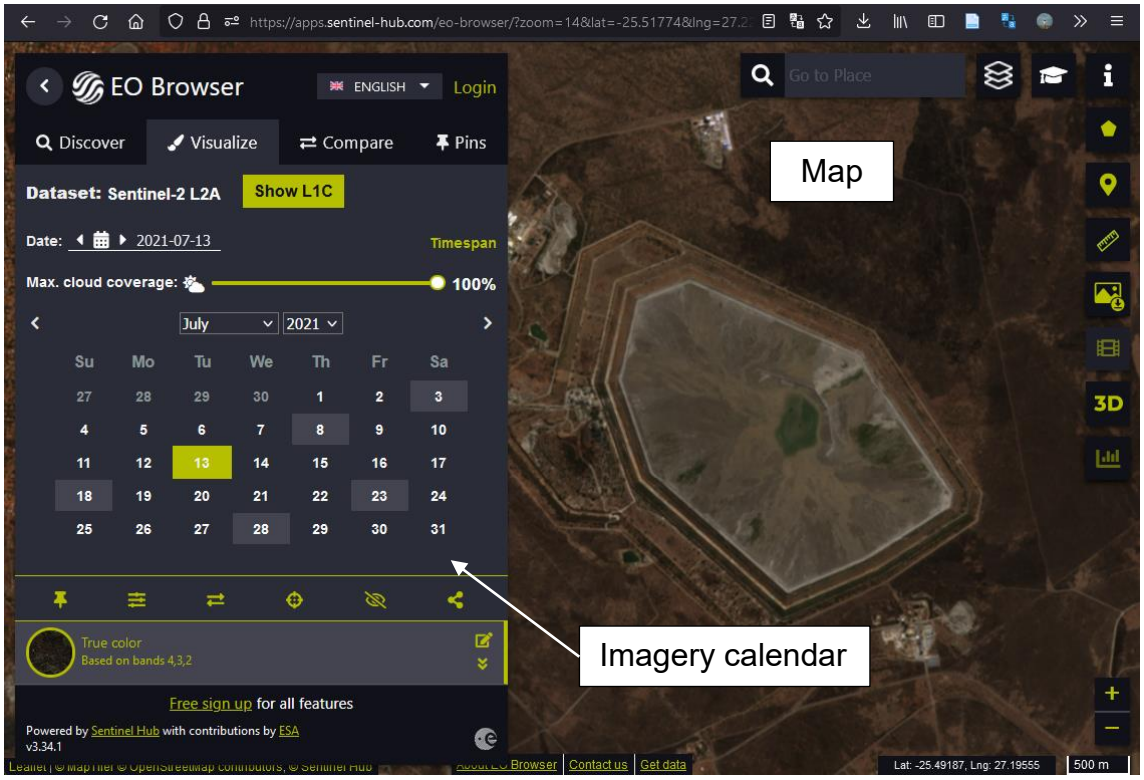


Figure 3-11: Sentinel Hub EO Browser user interface.

The Sentinel Hub EO Browser interface was used to visually inspect Sentinel-2 imagery in chronological order, using the imagery calendar and map shown in Figure 3-11. Sentinel-2 was visually inspected for cloud presence alongside PlanetScope using Planet Explorer, discussed below. Dates of selected Sentinel-2 images were listed for retrieval from the Google Earth Engine data catalogue.

3.3.2 Planet Explorer

PlanetScope data is accessible via a web-based interface managed by Planet Labs PBC, called Planet Explorer. The platform provides users an intuitive interface to browse the PlanetScope imagery catalogue and inspect selected images as shown in Figure 3-12. Images selected from the Planet Explorer imagery catalogue were ordered and processed for download as orthorectified surface reflectance asset types.

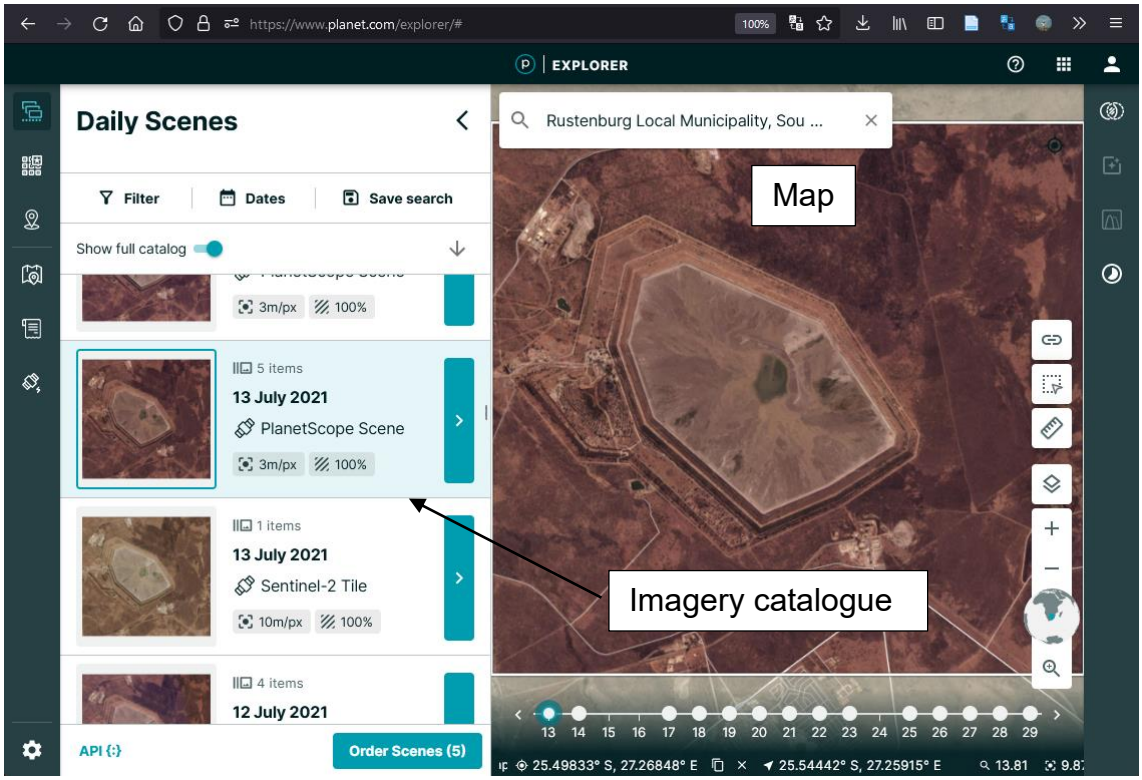


Figure 3-12: Planet Explorer web interface.

The Planet Explorer web interface was used alongside Sentinel Hub EO browser to visually inspect both imagery sets in parallel. Access to PlanetScope data was enabled through a research licence agreement which provided a download quota of a maximum of 50 images or 5 000 km^2 per month.

3.3.3 Google Earth Engine

Google Earth Engine (GEE) is a platform that allows users to run geospatial analysis on Google's computing infrastructure (Gorelick et al., 2017). The system is comprised of an analysis engine and a large data catalogue that includes a comprehensive archive of open access earth observation imagery. The platform is free to use for research and non-profit work. The Code Editor is an integrated development environment (IDE) that provides web-based access to the GEE JavaScript application programming interface (API).

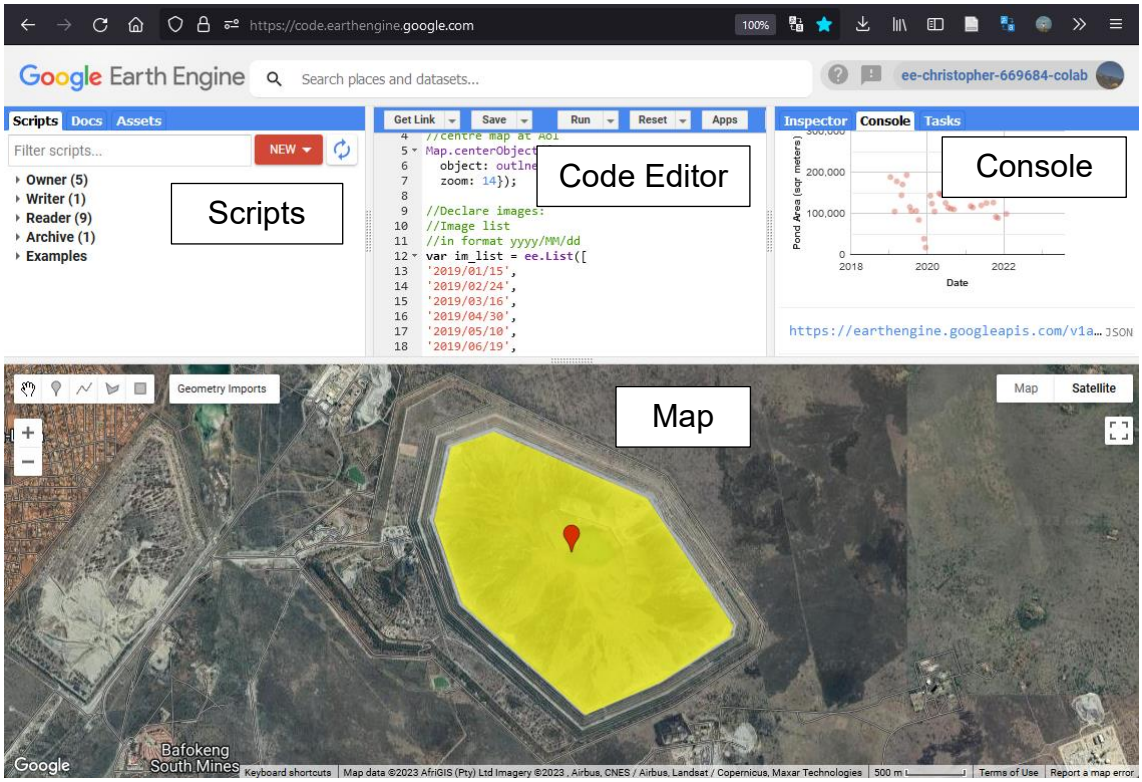


Figure 3-13: Google Earth Engine JavaScript Code Editor interface.

The Code Editor IDE provides access to the user's library of scripts, a comprehensive library of available functions and personal data assets from the top lefthand panel shown in Figure 3-13. The top central panel in Figure 3-13 is the Code Editor and is where code is written and debugged. Analysis results and code output are presented in the map and in the console located in the bottom and top righthand panels, respectively, in Figure 3-13. In addition, current and past output tasks can be monitored, and the map data inspected from the top righthand panel. Google Earth Engine was used to pre-process and download Sentinel-2 imagery and allowed the aggregation and iterative analysis of hundreds of Sentinel-2 images needed to investigate image thresholding. Sentinel-2 imagery was downloaded from GEE after the data was cropped to the area of interest. When required, top of atmosphere reflectance Sentinel-2 imagery was atmospherically corrected using the SIAC tool on GEE.

3.3.4 CDNGI Geospatial Portal and SkySat Tasking Dashboard

Very high-resolution imagery was sourced from the catalogue of aerial imagery on the CDNGI Geospatial Portal, shown in Figure 3-14, and by tasking SkySat image acquisitions via the Planet Tasking Dashboard, shown in Figure 3-15.

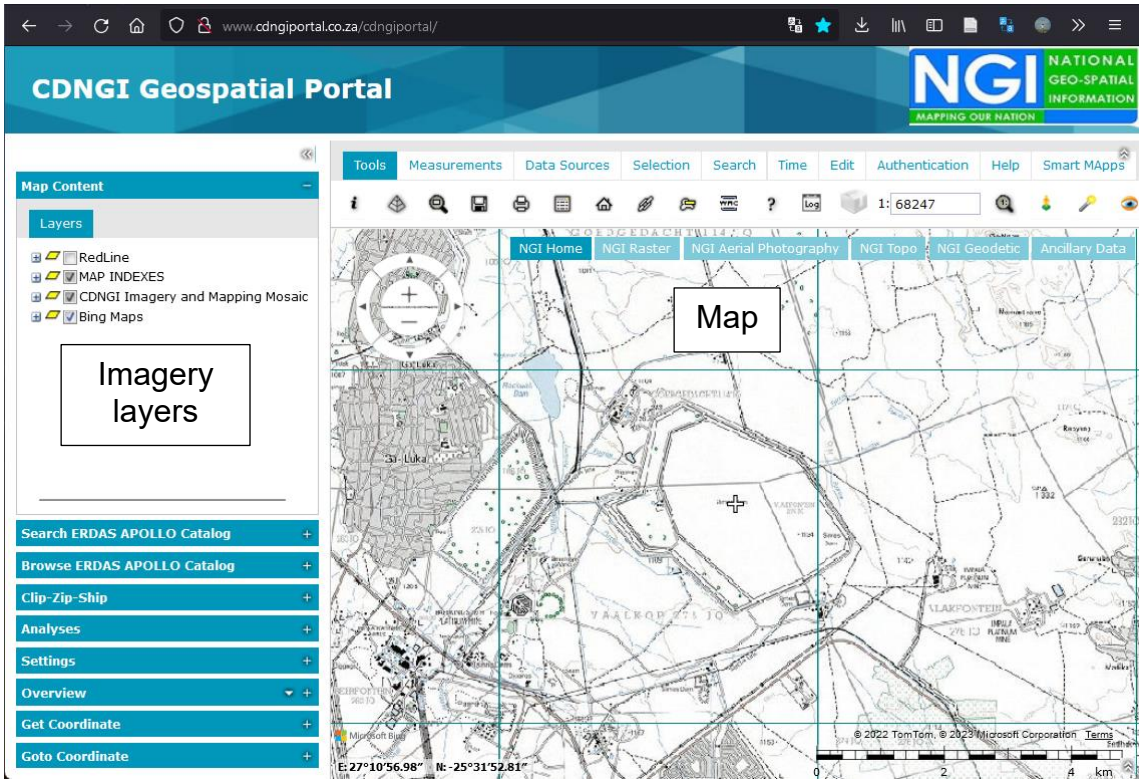


Figure 3-14: CDNGI Geospatial Portal.

Imagery was identified on the CDNGI Geospatial Portal, Figure 3-14 above, using the available imagery layers. The imagery can be inspected via the map interface. Suitable images were ordered directly from the CDNGI by email correspondence.

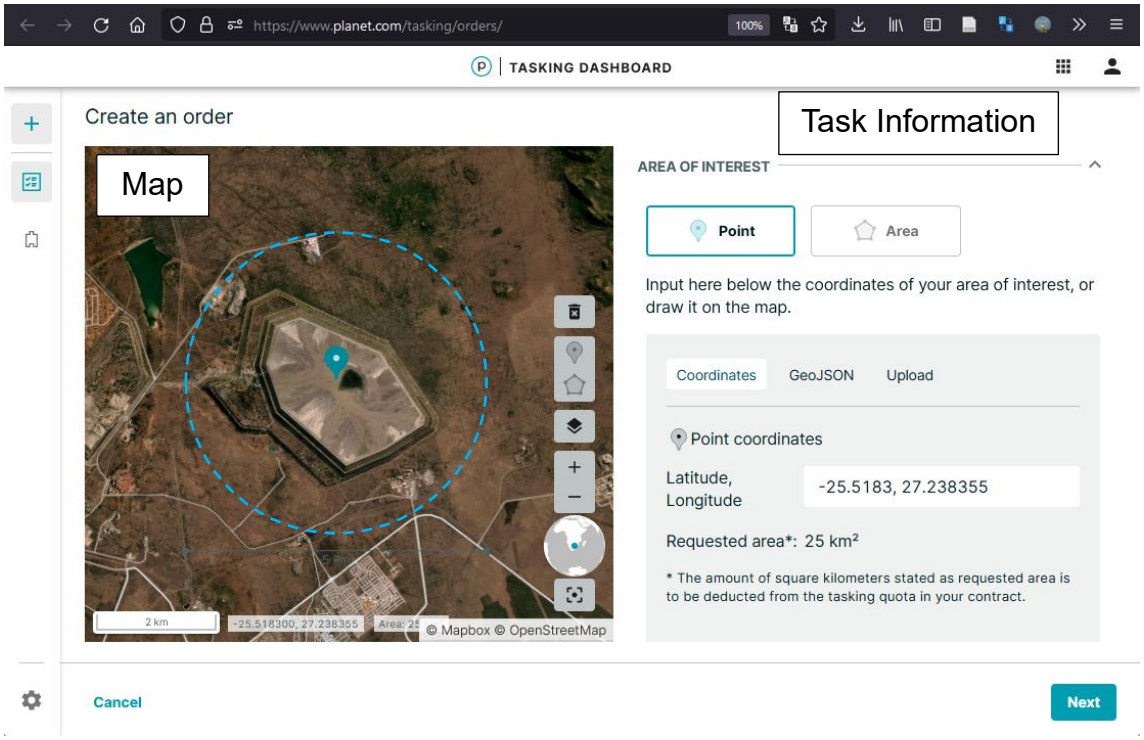


Figure 3-15: SkySat Tasking Dashboard.

SkySat imagery was tasked by requesting a point acquisition (a circle of 5 km diameter) within a two-week window period, as shown in Figure 3-15. To increase the probability of acquiring a SkySat image on the same day as a Sentinel-2 image, the start of a task was manually timed to coincide with a Sentinel-2 pass and a clear weather forecast for the area of interest. This did not guarantee coinciding acquisitions but was successful on occasions when there were no competing orders in the region and low cloud cover prevailed. Once a SkySat image had been successfully acquired the image was inspected and downloaded from the Planet Explorer interface. SkySat imagery can be processed by Planet Labs to various product levels, referred to as ‘assets’. Orthorectified surface reflectance assets were downloaded for local analysis.

3.3.5 QGIS

QGIS is an open source geospatial information system (GIS) application (QGIS.org, 2022). The system incorporates several open-source libraries in a graphical user interface that provides a comprehensive set of geospatial analysis

tools. The interface, shown in Figure 3-16, provides a generic layout of QGIS which can be customised. Important window interfaces in Figure 3-16 are the Map (centre), Layers catalogue (left) and Processing Toolbox (right).

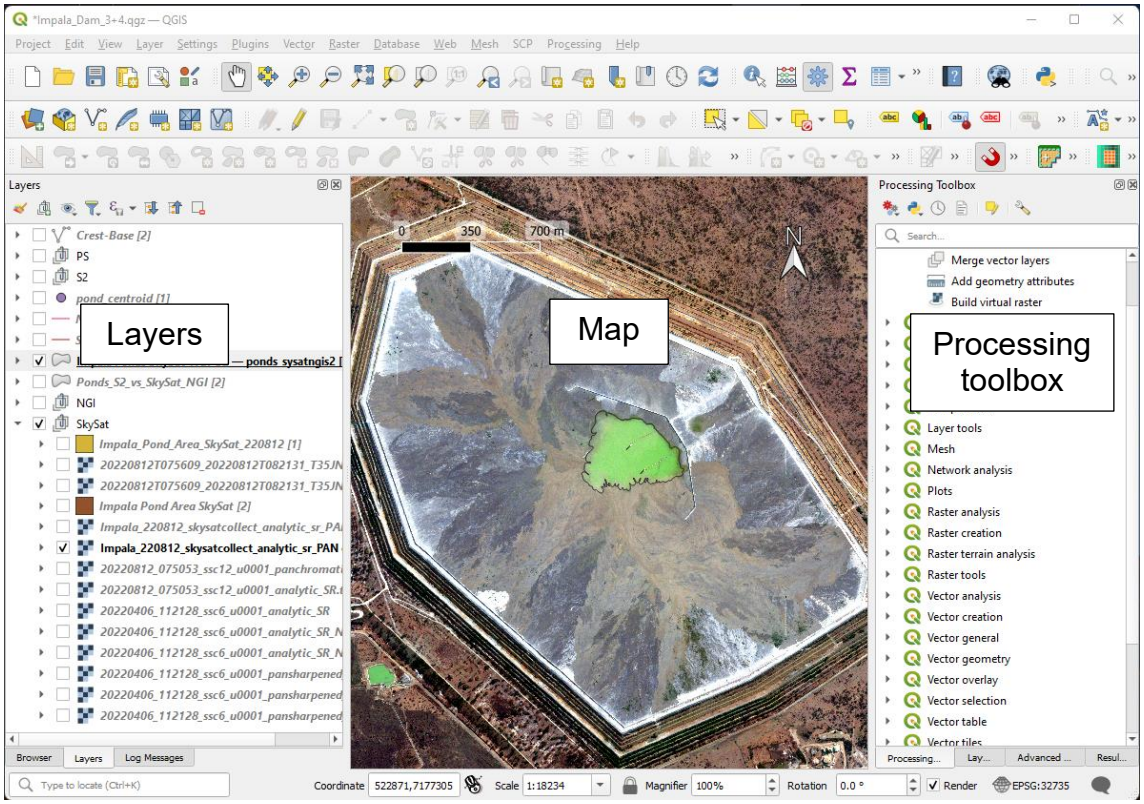


Figure 3-16: QGIS 3.28 interface.

Local images were catalogued and analysed in QGIS using the local Universal Transverse Mercator (UTM) coordinate projection for the sites investigated (EPSG:32735 - WGS 84 / UTM zone 35S). Visually assessed ponds were manually digitised as polygons using the Geospatial Data Abstraction Library (GDAL) vector creation tools in the QGIS Processing Toolbox. Vector database files were saved in GeoPackage format. Metadata, such as the date of the image and the imaging platform were recorded for each feature in the attributes table of the pond data vector file.

3.4 Data analysis

3.4.1 Image processing

Using QGIS, multispectral images were visualised in natural colour, near infrared (NIR) and the normalised difference water index (NDWI) as proposed by McFeeters (1996). Necessarily, visible spectrum images were viewed in natural colour only.

The NDWI can be used to amplify the presence of water using bands sensed in the visible and near infrared spectrum. The NDWI shows positive correlation to water and was computed for all multispectral imagery using green and NIR reflectance in a pixelwise calculation, as shown in Equation 1.

$$NDWI = \frac{R_{Green} - R_{NIR}}{R_{Green} + R_{NIR}} \qquad \textbf{Equation 1}$$

NDWI readings can vary between upper and lower limits of -1.0 and +1.0 and in practice usually lie between -0.8 and +0.8.

NIR reflectance was also used as a water-detection metric. Due to water's high absorption of the bandwidth, NIR shows a negative correlation to the presence of surface water. NIR reflectance readings are usually between 0.01 and 0.50.

Digital imagery visualisation was standardised. Natural colour imagery was viewed with linear reproduction stretched to minimum and maximum red, green and blue band values selected from the 1st and 98th percentile pixel values of a typical image for each site. The same natural colour symbology was then applied to all images for the site. NIR and NDWI data were viewed in set ranges between 0.0 and 0.3 and -0.75 and 0.75 respectively using the colour ramp in Figure 3-17.



Figure 3-17: NIR and NDWI colour ramp.

3.4.2 Visual image analysis

Sentinel-2 and reference imagery were visually assessed to digitise the edge of the tailings pond in each image. Visual image assessment was standardised by visualising each image independently in natural colour, NIR and the NDWI simultaneously in parallel synchronized map views, as illustrated in Figure 3-18 and Figure 3-19. The pond-beach boundary was delineated using visual imagery queues, such as the shape, tone or colour and texture of surfaces visualised in each image (Lillesand et al., 2015) . It is important to note the inherent difficulty visually interpreting imagery (Svatonova, 2016; Lloyd et al., 2002). Inherent differences in imagery introduced by changing atmospheric conditions, seasonal changes in illumination and differing sensor types, in the case of PlanetScope, all change the appearance of surface features in imagery. Furthermore, natural changes to the conditions on the surface of a tailings dam, such as growth and senescence of vegetation, changes to soil moisture levels and sun glint off water bodies further change the appearance of surface features. Such imagery differences and changes to the typical appearances of surface types requires the imagery interpreter to adjust interpretation techniques, potentially introducing errors. Furthermore, the transition from tailings beach to supernatant pond often requires user interpretation. For example, approaching the pond from the beach, dry tailings may become moist closer to the pond as pore water is drawn to the surface via capillary action. Then, adjacent to the pond the tailings may be saturated. The pond then begins, but only as a thin film of water a few millimetres thick above submerged tailings before becoming deeper approaching the decant (Blight, 2009:p.307). This transition makes it difficult to create a binary distinction

between pond and beach and therefore requires interpretation, introducing uncertainty to measurements.

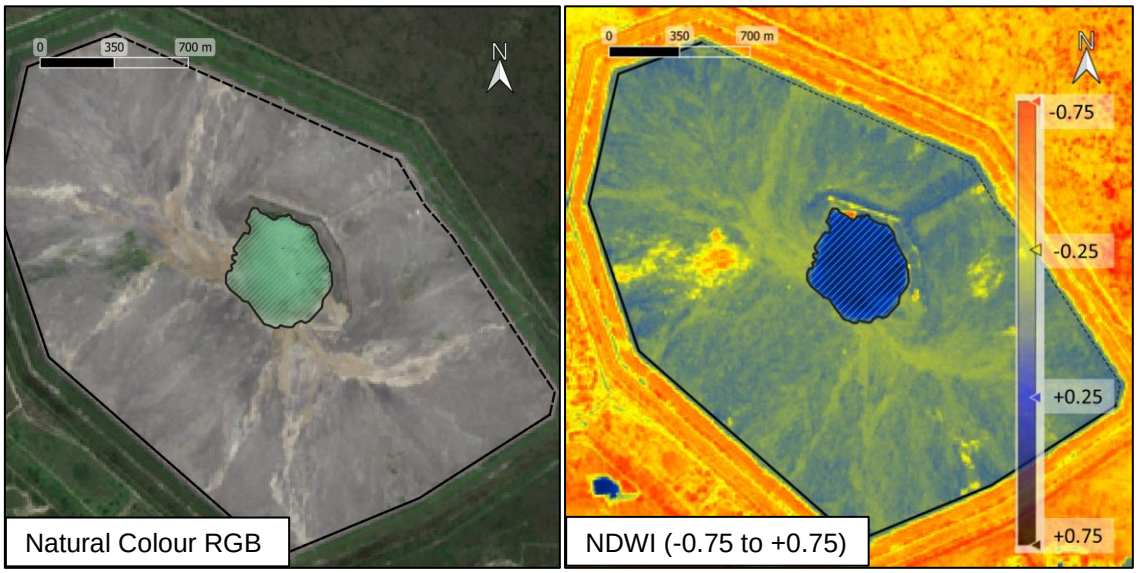


Figure 3-18: Example Sentinel-2 visually assessed pond (acquired 2019-01-15).

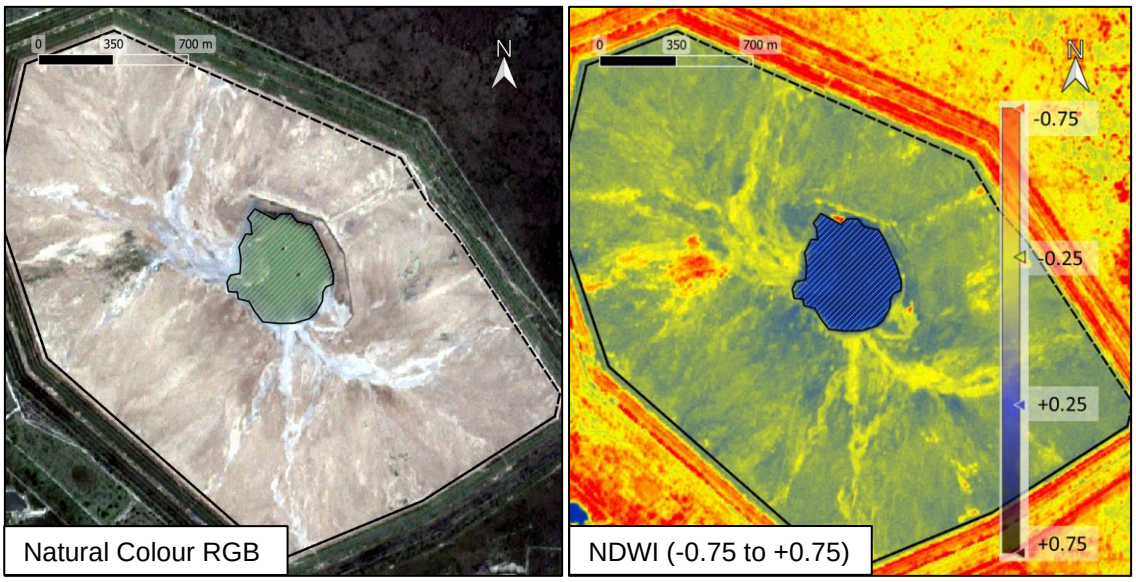


Figure 3-19: Example PlanetScope visually assessed pond area (acquired 2019-01-15).

All data was interpreted by the author and standard image interpretation cues were used to visually distinguish the tailings pond from the tailings beach. In the

natural colour images cues were obtained from the colour and the texture of the different surfaces. Visual interpretation cues from NIR and NDWI imagery were taken from the reflectance and index measurements respectively; with supernatant water presenting a low NIR reflectance and high NDWI and vice versa for the tailings beach.

Derived from the digitised pond edge are leading indicator metrics relevant to tailings dam monitoring, namely, the pond plan area, minimum beach length and the distance of each pond centroid to the mean centroid of all the pond areas as visualised in Figure 3-20, below.

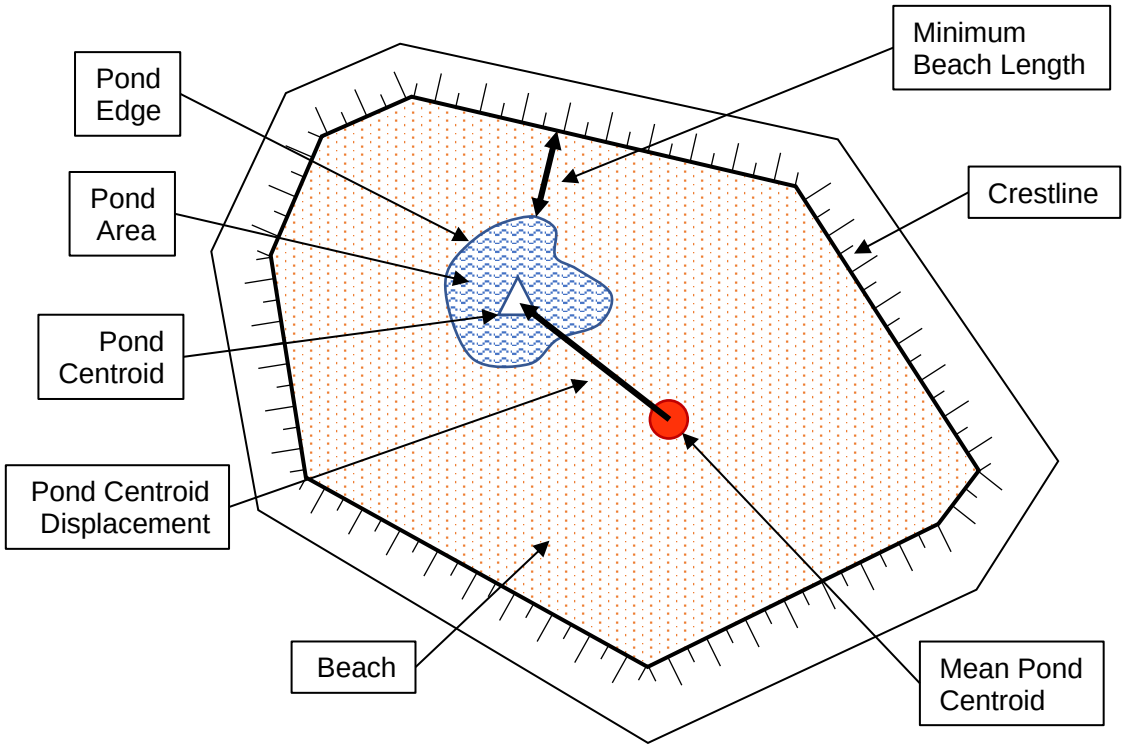


Figure 3-20: Visual representation of pond related tailings dam safety metrics.

The measurement of tailings dam leading indicators was achieved through tailored use of the vector processing tools in QGIS. Each pond was delineated as a closed polygon in a vector database file. Where more than one pond existed in an image, both were delineated, dated and labelled alphabetically according to area. Geometry attributes were added to each pond polygon, namely the pond

area, the date and other metadata relevant to the site. A polyline was placed at the crestline of each site that served as the target against which to estimate the minimum beach length. The minimum beach length was then calculated for each pond as the shortest distance between the pond polygon edge and the site crestline. Pond centroid displacement was calculated as the distance of a pond polygon's centroid to the mean centroid location of all ponds in the dataset. All areas and distances were calculated using ellipsoidal geometries to reduce errors incurred due to projection.

Visual assessment of the very high-resolution reference imagery utilised the same interpretation cues as were used for PlanetScope and Sentinel-2 imagery. Where very high-resolution reference imagery did not have a near infrared band, only inspection of the natural colour imagery could be conducted. The lack of spectral data in the aerial and drone photographs was compensated for by the very high spatial resolution (<0.25 m) of the imagery which allowed inspection of very fine textures, such as ripples or waves in the pond water.

3.4.3 Image threshold analysis

Visual assessment of imagery entails making an educated estimate of the edge of the tailings beach and start of the decant pond and digitising this edge. Several features of the imagery may be used by the GIS operator to estimate this boundary, such as the colour and the texture of surfaces in the imagery. However, while visual inspection is a robust method for digitising of features in imagery, it is time consuming and requires human input. Automated thresholding presents a simple tool to derive large scale data from the ever-growing archive of public satellite imagery. Thresholds can be used to differentiate water bodies from adjacent ground surface features and are computationally simple to implement (Zupanc et al., 2019; Sekertekin, 2021; Tottrup et al., 2022). However, optimum threshold values in the context of tailings dam monitoring need to be determined and assessed for suitability. The process followed in this work is described in the section below.

3.4.3.1 Histogram and transect

The tailings beach is analogous to a bare soil or sand surface. It should thus present a higher reflectance in the near-infrared part of the spectrum than in the visible. Conversely, the tailings pond, being a water body, should have a lower reflectance in the near infrared part of the spectrum than in the visible (Jensen, 2015; Lillesand et al., 2015). The spectral response profiles of soil and water are provided in Figure 3-21 below, along with other typical earth surface materials, to support this notion. If the tailings plateau area is made up of two surface types, the tailings beach and the pond, which we expect to have a high and a low near infrared response respectively, we should also expect to see a bimodal histogram of the pixel data from the plateau area in the near infrared band. One mode representing the pond and the other representing the tailings beach.

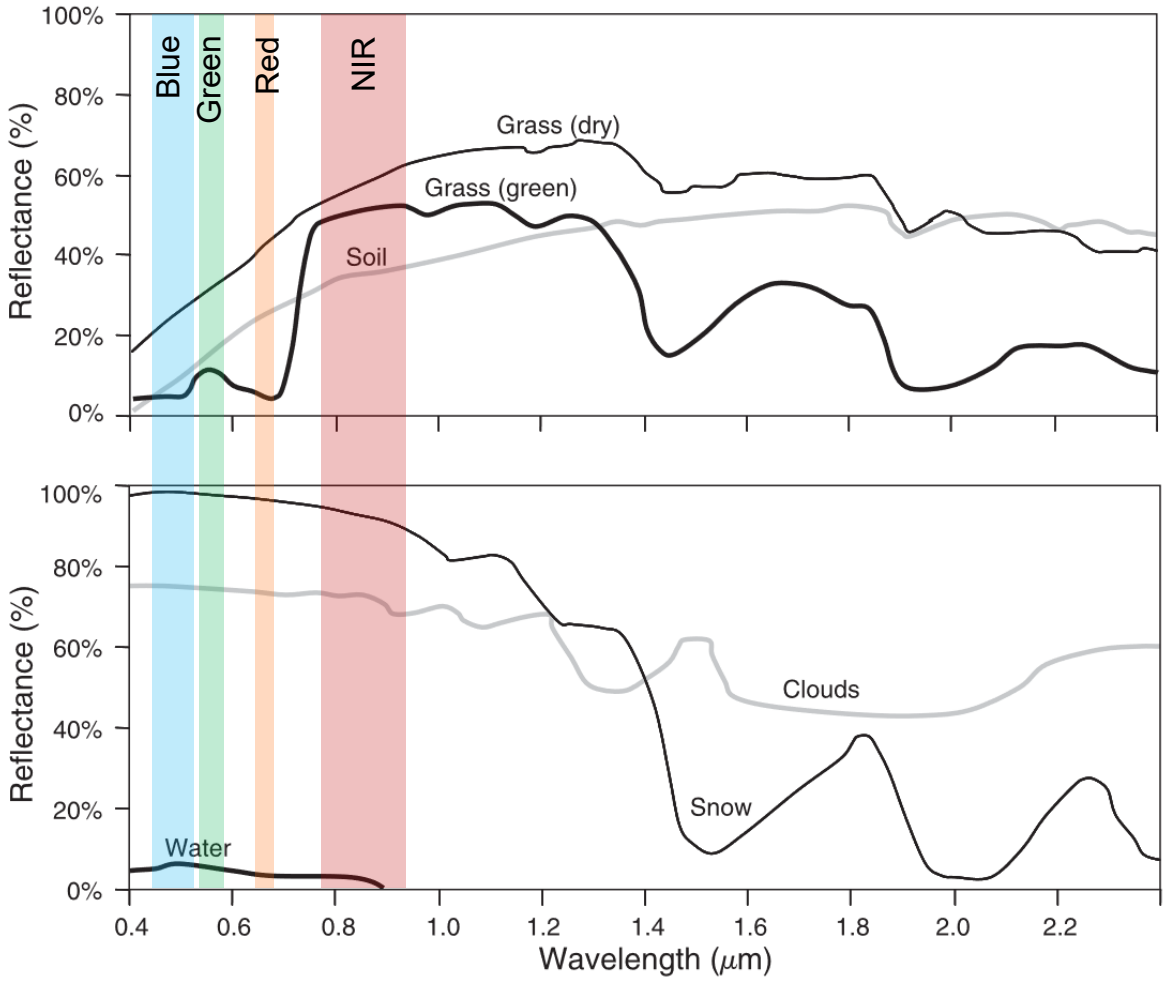


Figure 3-21: Spectral profiles of various land covers adapted from Lillesand, Kiefer & Chipman (2015:p.17) with Sentinel-2 10 m bands overlayed.

As the plateau area of an operational tailings dam is composed predominantly of two surfaces, beach and water, aerial imagery classification need only distinguish between a binary set of material classes. Furthermore, as these surfaces should be spectrally dissimilar in the near infrared (Figure 3-21) a threshold value may exist by which the supernatant pond can be differentiated from the tailings beach.

Histogram analysis can establish a range of threshold values and in many cases can be used to determine an optimum threshold for binary classification of an image (Sekertekin, 2021; Tottrup et al., 2022). A bimodal histogram represents data that contains two distinct groups that can potentially be separated from one another using a threshold value somewhere between the two modes. On the other hand, a histogram with only one mode, or no clear separation between modal groups, may represent data not separatable by threshold. Histograms of aggregated Sentinel-2 imagery for each study site were assessed for bimodal distribution, as presented in Appendix-B.

An example of a schemaic bimodal histogram of NIR reflectance sampled from within the crestline of a hypothetical tailings facility is shown in Figure 3-22 below. In this example, the histogram indicates two unique classes of data represented by the two distint modes and a range of values seprating the two calsses of data.

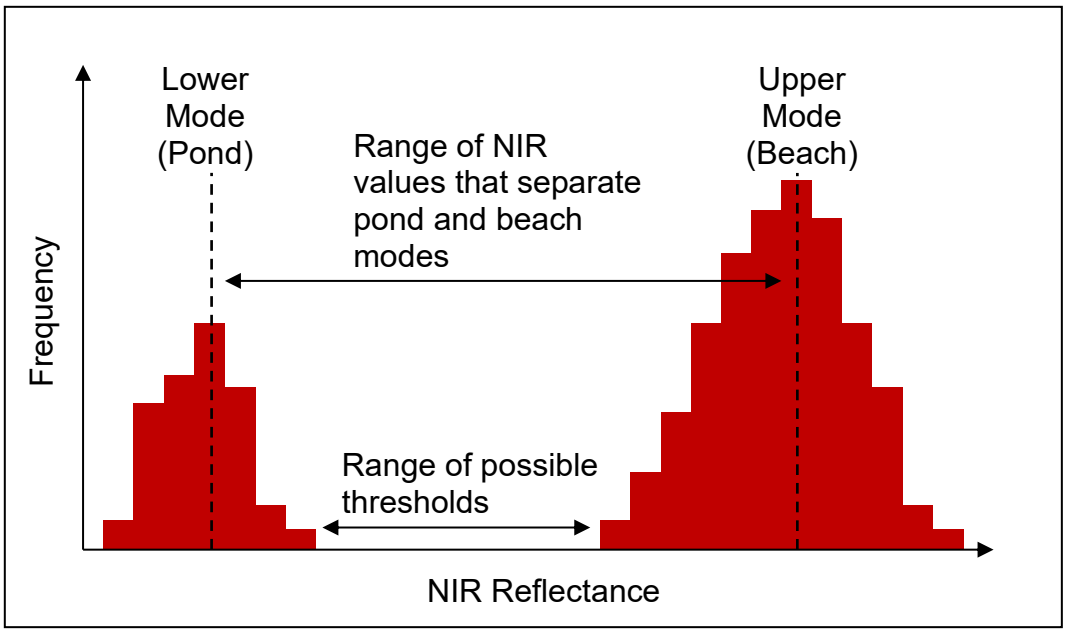


Figure 3-22: Schematic histogram of the near infrared reflectance sampled from within the crestline.

In Figure 3-22 the lower mode should represent data from the pond while the upper mode should represent data from the beach. This same thinking applies to the NDWI but with the upper mode representing water and the lower mode representing the beach.

A second pass at assessing a probable threshold range was conducted taking the transect of an image dataset through the average location of the decant pond, as shown in Figure 3-23

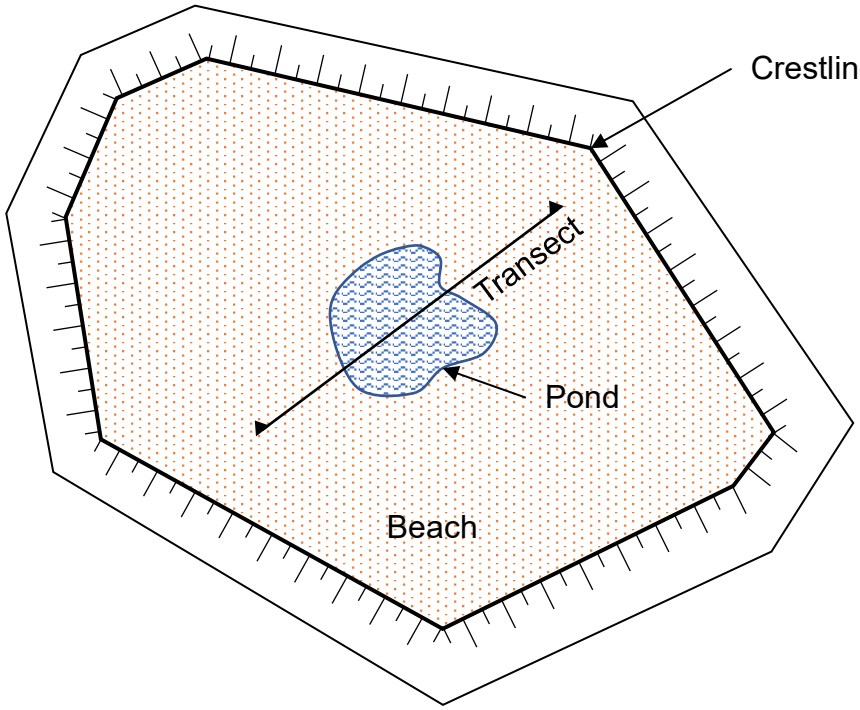


Figure 3-23: Schematic image of a tailings dam and transect, indicating the pond, beach and crestline.

Pixelwise statistics of the image dataset can be plotted along the transect, as shown in Figure 3-24, providing spatial trends in the data. In the case of the NIR reflectance on a typical tailings dam (Figure 3-23), the minimum value obtained from the transect through the beach and the maximum value obtained though the pond, provide a potential range of values that should separate the two surfaces from each other in every image in the dataset assessed, as shown in Figure 3-24 a). This same methodology may be applied to the NDWI but taking

minimum values from the pond and maximum values from the beach, as shown in Figure 3-24 b) Transects of the ponds at each of the sites investigated are available in Appendix-B.

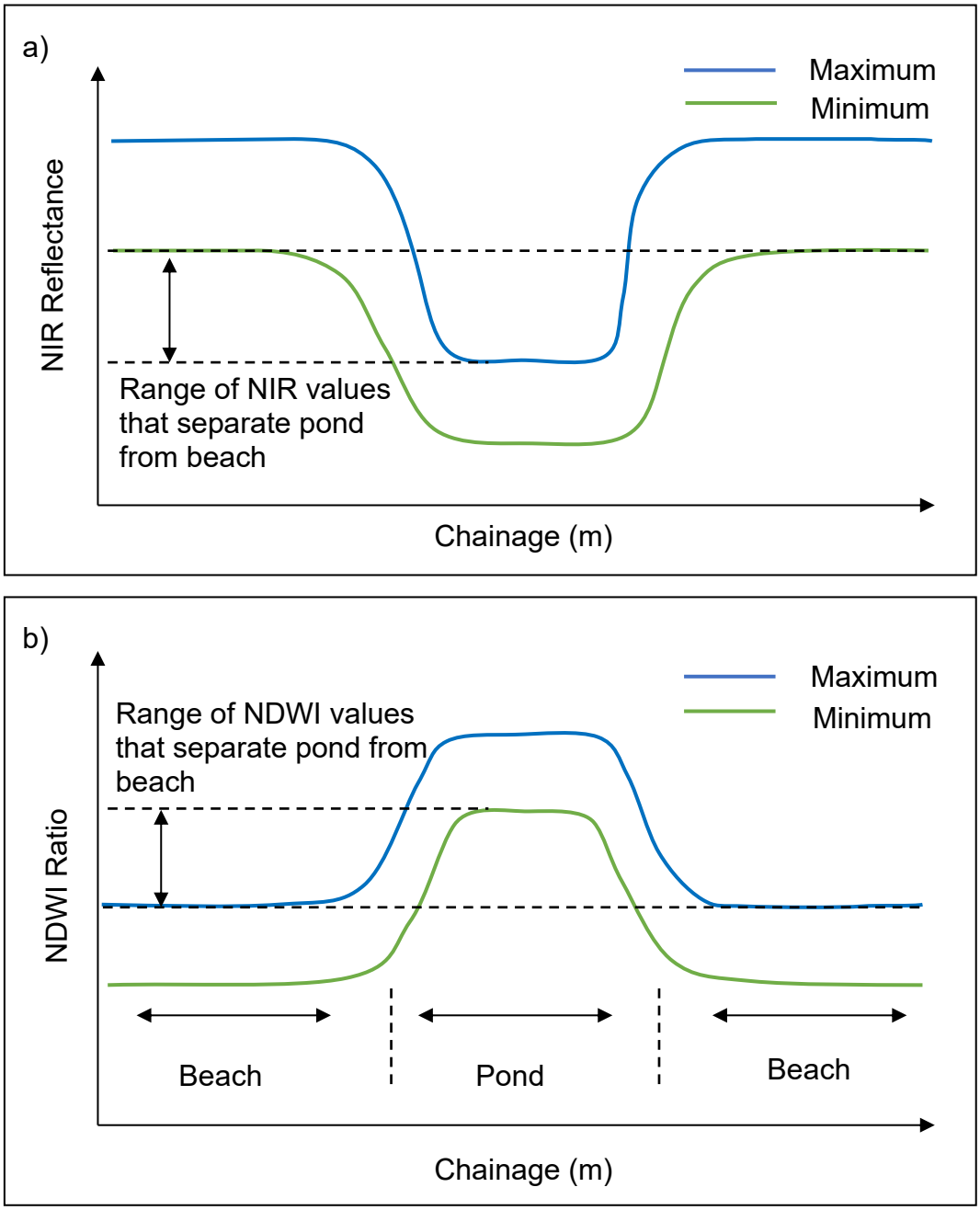


Figure 3-24: Schematic of the interpretation of a transect through a) NIR and b) NDWI imagery data.

Histogram and transect analysis of aggregated data can provide generalisations of the spectral properties of an imagery dataset for a site and inform the potential range of threshold values. However, refinement of the threshold for an imagery dataset is also required should an optimum be sought. Such threshold derivation is discussed in the following section.

3.4.3.2 Optimal threshold calculation

To determine optimum NIR and NDWI threshold values, visually assessed pond areas in Sentinel-2 imagery were used as training data against which threshold derived pond areas from the same Sentinel-2 imagery were compared. By leveraging the data catalogue and computational power of Google Earth Engine, multiple discrete threshold values were used estimate pond areas the pre-selected Sentinel-2 dataset. To produce an area measurement from an image using a threshold value, binary images were computed by assigning a value of unity to pixels with measurements below the NIR threshold and above the NDWI threshold. All other pixels were assigned a value of zero. Binary images were then vectorised, providing a polygon bordering pixels classified as water for the given threshold. The computed pond area for each threshold value was compared to an area calculated from the visually assessed training dataset and the error (difference) between the two areas computed. The square of the error was summed for each threshold for the image collection to provide a measure of the effectiveness of each threshold. The optimum threshold is that value for which the sum of square error is minimised for the images assessed. For each compartment at each site, a single optimum threshold was obtained as the optimum threshold value for all imagery in the three-year study period (i.e. 36 images per site). To assess threshold change with time the process was repeated using one-year long datasets (i.e. 12 images per site) for each of the three years of the original dataset.

The computational procedure for the NDWI is described in Figure 3-25. The same algorithm applies to the NIR band except with the threshold decision criterion reversed.

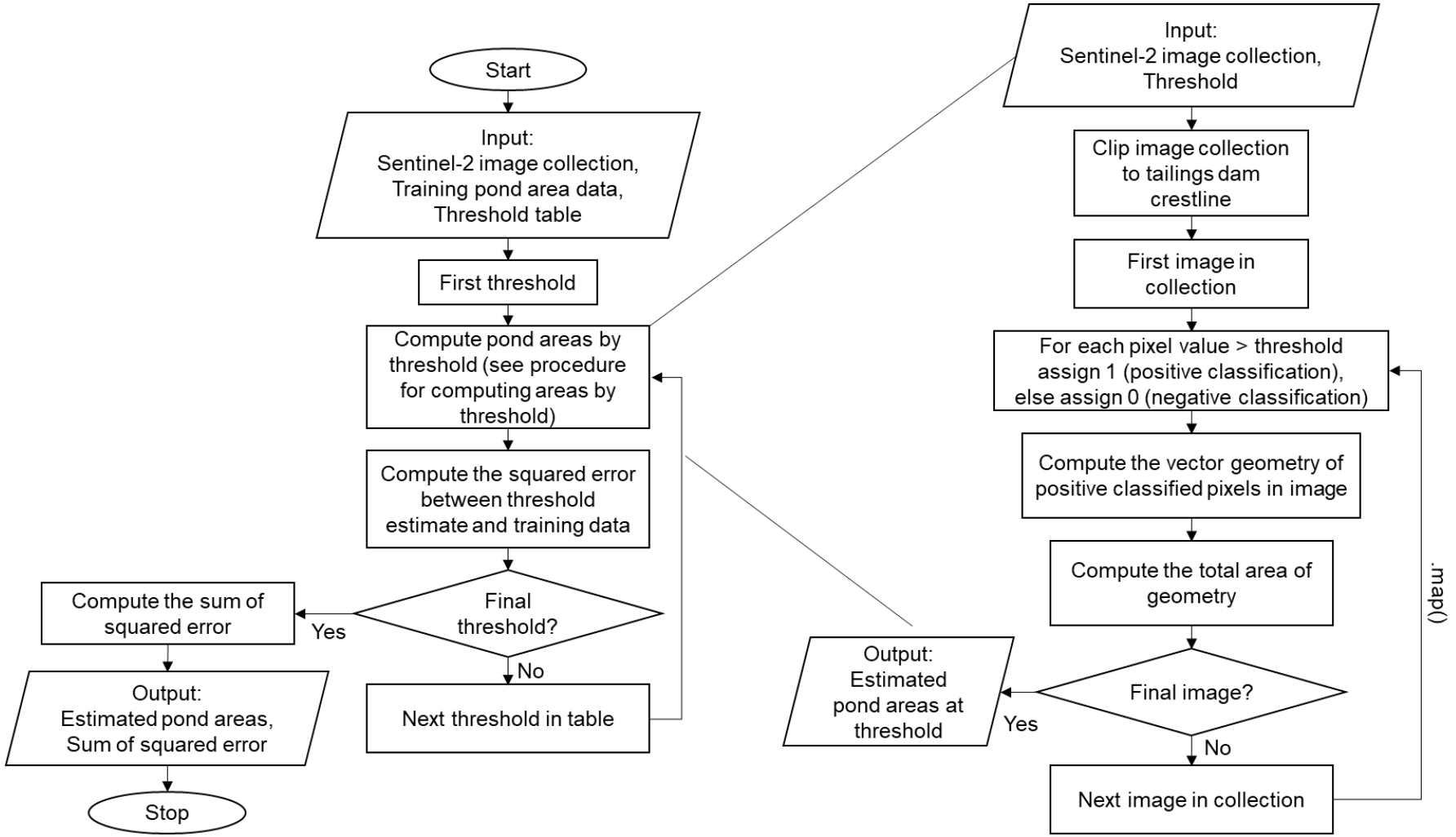


Figure 3-25: Algorithm for automated calculation of the pond area in an image collection by multiple thresholds and estimation of an optimum threshold[1].

1) The algorithm presented applies to the NDWI which is positively correlated to the presence of water. The same algorithm can be applied to NIR but with the greater than (<) decision criterion reversed to a less than (>).

An example of the expected relationship between threshold values and the sum of square error is provided in Figure 3-26. It is anticipated that some optimum threshold should exist that globally minimises the sum of square error for the images in a dataset.

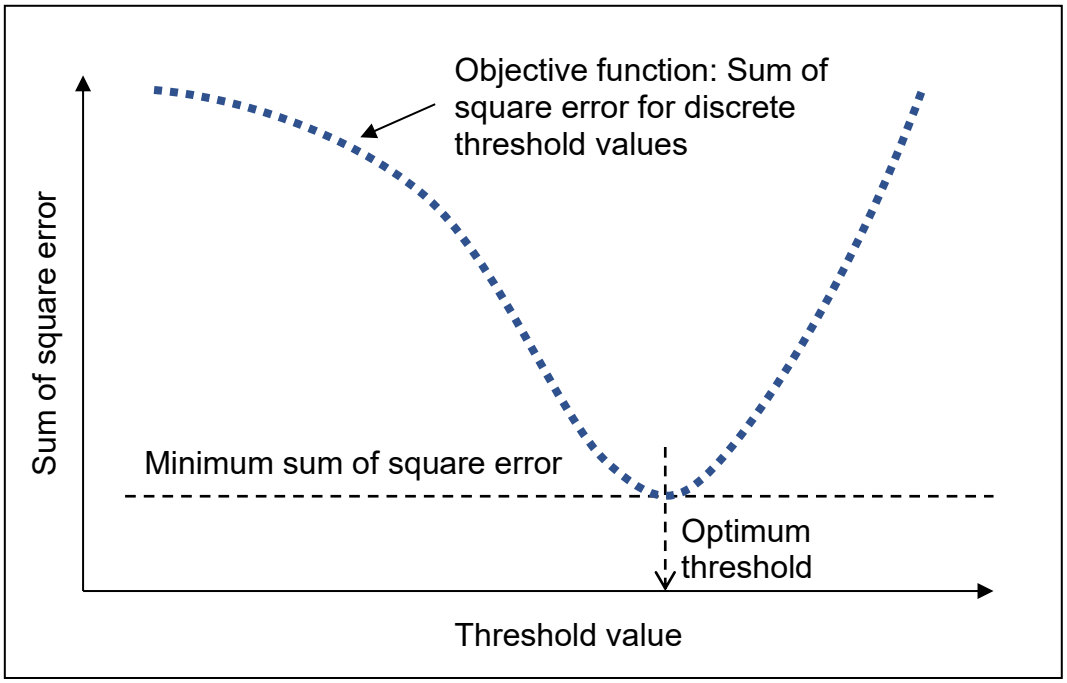


Figure 3-26: Example of the expected relationship between varying threshold values and the sum of square error and the optimum threshold.

3.4.4 Accuracy assessment

To assess the accuracy of Sentinel-2 decant pond measurements the data is compared to reference measurements.

Measurements estimated by visual assessment and threshold of Sentinel-2 are compared to reference measurements by calculating the ratio of each pair of measurements (Equation 2). By assessing the mean and standard deviation of a sample of measurement ratios from the imagery dataset inferences can be made regarding the agreement between Sentinel-2 and the reference data. The mean of the measurement ratio provides an indication of accuracy and the standard deviation an indication of precision.

$$Measurement\ Ratio,\ X = \frac{Sentinel\text{-}2}{Reference} \qquad \textbf{Equation 2}$$

To assess the presence of systematic bias, the mean measurement ratio ($\bar{X}$) for each sample is compared to a null hypothesis measurement ratio (μ_0). The null hypothesis is taken as the measurement ratio of an unbiased sample, i.e. $\mu_0 = 1.0$. If there is a tendency of Sentinel-2 to systematically under or overestimate a certain pond measurement, the mean measurement ratio will be statistically different from unity. Significance is assessed by computing the probability (p-value) that the mean measurement ratio may have been obtained by random sample error using the test statistic, T_0 per Equation 3, in a double sided t-test (Student, 1908; Montgomery & Runger, 2011:p.310) and the t-distribution percentile point table published by Montgomery and Runger (2011:p.711). Statistical significance defined as a p-value of less than 0.05.

$$T_0 = \frac{\bar{X} - \mu_0}{S/\sqrt{n}} \qquad \textbf{Equation 3}$$

For example: A value of the mean pond area ratio (A_{S2}/A_{PS}) of greater than one indicates that Sentinel-2 on average estimated a larger pond than PlanetScope and vice versa for a value of less than one. The probability that the mean pond area ratio measured was due to random sampling error is computed using the t-test, described above. A mean pond area ratio that is statistically different from unity, indicates that Sentinel-2 systematically under or overestimates the pond area compared to the reference dataset, indicating bias. If the mean of the pond area ratio for the sample is equal to one, the sample can be said to have no bias.

In the case of assessing the bias of threshold derived data, comparison is made between the mean measurement ratio of the threshold derived data and a null hypothesis obtained from the statistics of the training data used to establish that threshold. I.e., the mean pond area is compared to a null hypothesis taken as the mean pond area ratio of the training dataset when compared to the reference dataset. For example, if the optimum threshold is based on an algorithm that attempts to match the measurements made in a training dataset, and that training

dataset exhibits a bias, a perfect classifier would exhibit the exact same bias. Therefore, if the training dataset, i.e. visual assessment of Sentinel-2, exhibits a bias $(\mu <> 1.0)$, a threshold derived dataset trained to match the visually assessed data should exhibit similar bias. So, if a statistically significant bias is present in the training dataset, threshold derived data is compared using a null hypothesis of $\mu_0 <> 1.0$ obtained from the mean measurement ratio $(\bar{X})$ of the training dataset. If no such bias is found in the training data, then the threshold derived data is compared to an unbiased estimator with a null hypothesis of $\mu_0 = 1.0$.

Deviation of Sentinel-2 to the reference data can be inferred from the standard deviation (S) of the measurement ratio sample. In engineering practice, the confidence a practitioner can place in a measurement tool is associated with the precision of that tool. The standard deviation in the sample of the measurement ratio serves as a measure of precision. The criticality of the measurement is also important when defining a required precision. Measurements critical to the safety of tailings dams should be made using tools of known high precision. Earth observation data is not intended to alone provide critical data or to replace current best practice but is suggested as a source of supplementary public information. Therefore, pond measurement precision using earth observation data does not necessarily need to meet or surpass best practice. It is taken here that a standard deviation in the measurement ratio of less than 0.10 indicates adequate precision. For example, assuming a normal distribution of measurement ratios, a standard deviation of 0.10 indicates that approximately 95% of the measurements will fall within ±0.20 of the mean, or within 20% above and below the mean (Montgomery & Runger, 2011:p.120).

Examples of the NIR and NDWI threshold derived pond area compared to the reference pond area based on PlanetScope imagery is shown in Figure 3-27 and Figure 3-28 respectively below. The ratio of the areas shown in the adjacent images is the measurement ratio $X = A_{S2\text{-}Thresh}/A_{PS}$.

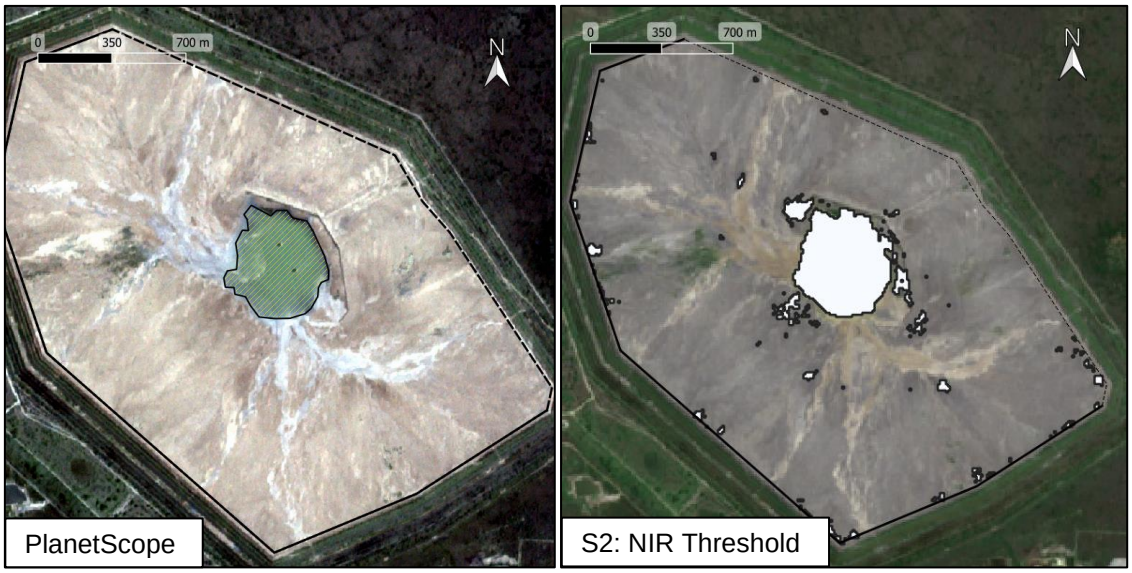


Figure 3-27: Example of PlanetScope vs S2 (Sentinel-2) NIR threshold derived pond.

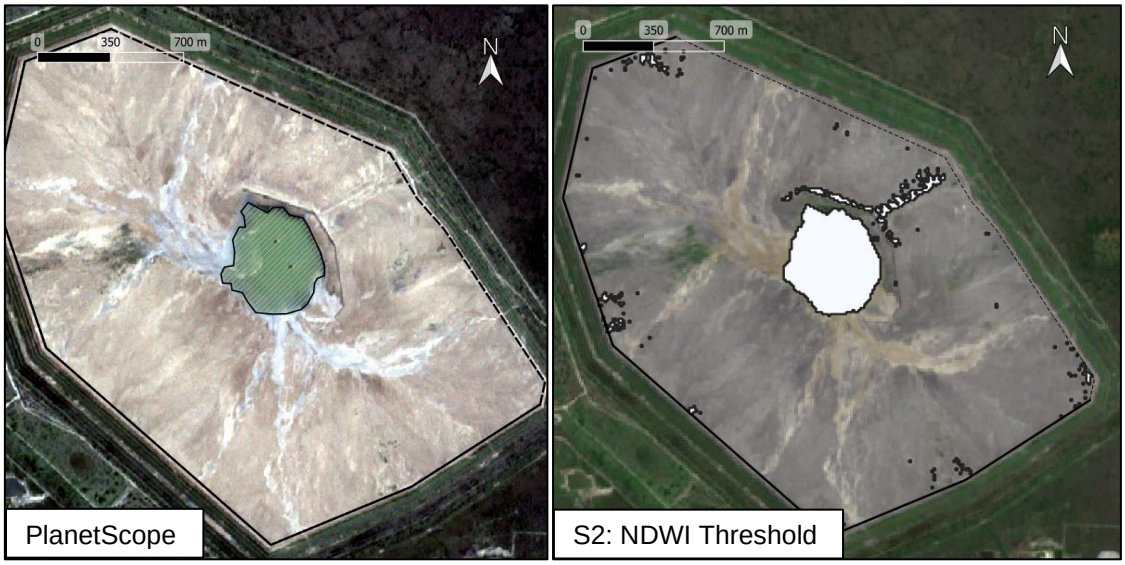


Figure 3-28: Example of PlanetScope vs S2 (Sentinel-2) NDWI threshold derived pond.

3.4.5 Imagery temporal separation

The temporal separation between a Sentinel-2 image and the reference image may be a source of error other than the inherent difference in the data being investigated. In acquiring imagery, temporal separation between input and reference imagery was kept to a practical minimum. However, some temporal separation does exist between the data. To assess the impact of temporal separation, the absolute temporal separation (Equation 4) is compared to a measure of agreement between the data, in this case the normalised absolute area difference (Equation 5).

$$Absolute\ temporal\ separation,\ \Delta T = |T_{S2} - T_{PS}| \qquad \textbf{Equation 4}$$

$$Normalised\ absolute\ area\ difference,$$

$$\left|\frac{\Delta A}{A_{ref}}\right| = \frac{|A_{S2} - A_{PS}|}{A_{PS}} = \left|\frac{A_{S2}}{A_{PS}} - 1\right| \qquad \textbf{Equation 5}$$

If there is correlation between the absolute temporal separation and area difference, then it can be inferred that temporal separation contributed to the area differences measured. Lack of correlation suggests that the effects of temporal separation may be neglected.

4 RESULTS AND DISCUSSION

4.1 Introduction

The results of this work fall into two categories. The first is georeferenced pond data derived by visual assessment of Sentinel-2 imagery. The second is a set of site-specific thresholds of Sentinel-2 near infrared (NIR) reflectance and the normalised difference water index (NDWI) and corollary pond areas. In both cases pond data derived from visually assessed reference imagery is compared to data obtained from Sentinel-2. Visually assessed pond data comprises pond area, minimum beach length and pond centroid displacement and a comparison of these measurements to data generated by visual assessment of the reference datasets. Data derived by automated threshold is comprised of pond area only, followed by comparison of this data to the reference datasets.

4.2 Data derived by visual assessment

4.2.1 Pond area

4.2.1.1 Temporal pond area data

Pond area data obtained by visual assessment of 10 m spatial resolution Sentinel-2 imagery for the three-year period between the start of 2019 and the end of 2021 follows. Figure 4-1 presents this pond area data on the ordinate with time on the abscissa for the study sites investigated. The figure provides a graphical representation of the range of pond areas in the investigation and the spread of the data temporally between the start of 2019 and the end of 2021. The data presented in Figure 4-1 indicates a range of the pond area values predominantly between 2 $x10^3$ to 2 $x10^6$ m^2. Note the ordinate is displayed on a logarithmic scale.

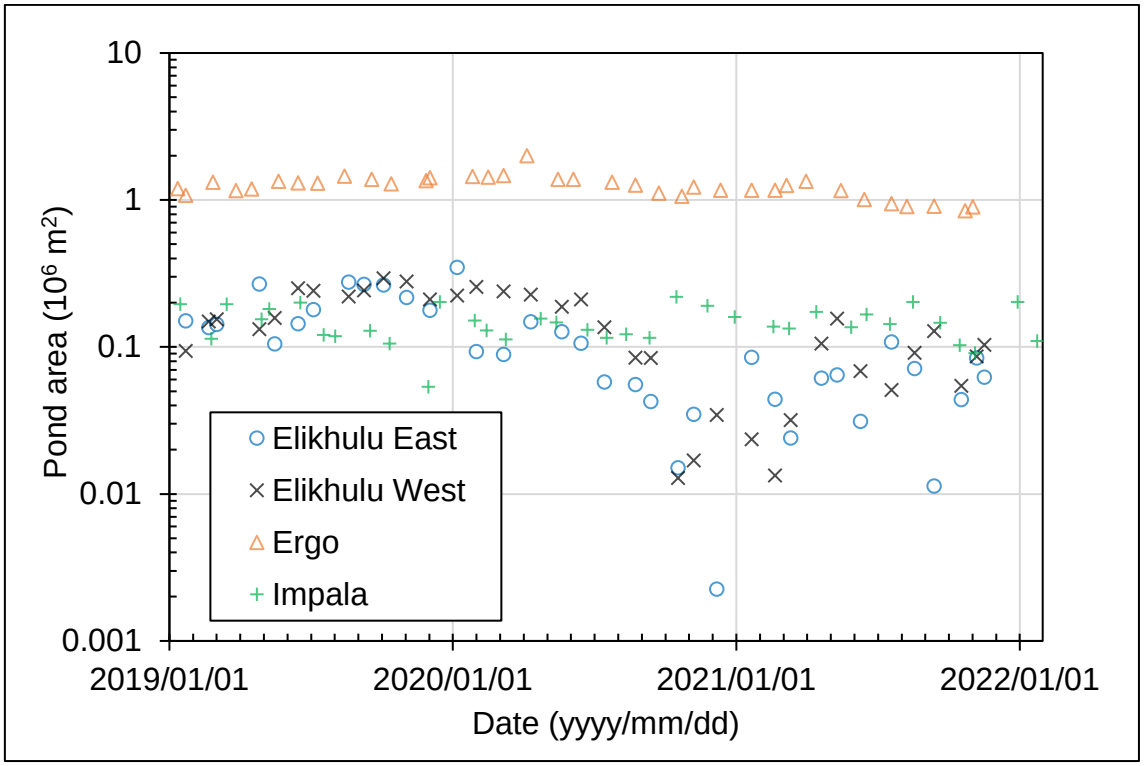


Figure 4-1: Pond area with image acquisition time delineated by visual assessment of Sentinel-2.

4.2.1.2 Comparison of Sentinel-2 and PlanetScope pond area data

To assess the agreement between Sentinel-2 and the PlanetScope reference dataset, pond areas by visual assessment are compared in a pairwise manner. Each data point in Figure 4-2 represents a date matched image pair. Figure 4-2 a) provides a 1:1 plot of the pond area data obtained from the two datasets. Figure 4-2 b) then depicts a subset focusing on smaller pond sizes.

Figure 4-2 a) indicates good correlation between visually assessed pond area data obtained from Sentinel-2 and PlanetScope. A statistically significant bias of Sentinel-2 imagery to estimate a larger pond size than PlanetScope is apparent in the data. On average, Sentinel-2 pond measurements estimated a pond 1.053 times larger than the reference measurement with a standard deviation of 0.215.

Considering data from individual sites, this positive bias is evident for the large pond areas obtained from Ergo as well as the smaller ponds at Impala. On average Sentinel-2 estimated pond areas 1.036 times larger than the reference

at Ergo with a standard deviation of 0.041 ($p<0.001$). Although the pond areas estimated by Sentinel-2 at Ergo are only 3.6% larger, on average, than those measured in PlanetScope, this result is statistically significant ($p<0.05$). This indicates that Sentinel-2 systematically overestimated the pond area in the sample measured at Ergo. Similarly, for data from Impala, Sentinel-2 measured ponds on average 1.11 times larger than the same pond measured in reference imagery with a standard deviation of 0.093 ($p<0.001$). While these bias results may be statistically significant the amount of bias is constrained to less than 5% at Ergo and less than 15% at Impala. The standard deviation of the data is less than 0.05 and 0.10 for the sample taken from Ergo and Impala, respectively. This indicates that two thirds of measurements are within 10% of the mean for these sites. This is therefore a predictable and contained bias.

The narrowed pond area range and domain depicted in Figure 4-2 b) between 0 to 400 $x10^3$ m^2 provides a scale at which pond data obtained from Elikhulu and Impala can be better visualised. Data from Elikhulu East and West also indicate that on average visual assessment of Sentinel-2 yields pond areas larger than the reference measurement. However, due to proximity of the means to the null hypothesis and the higher standard deviations, 0.395 and 0.134 for Elikhulu East and West respectively, the mean pond area ratios measured are not statistically significant. Statistics of the data are summarised in Table 4-1. This higher standard deviation signifies a greater degree of dispersion from the mean in the results for Elikhulu when compared to the data obtained from Impala and Ergo, where lower standard deviation is reported.

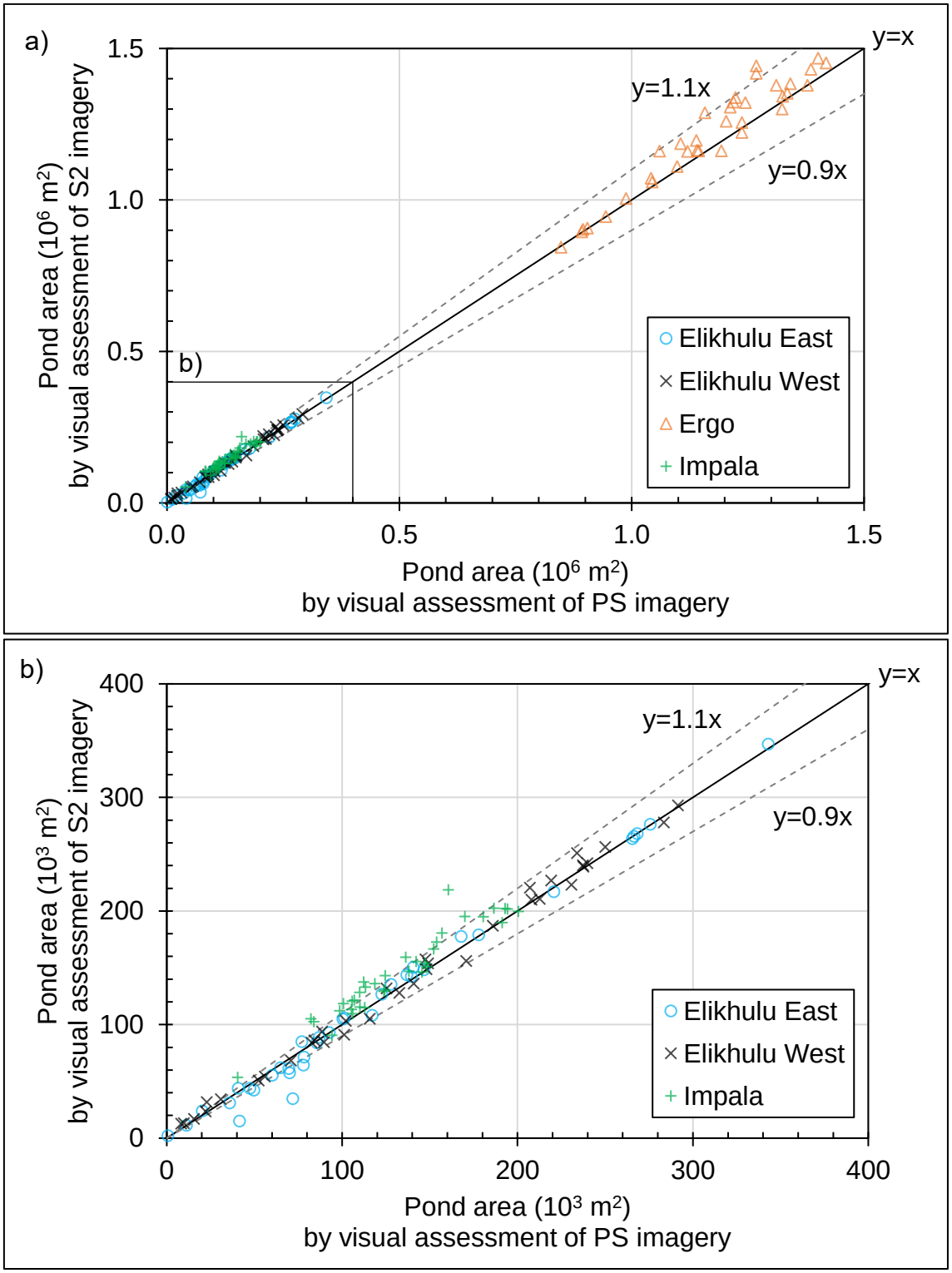


Figure 4-2: Agreement between pond area measurements a) of all pond sizes and b) ponds smaller than 400 x10³ m² delineated by visual assessment of Sentinel-2 (S2) and PlanetScope (PS) imagery.

Figure 4-3 provides the relationship between the pond area ratio and the pond area magnitude. In general, the smaller the pond area, the greater the deviation of the pond area ratio is from one. Small pond areas exhibited a large range in the pond area measurement ratio of $0.4 < A_{S2} / A_{PS} < 1.6$ (barring an outlier from Elikhulu East), this range narrowed to $0.97 < A_{S2} / A_{PS} < 1.12$ for the large ponds of the Ergo dam.

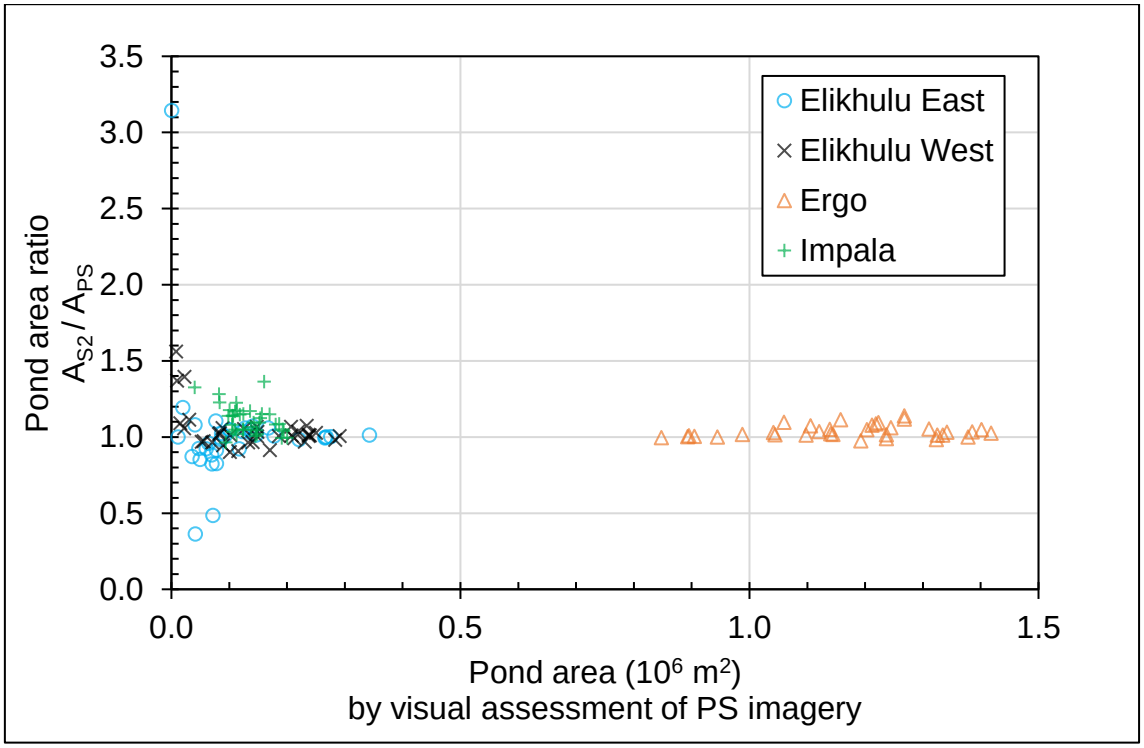


Figure 4-3: Ratio of the area obtained by S2 (Sentinel-2) to PS (PlanetScope) versus pond area magnitude.

The histogram of the pond area ratio for the data is presented in Figure 4-4 below. Most of the pond area ratio data falls within 0.80 and 1.25 with a mode between 1.00 and 1.05. Two omission (i.e. a practical failure to meaningfully detect a pond) and two commission (i.e. an inclusion of area such that pond was detected where no pond should exist) errors occurred in the pond measurements, where the measurement ratio is less than 0.50 and greater 1.50 respectively, seen in Figure 4-4. These errors occurred at Elikhulu East and West by inspection of Figure 4-3, above.

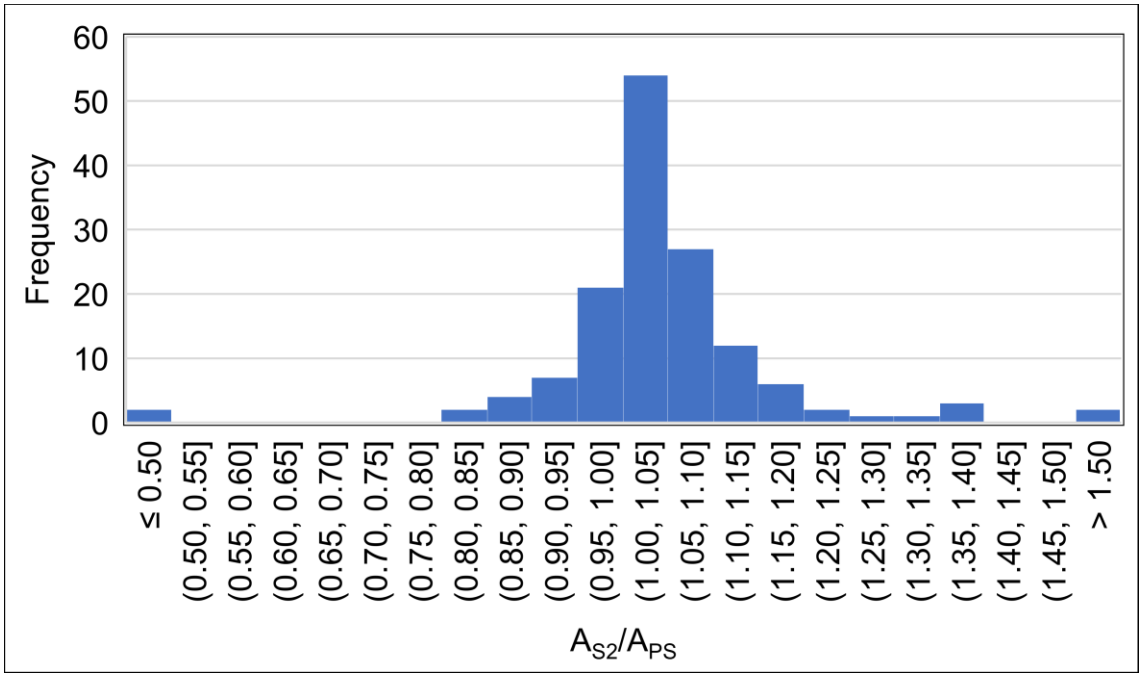


Figure 4-4: Histogram of A_{S2} (Area by Sentinel-2) to A_{PS} (Area by PlanetScope) pond area ratio.

Table 4-1: Visually assessed Sentinel-2 versus PlanetScope pond area data statistics

Site	**Mean Ratio** A_{S2} / A_{PS} $(\bar{X})$	**Mean Ratio Difference** $(\bar{X} - \mu_0)$	**Sample Std. Dev.** (S)	**Sample size** (n)	**P-value** (Indicating statistically significant mean ratio)
Elik. East	1.018	0.018	0.395	36	>0.5
Elik. West	1.043	0.043	0.134	36	>0.05
Ergo	1.038	0.038	0.041	36	<0.01
Impala	1.112	0.112	0.093	36	<0.001
All	1.053	0.053	0.215	144	<0.01

There is a high degree of correlation (~+1.0) between the data derived from Sentinel-2 and PlanetScope imagery shown in Figure 4-2. However, considering the overall standard deviation of the area measurement ratio (A_{S2}/A_{PS}) of 0.215, there is also a high degree of scatter in the data. This deviation is, however, primarily associated with the data from Elikhulu East and to a lesser degree Elikhulu West, with standard deviations of 0.395 and 0.135 for these

compartments respectively. This scatter likely arises because of the inherent difficulty of visually classifying imagery data where geomembrane is exposed alongside pond water and tailings slurry. The standard deviation reported in the data from Ergo and Impala are below 0.10 and therefore suggest a suitable precision of the pond area measurements by Sentinel-2 at these sites.

4.2.1.3 Temporal separation versus area measurement differences

To assess the effect of temporal separation on pond area measurements, the temporal separation (Equation 4) of image pairs and the pond area difference (Equation 5) is investigated in the figures that follow.

Figure 4-5 provides a plot of the absolute temporal separation of the Sentinel-2 and PlanetScope image pairs against the normalised area difference between ponds delineated in the images. Of note, all images were acquired within a maximum temporal separation of 72 hours and most image pairs were acquired on the same day. No systematic trend or relationship is apparent between the normalised absolute area difference and temporal separation. This is likely due to temporal separations that were small enough to not introduce significant amounts of error between the input and reference datasets. Furthermore, data points with the largest temporal separation come from Ergo where the data exhibited good agreement between Sentinel-2 and the reference measurements. Further work is necessary to establish the maximum acceptable temporal separation between input and reference imagery for tailings dam pond monitoring.

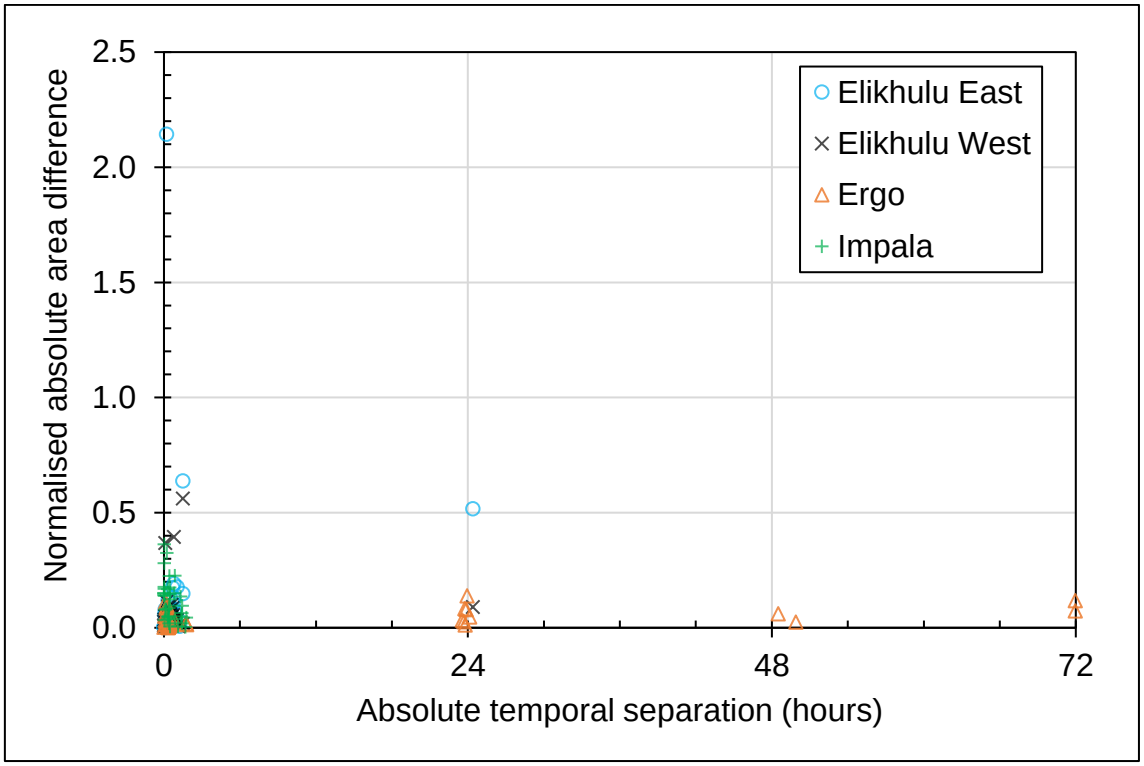


Figure 4-5: Temporal separation versus normalised absolute pond area difference.

As most of the image pairs were acquired within a few hours, a reduced temporal separation domain is plotted in Figure 4-6. There is no systematic trend or strong correlation apparent between the temporal separation of the images and the pond area difference, based on the data in the figure.

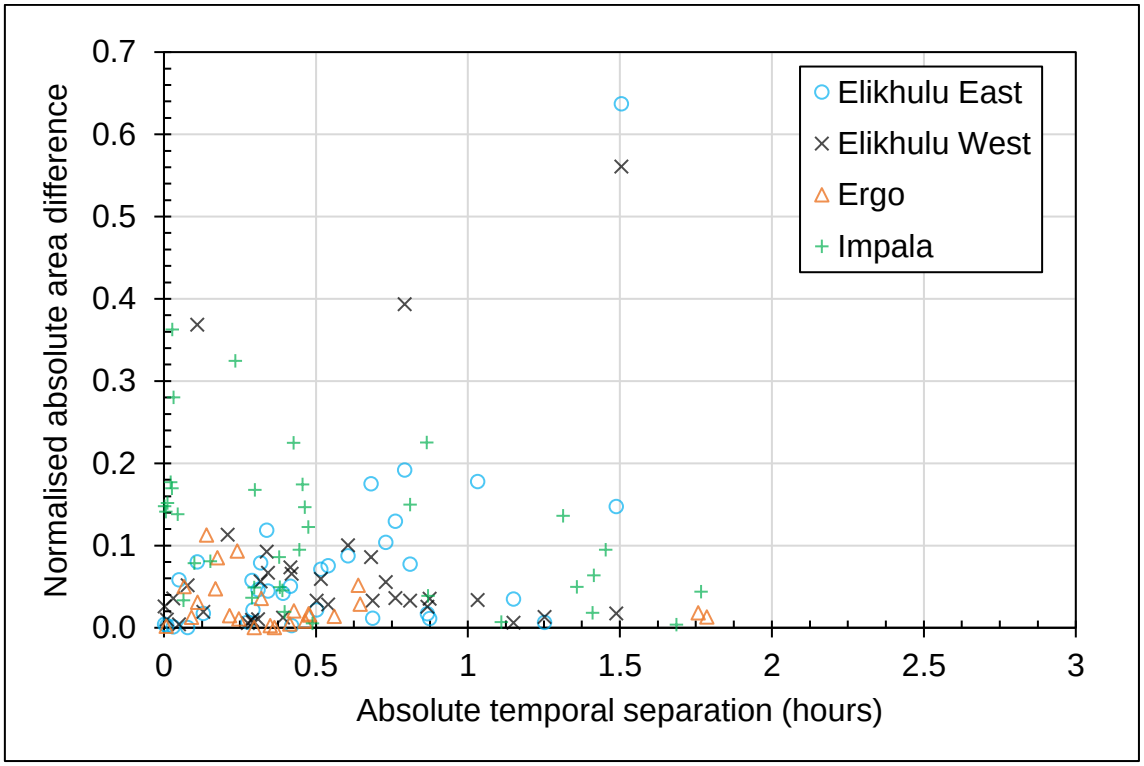


Figure 4-6: Temporal separation over a narrowed domain versus normalised absolute pond area difference.

The difference in pond area measurements should exhibit a direct correlation with greater temporal separation. The rationale being that the longer the time between image acquisitions, the greater the likelihood that the ground conditions captured in the two images are different. Another factor in this hypothetical relationship is the rate of change of ground conditions. Certain events cause a rapid change in the ground conditions observable in satellite images, such as a flood or a landslide. Other events may cause a slow and gradual change in ground conditions, such as construction works or seasonal changes in vegetation or landcover. The former would be observed as an abrupt change occurring between two successive images while the latter might be gradually observed as steps in a timeseries of images. If temporal separation between the Sentinel-2 and PlanetScope images interpreted played a significant role in the area differences measured, it is expected to see an increase in area differences with increasing temporal separation. As no such correlation is apparent, the temporal

separation between the images assessed in this study is sufficiently small to have not contributed significantly to measurement error.

4.2.1.4 Reference satellite generation versus area measurement differences

The PlanetScope constellation is comprised of three generation of satellites spanning back to 2017. The later generation of PlanetScope satellites have similar spectral response curves to Sentinel-2. Therefore, a higher level of agreement between Sentinel-2 and the later generation PlanetScope satellites compared to the first-generation is plausible. Of the PlanetScope images analysed as reference data here, 49 % were acquired by Dove Classic satellites, 22 % by Dove-R satellites and 29 % by SuperDove satellites. This data represents a 49:51 split between the first-generation Bayer Array and later 'Butcher Block' sensor designs. The data presented in Figure 4-7 is a comparison of the mean normalised absolute area difference measured by Sentinel-2 and the different PlanetScope satellites for each of the sites investigated. The data does not conclude lower area differences between Sentinel-2 and the later generation PlanetScope satellites. However, if we restrict the analysis to the Ergo and Impala facilities the area difference is on average lower for the more recent Dove-R and SuperDove satellite generations. In general, for all the sites Dove-R and Sentinel-2 area measurements were the closest matching. Only data from the Elikhulu ponds shows a large difference between the areas measured by Sentinel-2 and the SuperDove satellites. This difference may be due to site-specific conditions and not due to inherent differences between the two imagery sources. Further work is needed to isolate the effects of the different PlanetScope satellite generations on pond area measurements.

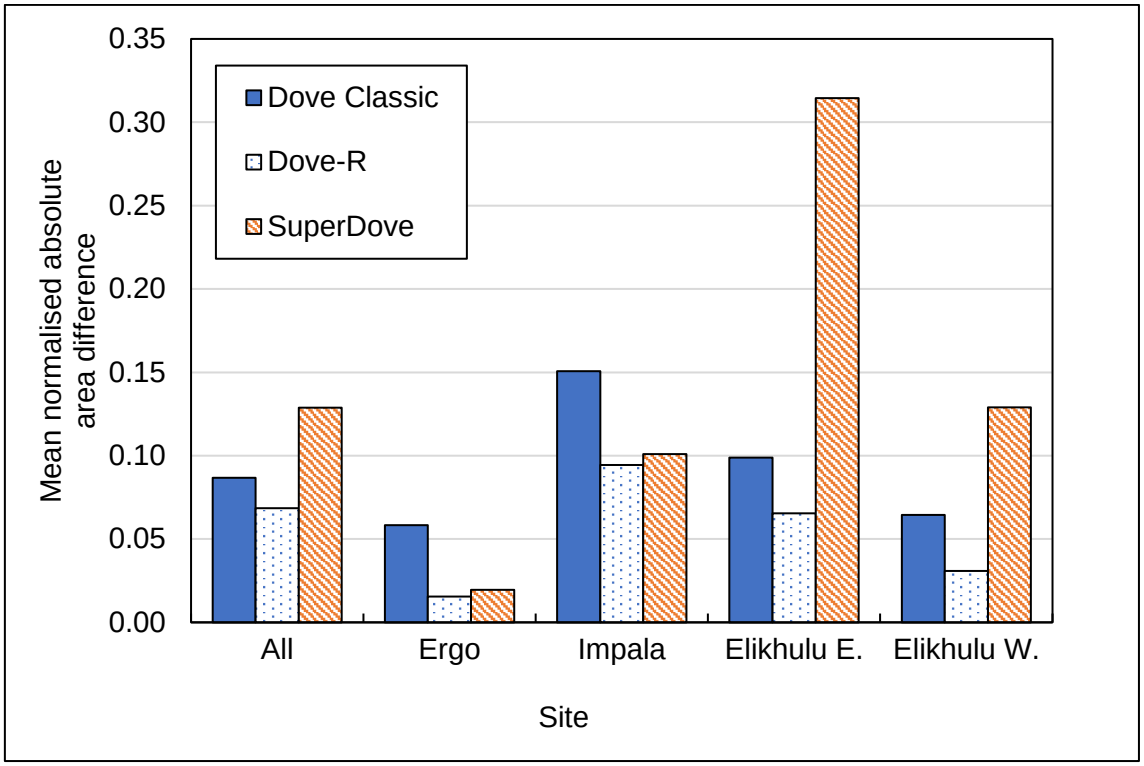


Figure 4-7: A comparison of PlanetScope satellite generation and the mean normalised absolute area difference recorded at each site.

4.2.1.5 Comparison of Sentinel-2 to very high-resolution reference data

PlanetScope and Sentinel-2 are similar earth observation systems in terms of spatial (≤10 m) and spectral resolution in the visible and near infrared bands. It is therefore prudent to also make comparison to data of significantly higher spatial resolution. To this end, Sentinel-2 is compared to sub-meter resolution aerial orthophoto and satellite data. Temporal separation between Sentinel-2 and SkySat images was reduced to same day acquisition. The temporally nearest Sentinel-2 images were used for comparison to aerial orthophoto imagery. Comparison of Sentinel-2 pond area to very high-resolution reference data is displayed in Figure 4-8 below.

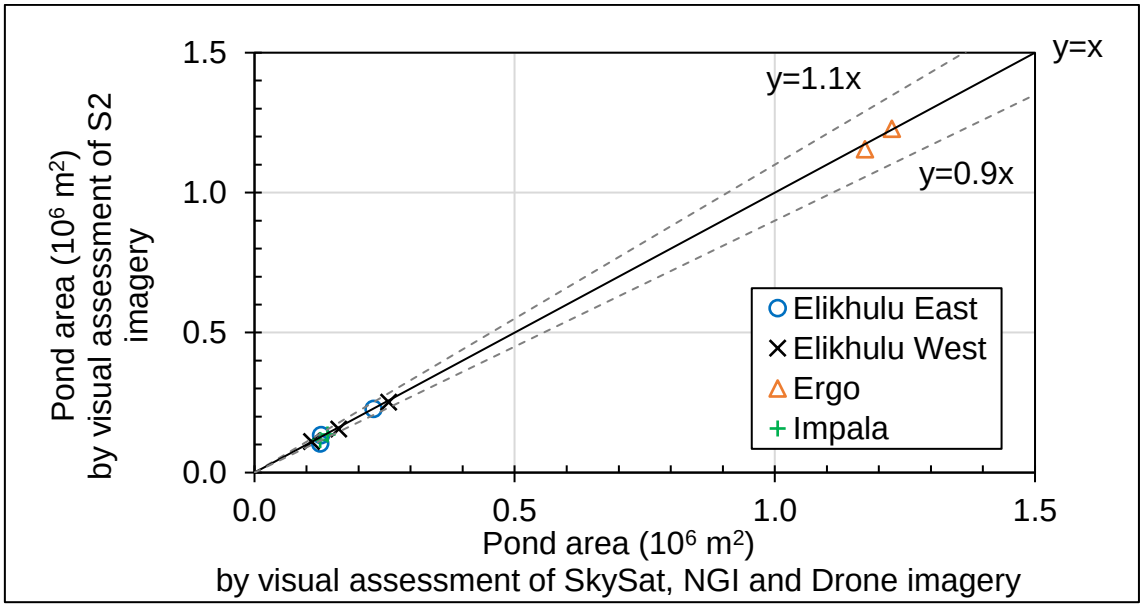


Figure 4-8: Summary of pond area by visual assessment of Sentinel-2 (S2) versus very high-resolution reference imagery.

Visually the data obtained from Sentinel-2 agrees very closely with the data obtained by very high-resolution reference data sources. On average Sentinel-2 measurements were a factor of 0.97 times below the very high-resolution reference measurements, or within 3%, with a low standard deviation of 0.062. Based on the data available, there is no bias of Sentinel-2 to over or underestimate the pond area obtained by the very high-resolution reference imagery. The statistics of the data in Figure 4-8 are summarised in the table below.

Table 4-2: Sentinel-2 versus very high-resolution reference pond area data statistics

Mean Ratio A_{S2} / A_{PS} $(\bar{X})$	**Mean Ratio Difference** $(\bar{X} - \mu_0)$	**Sample Std. Dev.** (S)	**Sample size** (n)	**P-value** (indicating statistically significant bias)
0.97	-0.03	0.062	10	>0.1

As the sample size is small (10 measurements) the significance level of the results should be considered with caution. It can be concluded, nonetheless, that for this sample, Sentinel-2 agreed well with the very high-resolution reference measurements.

4.2.2 Minimum beach length

4.2.2.1 Temporal minimum beach length data

A similar analysis to that presented on pond areas in the previous section was conducted for the minimum beach length of the tailings dams. As previously stated, this data is derived from visual assessment of the pond in satellite imagery. Figure 4-9 presents the temporal behaviour of the minimum beach length for the four study site ponds.

In Figure 4-9, Elikhulu East and West begin with minimum beach lengths near zero. This coincides with commissioning of the facility when the basin is first inundated with tailings. Beaches are then established in early 2020 and the minimum beach lengths stabilise thereafter at between 250 m and 500 m. The minimum beach length at Ergo is 200 m in early 2019 and then systematically reduces to a near zero value in late 2019 and early 2020. The minimum beach is then re-established above 100 m in late 2020 through to the end of 2021. The low minimum beach length readings coincide with larger pond area readings and may indicate a period when the operators of the site experienced trouble maintaining the water balance. Long beaches are maintained at Impala through the study period and never reduce to values of less than 600 m.

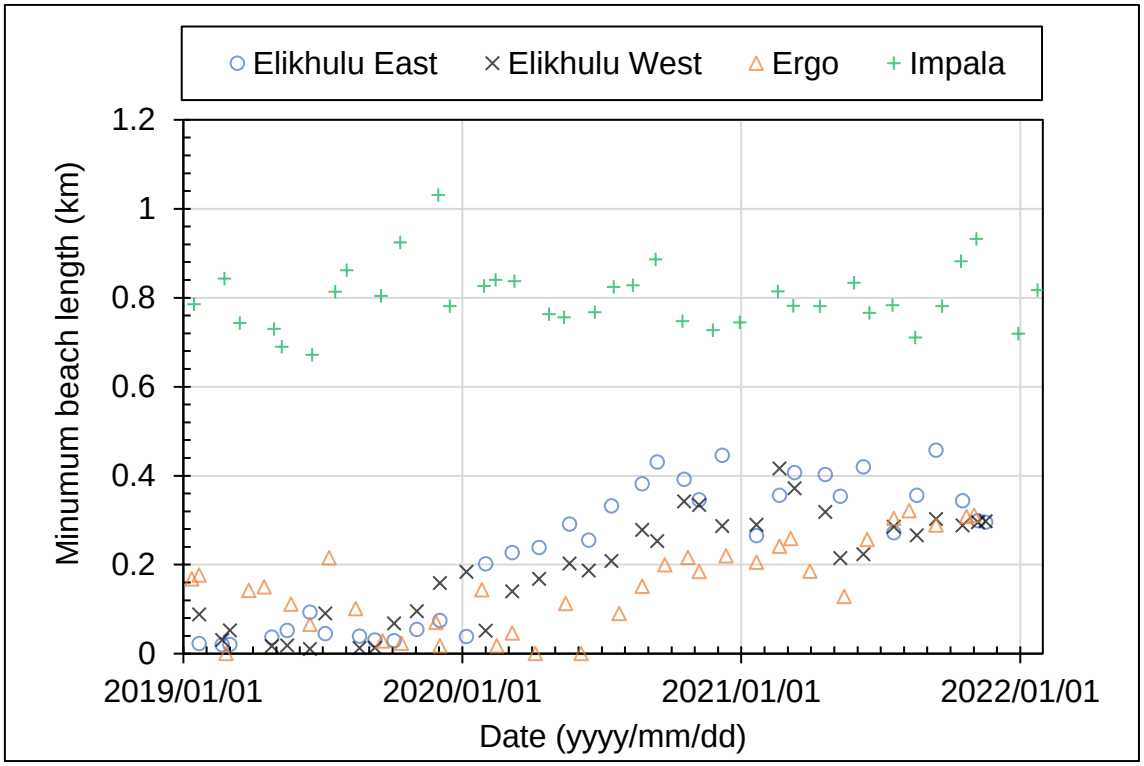


Figure 4-9: Minimum beach lengths delineated by visual assessment of S2 (Sentinel-2) and PS (PlanetScope) imagery.

4.2.2.2 Comparison of Sentinel-2 and PlanetScope minimum beach length data

Figure 4-10 indicates good correlation between pond measurements made using Sentinel-2 and PlanetScope reference imagery. A high degree of scatter as well as a tendency of Sentinel-2 to underestimate the minimum beach length is observed in the data obtained from Ergo.

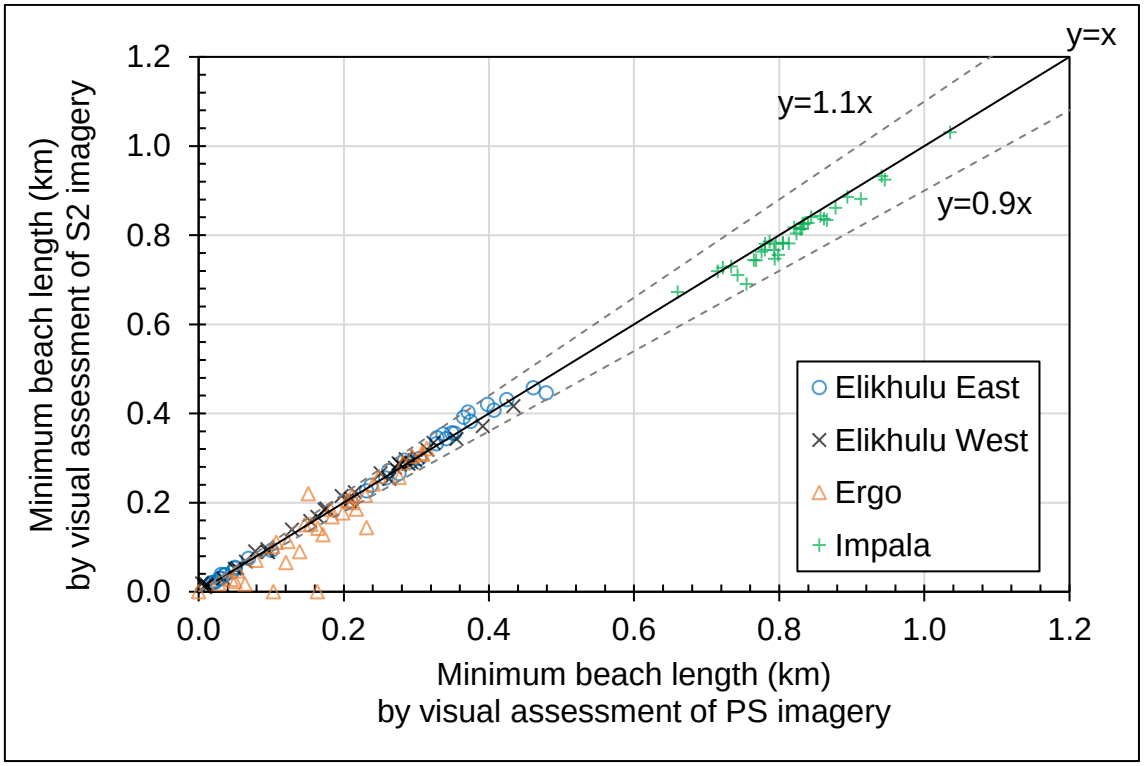


Figure 4-10: Agreement between minimum beach lengths determined by visual assessment of Sentinel-2 (S2) and PlanetScope (PS) imagery.

Figure 4-11 presents the relationship between the minimum beach length measurement ratio and the magnitude of the minimum beach length. The deviation of the minimum beach length ratio from one is greater for shorter minimum beach lengths. It can be observed that the measurement ratio from data at Elikhulu West and Ergo deviate significantly from a value of one.

Statistical data in Table 4-3 indicates that beach length data from Ergo and Elikhulu West presents a higher standard deviation than measurements made at Elikhulu East and Impala, corroborated by the presentation of data in Figure 4-11. Considering all the data there is no statistically significant bias in the Sentinel-2 measurements of the minimum beach length compared to the reference data. However, considering data from Ergo and Impala alone, there is a statistically relevant tendency of Sentinel-2 to underestimate the minimum beach length. This corresponds to the tendency of Sentinel-2 to overestimate the pond area at these sites. The mean minimum beach length ratios for Ergo and Impala are 0.839 and 0.979 with standard deviations of 0.294 and 0.020 respectively. The respective

p-values are <0.01 and <0.001 for Ergo and Impala indicating that there is a statistically significant bias of Sentinel-2 to estimate shorter minimum beach lengths than the reference at these sites.

In general, the minimum beach length ratio presented a high standard deviation, which suggests low precision measurements. Interestingly certain sites provided low standard deviations, namely Elikhulu East and Impala.

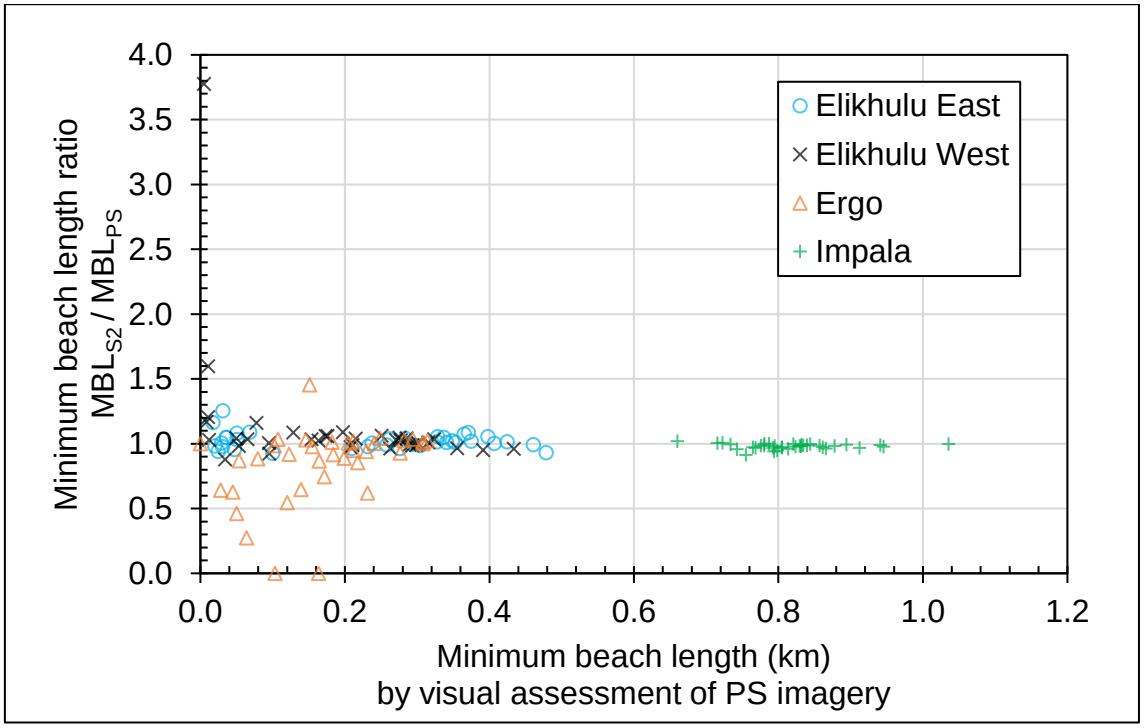


Figure 4-11: Ratio of the minimum beach length obtained by S2 (Sentinel-2) to PS (PlanetScope) versus minimum beach length magnitude.

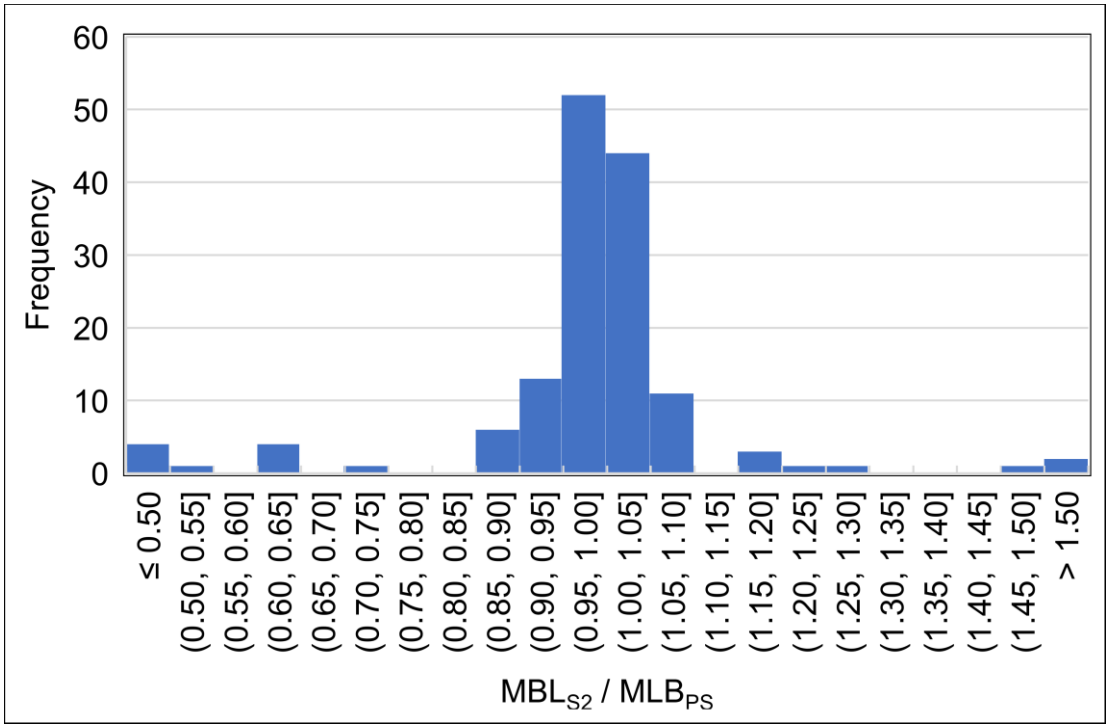


Figure 4-12: Histogram of the ratio of the MBL (minimum beach length) measured by Sentinel-2 to PlanetScope.

Table 4-3: Visually assessed Sentinel-2 versus PlanetScope minimum beach length data statistics

Site	Mean Ratio $\mathrm{MBL}_{S2} / \mathrm{MBL}_{PS}$ $(\bar{X})$	Mean Ratio Difference $(\bar{X} - \mu_0)$	Sample Std. Dev. (S)	Sample size (n)	P-value (indicating statistically significant bias)
Elik. East	1.021	0.021	0.063	36	>0.05
Elik. West	1.116	0.116	0.470	36	>0.1
Ergo	0.839	-0.161	0.294	36	<0.01
Impala	0.979	-0.021	0.020	36	<0.001
All	0.989	-0.011	0.294	144	>0.5

4.2.2.3 Comparison of Sentinel-2 to very high-resolution reference data

Minimum beach length measurements made by visual assessment of the pond in Sentinel-2 imagery are compared to measurements made using very high-resolution reference data, as displayed in Figure 4-13, below.

Sentinel-2 derived minimum beach length measurements agreed well with the very high-resolution reference data, given the correlation in Figure 4-13. There is no bias reported for Sentinel-2 to under or overestimate minimum beach length measurements, as reported in Table 4-4. The standard deviation of the measurement ratio is, however, relatively high at 0.141 which indicates low precision of the Sentinel-2 minimum beach length measurements when compared to measurements made in the very high-resolution reference imagery.

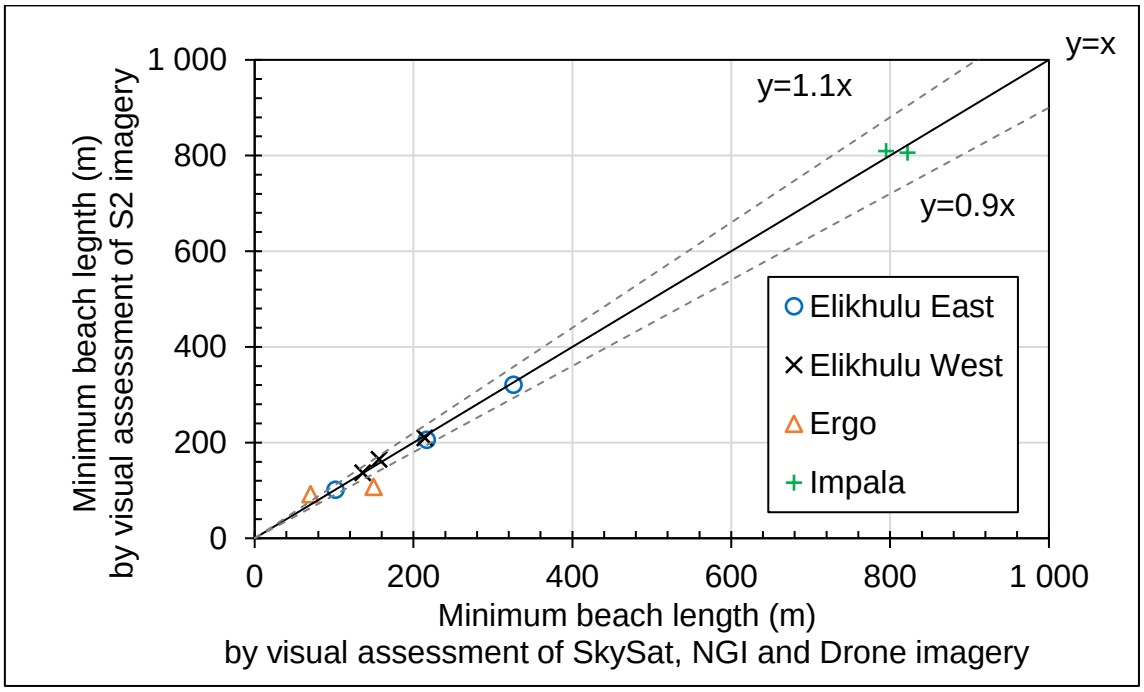


Figure 4-13: Summary of minimum beach length by visual assessment of Sentinel-2 (S2) versus very high-resolution reference imagery.

Table 4-4: Sentinel-2 versus very high-resolution reference minimum beach length data statistics

Mean Ratio $\mathrm{MBL_{S2}} / \mathrm{MBL_{PS}}$ $(\bar{X})$	**Mean Ratio Difference** $(\bar{X} - \mu_0)$	**Sample Std. Dev.** (S)	**Sample size** (n)	**P-value** (indicating statistically significant bias)
1.00	0.00	0.141	10	>0.5

4.2.3 Pond centroid displacement

4.2.3.1 Temporal pond centroid displacement data

Figure 4-14 presents the distance of individual pond centroids to the mean pond centroid location. Impala and Ergo are both facilities that were established decades prior to this study, while Elikhulu was commissioned during this study period and therefore the commissioning phase is part of this investigation. Both Impala and Ergo present pond centroid displacement values of less than 100 m. Comparatively, both compartments at Elikhulu present much larger and less stable pond centroid displacements with time. As the Elikhulu facility was commissioned, a pioneering layer of tailings was placed to cover the initial footprint area. Until the tailings surface had achieved a contiguous layer, the pond exhibited a tendency to drift laterally within the footprint, exhibited as a high pond centroid displacement value in Figure 4-14.

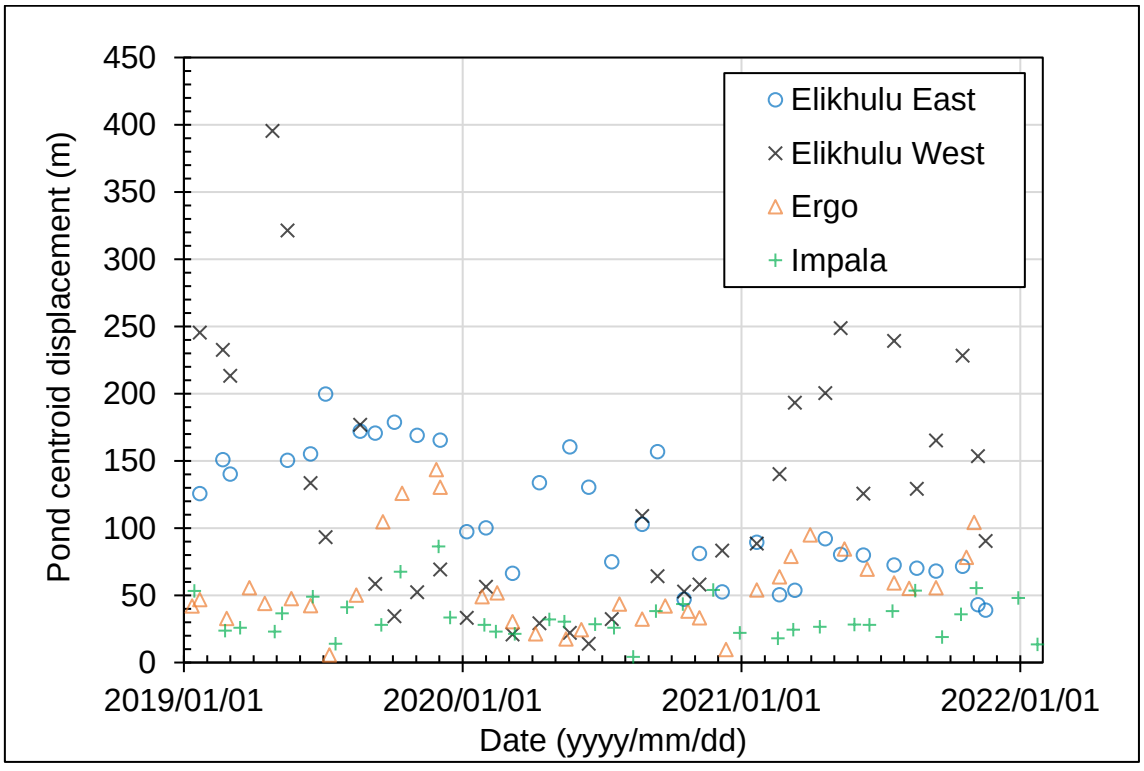


Figure 4-14: Pond centroid displacement delineated by visual assessment of Sentinel-2 imagery.

4.2.3.2 Comparison of Sentinel-2 and PlanetScope pond centroid displacement data

Figure 4-15 provides a 1:1 plot of pond centroids obtained from Sentinel-2 to those obtained from PlanetScope. There is a good correlation between the pond centroid data derived from PlanetScope and Sentinel-2 imagery, with most Sentinel-2 data falling within 10% of PlanetScope. No statistically significant bias of Sentinel-2 compared to the reference dataset is observed when inspecting all the data or the individual sites. See Table 4-5 for the statistical summary of the comparison of Sentinel-2 to PlanetScope centroid displacement data.

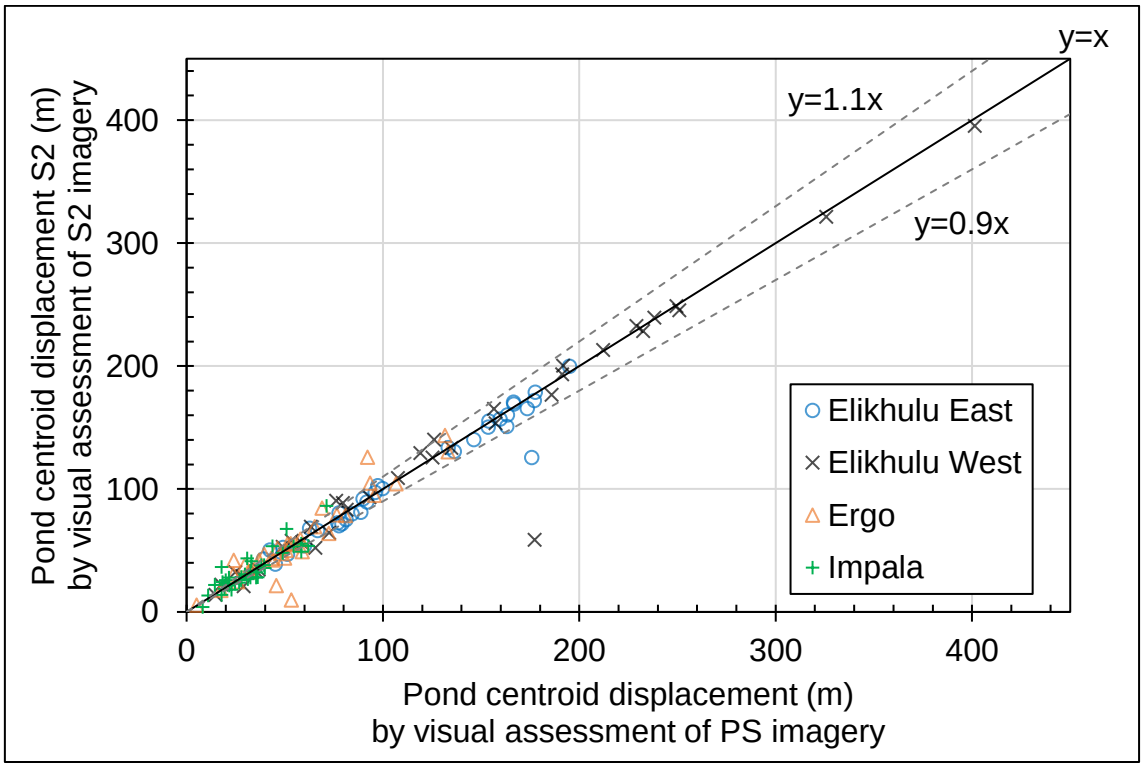


Figure 4-15: Agreement between pond centroid movement by visual assessment of S2 (Sentinel-2) and PS (PlanetScope) imagery.

Figure 4-16 below provides a plot of the pond centroid displacement ratio to the magnitude of the pond centroid displacement. As for the other measurement ratios discussed in the prior sections of this chapter, there is greater deviation of the pond centroid displacement ratio from a value of one as the magnitude of the

centroid displacement decreases. No trends are apparent in the data and the scatter appears random.

The standard deviation of the pond centroid displacement measurement ratio for all the data is moderate to high, with a value of 0.20 calculated. On a site-by-site basis, standard deviation in the measurement ratio is high, except for the data obtained at Elikhulu East, where a standard deviation of 0.08 is reported. The displacement of the pond centroid is not a critical measurement of dam safety, but rather a measurement that can provide insight into trends in the behaviour of the water body atop a tailings facility. If multiple readings of the tailings pond centroid indicate that the pond is displacing from its mean or intended location, coupled with short minimum beach lengths and / or large pond area readings, it may signal poor pond control and tailings operational shortcomings. These circumstances could be used to trigger a safety warning and flag the need for closer inspection of the site. Such measurements are screening tools and so do not need the precision required for safety critical measurements. Therefore, Sentinel-2 pond centroid displacement data, although not highly precise can provide an indication of pond displacement trends in time.

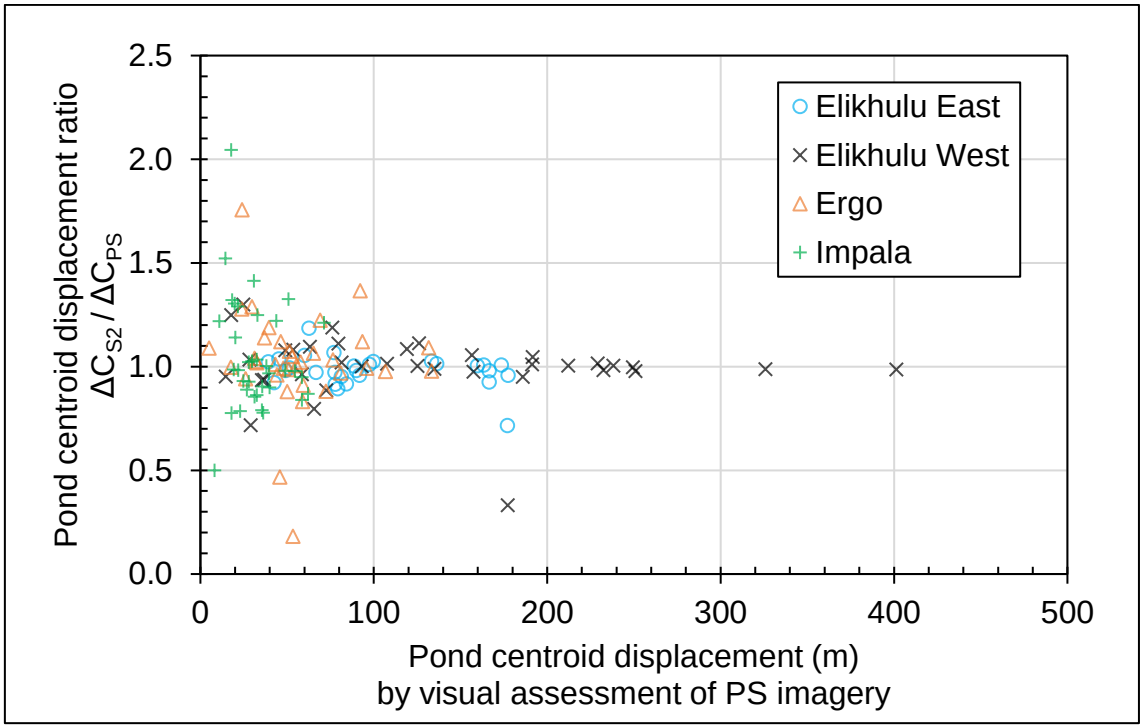


Figure 4-16: Ratio of the pond centroid displacement obtained by S2 (Sentinel-2) to PS (PlanetScope) versus pond centroid displacement magnitude.

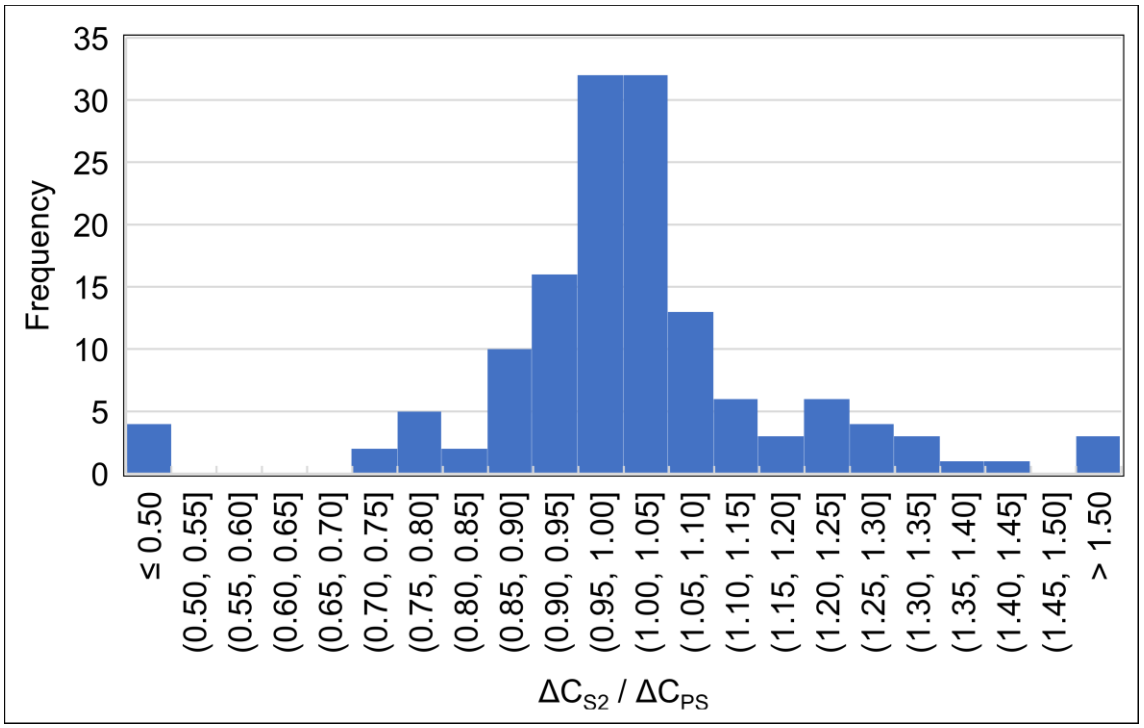


Figure 4-17: Histogram of the S2 (Sentinel-2) to PS (PlanetScope) centroid displacement ratio.

Table 4-5: Visually assessed Sentinel-2 versus PlanetScope minimum beach length data statistics

Site	Mean Ratio $\Delta C_{S2} / \Delta C_{PS}$ $(\overline{X})$	Mean Ratio Difference $(\overline{X} - \mu_0)$	Sample Std. Dev. (S)	Sample size (n)	P-value (indicating statistically significant bias)
Elik. East	0.978	-0.022	0.080	36	>0.1
Elik. West	0.996	-0.004	0.156	36	>0.5
Ergo	1.026	0.026	0.241	36	>0.5
Impala	1.050	0.050	0.274	36	>0.2
All	1.013	0.013	0.203	144	>0.4

4.2.3.3 Comparison of Sentinel-2 to very high-resolution reference data

Pond centroid displacements were also derived from visually assessed very high-resolution reference imagery. The Elikhulu drone orthophoto imagery was stored in a local datum that could not be reprojected into the UTM projection used for the remaining data from SkySat and the CDNGI. Therefore, the displacement of the pond centroid in the drone imagery to the mean pond centroid could not be ascertained due to the incompatible projections of the two locations. As a result, there are two fewer data points in the very high-resolution reference dataset for pond centroid displacement. Nonetheless, Sentinel-2 derived pond centroid displacements corresponds well to the very high-resolution reference measurements, with little to no bias measured and a very small standard deviation of 0.047.

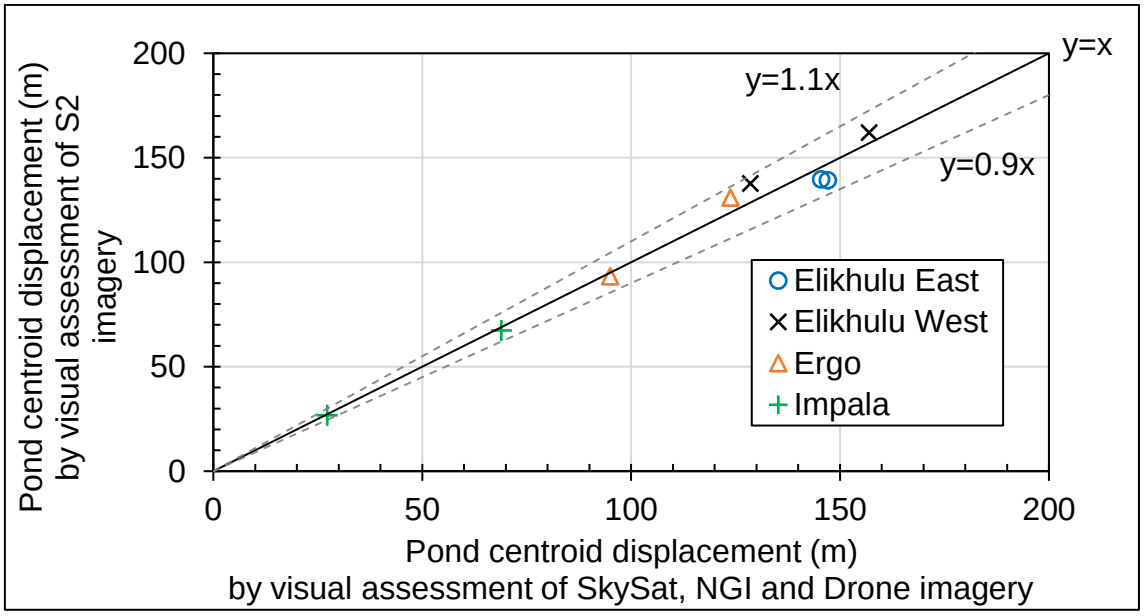


Figure 4-18: Summary of pond centroid displacement by visual assessment of Sentinel-2 (S2) versus very high-resolution reference imagery.

The statistics of data are summarised in Table 4-6. The pond centroid data obtained by Sentinel-2 compares very well with the very high-resolution reference data, indicating good accuracy with a mean measurement ratio of 1.00 and standard deviation of less than 0.05. This is contradictory to the comparison of Sentinel-2 to the high-resolution PlanetScope data, which indicated a high standard deviation. It could be that the very high-resolution dataset was not a large enough sample to be representative of the underlying population being sampled. Alternatively, it may also suggest that some measurement inaccuracies have been introduced by the PlanetScope reference data, possibly as a result of image georeferencing and dataset co-registration inaccuracies.

Table 4-6: Sentinel-2 versus very high-resolution reference pond centroid displacement data statistics

Mean Ratio $\Delta C_{S2} / \Delta C_{PS}$ $(\bar{X})$	**Mean Ratio Difference** $(\bar{X} - \mu_0)$	**Sample Std. Dev.** (S)	**Sample size** (n)	**P-value** (indicating statistically significant bias)
1.00	0.00	0.047	8	>0.5

4.2.4 Minimum beach length versus pond area

Figure 4-19 illustrates an inverse correlation between pond area and minimum beach length at each site. This is an expected relationship. As the pond expands in area, within the finite bounds of the tailings crest, it must get closer to the outer boundary of the tailings dam. The tailings ponds assessed indicate that as the pond increases in area the minimum beach length decreases with correlation values of between -0.75 and -0.80. Interestingly, each site occupies a distinct region of the pond area versus minimum beach length space, shown in Figure 4-19. Of note are the differences between Impala and Ergo. Impala is managed with a small pond and long beaches, while in comparison, Ergo has significantly shorter beaches and a larger pond area. Short beaches and a large pond indicate a lower beach freeboard and a greater amount of water stored atop a facility, relative to the same facility with long beached and a smaller pond. Both measures signify a higher risk associated with the facility. A plot of pond area versus minimum beach length could be used to provide operators with an indication of a tailings dam's status. Different zones of pond size and minimum beach length could be incorporated into the plot based on site-specific operational and regulatory requirements.

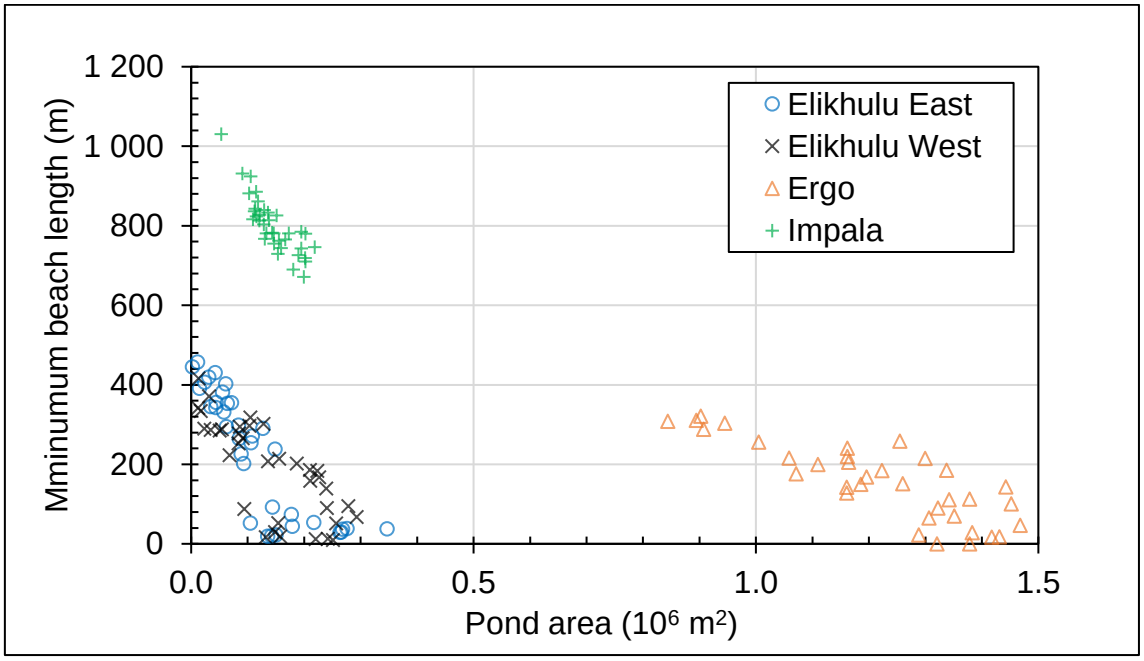


Figure 4-19: Pond area versus minimum beach length delineated by visual assessment of Sentinel-2 imagery.

4.3 Sentinel-2 thresholds and threshold derived data

4.3.1 Near infrared (NIR) threshold

Upper and lower bounds of the NIR threshold were investigated by analysis of the histogram and transect of aggregated NIR image data, available in Appendix-B. A summary of this data is presented in Table 4-7, below, with links to the relevant figures in the appendix. The histogram modes are reported as well as potential upper and lower bound thresholds based on transect of aggregated imagery data taken through the pond location.

Table 4-7: Sentinel-2 NIR 2019 to 2021 histogram and transect assessment results

Site	NIR Threshold (Reflectance scaled by 10^4)					
	Histogram	Mode Low	Mode High	Transect	Low	High
Elik. East	Figure 8-2	2 200	3 240	Figure 8-4 a)	-	-
Elik. West	Figure 8-11	2 080	2 680	Figure 8-13 a)	-	-
Ergo	Figure 8-20	80	2 500	Figure 8-22 a)	600	2 000
Impala	Figure 8-27	350	1 410	Figure 8-29 a)	-	-

All the sites presented bimodal NIR histograms. However, the histogram modes were not clearly separate for the Elikhulu East and West sites. Ergo and Impala histograms showed two distinct groups of pixels, one presumably representing the decant pond and the other the tailings beach.

Upper and lower bound NIR thresholds using the maximum and minimum statistics could only be obtained from the transect at Ergo. Minima and maxima of the transect data from the other sites did not provide coherent ranges of NIR to separate the pond and beach. It is possible that the maximum and minimum image statistics used are too stringent and instead confidence intervals should be used in future to investigate a suitable threshold range.

An iterative analysis of multiple discrete thresholds was performed and compared to Sentinel-2 visually interpreted pond area training data. Figure 4-20 illustrates the processes followed to determine optimum thresholds for imagery datasets for each of the study sites. As illustrated by the callouts in Figure 4-20, the threshold

value that provides the lowest summed square error for a given dataset is taken as the optimum threshold. This procedure is performed on yearly image sets of 12 images, to determine the year-on-year threshold, and again for all 36 images in the main study period to determine the single optimum threshold. Interestingly in Figure 4-20 a) and b), the 2021 year-on-year thresholds at Elikhulu East and West presented much lower square error sums compared to the threshold of the preceding years. This suggests a significant improvement in the threshold's performance in matching the training data.

Table 4-8 presents the threshold derivation results. All analyses were able to identify an optimum threshold. i.e. a global minimum was contained in the least square error data. Suitability of the thresholds is assessed by comparison of pond data derived by the thresholds to the reference dataset. Thresholds for Ergo and Impala remained close to one another; the year-on-year thresholds are similar to the single optimum threshold. However, the threshold values from Elikhulu East and West jump significantly in 2021 compared to values obtained in 2019 and 2020. The 2021 thresholds are also significantly different to the single optimum thresholds for the two Elikhulu compartments, which fall within the range of the 2019 and 2020 year-on-year thresholds.

By the start of 2021 the geomembrane at Elikhulu is essentially covered with deposited tailings. As the geomembrane covers a relatively large portion of the basin and is black in colour with low reflectance of visible and near infrared light, it presents a significant spectral feature within the tailings dam footprint requiring distinction from the pond. The geomembrane is covered at Elikhulu in late 2020 and so, is not appreciably visible in imagery after the start of 2021. While the floodable surface area of a tailings dam is made up of exposed geomembrane alongside dry tailings beach and decant pond, a binary spectral threshold will need to correctly identify the pond as different from both the geomembrane and the tailings beach. This is only possible if the geomembrane is spectrally different from the decant pond but similar to the tailings beach in the NIR. This is not necessarily the case as both geomembrane and the decant pond have low NIR reflectance. Therefore the presence of geomembrane introduces a surface that may easily be misclassified as decant pond and introduce significant

measurement error. It is fitting to adopt a new optimum threshold value based on the site characteristics once the exposed geomembrane is covered by tailings. Furthermore, the presence of geomembrane, with low NIR reflectance, explains the absence of a bimodal histogram of the aggregated NIR image for the period between the start of 2019 and end 2021 at the Elikhulu site.

Due to the geomembrane's presence in 2019 and 2020 and its absence in 2021, updated NIR thresholds of 2 360 and 2 280 were used for automatic delineation of the pond at Elikhulu East and West from the start of 2021 onward. The single optimum threshold was used prior to 2021.

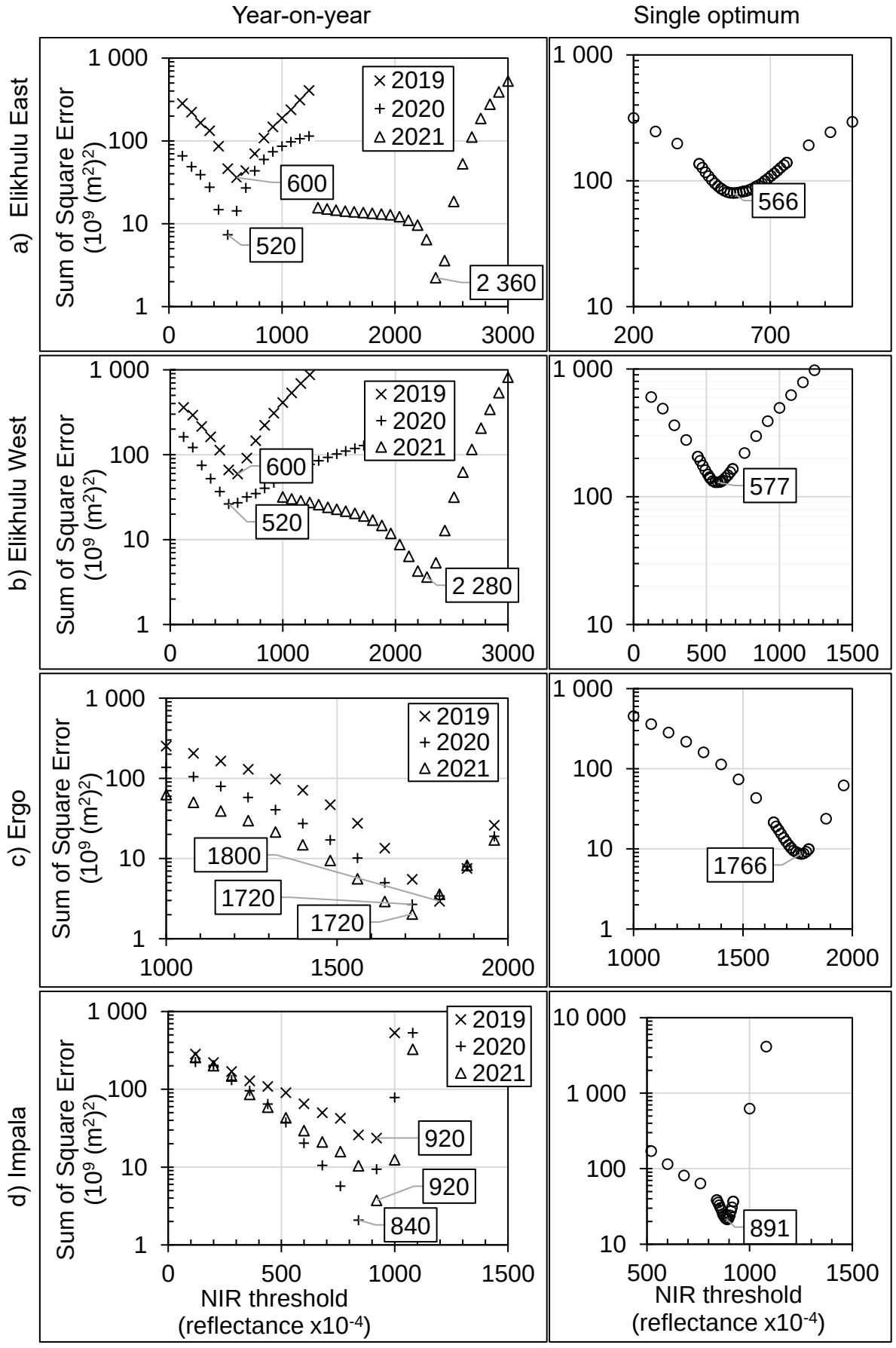


Figure 4-20: NIR threshold derivation by minimum sum of square errors.

Table 4-8: Sentinel-2 NIR threshold values obtained by training against visually assessed pond area data

Site	NIR Threshold (Reflectance scaled by 10^4)			
Period:	**2019**	**2020**	**2021**	**Single Optimum**
Elikhulu East	600	520	2 360	566
Elikhulu West	600	520	2 280	577
Ergo	1 800	1 720	1 720	1 766
Impala	920	840	920	891

NIR threshold derived pond data is compared to the PlanetScope reference dataset in Figure 4-21, on the following page. Figure 4-22 presents the measurement ratio of the area obtained by Sentinel-2 NIR threshold to PlanetScope versus pond area magnitude. This figure is analogous to Figure 4-3 but indicates a higher degree of scatter in the pond area ratio for the smaller pond sizes in Figure 4-21 b). A comparison of the area measurements of the two datasets is presented in the histogram of pond area ratios in Figure 4-23 thereafter. Statistics of a comparison of Sentinel-2 threshold derived pond areas is summarised in Table 4-9.

The histogram of pond area ratio, shown in Figure 4-23, indicates 15 pond omission errors occurred, where A_{S2} / A_{PS} is less than 0.50. The modal value of the data sits between 1.00 and 1.05, similar to visual assessment. Five commission errors occurred where A_{S2} / A_{PS} is greater than 1.50. By inspection of Figure 4-22, omission and commission errors occurred for the smaller ponds at Elikhulu and Impala.

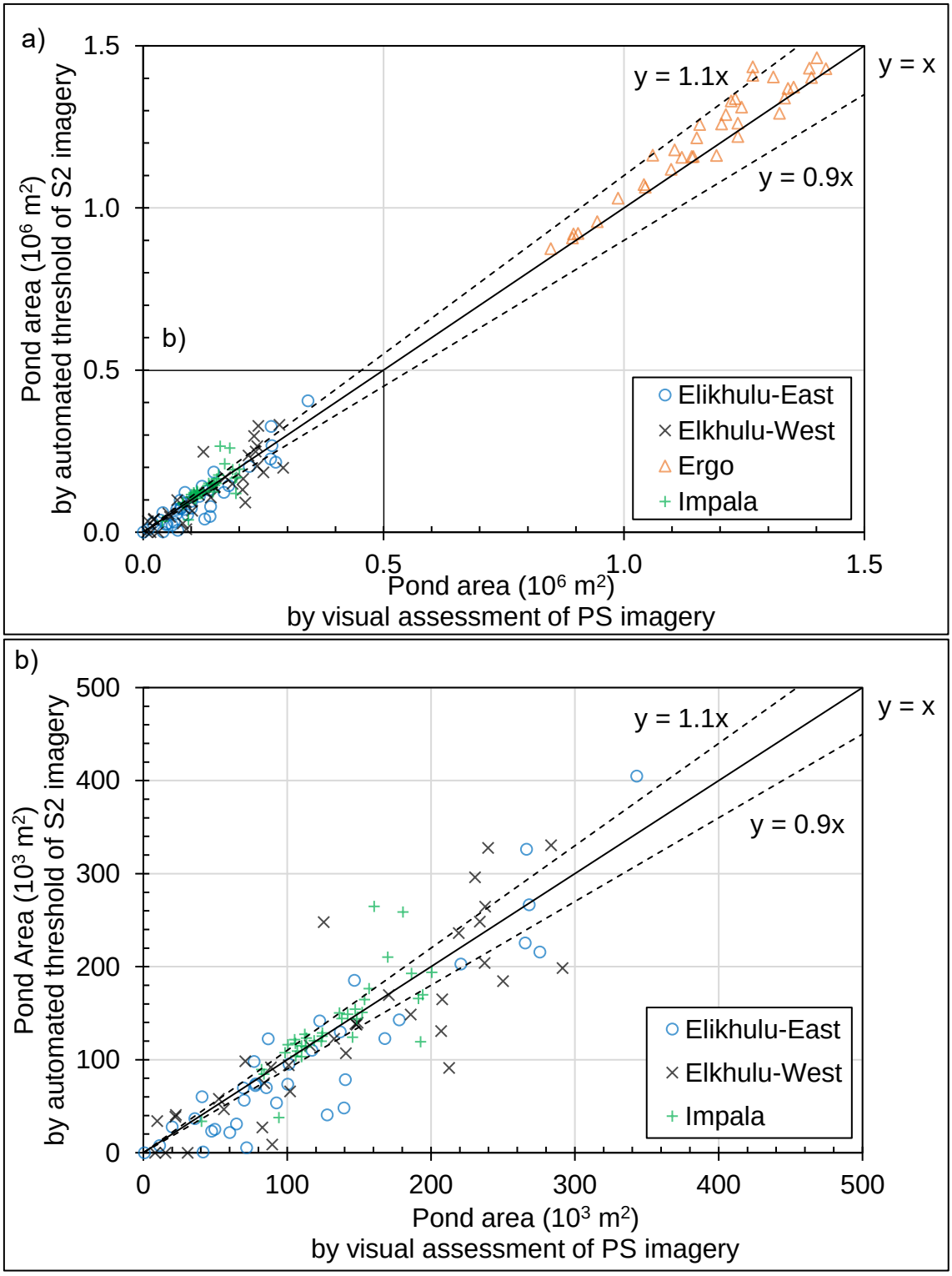


Figure 4-21: Pond area by S2 (Sentinel-2) NIR threshold versus visually assessed PS (PlanetScope) imagery.

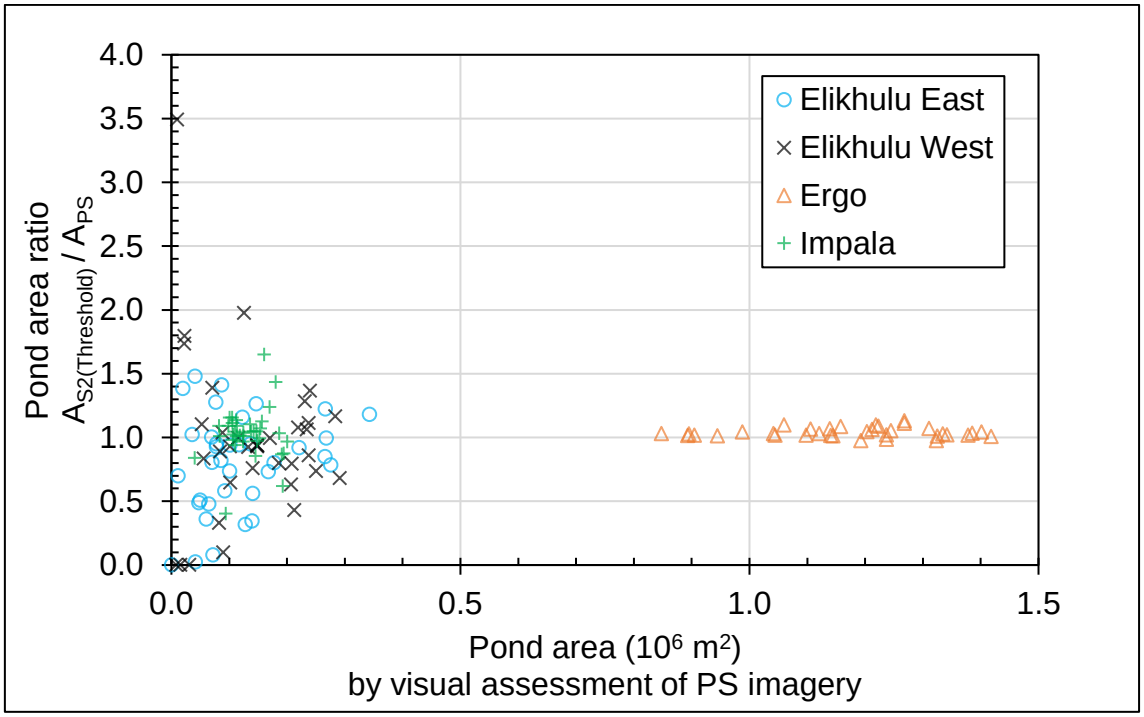


Figure 4-22: Ratio of the area obtained by Sentinel-2 (S2) NIR threshold to PS (PlanetScope) versus pond area magnitude.

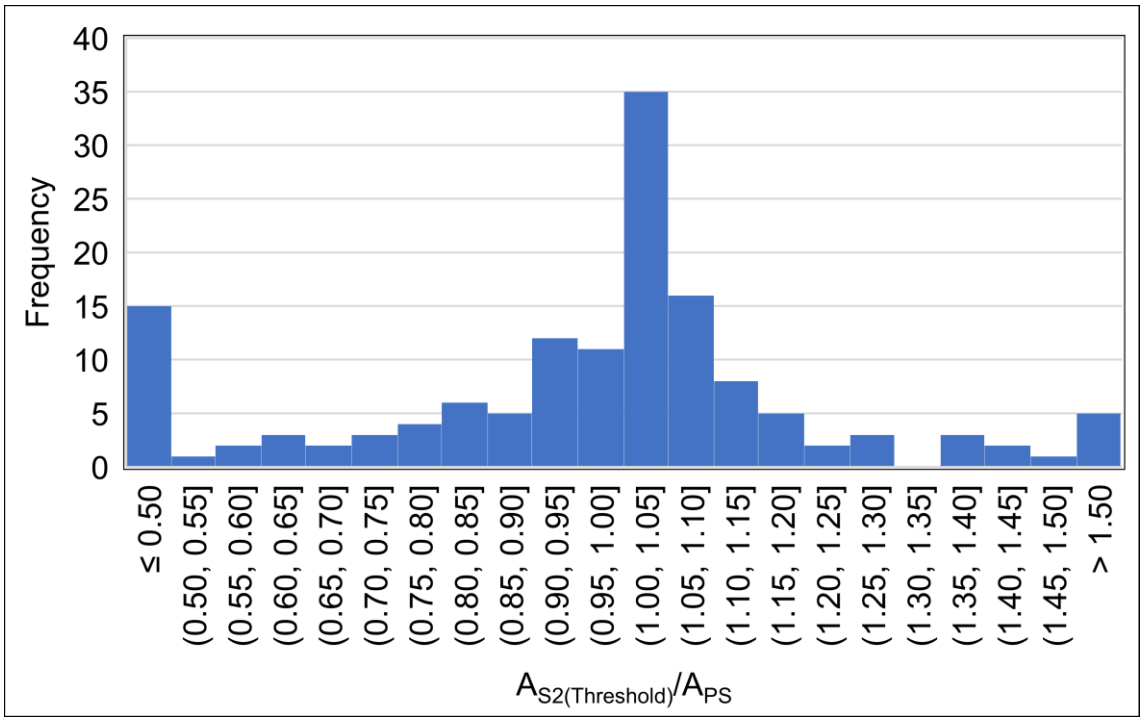


Figure 4-23: Histogram of the ratio of area obtained by S2 (Sentinel-2) NIR threshold to PS (PlanetScope).

Referring to the results in Table 4-9, below, ponds delineated by NIR threshold underestimate the pond area compared to visual assessment of the reference dataset by 9.3%. The pond areas are statistically significantly different to those derived by visual assessment of Sentinel-2 ($p<0.01$). The standard deviation of the pond area ratio by NIR threshold versus the reference dataset is 0.390, which is greater than the visually interpreted sample which is of practical importance to stakeholders who may wish to implement spectral NIR thresholding for pond delineation. As a larger standard deviation in the pond area measurement ratio indicates a greater degree of scatter in the parameter, lower precision in pond area measurement may be anticipated.

On a site-specific basis, NIR thresholding performed adequately at Ergo where the mean pond area ratio of 1.040 and standard deviation of 0.037 which is close to the values obtained by visual assessment. This is likely due to the spectral characteristics of the tailings beach and decant pond at Ergo which make it amenable to binary spectral threshold classification in NIR. Typically, the site has bright beaches and a deep dark decant pond in the NIR spectrum. In general, however, NIR thresholding did not perform as well as visual assessment in delineating pond areas at Elikhulu East and West and Impala. Elikhulu East NIR threshold derived pond area data reported a significantly lower mean pond area ratio with a similar standard deviation when compared to visual assessment of the imagery from the site; a mean area ratio of 0.805, with a standard deviation of 0.383, by NIR threshold compared to a mean area ratio of 1.018, with a standard deviation of 0.395, by visual assessment. Elikhulu West did not report a significantly different mean area ratio but did report greater scatter in the area ratio compared to visual assessment, with a standard deviation of 0.632 in the threshold data compared to 0.134 from visual assessment. The pond area ratio results from Impala are significantly different to the same results obtained by visual assessment; the data from the site reports a lower mean area ratio with higher standard deviation. The mean area ratio is 1.029 compared to 1.112, with a standard deviation of 0.198, compared to 0.093, for NIR threshold statistics compared to visual assessment, respectively.

Table 4-9: Statistics of NIR threshold derived Sentinel-2 pond area data versus PlanetScope reference data

Site	Mean Ratio A_{S2} / A_{PS} $(\bar{X})$	Mean Ratio Null Hypothesis (μ_0)	Mean Ratio Difference $(\bar{X} - \mu_0)$	Sample Std. Dev. (S)	Sample Size (n)	P-value (indicating statistically significant difference to visual assessment)
Elik. East*	0.805	1.0	-0.195	0.383	36	<0.01
Elik. West*	0.965	1.0	-0.035	0.632	36	>0.5
Ergo	1.040	1.038	0.003	0.037	36	>0.5
Impala	1.029	1.112	-0.083	0.198	36	<0.02
All - NIR Threshold*	0.960	1.053	-0.093	0.390	144	<0.01
All - Vis. Assess.	1.053	-	0.053	0.215	144	-

*Dataset obtained where the NIR threshold was updated from the start of 2021 due to inundation of the geomembrane basin indicating a change to the composition of the surfaces of the facilities. Data can be viewed explicitly for Elikhulu East in Figure 8-5 and Figure 8-6 and Elikhulu West in Figure 8-14 and Figure 8-15 in Appendix-B.

4.3.2 Normalised difference water index (NDWI) threshold

The procedure of determining NDWI thresholds and assessing threshold suitability is identical to that followed for the NIR spectral threshold. First upper and lower bounds of the NDWI threshold are investigated by analysis of histogram modes and transect minima and maxima. Table 4-10 summarises these results with links to the relevant figures in Appendix-B provided.

Table 4-10: Sentinel-2 NDWI 2019-2021 histogram and transect assessment results

Site	NDWI Threshold (Ratio between -1 and 1)					
	Histogram	Mode Low	Mode High	Transect	Low	High
Elik. East	Figure 8-3	-0.065	0.245	Figure 8-4 b)	-	-
Elik. West	Figure 8-12	-0.085	-	Figure 8-13 b)	-	-
Ergo	Figure 8-21	-0.160	0.805	Figure 8-22 b)	0.00	0.26
Impala	Figure 8-28	-0.045	0.555	Figure 8-29 b)	-	0.10

All the sites presented bimodal histograms except for Elikhulu West. As discovered in NIR, separation of the histogram modes was not as clear for the Elikhulu East and West as it was for Ergo and Impala. This indicates that a suitable single optimum NDWI threshold may not exist for the Elikhulu compartments in the date range analysed (2019-2021). Ergo and Impala histograms showed two distinct groups of NDWI pixels. Upper and lower bound NDWI thresholds using the maximum and minimum statistics could only be obtained from the transect at Ergo, however, an upper bound could be ascertained from the transect at Impala. Transects at Elikhulu could not provide upper or lower bounds to the range of NDWI values able to distinguish the pond and beach. As noted in the assessment of the NIR transect and histogram, it is possible that the maximum and minimum statistics used are too stringent and instead confidence intervals could be investigated in future.

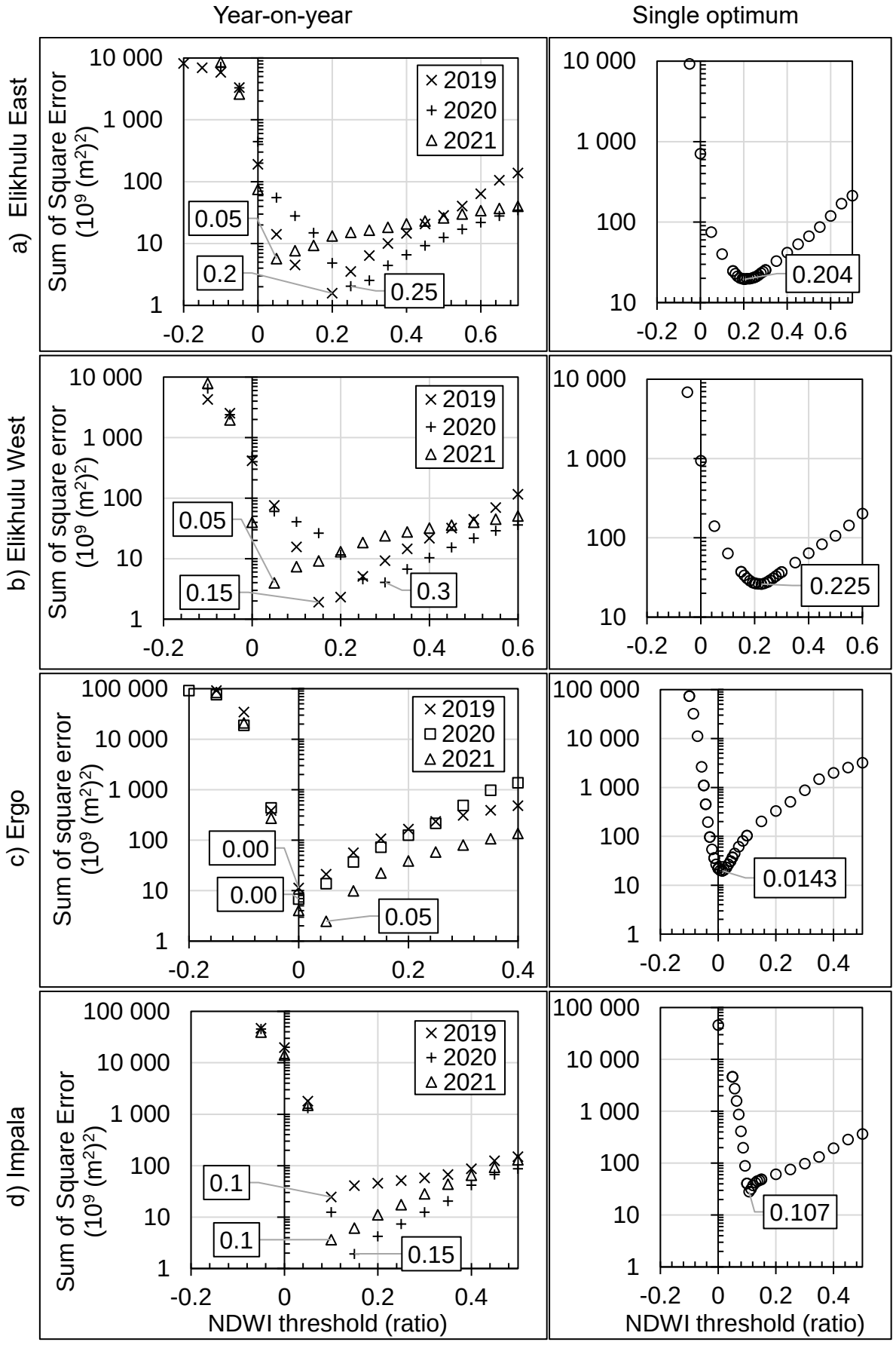


Figure 4-24: NDWI threshold derivation by minimum sum of square error.

As conducted for NIR, an iterative analysis of various discrete NDWI thresholds for each of the sites is presented in Figure 4-24. Square errors are computed against the same training dataset as was used for NIR, i.e. pond area data from visually assessed Sentinel-2 imagery.

Table 4-11 provides a summary of the results of the threshold derivation in Figure 4-24, which are flagged by the data callouts in the figure. A comparison of NDWI threshold derived pond areas to the reference dataset is presented in Figure 4-25. From the results in Table 4-11, year-on-year thresholds for Ergo and Impala did not deviate far from the single optimum threshold. Threshold values for Elikhulu East and West decrease in 2021 compared to values obtained in 2019 and 2020, analogous to the jump seen in NIR thresholds in Table 4-8. The Elikhulu 2021 NDWI thresholds are also different to the single optimum thresholds, where the single optimum thresholds from Elikhulu East and West fall within the range of the 2019 and 2020 year-on-year thresholds. This deviation is due to the presence of exposed geomembrane in 2019 and 2020 and its absence in 2021, as previously discussed in section 4.3.1. An updated NDWI threshold of 0.05 is used for automatic delineation of the ponds at Elikhulu East and West from the start of 2021. The single optimum threshold was used prior to 2021. This is equivalent to the process followed for NIR due to the inundation of the exposed geomembrane in late 2020. Interestingly, the sum of square error of the optimum thresholds for Elikhulu East and West in Figure 4-24 a) and b), is significantly lower than the same values reported for NIR in Figure 4-20 a) and b). This indicates that a single optimum NDWI threshold may perform better than a single optimum NIR threshold for the Elikhulu East and West ponds.

Table 4-11: NDWI threshold values obtained by training against visually assessed pond areas

Site	NDWI Threshold (Ratio between -1 and 1)			
Period:	2019	2020	2021	Single Optimum
Elikhulu East	0.20	0.20	0.05	0.204
Elikhulu West	0.15	0.30	0.05	0.225
Ergo	0.00	0.00	0.05	0.014
Impala	0.10	0.10	0.15	0.107

NDWI threshold derived pond data is compared to the PlanetScope reference dataset in Figure 4-25. Figure 4-26 presents the measurement ratio of the area obtained by Sentinel-2 NDWI threshold to PlanetScope versus pond area magnitude. This figure is analogous to Figure 4-3, which displays pond area data from visual assessment of Sentinel-2 against pond area data from PlanetScope. By visual inspection the scatter of the data points in the two figures appears similar. The sample of the ratios of areas derived by NDWI threshold of Sentinel-2 to the areas derived by visual assessment of PlanetScope is summarised in the histogram in Figure 4-27. Statistics of the comparison of Sentinel-2 threshold derived pond areas to the reference dataset are summarised in Table 4-12, following the histogram.

The histogram of pond area ratio indicates eight pond omission errors occurred, where A_{S2} / A_{PS} is less than 0.50. The modal value of the data sits between 1.00 and 1.05, similar to visual assessment. Four commission errors occurred where A_{S2} / A_{PS} is greater than 1.50. This is an improvement over NIR, but still significantly worse performance than visual assessment. By inspection of Figure 4-26, it is apparent that the omission and commission errors occurred for the smaller Elikhulu and Impala ponds.

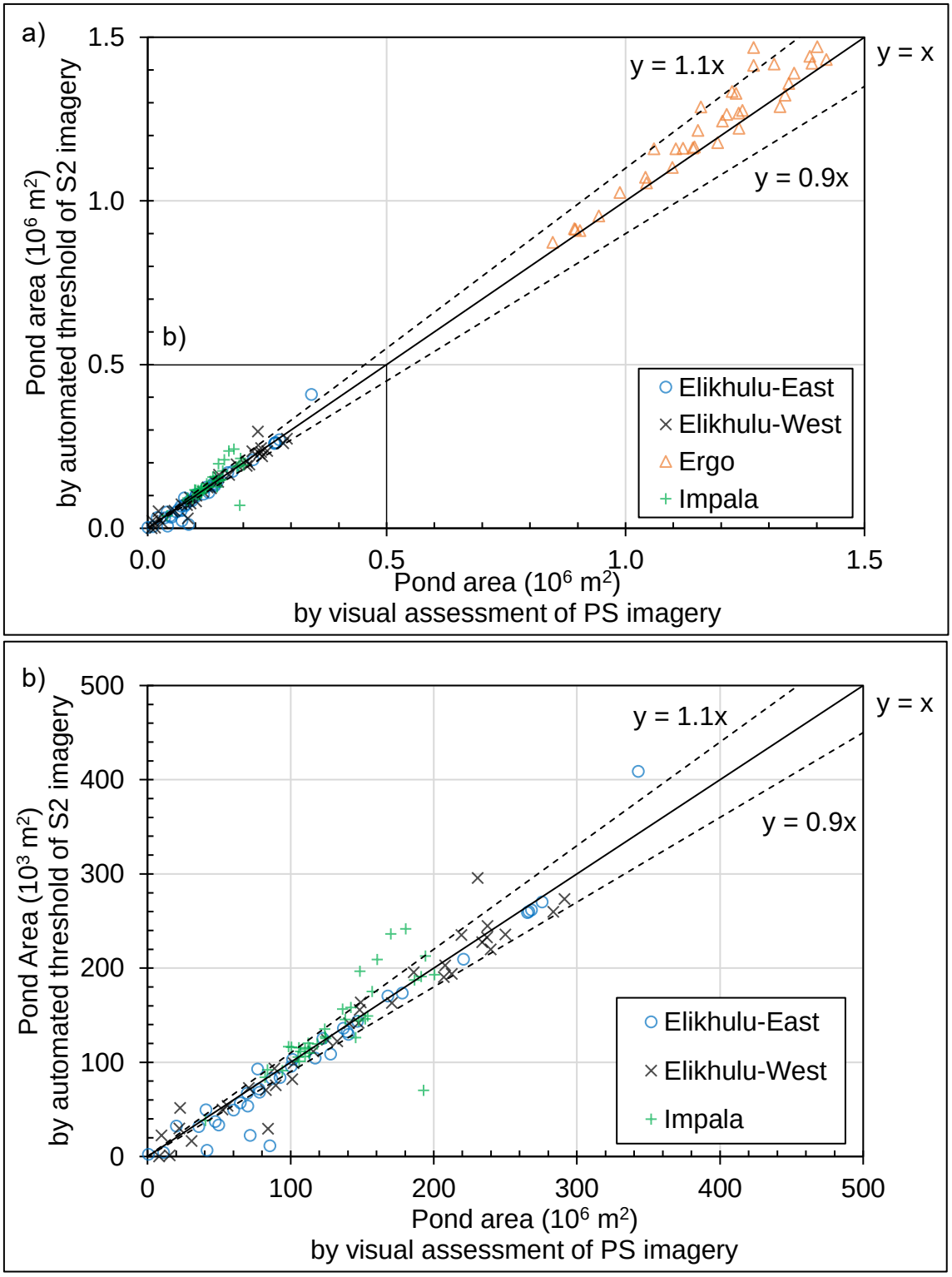


Figure 4-25: Pond area by S2 (Sentinel-2) NDWI threshold versus visually assessed PS (PlanetScope) reference imagery.

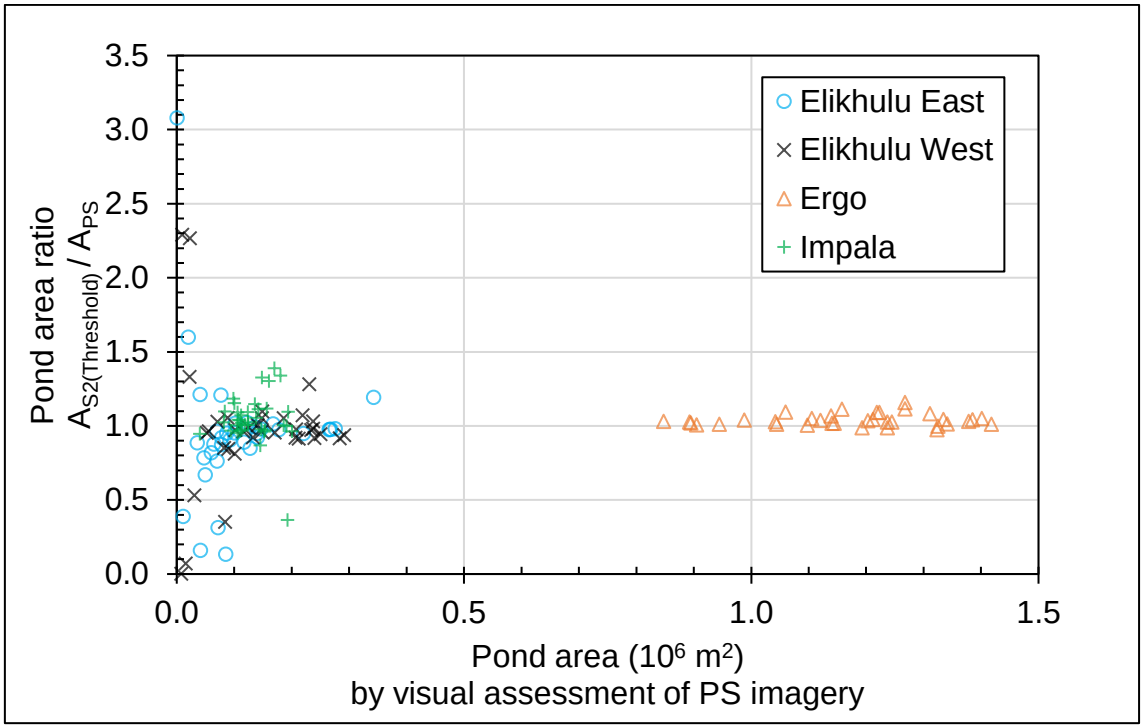


Figure 4-26: Ratio of the area obtained by Sentinel-2 (S2) NDWI threshold to PS (PlanetScope) versus pond area magnitude.

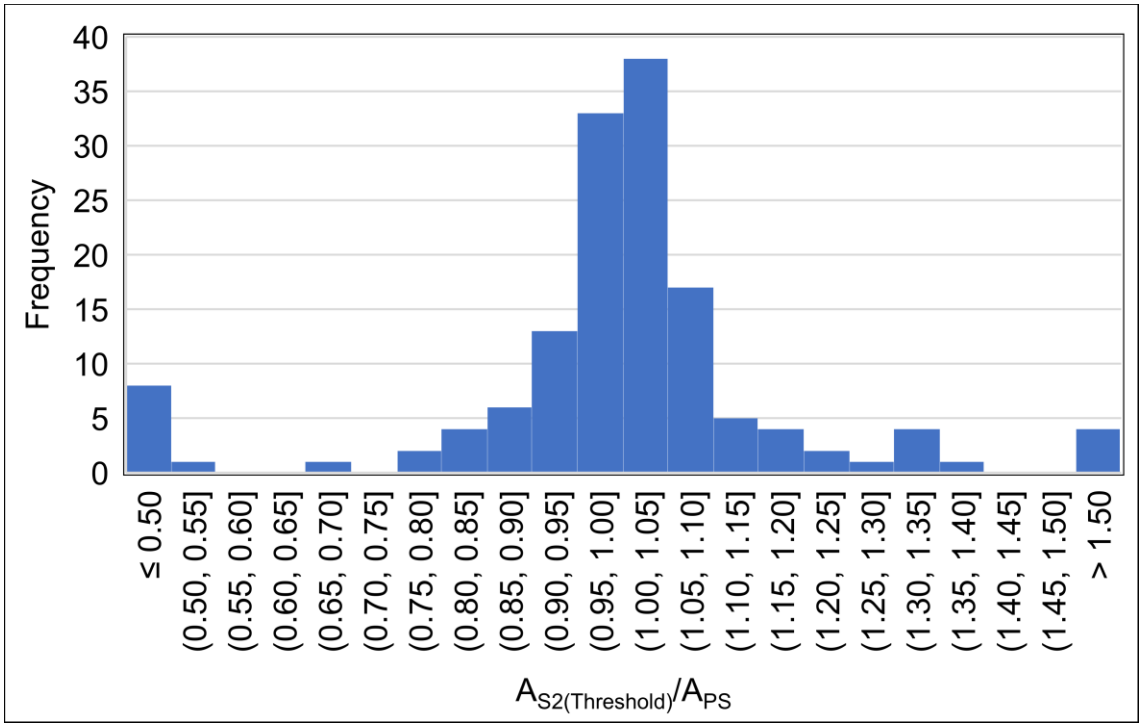


Figure 4-27: Histogram of the ratio of area obtained by S2 (Sentinel-2) NDWI threshold to PS (PlanetScope).

Referring to the statistics in Table 4-12, below, ponds delineated by NDWI threshold estimate pond areas 1.002 times the areas measured by visual assessment of the reference dataset, which is not statistically different from visual assessment ($p>0.05$). The standard deviation of the pond area ratio by NDWI threshold versus the reference dataset is 0.321. The standard deviation in the measurement ratio is greater than visual assessment and of practical significance where pond measurements need to have a required level of certainty.

NDWI thresholding performed adequately at Ergo, with a mean pond area ratio of 1.039 and standard deviation of 0.040 which are close to the values reported for visual assessment of Sentinel-2. The mean pond ratio is not significantly different to visual assessment ($p>0.5$). As discussed in section 4.3.1, this is likely due to the spectral characteristics of the dry tailings beach and decant pond at Ergo.

Both Ergo and Impala presented lower standard deviations of the pond area measurement ratio than Elikhulu East and West. The pond area measurement ratio result from Impala is significantly different to the same results by visual assessment with a higher standard of 0.167 by threshold compared to 0.093 by visual assessment. This is similar, but not as pronounced as the difference between NIR threshold and visual assessment derived data for Impala.

Table 4-12: Statistics of NDWI threshold derived Sentinel-2 pond area data versus PlanetScope reference data

Site	**Mean Ratio** A_{S2} / A_{PS} $(\bar{X})$	**Mean Ratio Null Hypothesis** (μ_0)	**Mean Ratio Difference** $(\bar{X} - \mu_0)$	**Sample Std. Dev.** (S)	**Sample Size** (n)	**P-value** (indicating statistically significant difference to visual assessment)
Elik. East*	0.947	1.0	-0.053	0.459	36	>0.4
Elik. West*	0.977	1.0	-0.023	0.417	36	>0.5
Ergo	1.039	1.038	0.002	0.040	36	>0.5
Impala	1.045	1.112	-0.067	0.167	36	<0.05
All - NDWI Threshold*	1.002	1.053	-0.050	0.321	144	>0.05
All - Vis. Assess.	1.053	-	0.053	0.215	144	-

*Dataset obtained where the NDWI threshold was updated from the start of 2021 due to inundation of the geomembrane basin indicating a change to the composition of the surfaces of the facilities. Data can be viewed explicitly for Elikhulu East in Figure 8-7 and Figure 8-8 and Elikhulu West in Figure 8-16 and Figure 8-17 in Appendix-B.

4.3.3 Visual assessment, NIR and NDWI thresholds compared

Pond area data derived by visual assessment of Sentinel-2 imagery serves as a baseline against which to compare analogous NIR and NDWI threshold derived data. Table 4-14 provides a comparative summary of the statistics of the pond area ratio based on visual assessment, NIR and NDWI thresholding of Sentinel-2 imagery.

In general thresholding produced smaller area measurement ratios than visual assessment. In other words, thresholding tended to, on average, underestimate the pond area more often than visual assessment when compared to the reference dataset. The mean NIR threshold derived pond area ratio is statistically different to visual assessment, while that derived using NDWI thresholding is not, with a p value of <0.01 for NIR versus a p value of >0.05 for NDWI. Threshold derived data also presented greater scatter and a higher standard deviation in the pond area ratio compared to visual assessment. Furthermore, in general, the NIR threshold derived pond area ratio presented a greater degree of scatter when compared to NDWI derived data, with a standard deviation of 0.390 versus 0.321 for NIR and NDWI samples, respectively.

Further interpretation of the data shows that pond area ratios from the Ergo site derived by visual assessment, NIR and NDWI where all similar, without notable differences in the mean area ratios or sample standard deviations. Thresholding, however, tended to estimate smaller pond areas compared to visual assessment at Elikhulu East, Elikhulu West and Impala. Pond area ratios are generally smaller for NIR derived data with a higher standard deviation compared to NDWI for all sites investigated, barring minor difference reported from Ergo. Although Elikhulu East NIR derived pond area data reports a lower standard deviation than the NDWI derived data, this can be attributed to tendency of NIR to systemically underestimate the pond area. The mean area ratio form Elikhulu East is significantly different to that obtained by visual assessment, while the NDWI derived pond area data is not.

Table 4-13: Comparision of visual assessment, NIR and NDWI statistics

Site	Mean Area Ratio A_{S2} / A_{PS} $(\bar{X})$			Area Ratio Sample Standard Deviation (S)			P-value (indicating statistically significant difference of the threshold based mean ratio to visual assessment)	
	Vis. Assess.	NIR	NDWI	Vis. Assess.	NIR	NDWI	NIR	NDWI
Elik. East	1.018	0.805	0.947	0.395	0.383	0.459	<0.01	>0.4
Elik. West	1.043	0.965	0.977	0.134	0.632	0.417	>0.5	>0.5
Ergo	1.038	1.040	1.039	0.041	0.037	0.040	>0.5	>0.5
Impala	1.112	1.029	1.045	0.093	0.198	0.167	<0.02	<0.05
All	1.053	0.960	1.002	0.215	0.390	0.321	<0.01	>0.05

In general NDWI outperforms NIR thresholding. However, this observation is site specific as the data from the two thresholding methods performed similarly at Ergo where both methods exhibit similar performance compared to visual assessment.

4.3.4 Sentinel-2 threshold versus very high-resolution reference data

Threshold derived pond areas compared to very high-resolution reference areas are presented in Figure 4-28. As discussed previously, Elikhulu displayed variation in the thresholds obtained using different date subsets of the training data. Two thresholds of NIR and NDWI were adopted for Elikhulu, the single optimum threshold was used for images prior to 2021 and the 2021 threshold for images acquired in and after 2021.

Presented in Figure 4-28, NIR based thresholding on average estimates pond areas 0.76 times the very high-resolution reference data ($p<0.05$) with a high standard deviation of 0.30. NDWI threshold derived data showed good agreement with the very high-resolution reference data and did not show a statistically significant bias to over or underestimate the pond area ($P>0.2$). A standard deviation of 0.06 was measured, similar to visual assessment of the same data.

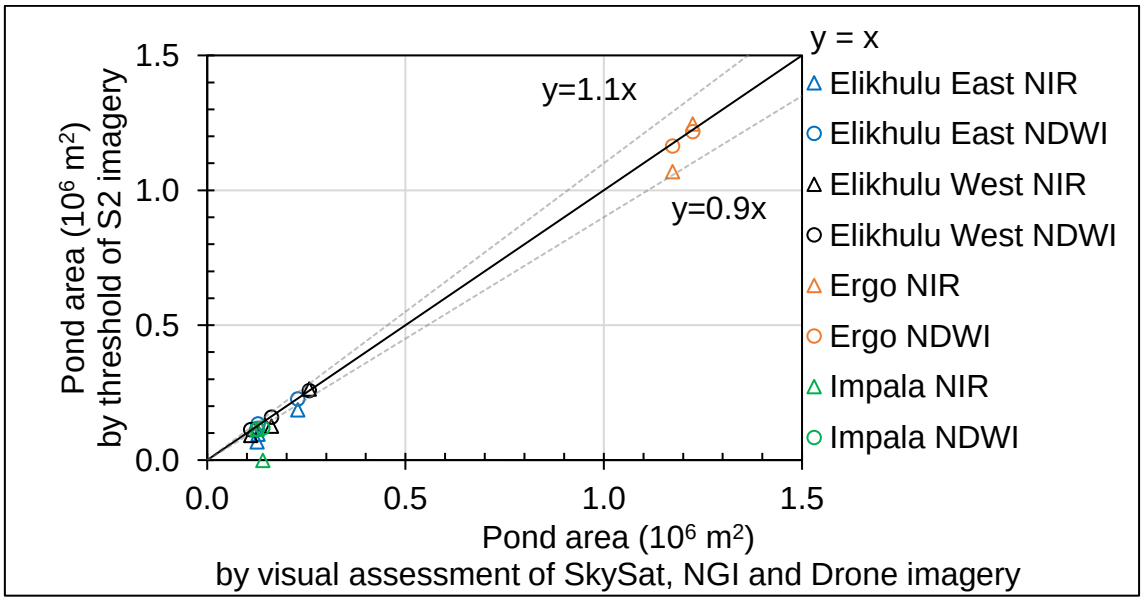


Figure 4-28: Pond area by S2 (Sentinel-2) NIR and NDWI thresholds versus visually assessed very high-resolution reference imagery.

Table 4-14: Statistics of threshold derived Sentinel-2 pond area data versus very high-resolution reference data

Measure-ment Metric	**Mean Ratio** A_{S2} / A_{PS} $(\bar{X})$	**Mean Ratio Null Hypothesis** (μ_0)	**Mean Ratio Difference** $(\bar{X} - \mu_0)$	**Sample Std. Dev.** (S)	**Sample Size** (n)	**P-value** (indicating statistical signifi-cance)
NIR	0.76	1.0	-0.24	0.30	10	<0.05
NDWI	0.98	1.0	-0.02	0.06	10	>0.2
Vis. assess.	0.97	-	-0.03	0.06	10	-

Based on the results on comparison of Sentinel-2 threshold to the very high-resolution reference data, NDWI provides an unbiased estimate of the pond area with a low standard deviation and performance close to visual assessment. NIR thresholding, on the other hand, tended to underestimate the pond area and presented a larger standard deviation than NDWI. This indicates that the NDWI thresholding method provided a more robust estimate of pond areas than NIR thresholding when comparing measurement to the very high-resolution reference dataset. This is in agreement with the comparisons of NIR and NDWI threshold derived data to the larger high-resolution (<5 m) reference dataset presented in sections 4.3.1, 4.3.2 and 4.3.3 above.

5 CONCLUSION

5.1 Summary of works

5.1.1 Justification and objective

The several large tailings dam disasters in the past decade bring to light the increasing severity of tailings dam failures. Coupled with systemic tailings dam stability issues, the importance of improving tailings dam monitoring systems is highlighted. The decant pond is a feature of tailings dams that provides insight into the operational state of the dam atop which it exists and is a surface feature amenable to remote sensing. The size and location of the decant pond provide insight into leading indicators of dam safety.

The objective of this study is to assess the use of public multispectral Sentinel-2 satellite imagery as a source of geospatial data on the tailings dam decant pond. This is achieved by delineation of the pond in Sentinel-2 imagery by visual assessment and thresholding and an assessment of the accuracy of the measurements made.

Three tailings dams in South Africa are investigated, presenting monitoring data on four decant ponds. Tailings dam decant pond data derived by visual assessment and automated threshold of Sentinel-2 imagery is compared to reference data obtained from higher spatial resolution imagery sources. The accuracy of Sentinel-2 tailings decant pond measurement is investigated by assessing the mean and standard deviation of the ratio of Sentinel-2 obtained to reference measurements.

5.1.2 Pond data from visual assessment of Sentinel-2

Georeferenced pond data based on visual assessment of Sentinel-2 imagery was compared to a reference dataset of finer spatial resolution and similar spectral quality. Sentinel-2 tended to over-estimate the pond area by a factor of 1.05 with a standard deviation of 0.22. However, data obtained by visual assessment of Sentinel-2 did not over or underestimate minimum beach lengths or pond centroid displacements. Similar levels of standard deviation are reported for pond area

and centroid displacement measurements. Minimum beach length measurement exhibited a higher standard deviation. Results are concisely summarised in Table 5-1 below.

Table 5-1: Sentinel-2 versus PlanetScope summary statistics

Measurement	**Mean Ratio** S2 / PS $(\bar{X})$	**Sample Std. Dev.** (S)	**P-value** (indicating statistically significant bias)
Pond area	1.05	0.22	<0.01
Min. beach	0.99	0.29	>0.5
Δ Centroid	1.01	0.20	>0.4

Comparison of data derived by visual assessment of Sentinel-2 to very high spatial resolution (<1.0 m) reference imagery indicates good agreement between the imagery sources. Sentinel-2 was able to measure dam safety metrics without any notable bias. Standard deviation in the results is also low for pond area and centroid displacement measurements. However, measurement of the minimum beach length exhibited a greater degree of scatter. Results are presented in Table 5-2 below.

Table 5-2: Sentinel-2 versus very high-resolution reference data summary statistics

Measurement	**Mean Ratio** S2 / PS $(\bar{X})$	**Sample Std. Dev.** (S)
Pond area	0.97	0.06
Min. beach	1.00	0.14
Δ Centroid	1.00	0.05

5.1.3 Pond delineation by threshold of Sentinel-2

Optimum thresholds of the near infrared (NIR) reflectance and the normalised difference water index (NDWI) of Sentinel-2 10 m imagery were determined by comparison of data generated by multiple iterative threshold values to visually assessed training data. The optimum threshold was selected using a least square error function. Pond polygon data was derived by automated thresholding using

the optimum threshold values. Where a significant change to a tailings dam's surface occurred, a revised threshold was adopted based on the new site characteristics. The thresholds derived are summarised in Table 5-3 below.

Table 5-3: Sentinel-2 NIR and NDWI thresholds

Site	NIR (reflectance x10^4)		NDWI (ratio -1 to +1)	
Elikhulu East	566	2 360*	0.204	0.05*
Elikhulu West	577	2 280*	0.225	0.05*
Ergo	1 766		0.014	
Impala	891		0.107	

*Adjustment to account for permanent change to the site's surface spectral characteristics.

To investigate the general suitability of pond data generated by automated threshold, pond areas by threshold are compared to the pond areas obtained by visual assessment of the reference imagery datasets. Overall, NIR automated thresholds tended to underestimate the pond area compared to visual assessment. NDWI on the other hand did not estimate pond areas with a statistically significant bias compared to visual assessment. NIR exhibited a higher standard deviation than NDWI. Both NIR and NDWI presented higher standard deviation than visual assessment alone, when compared to the reference dataset. Findings also indicate that threshold performance is site specific with NIR and NDWI thresholding performing similarly to visual assessment at the Ergo site. The results are summarised in Table 5-4 below.

Table 5-4: Sentinel-2 versus PlanetScope area data summary statistics

Measurement Metric	Mean Ratio A_{S2} / A_{PS} $(\bar{X})$	Sample Std. Dev. (S)	P-value (indicating statistically significant difference to visual assessment)
Visual assess.	1.05	0.22	-
NIR	0.96	0.39	<0.01
NDWI	1.00	0.32	>0.05

Pond areas obtained by automated NIR and NDWI threshold were also compared to pond area data obtained by visual assessment of very high spatial resolution

reference imagery. In this smaller dataset, NDWI was able to match the performance of visual assessment of Sentinel-2. NIR, however, again tended to underestimate the pond area and presented a greater standard deviation. These results are summarised in Table 5-5 below.

Table 5-5: Sentinel-2 versus very high-resolution reference pond area data summary statistics

Measurement Metric	Mean Ratio A_{S2} / A_{Ref} $(\bar{X})$	Sample Std. Dev. (S)
Visual assess.	0.97	0.06
NIR	0.79	0.26
NDWI	0.99	0.05

5.2 Conclusions

The analysis of visually assessed Sentinel-2 imagery presented herein yield the following insights:

- Sentinel-2 over-estimates the pond area by 5% compared to higher spatial resolution (<5 m) multispectral reference imagery.
- Sentinel-2 minimum beach length and pond centroid displacement measurements do not appear to have an estimation bias.
- The ratio of Sentinel-2 to reference measurements presented a standard deviation of 0.22, 0.29 and 0.20 for pond area, minimum beach lengths and pond centroid displacement measurements respectively. These values are considered too high for critical engineering measurements.
- Sentinel-2 estimated pond areas at the Ergo and Impala sites with low standard deviations of 0.04 and 0.09, respectively.
- Very good agreement between Sentinel-2 and the very high spatial resolution (<1.0 m) reference data is reported.

- The ratio of Sentinel-2 to very high spatial resolution reference measurements presented a standard deviation of 0.06, 0.14 and 0.05 for pond area, minimum beach lengths and pond centroid displacement measurements, respectively.

Automated thresholding allows a streamlined workflow process which could greatly reduce operational costs associated with delineating tailings decant ponds in the large archive of Sentinel-2 imagery. Specific thresholds were derived for each pond compartment of the investigated sites, four in total. Based on an analysis of pond data derived by thresholding of Sentinel-2 the following conclusions can be drawn:

- A single threshold for delineation of the pond in Sentinel-2 imagery is feasible. Careful consideration of the site characteristics is prudent. Consistent reflectance properties of the surfaces within the dam crestline are a requirement where a single threshold is to be applied. Changes in the reflectance properties of the materials composing the surface of a site warrant an update to the threshold.
- Assessment of a histogram and transect of the aggregated data to be classified can be used to screen for the feasibility of using a single threshold for the dataset. A bimodal histogram with clear separation of the modes and a clear range proposed by a transect are favourable features of a dataset for application of a single threshold.
- In general, NDWI outperforms NIR alone compared to visual assessment. However, performance is site specific.
- Data obtained at Ergo presented the best agreement and lowest standard deviation between Sentinel-2 threshold derived and reference measurements.
- NDWI matched the performance of visual assessment of the very high spatial resolution (<1.0 m) reference data. NIR tends to underestimate pond areas and tends to cause a greater number of pond omission errors than the NDWI.

5.3 Further work

This work contributes to better understanding how public multispectral satellite imagery can aid monitoring of the tailings dam decant pond and so improve dam construction surveillance and safety. To better understand how this data can aid tailings dam monitoring further sites should be investigated.

The full spectral resolution of Sentinel-2 was not investigated in this research due to the lower 20 m spatial resolution of the narrow NIR band (band 8A) and Shortwave Infrared (SWIR) bands (bands 11 and 12). It is, however, widely accepted that a modified NDWI, where the NIR band is replaced by a SWIR band, is less sensitive to water turbidity and can provide more stable measurements of surface water extent (Huang et al., 2018). Furthermore, it has also been shown that a modified NDWI can be calculated at a 10 m spatial resolution by pan sharpening the 20 m SWIR band (band 11) of Sentinel-2 (Du et al., 2016). This is a potential avenue to investigate where high turbidity tailings dam decant ponds need to be monitored.

In addition, this research focused on optical satellite imagery to monitor the pond. However, public Synthetic Aperture Radar (SAR) satellite missions (Sentinel-1) can provide earth observation data when cloud cover obstructs acquisition of optical data. This research did not investigate Sentinel-1 data as, on initial inspection, the decant pond and the tailings beach both presented similarly low SAR backscatter readings. Sentinel-1 could, however, be used in conjunction with Sentinel-2 to provide data when cloud cover obstructs the latter mission. Such hybrid earth observation frameworks have been shown to be more accurate for large scale surface water monitoring than optical data alone (Tottrup et al., 2022).

Improvements to the automated image classification scheme could be made using alternative pixel-based classification techniques. Such techniques might include image histogram derived thresholds (Otsu, 1979), edge detection (Canny, 1986) or more sophisticated classification frameworks such as support vector machine (Cortes & Vapnik, 1995). Furthermore, object-based classification could further improve the results (Myint et al., 2011).

Water monitoring dashboards such as the Bluedot Observatory (Zupanc et al., 2019) and the South African Mzansi Amanzi project (Department of Science and Innovation, 2022) showcase the utility of remotely sensed satellite data to monitor water reservoirs. The global tailings database (GRIDA, 2022) provides the most comprehensive geospatial archive of tailings storage facilities available to the public. The tailings database in conjunction with this research and the frameworks developed by water observatory projects provide the groundwork for a monitoring system where tailings dam decant ponds could be monitored at global scale with high temporal cadence. Such a platform would provide public data on the leading indicators of dam safety linked to the decant pond for eligible tailings dams in the global tailings database. This information would empower communities living downstream of tailings dams and aid the professionals tasked with ensuring their stability.

Given the ability of remotely sensed data to provide high temporal cadence data on the tailings pond, further work into the relationship of the tailings pond size and in-situ soil parameters could be investigated. Using remote monitoring systems, as proposed and investigated by Jacobsz et al., (2020) tailings dam pond location could be correlated to in-situ soil conditions such as the pore water pressure via the Internet of Things (IoT). This data could then be incorporated into tailings dam monitoring systems and further the progress towards attaining the information and frameworks necessary to build tailings dam digital twins. Furthermore, given the growing archive of remotely sensed data, pond location could be retrospectively investigated alongside the Cone Penetrometer (CPTu) tip and sleeve resistance profile. CPTu probe depth may be correlated to a deposition date using the historical rate of rise for a facility. CPTu readings could then be timestamped and temporally co-registered to a timeseries of satellite imagery. This may then allow direct high cadence correlation between pond location and in-situ soil parameters. Anecdotes concerning the pond history and tailings density, or shear strength could be corroborated or rejected.

6 REFERENCES

Atif, I., Ashraf, H., Cawood, F.T. & Mahboob, M.A. (2021) A Conceptual Digital Framework for Near Real-Time Monitoring and Management of Mine Tailing Storage Facilities. In: X.-N. Bui, C. Lee, & C. Drebenstedt (eds.). *Proceedings of the International Conference on Innovations for Sustainable and Responsible Mining*. Lecture Notes in Civil Engineering. 2021 Cham, Springer International Publishing. pp. 498–530. doi:10.1007/978-3-030-60839-2_27.

Bangira, T., Alfieri, S.M., Menenti, M. & van Niekerk, A. (2019) Comparing Thresholding with Machine Learning Classifiers for Mapping Complex Water. *Remote Sensing*. 11 (11), 1351. doi:10.3390/rs11111351.

Blight, G.E. (2009) *Geotechnical Engineering for Mine Waste Storage Facilities*. London, UK, CRC Press, Taylor & Francis Group.

Boswell, J. & Sobkowicz, J. (2018) Leading versus Lagging Indicators of Tailings Dam Integrity. In: *Proceedings of the 22nd International Conference on Tailings and Mine Waste*. October 2018 Keystone, Colorado, USA, UBC Studios, University of British Columbia. pp. 50–62.

Bowker, L.N. & Chambers, D.M. (2017) In the Dark Shadow of the Supercycle Tailings Failure Risk & Public Liability Reach All Time Highs. *Environments*. 4 (4), 75–96. doi:10.3390/environments4040075.

Bowker, L.N. & Chambers, D.M. (2015) *The Risk, Public Liability, and Economics of Tailings Storage Facility Failures*. https://earthworks.org/files/pubs-others/BowkerChambers-RiskPublicLiability_EconomicsOfTailingsStorageFacility%20Failures-23Jul15.pdf.

Bowker, L.N. & Chambers, D.M. (2021) *World Mine Tailings Failures Database from 1915 – 2021. Supporting global research in tailings failure root cause, loss prevention and trend analysis*. 15 September 2021. https://worldminetailingsfailures.org/ [Accessed: 15 September 2021].

Boyle, S.A., Kennedy, C.M., Torres, J., Colman, K., Pérez-Estigarribia, P.E. & Sancha, N.U. de la (2014) High-Resolution Satellite Imagery Is an Important yet Underutilized Resource in Conservation Biology. *PLOS ONE*. 9 (1), e86908. doi:10.1371/journal.pone.0086908.

Burger, S. (2022) Jagersfontein highlights standards, engineering capacity, technical knowledge gaps – SAICE. *Mining Weekly*. https://www.miningweekly.com/article/jagersfontein-highlights-standards-engineering-capacity-technical-knowledge-gaps-saice-2022-09-22/rep_id:3650.

Canny, J. (1986) A Computational Approach to Edge Detection. *IEEE Transactions on Pattern Analysis and Machine Intelligence*. PAMI-8 (6), 679–698. doi:10.1109/TPAMI.1986.4767851.

Casagrande, A. (1979) *Liquefaction and Cyclic Deformation in sands: A critical review*. In: Harvard Soil Mechanics Series. January 1979 Cambridge, Massachusetts, Pierce Hall. pp. 1–55.

Castro, G. (1969) *Liquefaction of Sands*. Ph.D. Thesis. Cambridge, Massachusetts., Harvard University.

Church of England (2021) *The Investor Mining and Tailings Safety Initiative*. 11 September 2021. https://www.churchofengland.org/about/leadership-and-governance/church-england-pensions-board/pensions-board-investments/investor-1 [Accessed: 11 September 2021].

Cortes, C. & Vapnik, V. (1995) Support-vector networks. *Machine Learning*. 20 (3), 273–297. doi:10.1007/BF00994018.

Das, B., M. & Soghan, K. (2014) *Principles of Geotechnical Engineering*. 8th, SI edition. Stamford, CT, Cengage Learning.

Department of Environmental Affairs (2013) *National Environmental Management: Waste Act, 2008 (Act No. 59 of 2008): National Norms and Standards for Disposal of Waste to Landfill, No. R. 636*. Government Gazette 36784 of 23 August 2013. Pretoria, Government Printer.

Department of Environmental Affairs (2015) *National Environmental Management: Waste Act, 2008 (Act No. 59 of 2008): Regulations Regarding the Planning and Management of Residue Stockpiles and Residue Deposits from a Prospecting, Mining, Exploration or Production Operation, No. R. 632*. Government Gazette 39020, 24 July 2015. Pretoria, Government Printer.

Department of Science and Innovation (2022) *Mzansi Amanzi*. 2022. https://www.water-southafrica.co.za/ [Accessed: 19 December 2022].

DJI (2022) *DJI Zenmuse L1 - Lidar and RGB Surveying Solution*. 2022. DJI. https://www.dji.com/photo [Accessed: 10 September 2022].

DRDGOLD Limited (2022) *The Crown-Ergo pipeline*. 2022. https://www.drdgold.com/our-business/ergo [Accessed: 10 September 2022].

Du, Y., Zhang, Y., Ling, F., Wang, Q., Li, W. & Li, X. (2016) Water bodies' mapping from Sentinel-2 imagery with Modified Normalized Difference Water Index at 10-m spatial resolution produced by sharpening the swir band. *Remote Sensing*. 8 (4). doi:10.3390/rs8040354.

ESA (2015) Sentinel User Handbook and Exploitation Tools (SUHET): Sentinel-2 User Handbook. *European Commission*. (Issue 1, Rev 2). https://sentinel.esa.int/documents/247904/685211/Sentinel-2_User_Handbook.

ESA (2022) *Sentinel-2 Spectral Response Functions (S2-SRF)*. 21 June 2022. Sentinel-2 Spectral Response Functions (S2-SRF). https://sentinel.esa.int/web/sentinel/user-guides/sentinel-2-msi/document-

library/-/asset_publisher/Wk0TKajiISaR/content/sentinel-2a-spectral-responses [Accessed: 10 August 2022].

Fisher, J.R.B., Acosta, E.A., Dennedy-Frank, P.J., Kroeger, T. & Boucher, T.M. (2018) Impact of satellite imagery spatial resolution on land use classification accuracy and modeled water quality. *Remote Sensing in Ecology and Conservation*. 4 (2), 137–149. doi:10.1002/rse2.61.

Fourie, A., Verdugo, R., Bjelkevik, M., Torres-Cruz, L.A. & Znidarcic, D. (2022) Geotechnics of mine tailings: A 2022 state of the art. In: *20th International Conference on Soil Mechanics and Geotechnical Engineering (Sydney)*. 2022 Sydney, Australia, Australian Geomechanics Society. p.

Franks, D.M., Stringer, M., Torres-Cruz, L.A., Baker, E., Valenta, R., Thygesen, K., Matthews, A., Howchin, J. & Barrie, S. (2021) Tailings facility disclosures reveal stability risks. *Scientific Reports*. 11 (1), 5353. doi:10.1038/s41598-021-84897-0.

GEE Data Catalogue (2022) *Sentinel-2 Datasets in Earth Engine | Earth Engine Data Catalog | Google Developers*. 2022. https://developers.google.com/earth-engine/datasets/catalog/sentinel-2 [Accessed: 13 December 2022].

Gorelick, N., Hancher, M., Dixon, M., Ilyushchenko, S., Thau, D. & Moore, R. (2017) Google Earth Engine: Planetary-scale geospatial analysis for everyone. *Remote Sensing of Environment*. 202, 18–27. doi:10.1016/j.rse.2017.06.031.

GRIDA (2022) *Global Tailings Portal*. 2022. https://tailing.grida.no/ [Accessed: 19 December 2022].

Hoffman, A. (2015) *Mount Polley Mine Tailings Storage Facility Breach 4 August 2014 Investigation Report of the Chief Inspector of Mines*.

Huang, C., Chen, Y., Zhang, S. & Wu, J. (2018) Detecting, Extracting, and Monitoring Surface Water From Space Using Optical Sensors: A Review. *Reviews of Geophysics*. 56 (2), 333–360. doi:10.1029/2018RG000598.

Huang, L.-K. & Wang, M.-J.J. (1995) Image thresholding by minimizing the measures of fuzziness. *Pattern Recognition*. 28 (1), 41–51. doi:10.1016/0031-3203(94)E0043-K.

Humphreys, D. (2020) Mining productivity and the fourth industrial revolution. *Mineral Economics*. 33 (1), 115–125. doi:10.1007/s13563-019-00172-9.

ICOLD (2001) *Tailings dams–risk of dangerous occurrences, lessons learnt from practical experiences (bulletin 121)*.

Implats (2022) *Impala Factsheet*. https://www.implats.co.za/pdf/operations/fact-sheets/2022/implats-fact-sheet-2022.pdf.

Jacobsz, S., Broekman, A., Basson, J. & Vandoorne, R. (2020) *Remote monitoring of a tailings dam using the Internet of Things*.

Jefferies, M. & Been, K. (2015) *Soil Liquefaction: A Critical State Approach, Second Edition*. Taylor & Francis.

Jensen, J.R. (2015) *Introductory Digital Image Processing: A Remote Sensing Perspective*. Pearson series in geographic information science. 4th edition. Illinois, USA, Pearson Education, Inc.

Koerner, R.M. (2012) *Designing with Geosynthetics*. 6th edition.

Lillesand, T., Kiefer, R.W. & Chipman, J. (2015) *Remote Sensing and Image Interpretation*. 7th edition. John Wiley & Sons.

Lloyd, R., Hodgson, M.E. & Stokes, A. (2002) Visual Categorization with Aerial Photographs. *Annals of the Association of American Geographers*. 92 (2), 241–266.

Lumbroso, D., Collell, M.R., Petkovsek, G., Davison, M., Liu, Y., Goff, C. & Wetton, M. (2021) DAMSAT: An Eye in the Sky for Monitoring Tailings Dams. *Mine Water and the Environment*. 40 (1), 113–127. doi:10.1007/s10230-020-00727-1.

Lyu, Z., Chai, J., Xu, Z., Qin, Y. & Cao, J. (2019) A Comprehensive Review on Reasons for Tailings Dam Failures Based on Case History. *Advances in Civil Engineering*. 2019. doi:10.1155/2019/4159306.

Martin, T.E. & McRoberts, E.C. (1999) Some considerations in the stability analysis of upstream tailings dams. In: *Proceedings of the sixth international conference on tailings and mine waste*. January 1999 Rotterdam, Netherlands. pp. 287–302.

McAllister, E., Payo, A., Novellino, A., Dolphin, T. & Medina-Lopez, E. (2022) Multispectral satellite imagery and machine learning for the extraction of shoreline indicators. *Coastal Engineering*. 174, 104102. doi:10.1016/j.coastaleng.2022.104102.

McFeeters, S.K. (1996) The use of the Normalized Difference Water Index (NDWI) in the delineation of open water features. *International Journal of Remote Sensing*. 17 (7), 1425–1432. doi:10.1080/01431169608948714.

McFeeters, S.K. (2013) Using the Normalized Difference Water Index (NDWI) within a Geographic Information System to Detect Swimming Pools for Mosquito Abatement: A Practical Approach. *Remote Sensing*. 5 (7), 3544–3561. doi:10.3390/rs5073544.

Mitchell, G., Turner, J. & Engels, J. (2018) Satellite-based Repeat Surveying of Tailings: A Cost-effective Alternative to Aerial Surveying. In: *Proceedings of The 22nd International Conference on Tailings And Mine Waste*. October 2018 Keystone, Colorado, USA. pp. 526–533.

Mondejar, J.P. & Tongco, A.F. (2019) Near infrared band of Landsat 8 as water index: a case study around Cordova and Lapu-Lapu City, Cebu, Philippines. *Sustainable Environment Research*. 29 (1), 16. doi:10.1186/s42834-019-0016-5.

Montgomery, D.C. & Runger, G.C. (2011) *Applied Statistics and Probability for Engineers: SI Version*. Fifth Edition. John Wiley & Sons Inc.

Morgenstern, N.R., Vick, S.G., Viotti, C.B. & Watts, B.D. (2016) *Report on the Immediate Causes of the Failure of the Fundão Dam*.

Morrill, J., Chambers, D.M., Harkinson, R., Kneen, J., Lapointe, U., Maest, A., Milanez, B., Personius, P., Turgeon, R. & Emerman, S. (2022) *Safety First: Guidelines for Responsible Mine Tailings Management*. https://earthworks.org/resources/safety-first-guidelines-for-responsible-mine-tailings-management/.

Morrison, K.F. & Gomide, P.C.R. (2019) Post-Córrego do Feijão: Continued Evolution of Tailings Dam Regulations in Brazil. *Tailings and Mine Waste*. 11.

Morrison, K.F., Pedrosa, H.G., dos Santos, G.J., Gomide, P.C.R. & Ferreira, A.M. (2018) Changes to Tailings Dam Regulation in Brazil in the Aftermath of Failures. In: *Proceedings of the 22nd International Conference on Tailings and Mine Waste*. October 2018 Keystone, Colorado, USA, UBC Studios, University of British Columbia. pp. 27–34.

Mudd, G.M. (2007) Global trends in gold mining: Towards quantifying environmental and resource sustainability. *Resources Policy*. 32 (1), 42–56. doi:10.1016/j.resourpol.2007.05.002.

Mudd, G.M. (2010) The Environmental sustainability of mining in Australia: key mega-trends and looming constraints. *Resources Policy*. 35 (2), 98–115. doi:10.1016/j.resourpol.2009.12.001.

Myint, S.W., Gober, P., Brazel, A., Grossman-Clarke, S. & Weng, Q. (2011) Per-pixel vs. object-based classification of urban land cover extraction using high spatial resolution imagery. *Remote Sensing of Environment*. 115 (5), 1145–1161. doi:10.1016/j.rse.2010.12.017.

Niekerk, H.J.V. & Viljoen, M.J. (2005) Causes and consequences of the Merriespruit and other tailings-dam failures. *Land Degradation & Development*. 16 (2), 201–212. doi:10.1002/ldr.681.

O'Donovan, C.G., Adam, E. & Torres-Cruz, L.A. (2022) Remote sensing of the decant pond of tailings dams: Insights from a South African case study. *Journal of the Southern African Institute of Mining and Metallurgy*. 122 (4), 167–172.

Olofsson, P., Foody, G.M., Herold, M., Stehman, S.V., Woodcock, C.E. & Wulder, M.A. (2014) Good practices for estimating area and assessing accuracy of land change. *Remote Sensing of Environment*. 148, 42–57. doi:10.1016/j.rse.2014.02.015.

Otsu, N. (1979) A Threshold Selection Method from Gray-Level Histograms. *IEEE Transactions on Systems, Man, and Cybernetics*. 9 (1), 62–66. doi:10.1109/TSMC.1979.4310076.

Pan African Resources (2017) *Elikhulu Tailings Retreatment Plant*. 7 November 2017. Pan African. https://www.panafricanresources.com/operations-at-a-glance-2/elikhulu-project/ [Accessed: 10 September 2022].

Pekel, J.-F., Cottam, A., Gorelick, N. & Belward, A.S. (2016) High-resolution mapping of global surface water and its long-term changes. *Nature*. 540 (7633), 418–422. doi:10.1038/nature20584.

Petley, D. (2022) Another tailings dam failure: the Williamson Mine in Tanzania. *The Landslide Blog*. https://blogs.agu.org/landslideblog/2022/11/08/williamson-mine-1/.

Planet (2022) *Planet Imagery Product Specifications*. https://assets.planet.com/docs/Planet_Combined_Imagery_Product_Specs_letter_screen.pdf.

Planet (2018) *Relative Spectral Response Curves (RSRs) for the Planet satellites*. 19 December 2018. Welcome to Planet Support. https://support.planet.com/hc/en-us/articles/360014290293-Do-you-provide-Relative-Spectral-Response-Curves-RSRs-for-your-satellites- [Accessed: 10 September 2022].

QGIS.org (2022) *QGIS Geographic Information System*. 2022. QGIS Association. https://www.qgis.org/ [Accessed: 1 February 2022].

Rana, N.M., Ghahramani, N., Evans, S.G., McDougall, S., Small, A. & Take, W.A. (2021) Catastrophic mass flows resulting from tailings impoundment failures. *Engineering Geology*. 292, 106262. doi:10.1016/j.enggeo.2021.106262.

Robertson, P.K., de Melo, L., Williams, D.J. & Wilson, G.W. (2019) *Report of the Expert Panel on the Technical Causes of the Failure of Feijão Dam I*. https://bdrb1investigationstacc.z15.web.core.windows.net/assets/Feijao-Dam-I-Expert-Panel-Report-ENG.pdf.

Roche, C., Thygesen, K. & Baker, E. (2017) *Mines tailings storage: Safety is no accident.* A UNEP Rapid Response Assessment. Nairobi and Arendal, United Nations Environment Programme. www.grida.no.

Rourke, H. & Luppnow, D. (2015) The Risks of Excess Water on Tailings Facilities and Its Application to Dam-break Studies. In: *Tailings and Mine Waste Management for the 21st Century,*. 27 July 2015 Sydney. pp. 1–6.

Rouse, J., Haas, R.H., Schell, J.A. & Deering, D. (1973) Monitoring vegetation systems in the great plains with ERTS. In: *Proceedings of the 3rd Earth Resource Technology Satellite (ERTS) Symposium*. 1973 pp. 48–62.

Santamarina, J.C., Torres-Cruz, L.A. & Bachus, R.C. (2019) Why coal ash and tailings dam disasters occur. *Science*. 364 (6440), 526–528. doi:10.1126/science.aax1927.

Sekertekin, A. (2021) A Survey on Global Thresholding Methods for Mapping Open Water Body Using Sentinel-2 Satellite Imagery and Normalized Difference Water Index. *Archives of Computational Methods in Engineering*. 28 (3), 1335–1347. doi:10.1007/s11831-020-09416-2.

Student (1908) The Probable Error of a Mean. *Biometrika*. 6 (1), 1–25. doi:10.2307/2331554.

Svatonova, H. (2016) Analysis of Visual Interpretation of Satellite Data. *ISPRS - International Archives of the Photogrammetry, Remote Sensing and Spatial Information Sciences*. XLI-B2, 675–681. doi:10.5194/isprs-archives-XLI-B2-675-2016.

Terzaghi, K., Peck, R.B. & Mesri, G. (1996) *Soil Mechanics in Engineering Practice*. Third. John Wiley & Sons.

Torres-Cruz, L.A. & O'Donovan, C. (2023) Public remotely sensed data raise concerns about history of failed Jagersfontein dam. *Scientific Reports*. 13 (1), 4953. doi:10.1038/s41598-023-31633-5.

Tottrup, C., Druce, D., Meyer, R.P., Christensen, M., Riffler, M., et al. (2022) Surface Water Dynamics from Space: A Round Robin Intercomparison of Using Optical and SAR High-Resolution Satellite Observations for Regional Surface Water Detection. *Remote Sensing*. 14 (10), 2410. doi:10.3390/rs14102410.

Turner, I.L., Harley, M.D., Almar, R. & Bergsma, E.W.J. (2021) Satellite optical imagery in Coastal Engineering. *Coastal Engineering*. 167, 103919. doi:10.1016/j.coastaleng.2021.103919.

UNEP (2022) *Joint statement on Jagersfontein tailings failure - ICMM, PRI and UNEP*. 15 September 2022. UN Environment Programme. http://www.unep.org/news-and-stories/statements/joint-statement-jagersfontein-tailings-failure-icmm-pri-and-unep [Accessed: 1 October 2022].

USGS (2019) *Landsat 8 (L8) Data Users Handbook*. Version 5.0 (LSDS-1574).

USGS (2022) *Landsat 9 Data Users Handbook*. Version 1.0 (LSDS-2082).

USGS (2010) *Landsat Data Continuity Mission Fact, Fact Sheet 2007-3093*.

Vermeulen, N.J. (2001) *The composition and state of gold tailings*. Thesis. University of Pretoria. https://repository.up.ac.za/handle/2263/23079.

Werner, T.T., Mudd, G.M., Schipper, A.M., Huijbregts, M.A.J., Taneja, L. & Northey, S.A. (2020) Global-scale remote sensing of mine areas and analysis of factors

explaining their extent. *Global Environmental Change*. 60, 102007. doi:10.1016/j.gloenvcha.2019.102007.

Yin, F., Lewis, P.E. & Gómez-Dans, J.L. (2022) Bayesian atmospheric correction over land: Sentinel-2/MSI and Landsat 8/OLI. *Geoscientific Model Development*. 15 (21), 7933–7976. doi:10.5194/gmd-15-7933-2022.

Zupanc, A., Aleksandrov, M., Batic, M., Lubej, M., Milcinski, G., Peressutti, D., Skerlavaj, A. & Zupanc, M. (2019) Bluedot water observatory - Cost effective near real time monitoring of global water resources. In: *Proceedings of the 2019 Living Planet Symposium*. 16 May 2019 Milan, Itlay, European Space Agency. p. https://www.researchgate.net/publication/333262569_Bluedot_water_observatory_-_Cost_effective_near_real_time_monitoring_of_global_water_resources.

7 APPENDIX-A: VERY HIGH-RESOLUTION REFERENCE IMAGERY

7.1 Elikhulu East

Very high-resolution and orthophoto data was acquired by drone for the Elikhulu site and used to delineate the tailings pond area, as presented below.



Figure 7-1: Orthophoto of Elikhulu East performed on 2020-03-02.

Based on the airborne imagery shown above, a tailings pond area of 126 300 m^2 was estimated by visual assessment. The closest cloud free Sentinel-2 images avalible for comaprision were acquired on 2020-02-26 and 2022-03-07, five days before and five days after the drone image. Manual visual assessment of these Sentinel-2 images presented pond areas of 124 500 m^2 and 81 900 m^2, respectively. For comparision purposes the average Sentinel-2 image pond area was used.

Futher to the drone survey imagery, two high-resolution SkySat sattalite images were acquried of the site without significant temporal seperation to the paired

Sentinel-2 image. The pond was delineated using the multispectral data provided by these images, shown below.

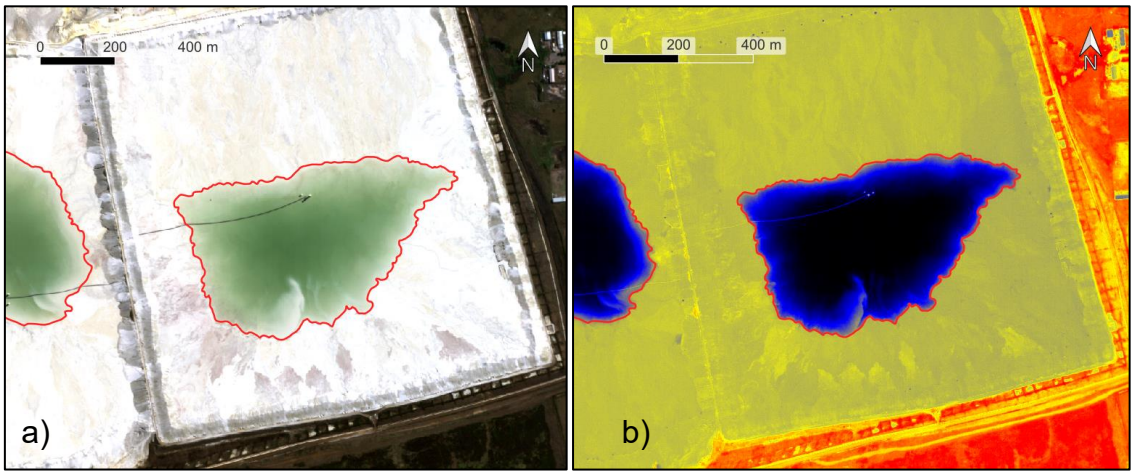


Figure 7-2: SkySat multispectral image acquired 2022-04-06 at 7:43 UTC, a) Natural Colour and b) NDWI.

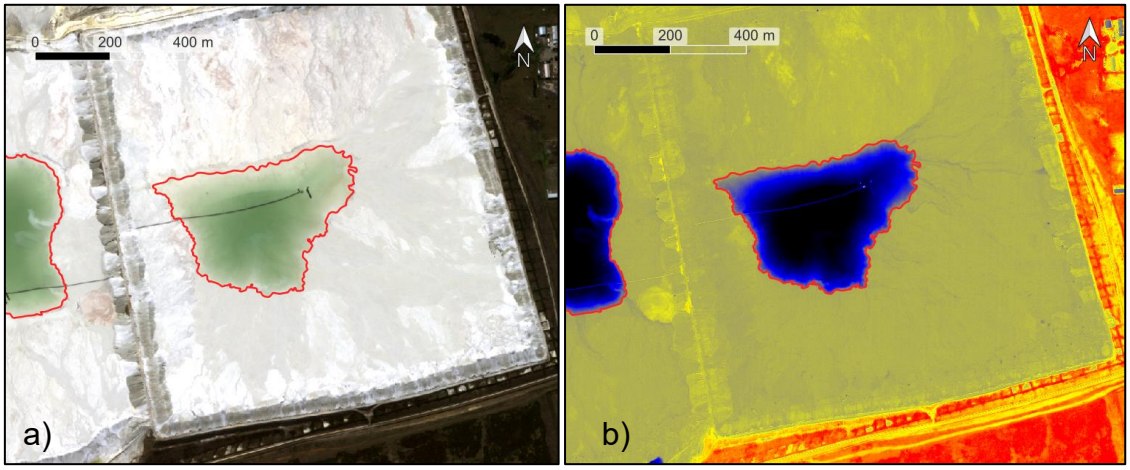


Figure 7-3: SkySat multispectral image acquired 2022-04-26 at 11:18 UTC, a) Natural Colour and b) NDWI.

The pond areas determined from the above SkySat data, using the natural colour and NDWI render of the site, were determined to be 228 800 m^2 and 128 200 m^2 for the 6th and 26th of April 2022 respectively. Cloud free Sentinel-2 images were acquired on the same day as both SkySat acquisitions, albeit at slightly different times of 07:46 UTC on both the 6th and 26th of April 2022. Manual visual assessment of the Sentinel-2 images yield pond areas of 227 700 m^2 for the site

on the 6th and 133 100 m^2 for the site on the 26th of April 2022. The manual visually assessed data from both Sentinel-2 and the very resolution images datasets is presented in the Figure 7-4 below. Sentinel-2 shows high correlation to the SkySat imagery, aided by the low temporal separation. There is, however, a discrepancy of greater than 10% between the pond areas measured in Sentinel-2 and the drone imagery, potentially because of the temporal separation of 5 days between the Sentinel-2 image acquired prior and post the drone image.

Table 7-1: Elikhulu East visually assessed very high-resolution reference and Sentinel-2 data

Very high-resolution reference				Sentinel-2		
Sensor	Date	Time (UTC)	Area ($x10^3m^2$)	Date	Time (UTC)	Area ($x10^3m^2$)
Drone	2020-03-02	Unknown	126.3	2020-02-26 2020-03-07	07:48 07:49	124.5 81.9
SkySat	2022-04-06	07:43	228.8	2022-04-06	07:46	227 7
SkySat	2022-04-26	11:18	128.2	2022-04-26	07:46	133 1

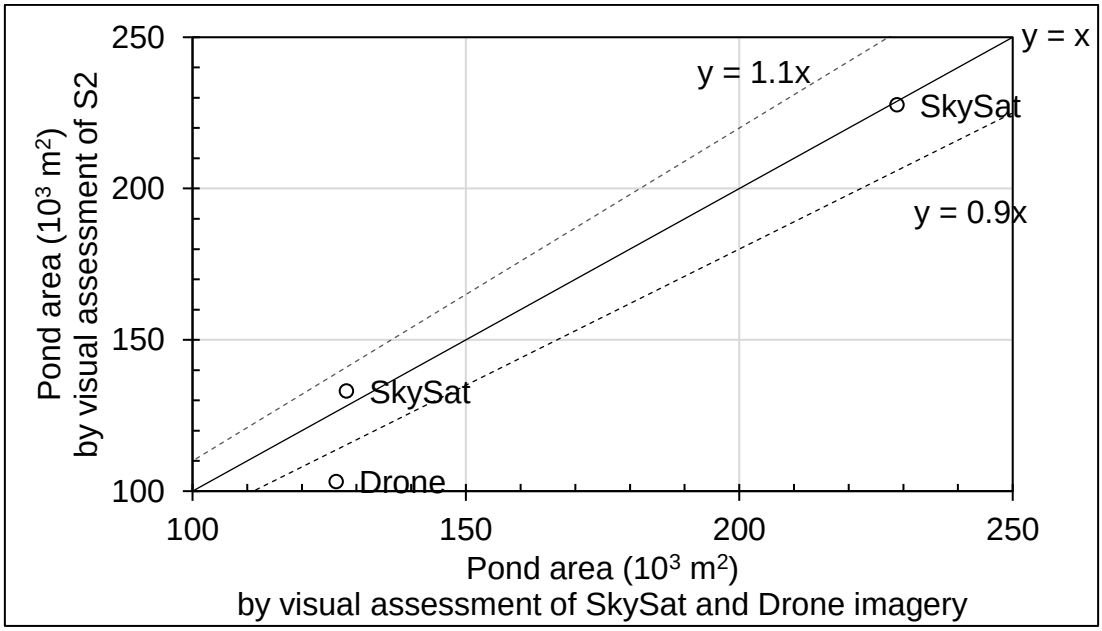


Figure 7-4: Elikulu-East - Comparison of pond area measured by visual assessment S2 (Sentinel-2) versus drone and SkySat very high-resolution reference data.

7.2 Elikhulu West

The same methodology as for Elikhulu East was followed for analysis of the tailings decant pond from very high-resolution imagery for Elikhulu West.

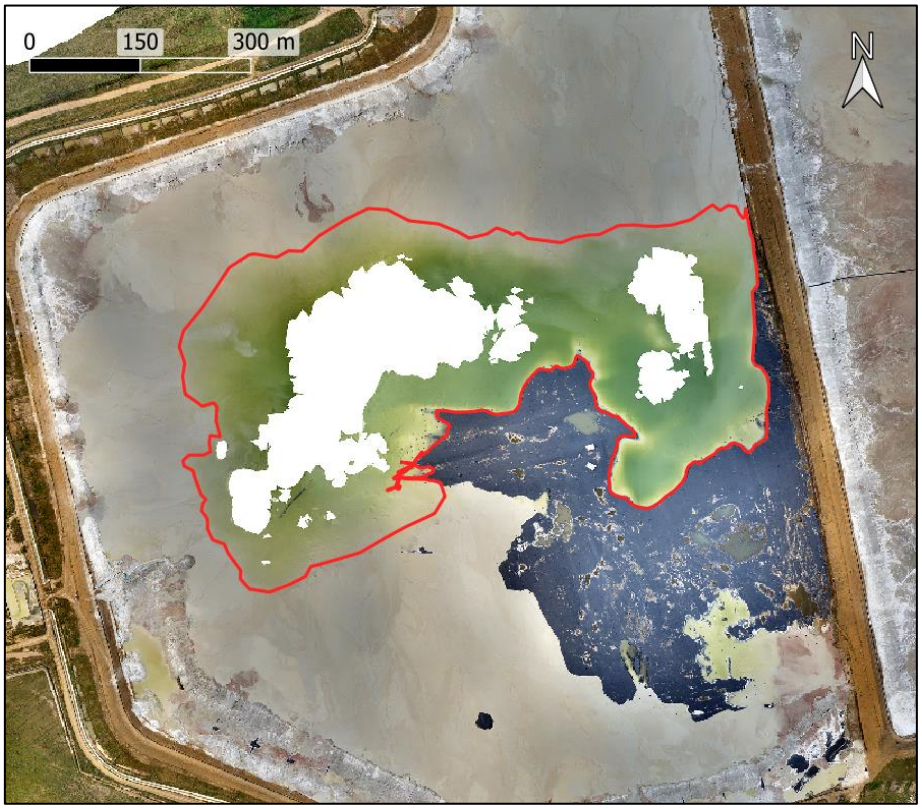


Figure 7-5: Orthophoto of Elikhulu West performed on 2020-03-02.

The closest cloud free Sentinel-2 images avalible for comaprision to the drone image in Figure 7-5 were acquired on 2020-02-26 and 2022-03-07

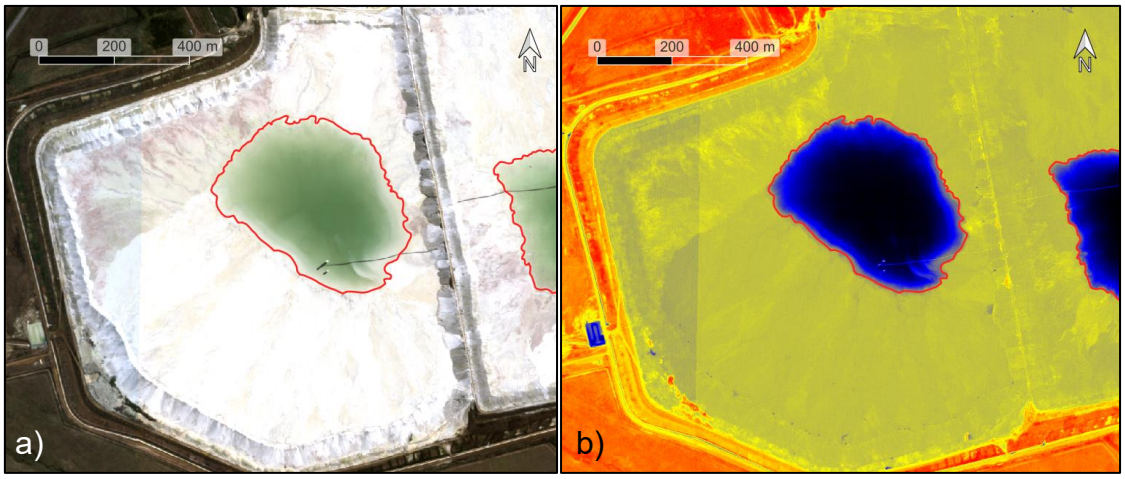


Figure 7-6: SkySat multispectral image acquired 2022-04-06 at 7:43 UTC, a) Natural Colour and b) NDWI.

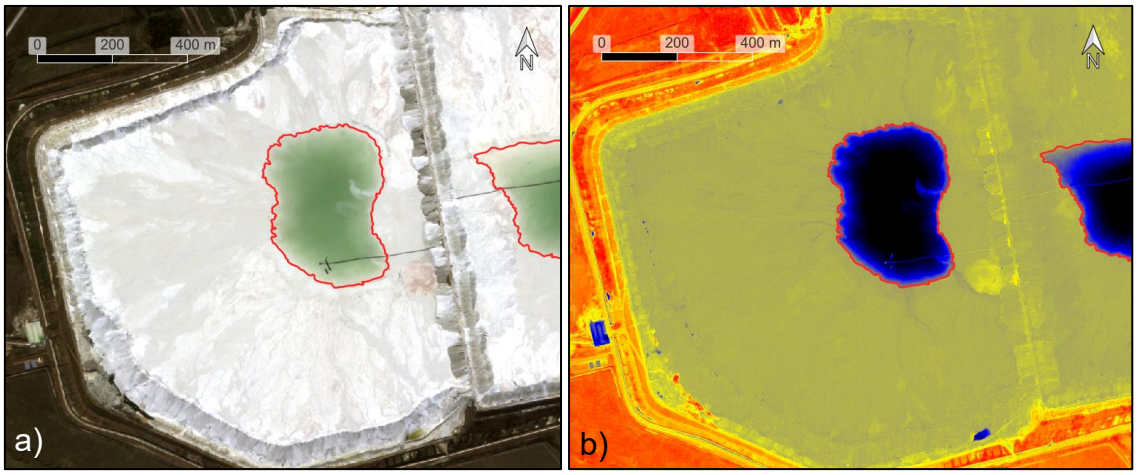


Figure 7-7: SkySat multispectral image acquired 2022-04-26 at 11:18 UTC, a) Natural Colour and b) NDWI.

Two high-resolution SkySat sattalite images were acquried of the site without significant temporal seperation to the paired Sentinel-2 image, shown in Figure 7-6 and Figure 7-7 above.

The results of visual assessment of this data are summarised in Table 7-2 below with a graphical representation in Figure 7-8.

Table 7-2: Elikhulu West visually assessed very high-resolution reference and Sentinel-2 data.

Very high-resolution reference				Sentinel-2		
Sensor	Date	Time (UTC)	Area ($x10^3 m^2$)	Date	Time (UTC)	Area ($x10^3 m^2$)
Drone	2020-03-02	Unknown	257.6	2020-02-26 2020-03-07	07:48 07:49	275.6 227.1
SkySat	2022-04-06	07:43	109.7	2022-04-06	07:46	111.1
SkySat	2022-04-26	11:18	162.1	2022-04-26	07:46	154.7

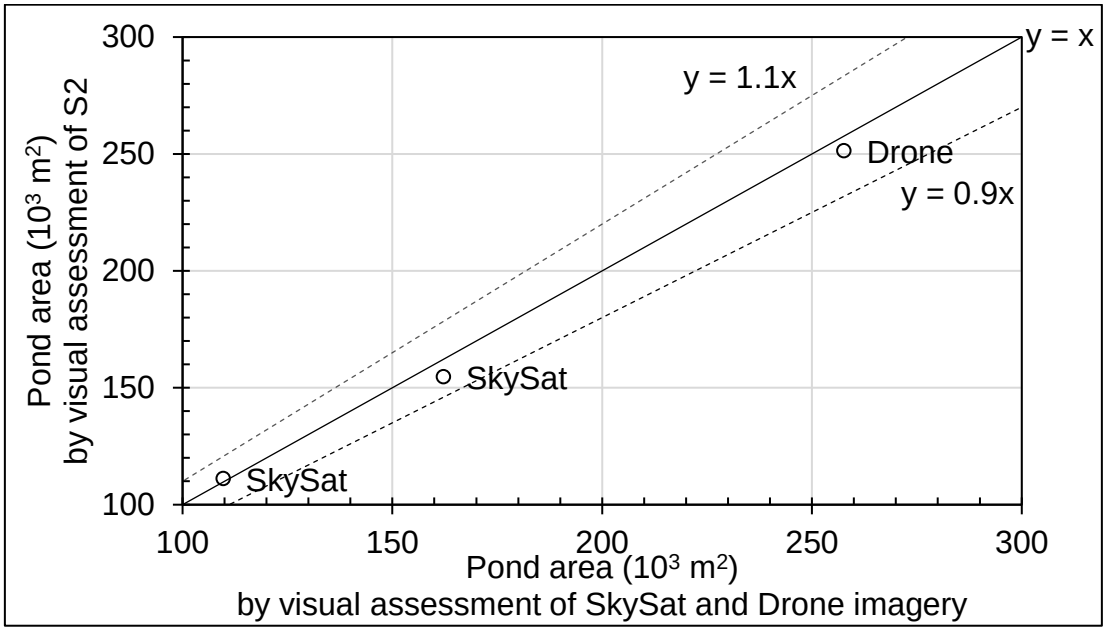


Figure 7-8: Elikhulu West - Comparison of pond area measured by visual assessment of S2 (Sentinel-2) versus drone and SkySat very high-resolution reference data

7.3 Ergo

One very high-resolution aerial orthophoto and one very high-resolution multispectral satellite image were acquired for Ergo.

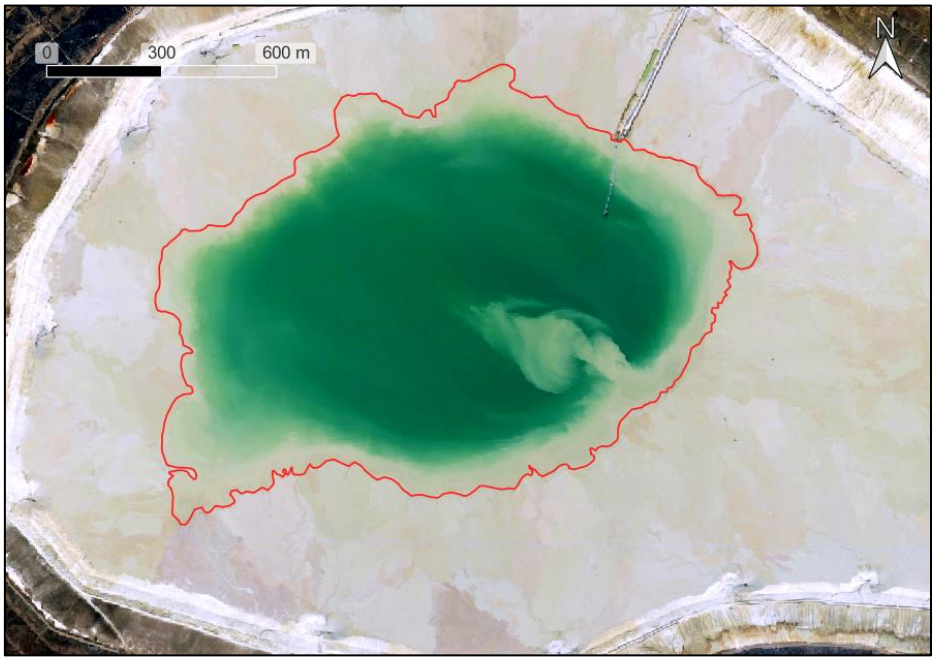


Figure 7-9: Orthophoto of Ergo on 2018-06-23.

The aerial photograph in Figure 7-9 above yielded an estimate of the pond area of 1.225 x10^6 m^2. Visual assessment of the Sentinel-2 image used for comparison was acquired on 2018-06-21 and provides a pond area estimate of 1.228 x10^6 m^2.

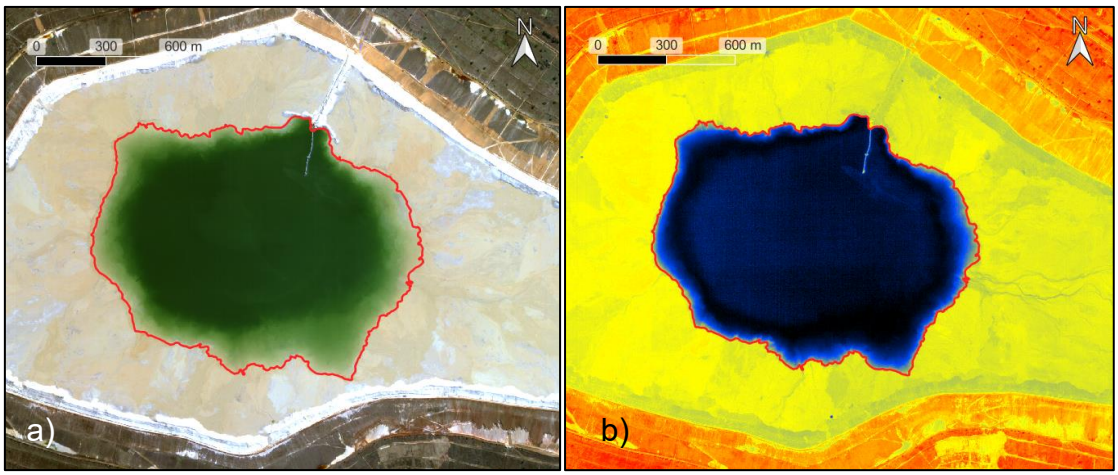


Figure 7-10: SkySat multispectral image acquired on 2022-04-26 at 07:56 UTC, a) Natural Colour and b) NDWI.

The Sentinel-2 comparison image to the SkySat image in Figure 7-10 was acquired on 2022-04-26 at 07:46 UTC.

Results of visual assessment of this imagery are summarised in Table 7-3 below and represented graphically in Figure 7-11.

Table 7-3: Elikhulu East visually assessed very high-resolution reference and Sentinel-2 data.

Very high-resolution reference				Sentinel-2		
Sensor	Date	Time (UTC)	Area ($x10^6 m^2$)	Date	Time (UTC)	Area ($x10^6 m^2$)
CDNGI aerial	2018-06-23	Unknown	1.225	2018-06-21	07:48	1.228
SkySat	2022-04-26	07:56	1.173	2022-04-06	07:46	1.155

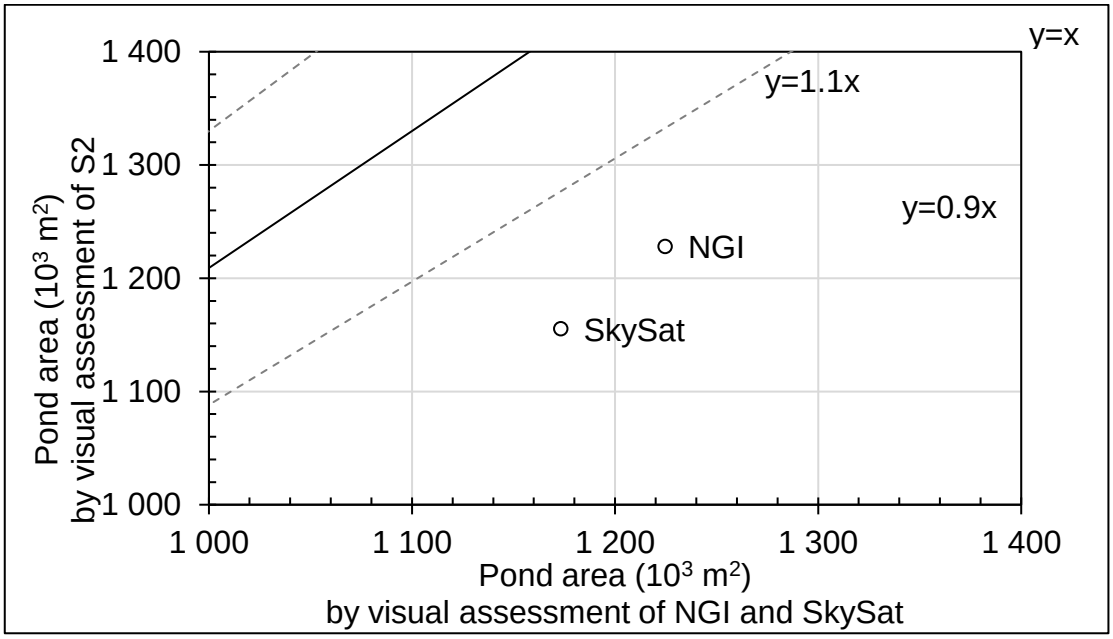


Figure 7-11: Ergo - Comparison of pond area measured by visual assessment S2 (Sentinel-2) and CDNGI and SkySat very high-resolution reference data.

7.4 Impala

One very high-resolution aerial orthophoto and one very high-resolution multispectral satellite image were acquired for Impala.



Figure 7-12: Orthophoto of Impala on 2021-03-27.

The Sentinel-2 comparison image to the aerial image in Figure 7-12 was acquired on 2021-03-30 at 07:56 UTC.

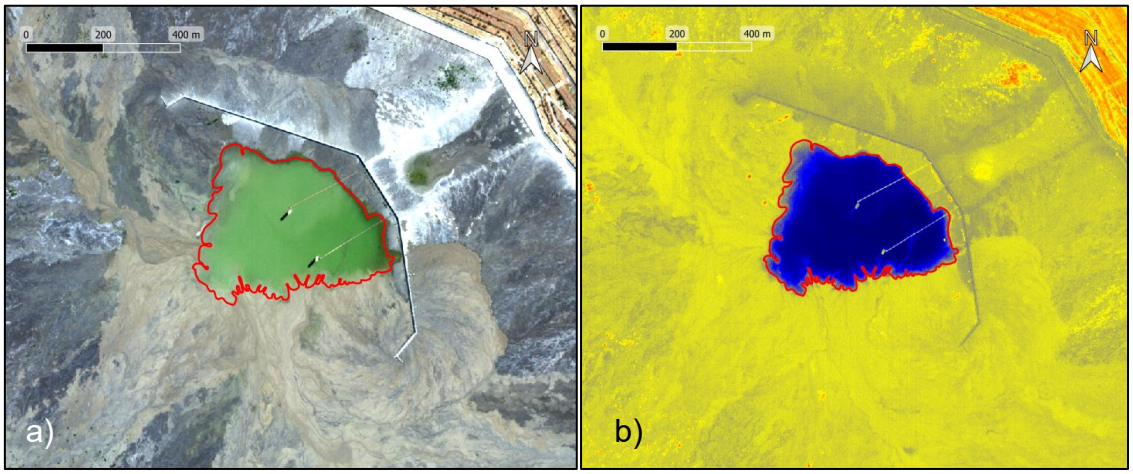


Figure 7-13: SkySat multispectral image acquired on 2022-08-12 at 07:51 UTC, a) Natural Colour and b) NDWI.

The Sentinel-2 comparison image to the SkySat image in Figure 7-13 was acquired on 2022-08-12 at 07:56 UTC.

Results of visual assessment of this imagery are summarised in Table 7-4 below and represented graphically in Figure 7-14.

Table 7-4: Impala visually assessed very high-resolution reference and Sentinel-2 data.

Very high-resolution reference				Sentinel-2		
Sensor	Date	Time (UTC)	Area ($x10^3 m^2$)	Date	Time (UTC)	Area ($x10^3 m^2$)
CDNGI aerial	2021-03-27	Unknown	126.2	2020-03-30	07:56	116.0
SkySat	2022-08-12	07:43	140.7	2022-08-12	07:56	135.8

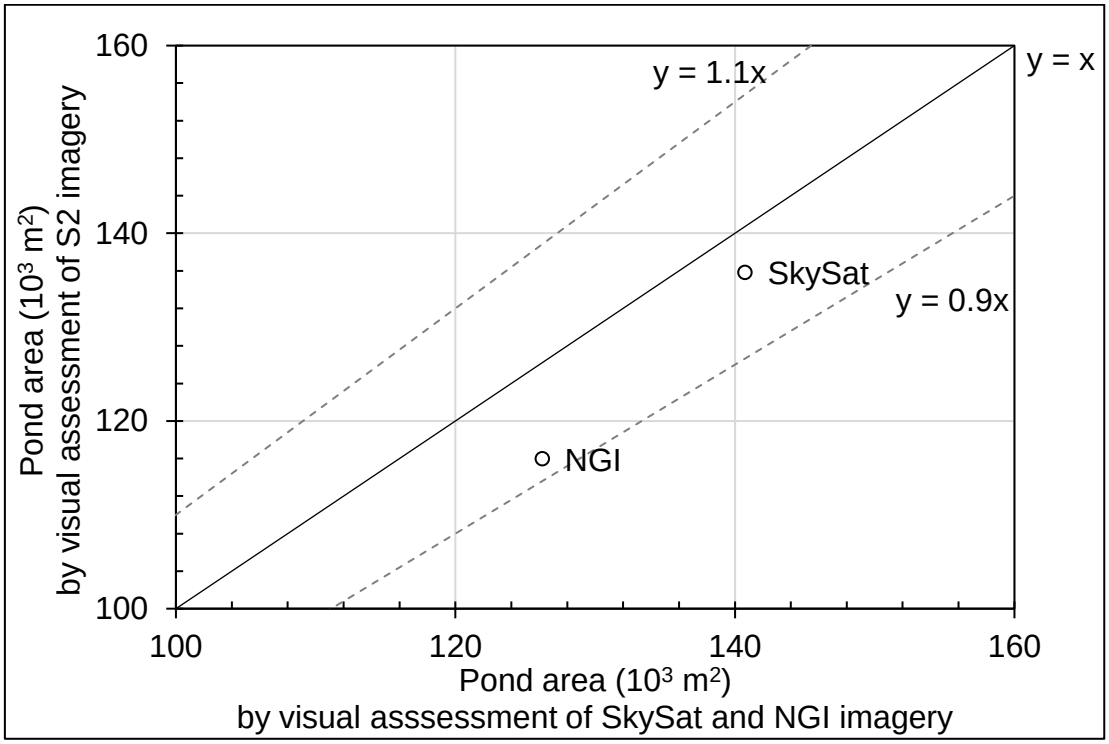


Figure 7-14: Impala - Comparison of pond area measured by visual assessment Sentinel-2 and CDNGI and SkySat very high-resolution reference data.

8 APPENDIX-B: SENTINEL-2 IMAGE THRESHOLD DERIVATIONS

8.1 Elikhulu East

8.1.1 Histogram and transect threshold assessment

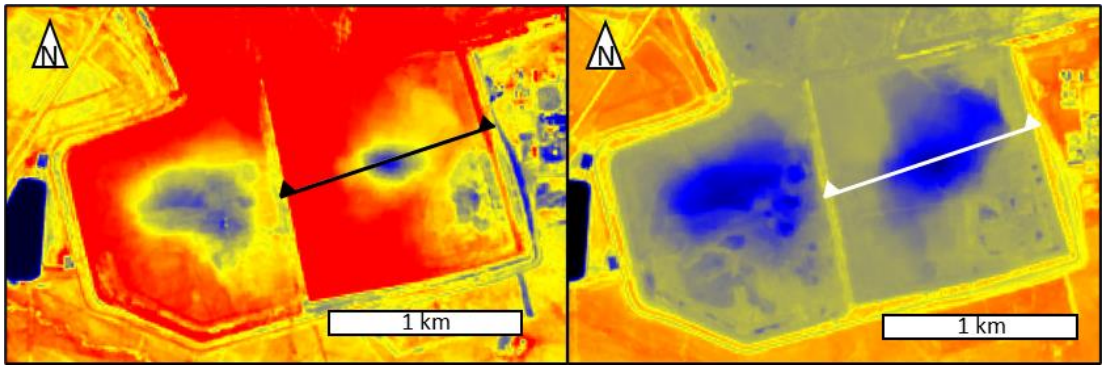


Figure 8-1: Elikhulu East: Mean images of near infrared reflectance (left) and normalised difference water index (right).

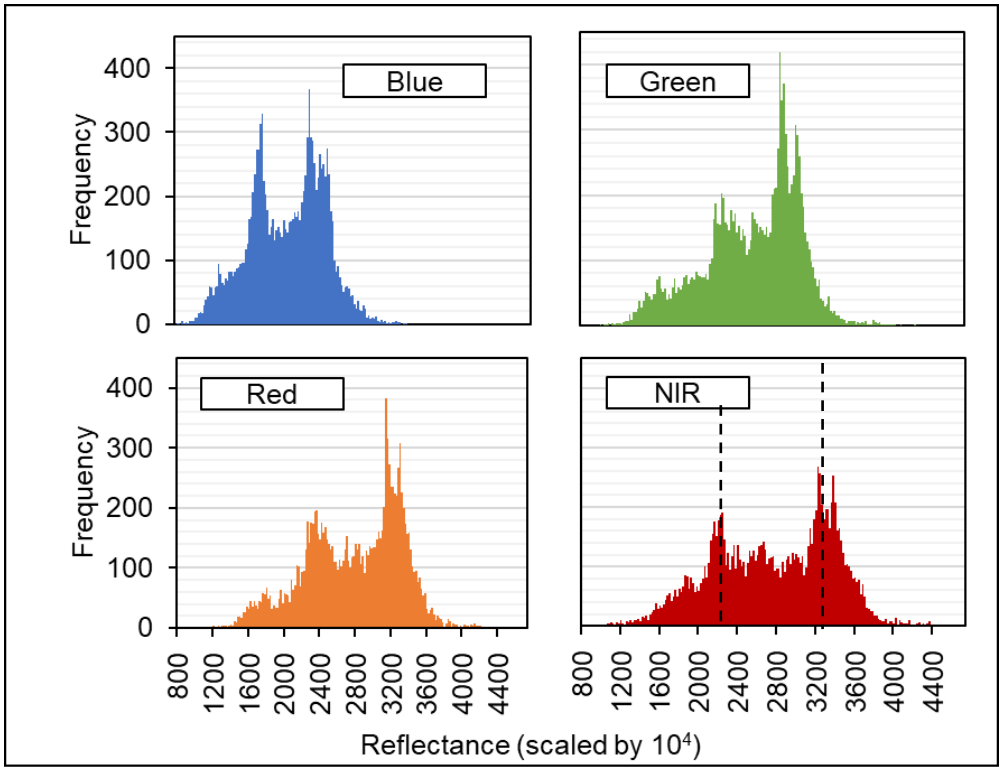


Figure 8-2: Elikhulu East histograms of the mean visible and near infrared (NIR) Sentinel-2 bands within the tailings plateau area.

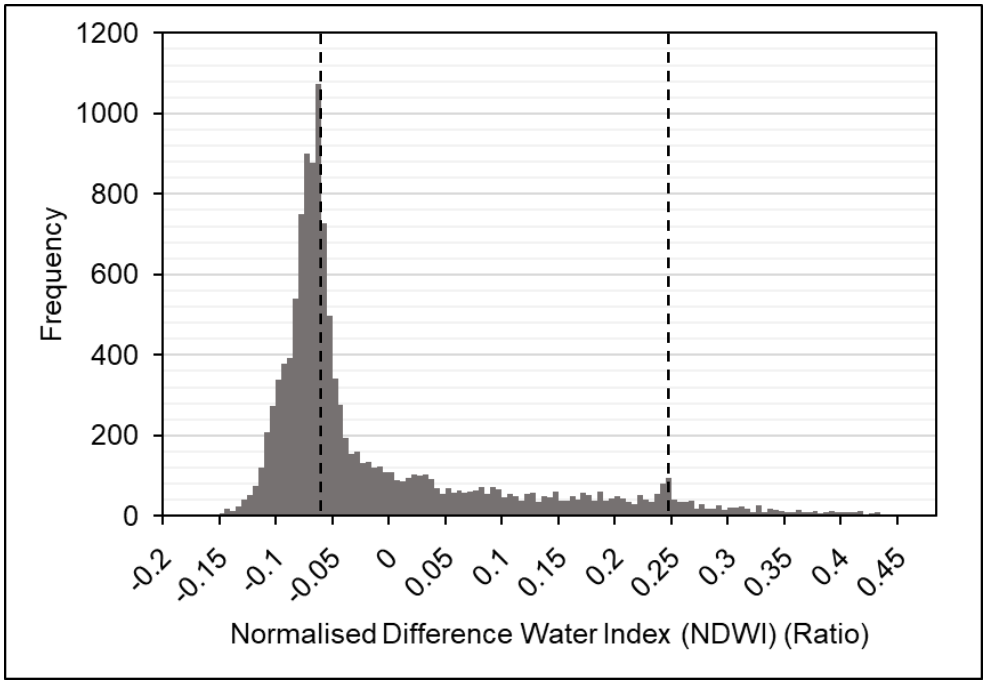


Figure 8-3: Elikhulu East histogram of the mean Sentinel-2 normalised difference water index (NDWI) within the tailings plateau area.

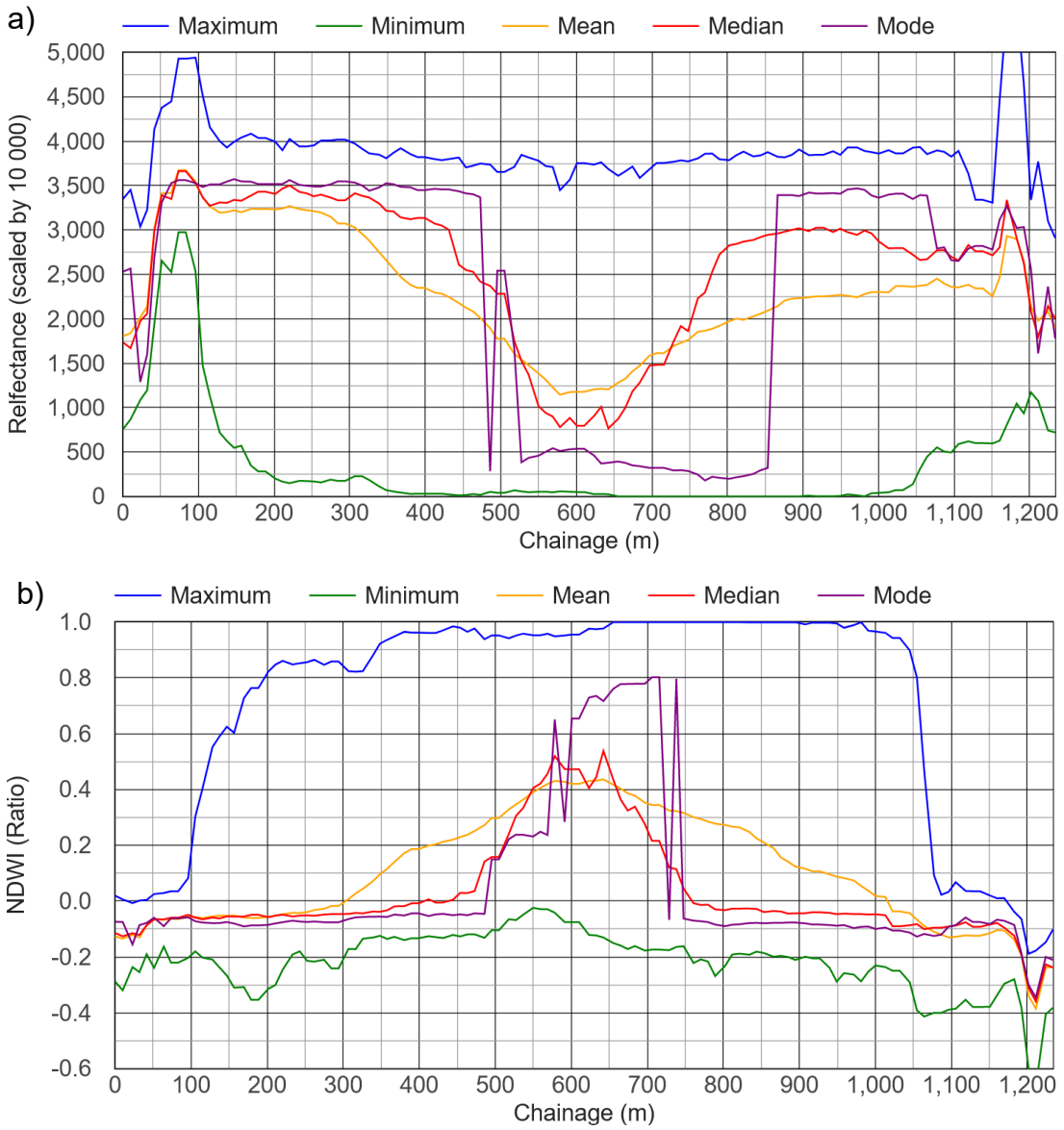


Figure 8-4: Elikhulu East a) NIR and b) NDWI transect statistics for the Sentinel-2 2019-2021 study period image collection.

8.1.2 NIR threshold derived pond area data

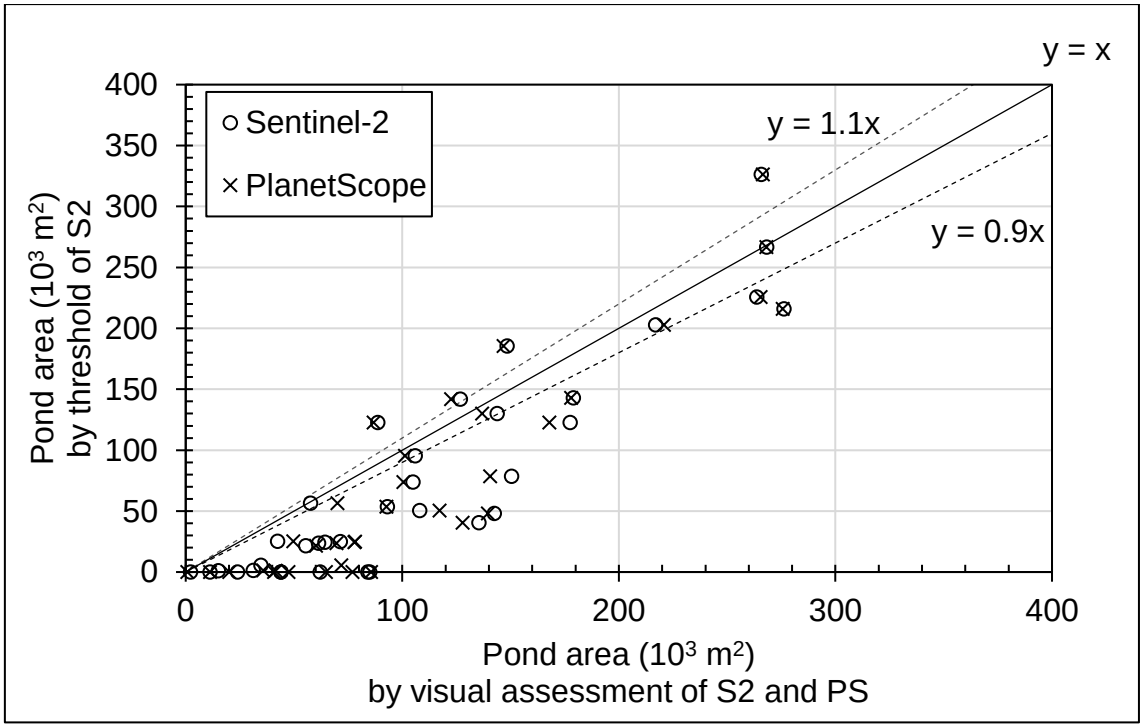


Figure 8-5: Elikhulu East pond area by NIR threshold of 566 vs. visual assessment.

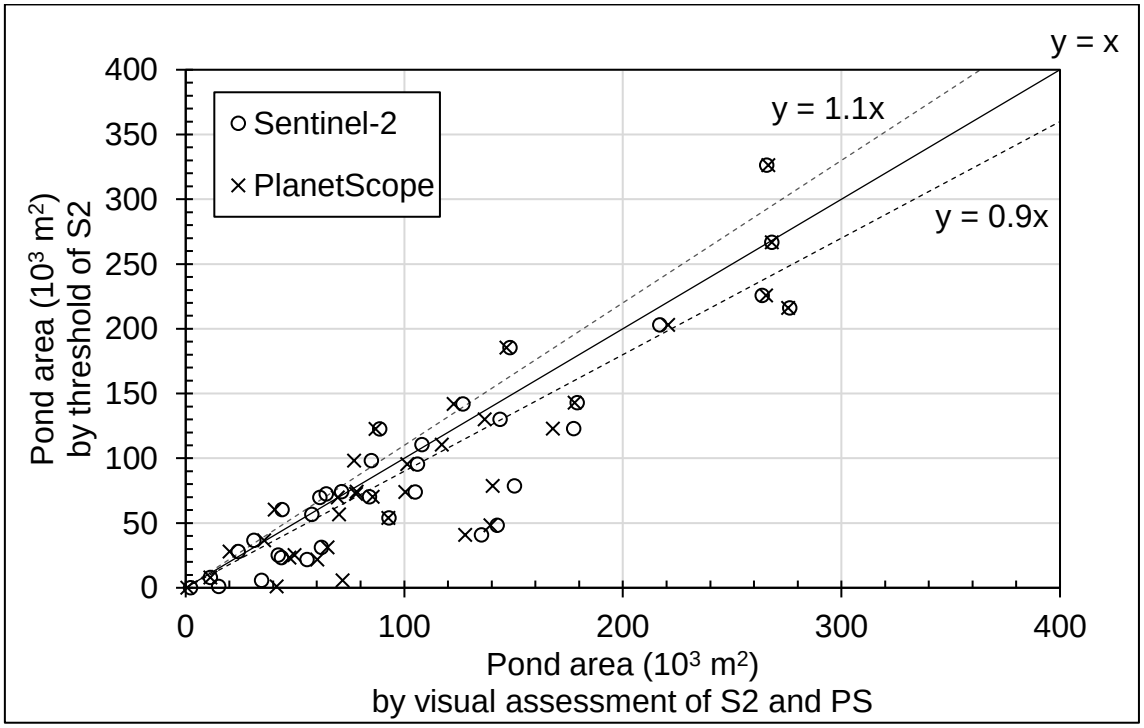


Figure 8-6: Elikhulu East pond area by NIR threshold of 566 before the start of 2021 and 2 360 thereafter vs. visual assessment.

8.1.3 NDWI threshold derived pond area data

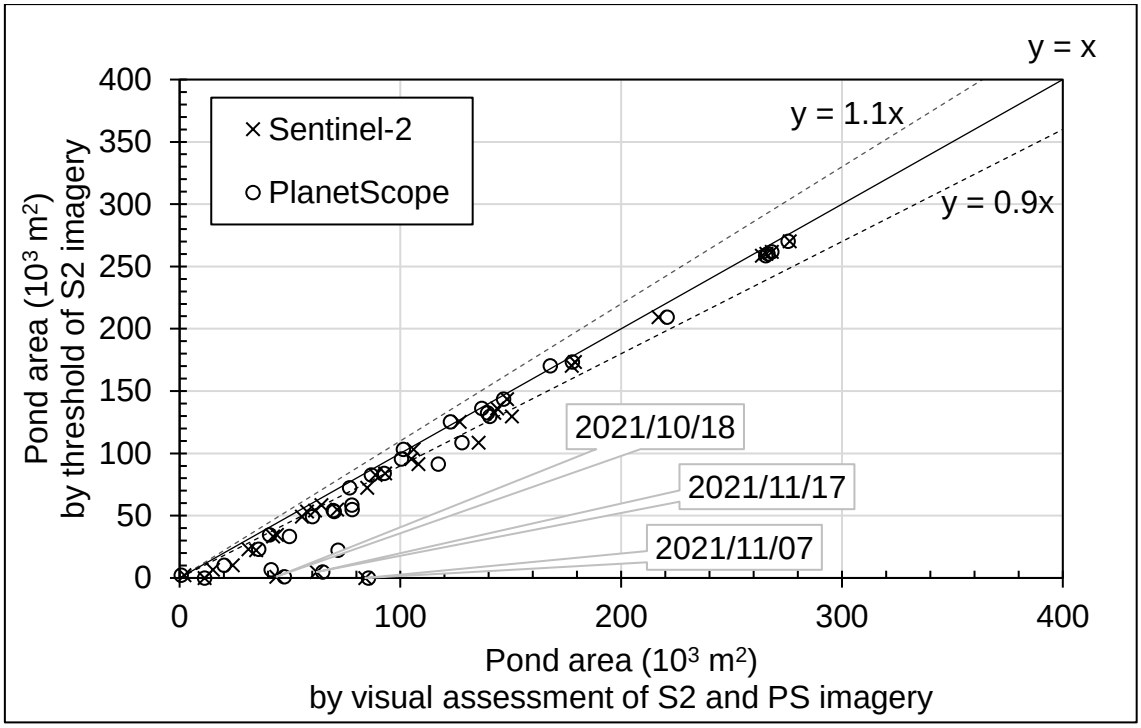


Figure 8-7: Elikhulu East pond area by NDWI threshold of 0.204 vs. visual assessment.

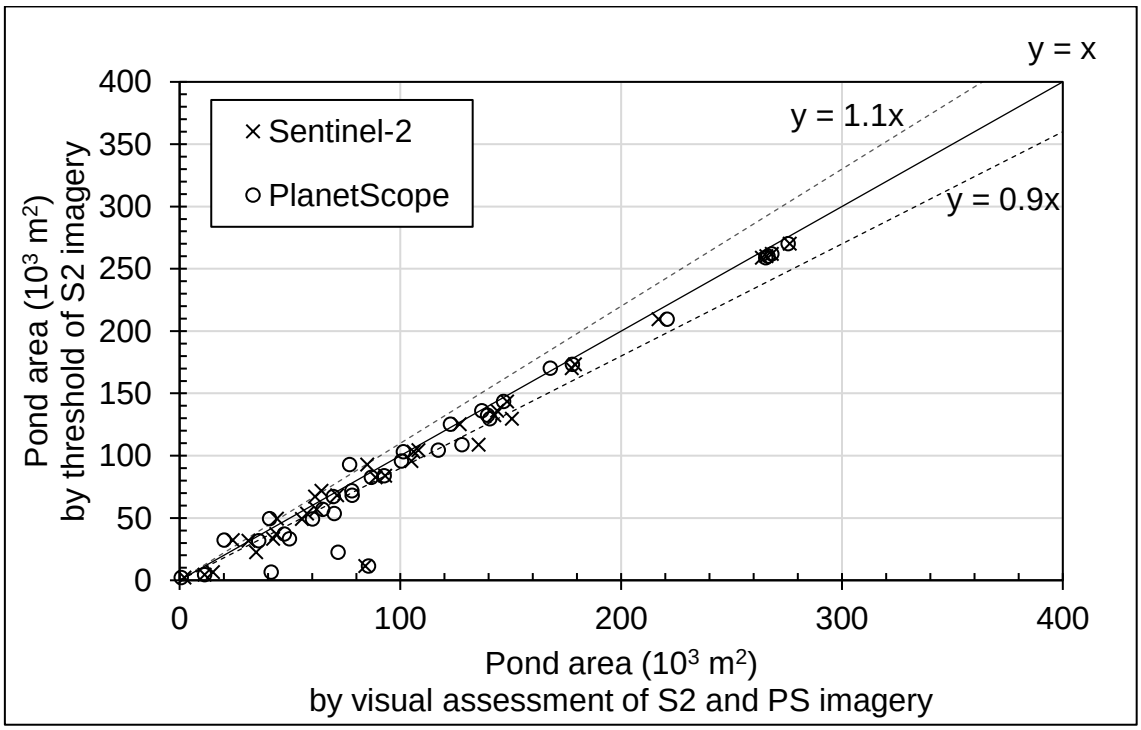


Figure 8-8: Elikhulu East pond area by NDWI threshold of 0.204 before the start of 2021 and 0.050 thereafter vs. visual assessment.

8.1.4 Threshold performance versus very high-resolution reference data

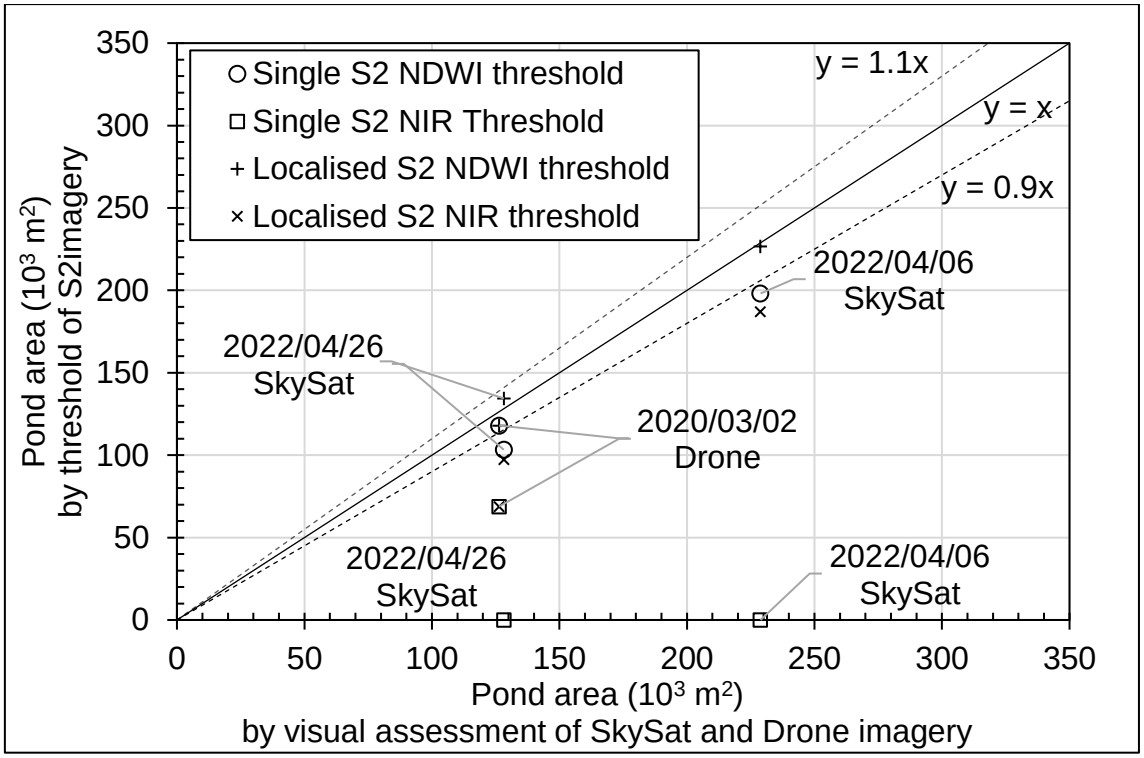


Figure 8-9: Elikhulu East: Pond area by visual assessment of very high-resolution reference imagery vs. threshold of Sentinel-2 (S2) imagery.

8.2 Elikhulu West

8.2.1 Histogram and transect assessment

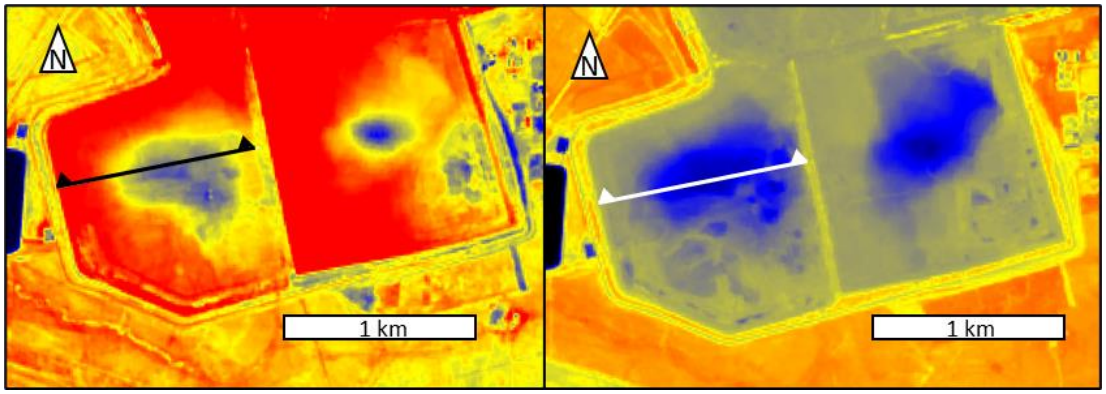


Figure 8-10: Elikhulu West: Mean images of near infrared reflectance (left) and normalised difference water index (right).

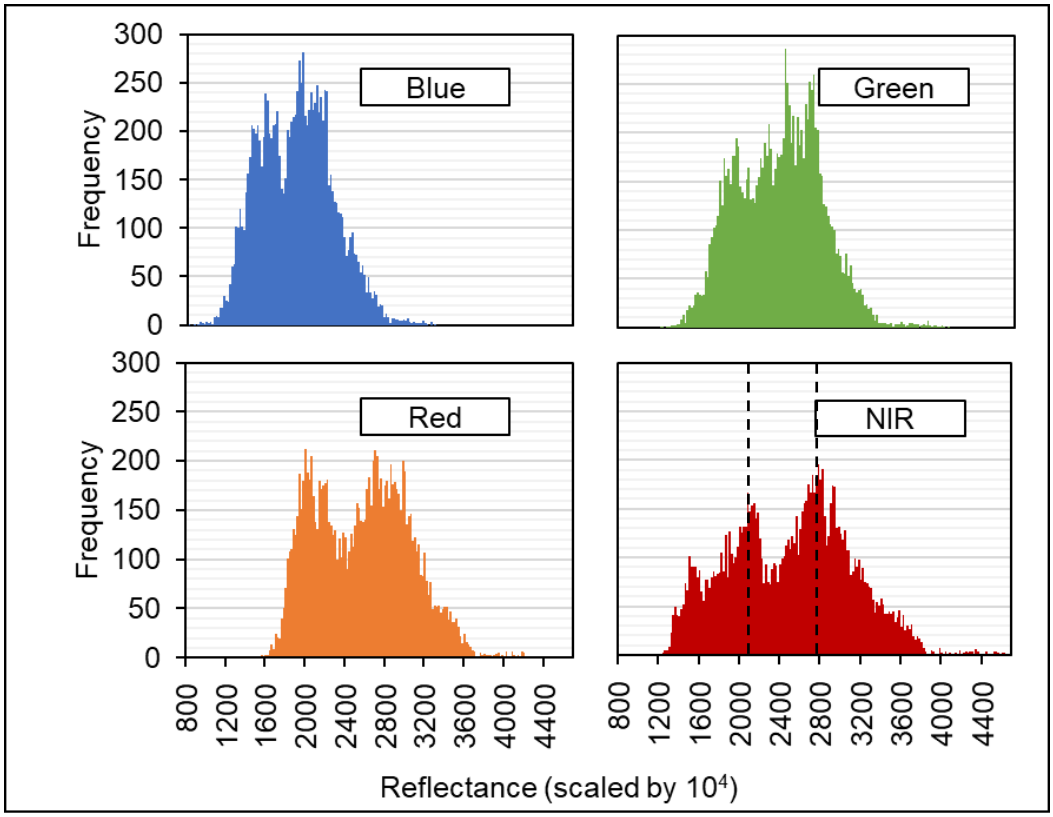


Figure 8-11: Elikhulu West histograms of the mean visible and near infrared (NIR) Sentinel-2 bands within the tailings plateau area.

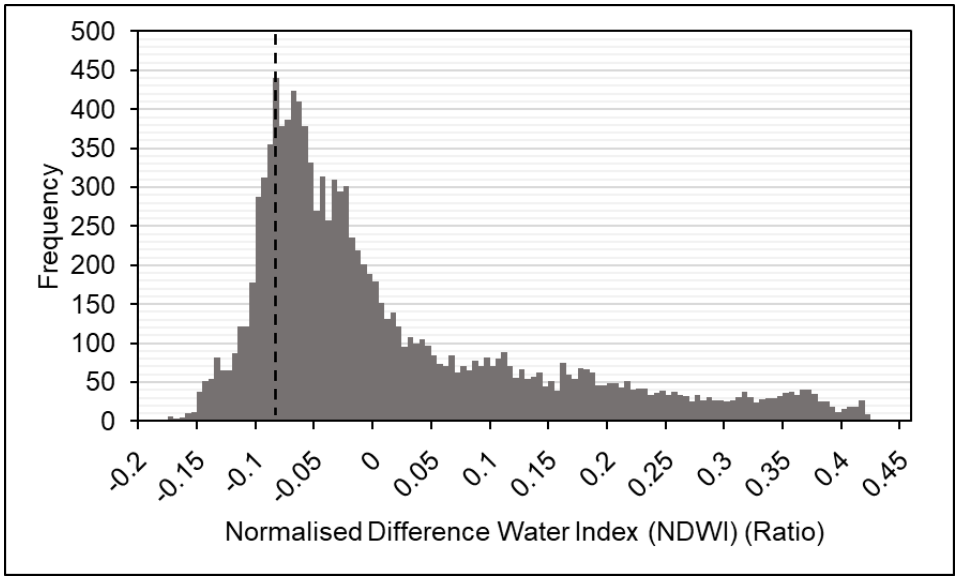


Figure 8-12: Elikhulu West histogram of the mean Sentinel-2 normalised difference water index (NDWI) within the tailings plateau area.

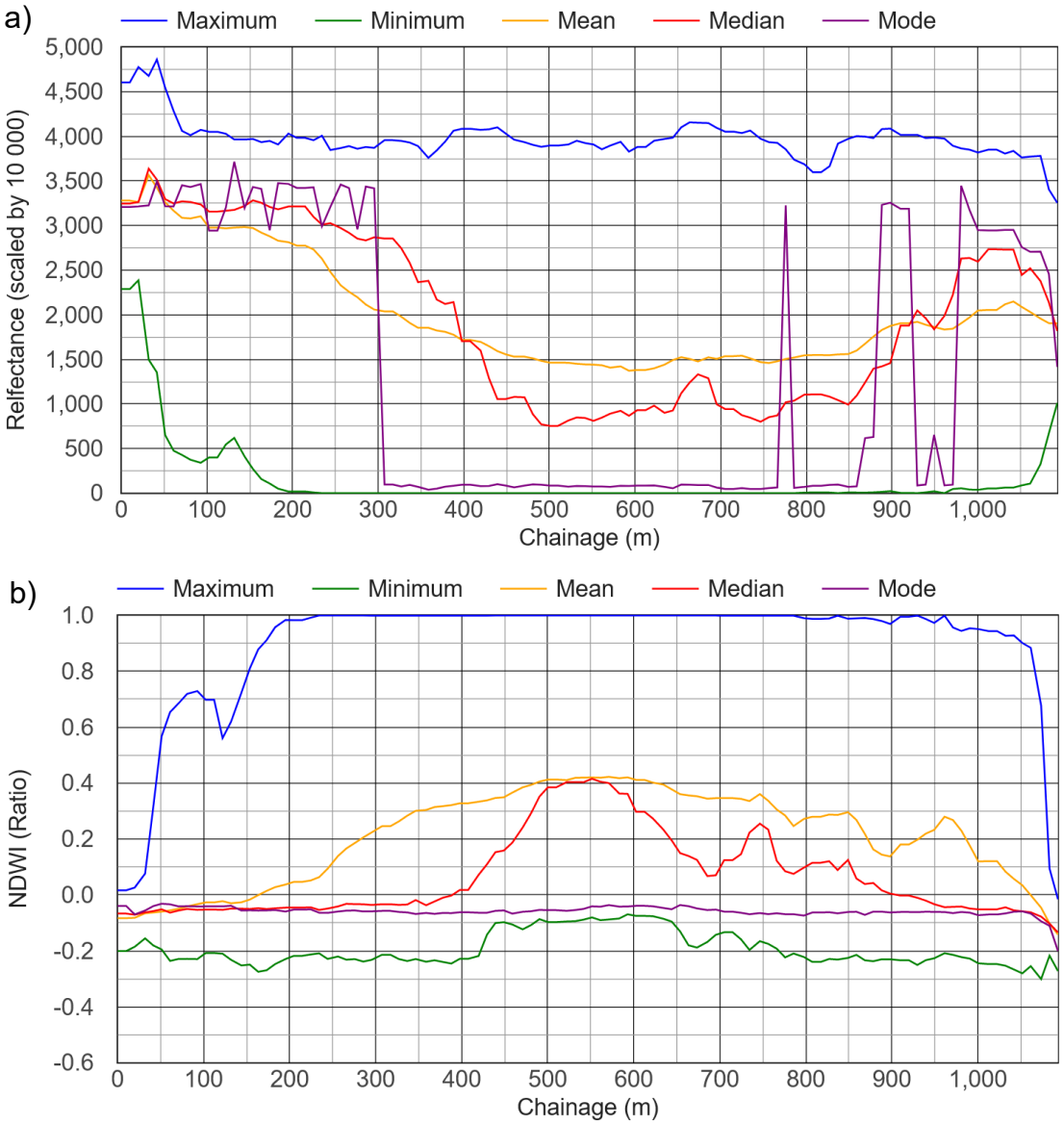


Figure 8-13: Elikhulu West a) NIR and b) NDWI transect statistics for the Sentinel-2 2019-2021 study period image collection.

8.2.2 NIR threshold derived pond area data

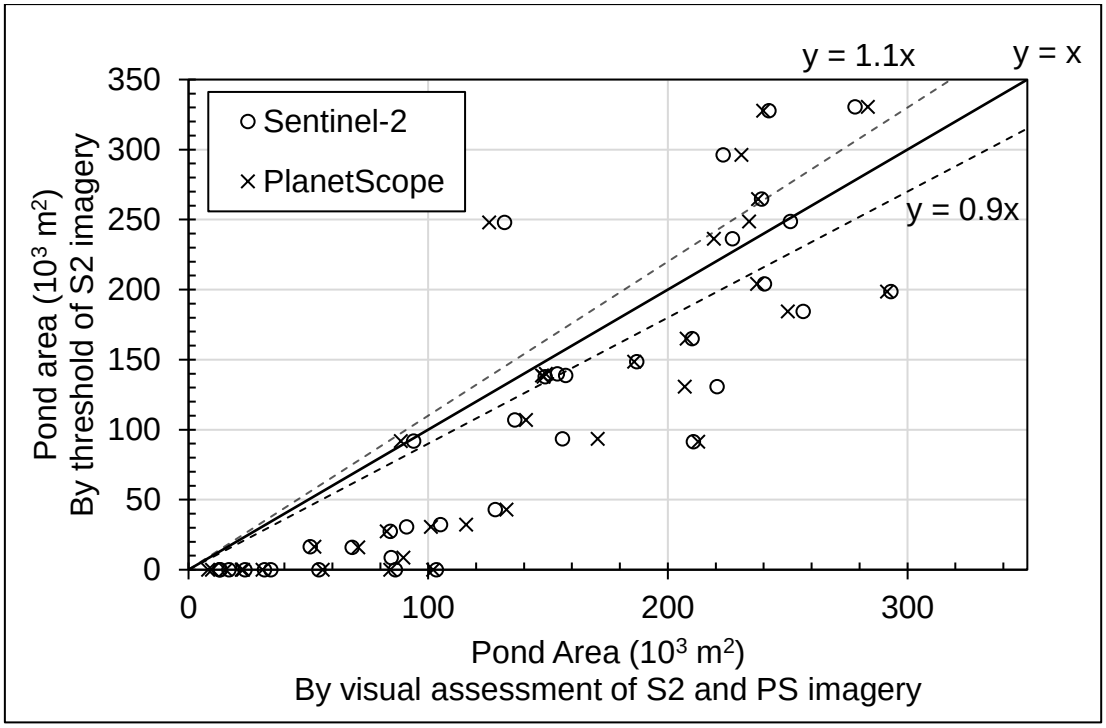


Figure 8-14: Elikhulu West pond area by NIR threshold of 577 vs. manual delineation.

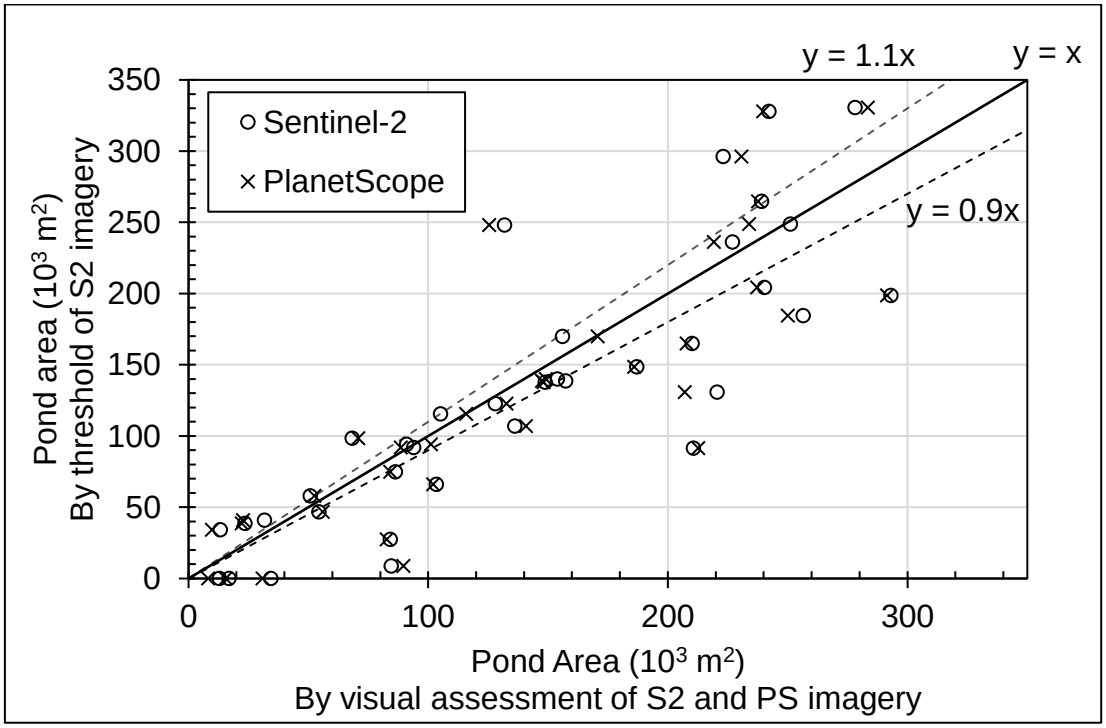


Figure 8-15: Elikhulu West pond area by NIR threshold of 577 before the start of 2021 and 2 280 thereafter vs. manual delineation.

8.2.3 NDWI threshold derived pond area data

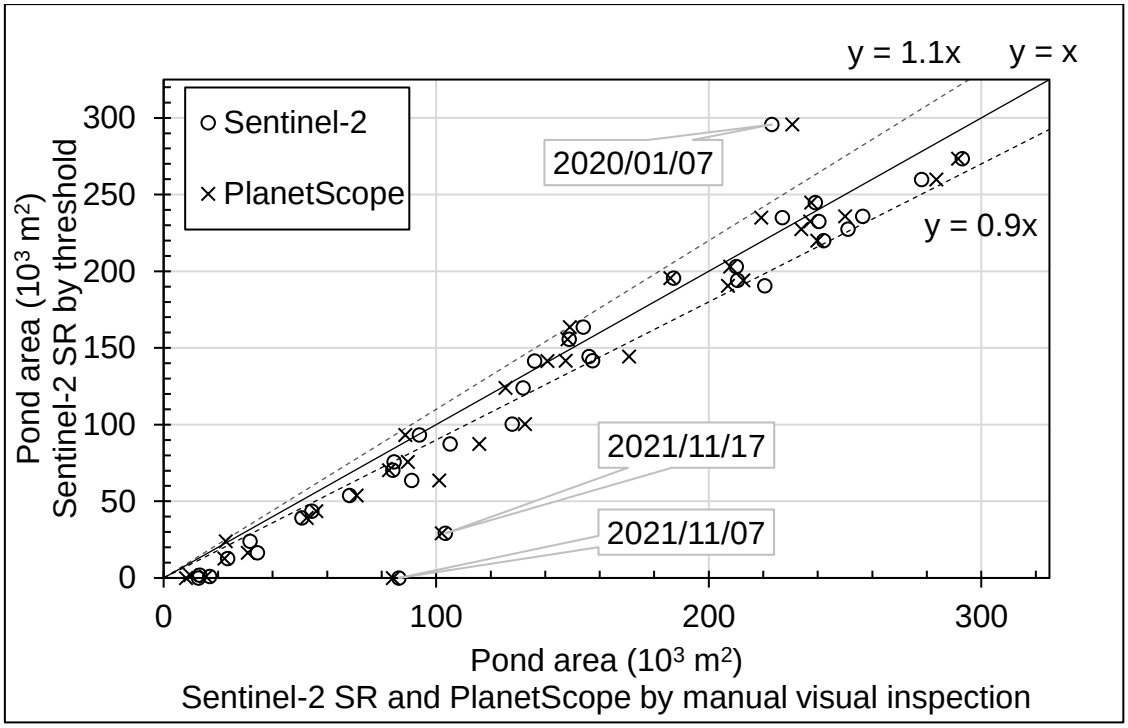


Figure 8-16: Elikhulu West pond area by NDWI threshold of 0.225 vs. manual delineation.

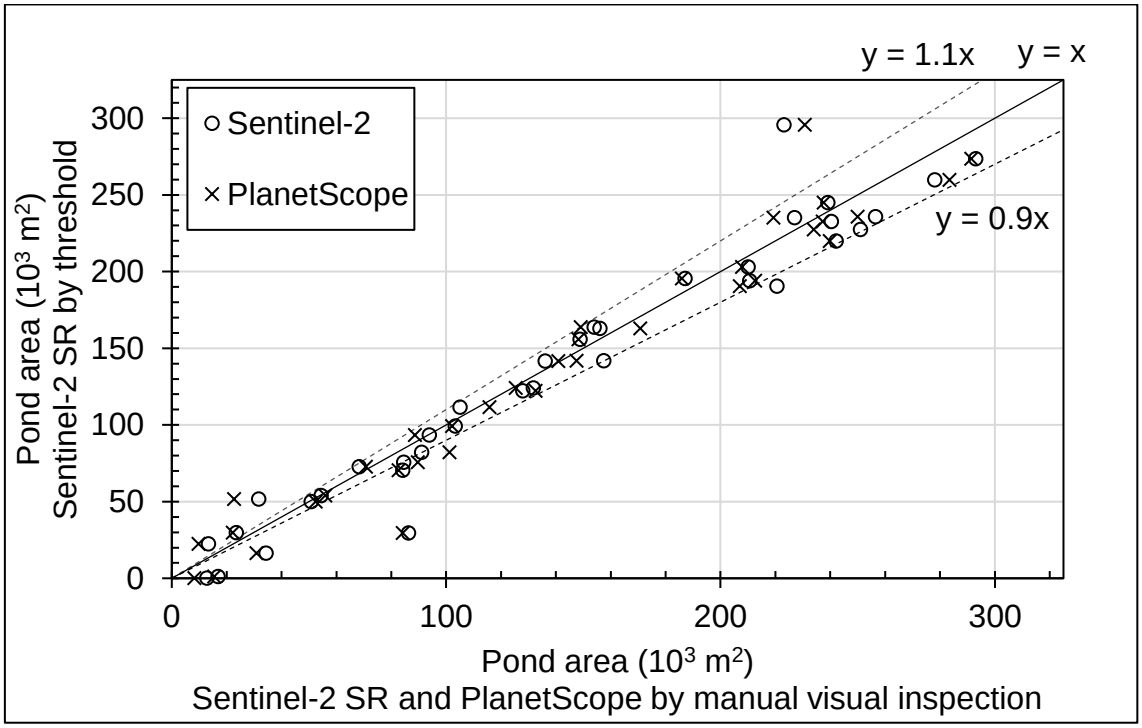


Figure 8-17: Elikhulu West pond area by NDWI threshold of 0.225 before the start of 2021 and 0.050 thereafter vs. manual delineation.

8.2.4 Threshold performance versus very high-resolution reference data

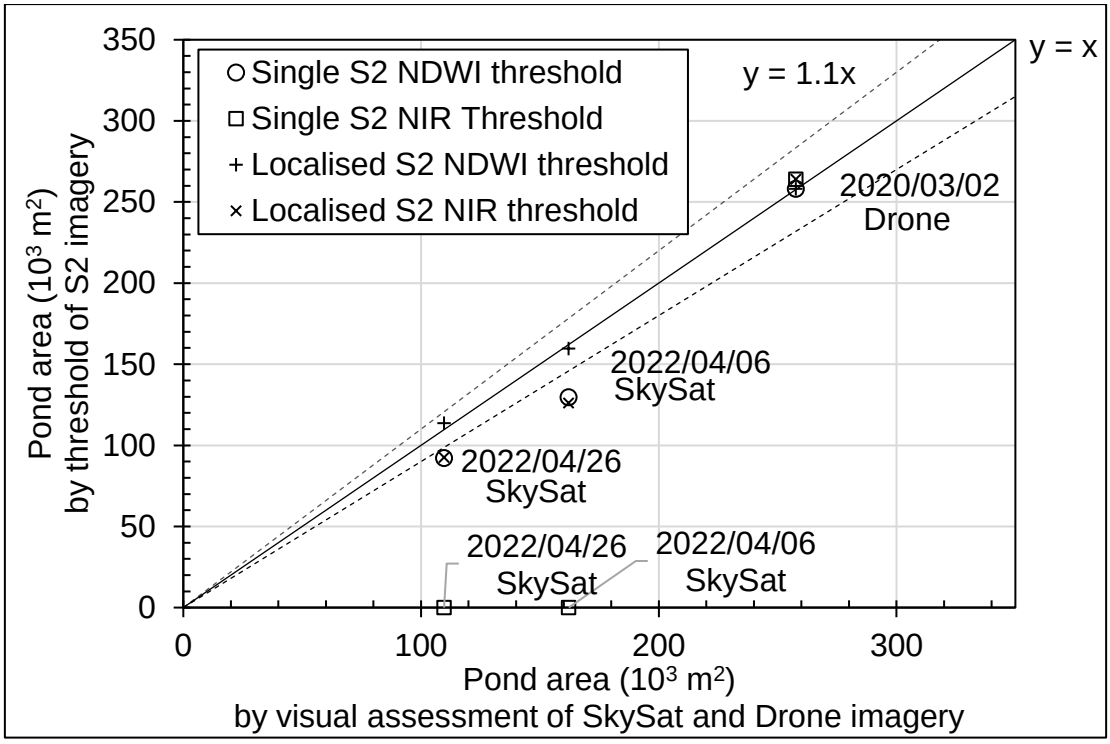


Figure 8-18: Elikhulu West pond area by visual assessment of very high-resolution reference imagery vs. threshold of Sentinel-2 (S2) imagery.

8.3 Ergo

8.3.1 Histogram and transect assessment

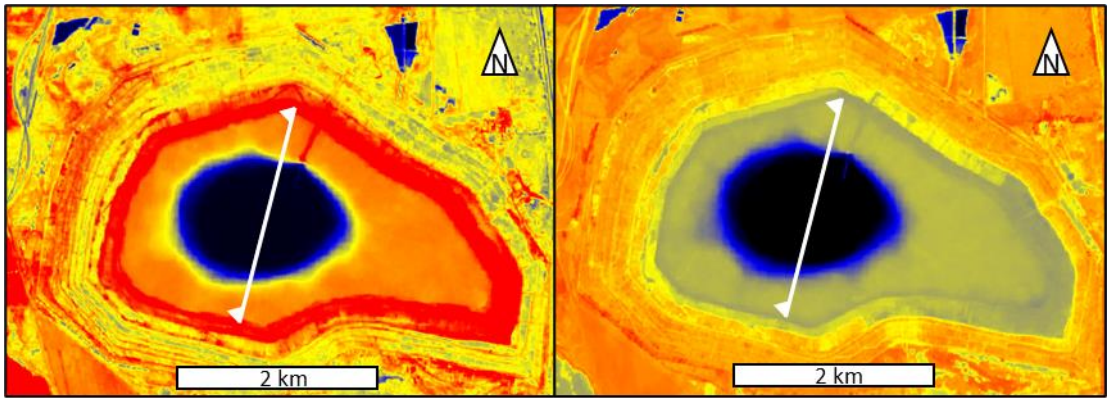


Figure 8-19: Mean images of near infrared reflectance (left) and normalised difference water index (right) with the transect line shown.

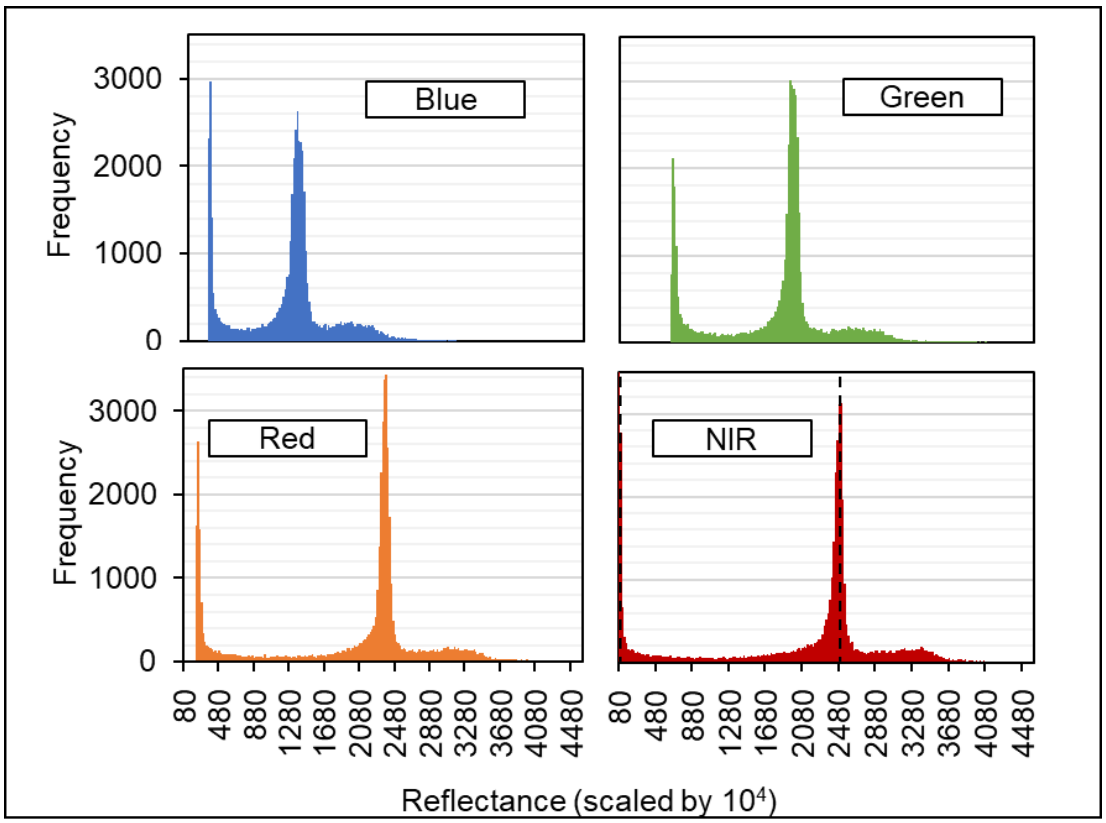


Figure 8-20: Ergo histograms of the mean visible and near infrared (NIR) Sentinel-2 bands within the tailings plateau area.

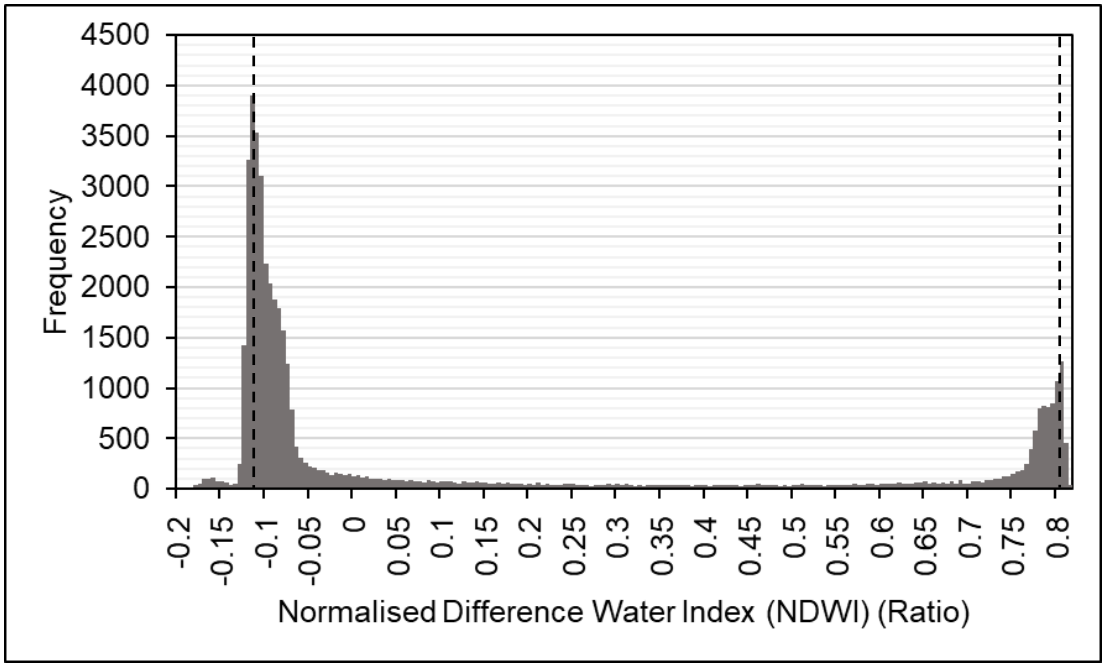


Figure 8-21: Ergo histogram of the mean Sentinel-2 normalised difference water index (NDWI) within the tailings plateau area.

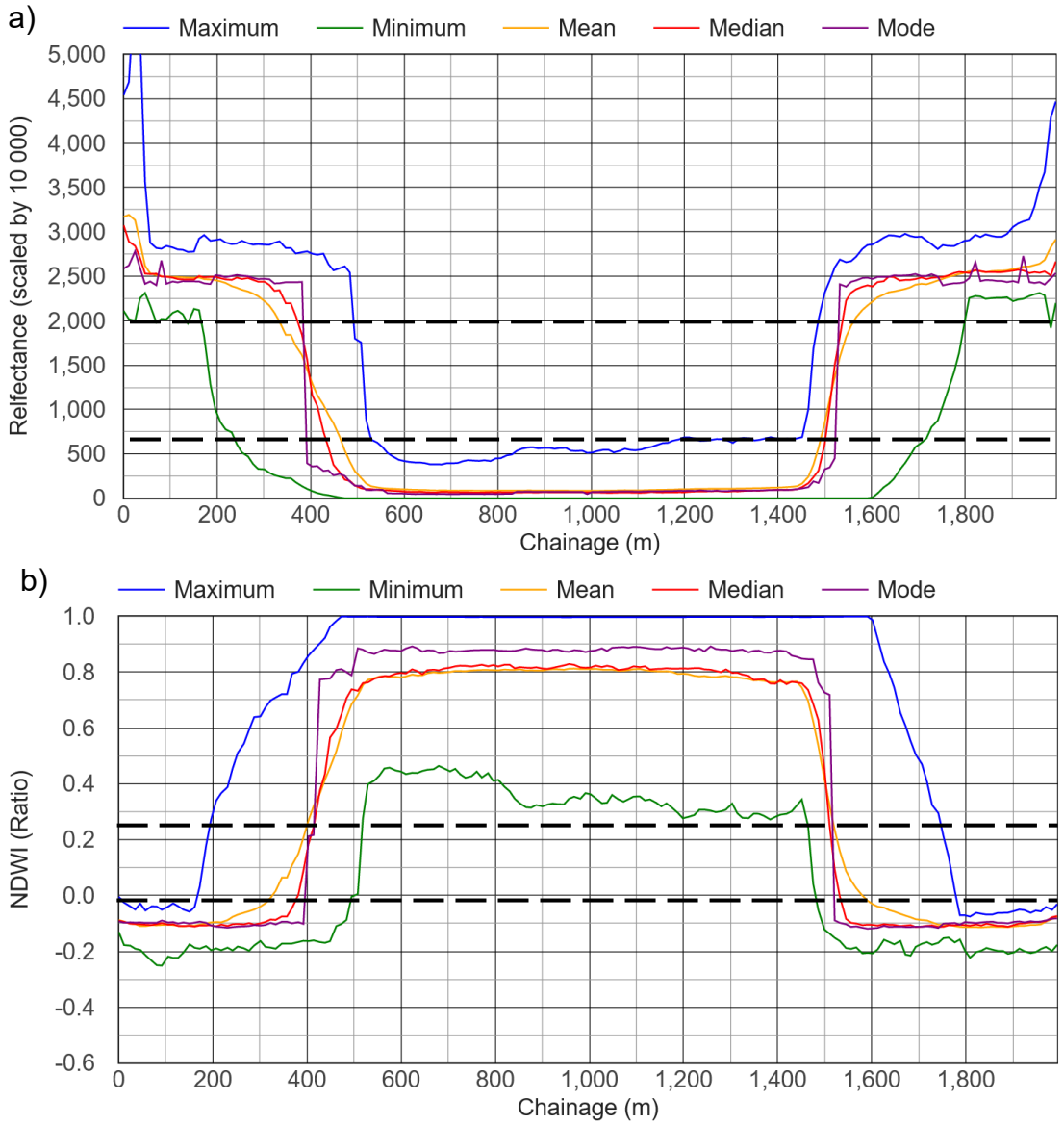


Figure 8-22: Ergo a) NIR and b) NDWI transect statistics for the Sentinel-2 2019-2021 study period image collection.

8.3.2 NIR threshold derived pond area data

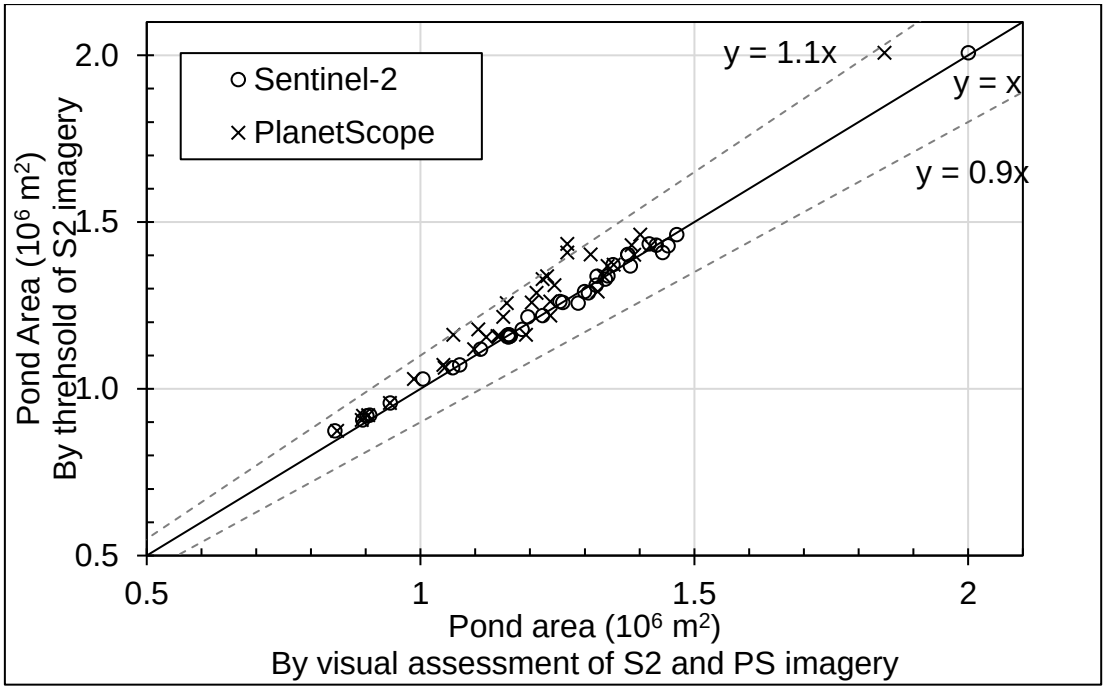


Figure 8-23: Ergo pond area by NIR threshold of 1 766 vs. visual assessment.

8.3.3 NDWI threshold derived pond area data

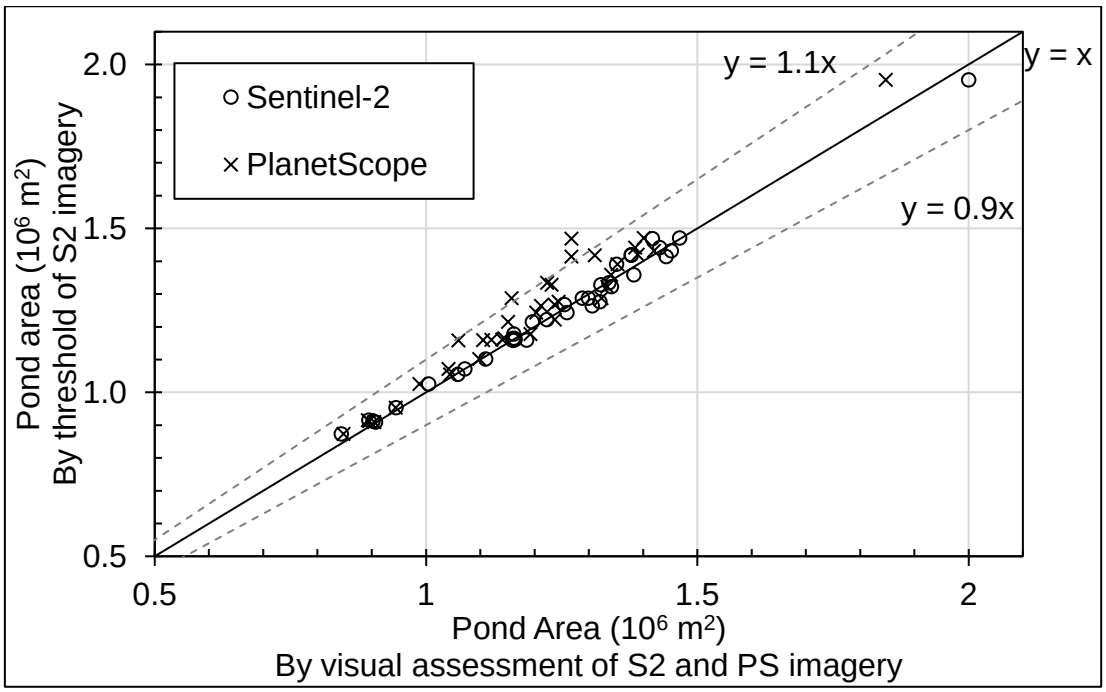


Figure 8-24: Ergo pond area by NDWI threshold of 0.0143 vs. manual delineation.

8.3.4 Threshold performance versus very high-resolution reference data

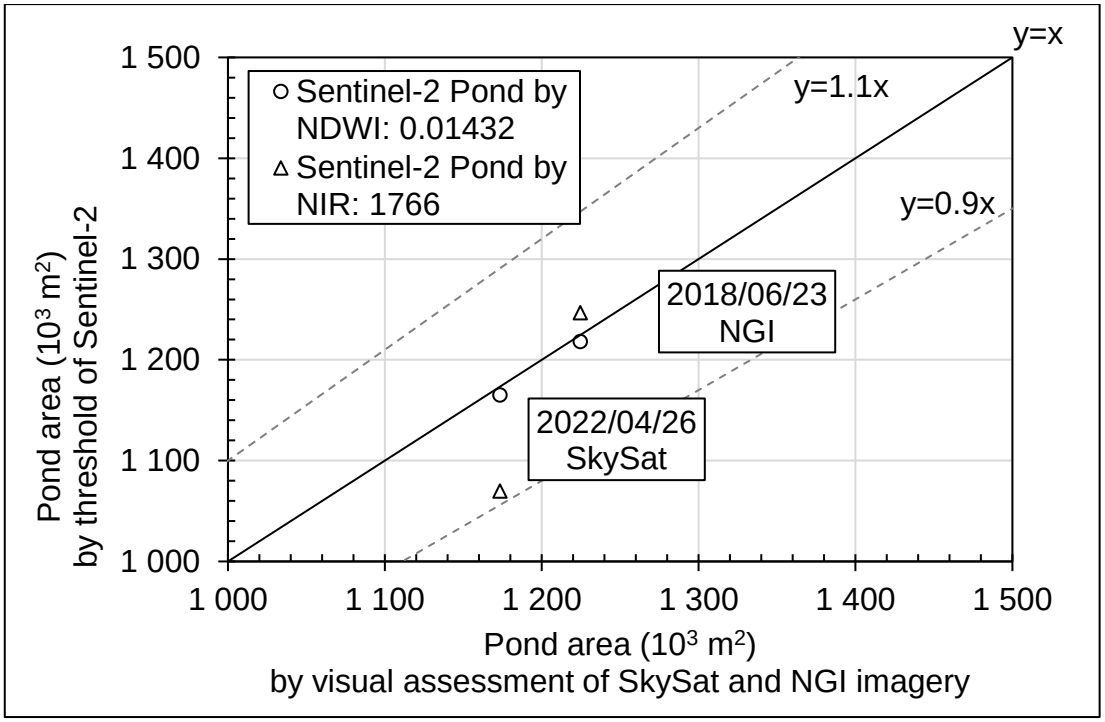


Figure 8-25: Ergo pond area by visual assessment of very high-resolution reference imagery vs. threshold of Sentinel-2 (S2) imagery.

8.4 Impala

8.4.1 Histogram and transect assessment

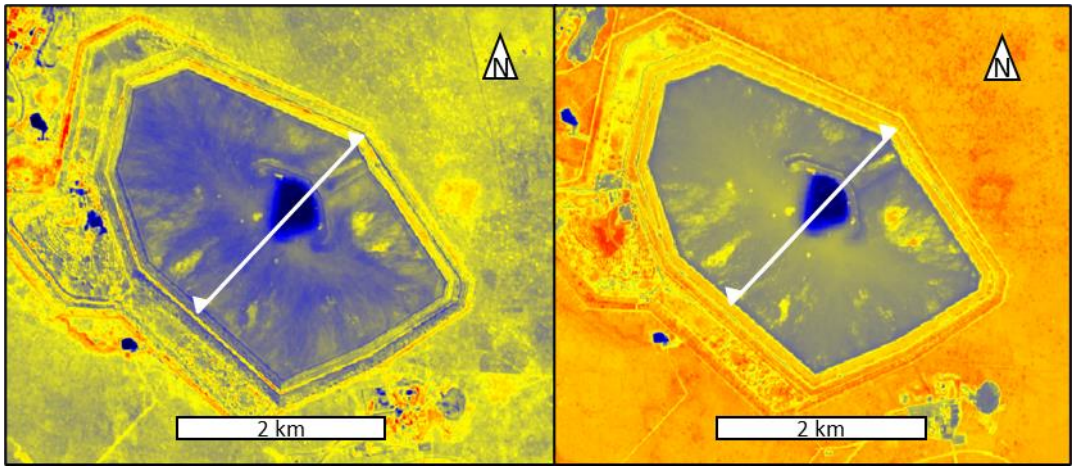


Figure 8-26: Mean images of near infrared reflectance (left) and normalised difference water index (right).

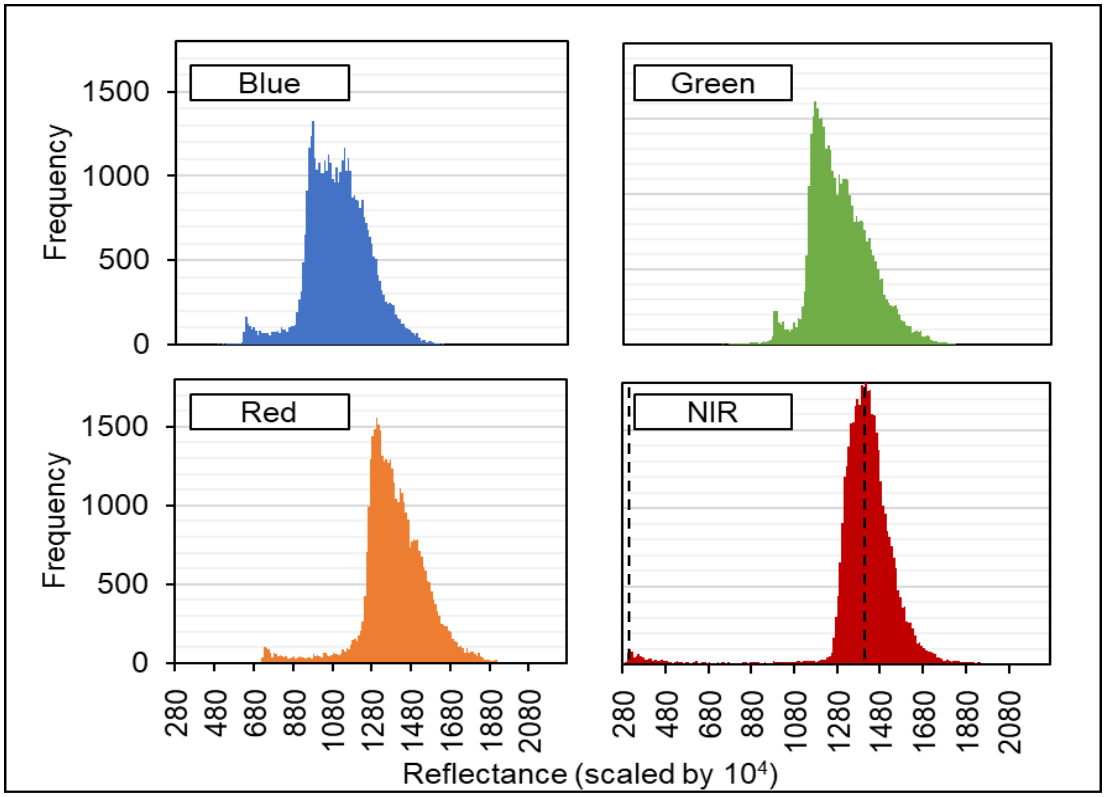


Figure 8-27: Impala histograms of the mean visible and near infrared (NIR) Sentinel-2 bands for the Impala basin area.

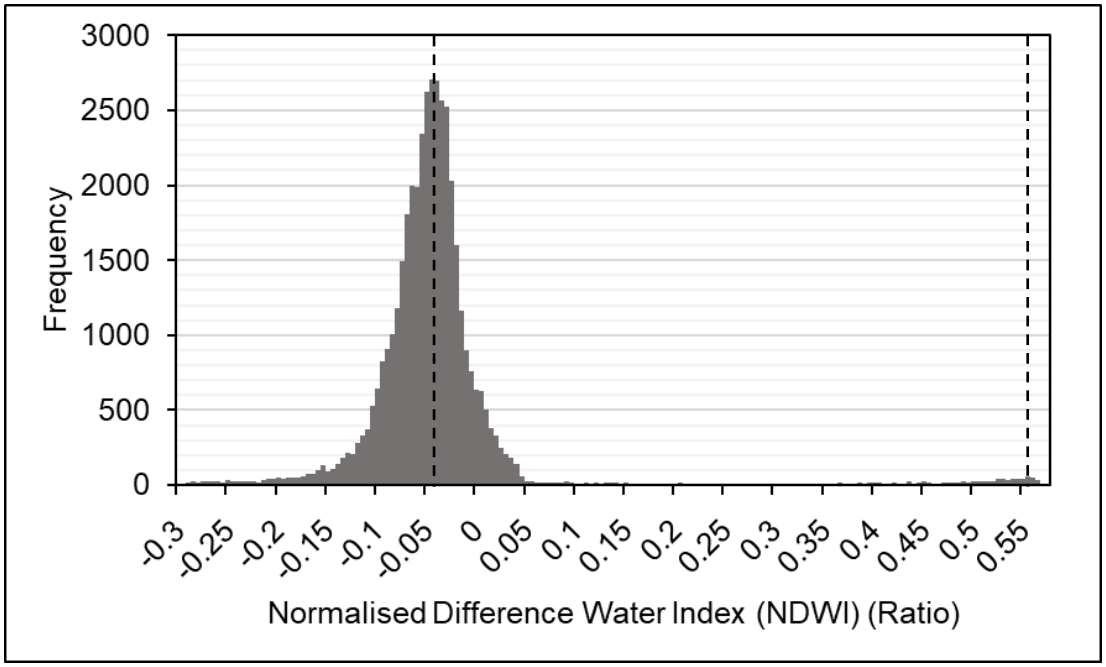


Figure 8-28: Impala histogram of the NDWI for Sentinel-2 averaged over the main study period of the Impala basin area.

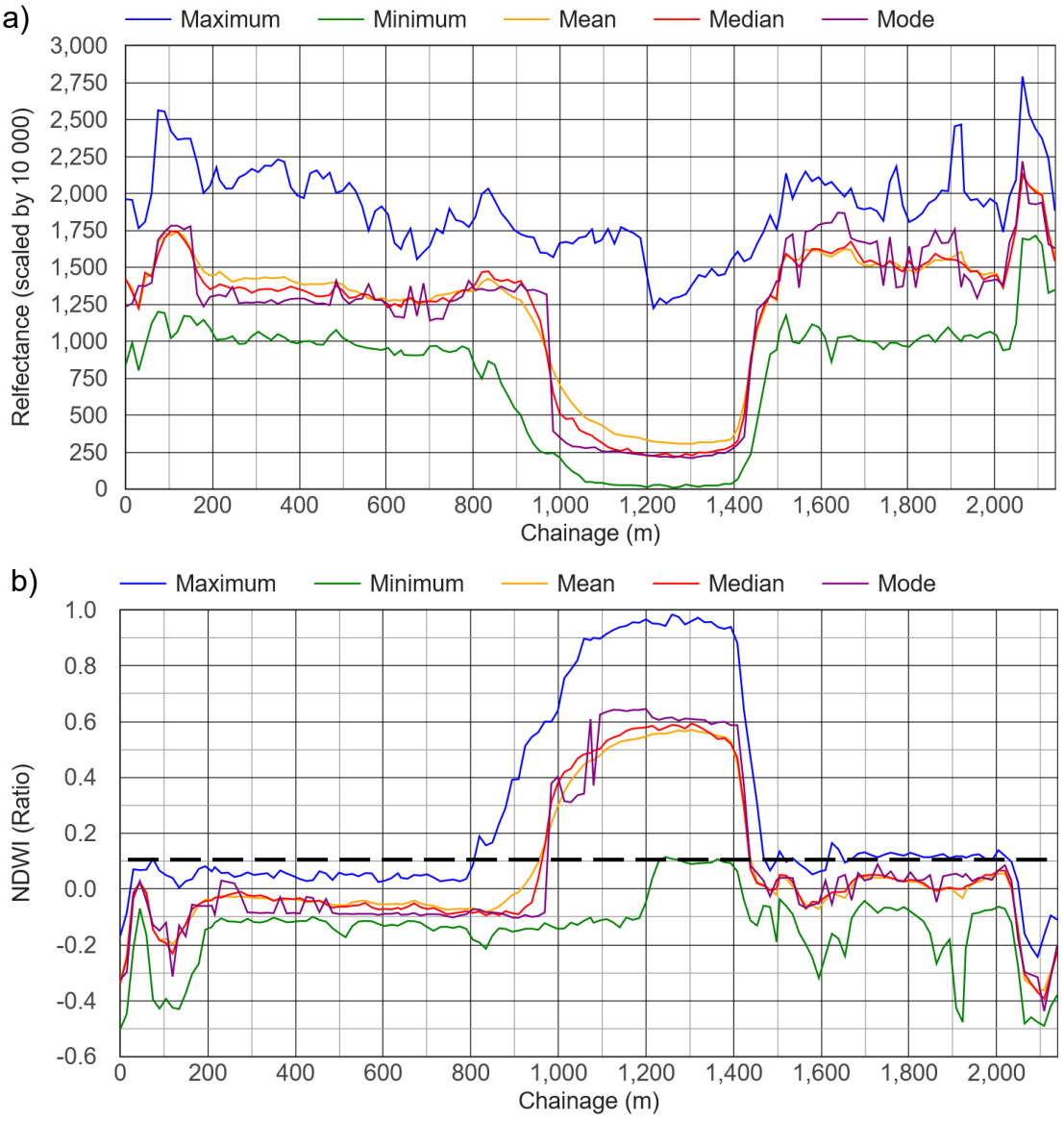


Figure 8-29: Impala a) NIR and b) NDWI transect statistics for the Sentinel-2 2019-2021 study period image collection.

8.4.2 NIR threshold

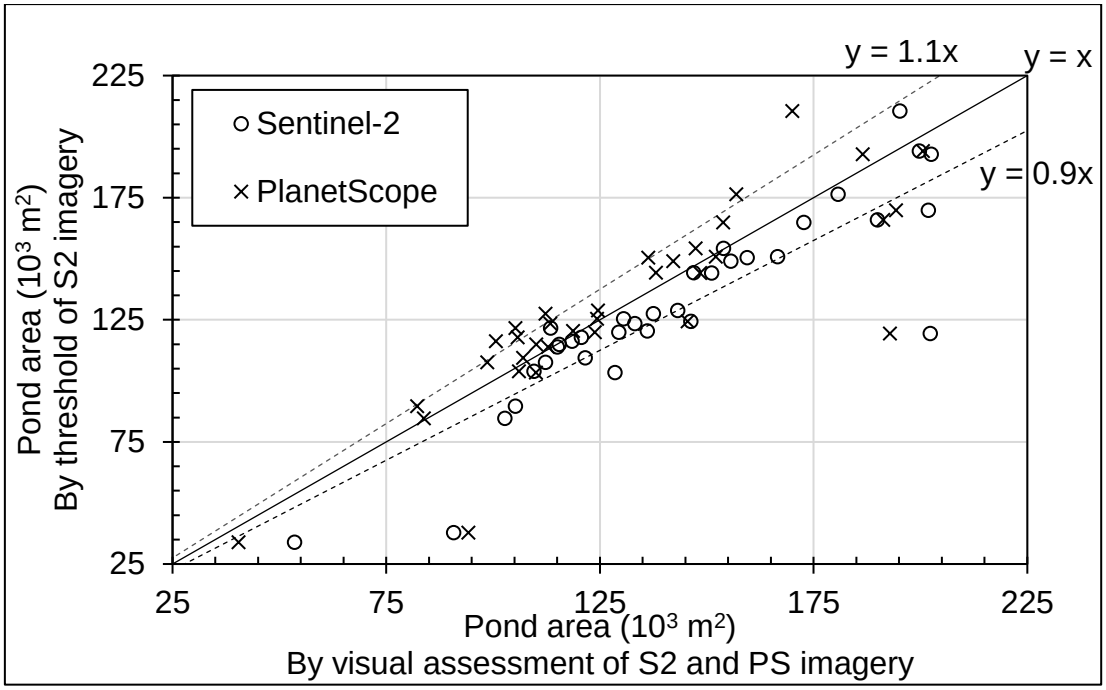


Figure 8-30: Impala pond area by NIR threshold of 891 vs. manual delineation.

8.4.3 NDWI threshold

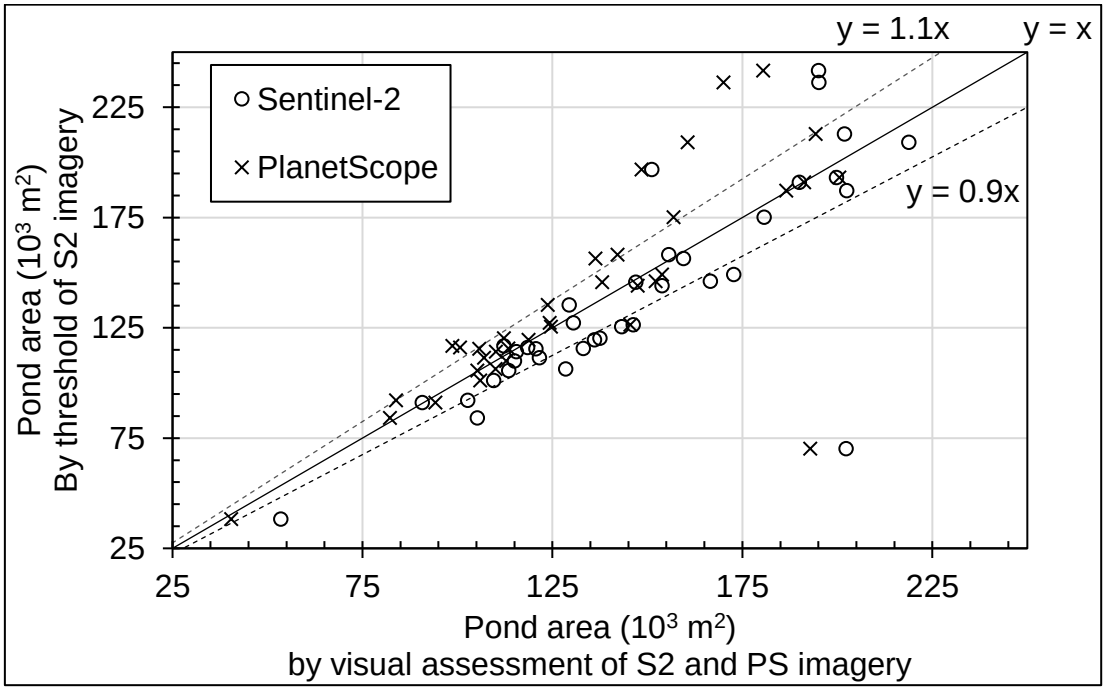


Figure 8-31: Impala pond area by NDWI threshold of 0.107 vs. manual delineation.

8.4.4 Threshold performance versus very high-resolution reference data

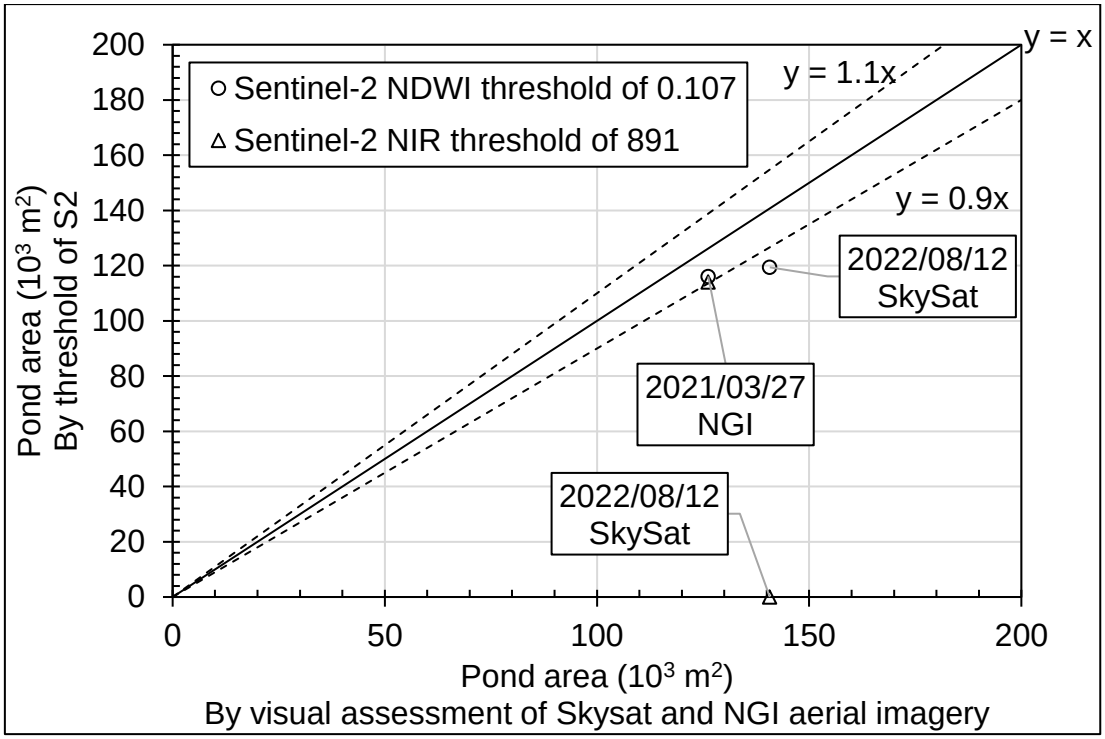


Figure 8-32: Impala pond area by visual assessment of very high-resolution reference imagery vs. threshold of Sentinel-2 (S2) imagery.

9 APPENDIX-C: CATALOGUE OF IMAGES

9.1 Elikhulu

Sentinel-2 Surface Reflectance Images. Downloaded from the GEE catalogue ImageCollection: “COPERNICUS/S2_SR/”.

Image	Date
20190122T075221_20190122T081410_T35JPL	2019/01/22
20190221T074931_20190221T081358_T35JPL	2019/02/21
20190303T074821_20190303T081357_T35JPL	2019/03/03
20190427T074619_20190427T081452_T35JPL	2019/04/27
20190517T074619_20190517T081019_T35JPL	2019/05/17
20190616T074619_20190616T081453_T35JPL	2019/06/16
20190706T074619_20190706T081656_T35JPL	2019/07/06
20190820T074611_20190820T081611_T35JPL	2019/08/20
20190909T074611_20190909T080510_T35JPL	2019/09/09
20191004T074749_20191004T080733_T35JPL	2019/10/04
20191103T075009_20191103T081457_T35JPL	2019/11/03
20191203T075209_20191203T080806_T35JPL	2019/12/03
20200107T075311_20200107T081135_T35JPL	2020/01/07
20200201T075039_20200201T080648_T35JPL	2020/02/01
20200307T074751_20200307T081122_T35JPL	2020/03/07
20200411T074609_20200411T080507_T35JPL	2020/04/11
20200521T074609_20200521T081640_T35JPL	2020/05/21
20200615T074621_20200615T080933_T35JPL	2020/06/15
20200715T074621_20200715T080806_T35JPL	2020/07/15
20200824T074621_20200824T081049_T35JPL	2020/08/24
20200913T074621_20200913T081626_T35JPL	2020/09/13
20201018T074929_20201018T081224_T35JPL	2020/10/18
20201107T075129_20201107T081540_T35JPL	2020/11/07
20201207T075319_20201207T080629_T35JPL	2020/12/07
20210121T075231_20210121T081059_T35JPL	2021/01/21
20210220T074941_20210220T081050_T35JPL	2021/02/20
20210312T074721_20210312T081050_T35JPL	2021/03/12
20210421T074611_20210421T081032_T35JPL	2021/04/21
20210511T074611_20210511T081050_T35JPL	2021/05/11
20210610T074611_20210610T081051_T35JPL	2021/06/10

20210720T074621_20210720T081054_T35JPL	2021/07/20
20210819T074611_20210819T081053_T35JPL	2021/08/19
20210913T074609_20210913T081216_T35JPL	2021/09/13
20211018T074931_20211018T081057_T35JPL	2021/10/18
20211107T075131_20211107T081054_T35JPL	2021/11/07
20211117T075211_20211117T081050_T35JPL	2021/11/17

PlanetScope 4 Band Imagery (downloaded from Planet Explorer)

Image	**Date**	**Sat. Gen.**
20190122_082321_104a_3B_AnalyticMS_SR	2019/01/22	PS2
20190221_081658_1050_3B_AnalyticMS_SR	2019/02/21	PS2
20190303_074349_0e2f_3B_AnalyticMS_SR	2019/03/03	PS2
20190314_074802_101e_3B_AnalyticMS_SR	2019/03/14	PS2
20190427_081009_0f21_3B_AnalyticMS_SR	2019/04/27	PS2
20190517_074946_1035_3B_AnalyticMS_SR	2019/05/17	PS2
20190616_074955_1025_3B_AnalyticMS_SR	2019/06/16	PS2.SD
20190706_093205_26_1065_3B_AnalyticMS_SR	2019/07/06	PS2
20190726_075419_0f36_3B_AnalyticMS_SR	2019/07/26	PS2.SD
20190820_075056_1003_3B_AnalyticMS_SR	2019/08/20	PS2
20190909_080543_53_105e_3B_AnalyticMS_SR	2019/09/09	PS2.SD
20191004_075058_1025_3B_AnalyticMS_SR	2019/10/04	PS2
20191103_080711_37_1058_3B_AnalyticMS_SR	2019/11/03	PS2
20191203_075041_1029_3B_AnalyticMS_SR	2019/12/03	PS2.SD
20200103_073124_0f3c_3B_AnalyticMS_SR	2020/01/03	PS2
20200107_073024_1050_3B_AnalyticMS_SR	2020/01/07	PS2
20200201_080640_92_105c_3B_AnalyticMS_SR	2020/02/01	PS2
20200307_075347_0f15_3B_AnalyticMS_SR	2020/03/07	PS2
20200411_071238_0f32_3B_AnalyticMS_SR	2020/04/11	PS2.SD
20200521_070741_0f36_3B_AnalyticMS_SR	2020/05/21	PS2
20200615_075057_1010_3B_AnalyticMS_SR	2020/06/15	PS2
20200715_091004_04_106a_3B_AnalyticMS_SR	2020/07/15	PS2
20200824_075143_1014_3B_AnalyticMS_SR	2020/08/24	PS2
20200913_064709_104e_3B_AnalyticMS_SR	2020/09/13	PSB.SD
20201018_064204_1050_3B_AnalyticMS_SR	2020/10/18	PSB.SD
20201106_075210_103c_3B_AnalyticMS_SR	2020/11/06	PSB.SD
20201207_081903_68_2307_3B_AnalyticMS_SR	2020/12/07	PSB.SD

20210121_072712_68_222b_3B_AnalyticMS_SR	2021/01/21	PS2
20210220_081724_93_2416_3B_AnalyticMS_SR	2021/02/20	PS2.SD
20210312_072318_43_2420_3B_AnalyticMS_SR	2021/03/12	PSB.SD
20210421_075015_1025_3B_AnalyticMS_SR	2021/04/21	PSB.SD
20210511_085143_07_106e_3B_AnalyticMS_SR	2021/05/11	PSB.SD
20210610_072511_93_2435_3B_AnalyticMS_SR	2021/06/10	PSB.SD
20210720_072219_19_245d_3B_AnalyticMS_SR	2021/07/20	PS2.SD
20210819_073432_01_222f_3B_AnalyticMS_SR	2021/08/19	PSB.SD
20210913_081025_22_2405_3B_AnalyticMS_SR	2021/09/13	PS2
20211018_084323_20_1058_3B_AnalyticMS_SR	2021/10/18	PS2
20211107_071854_45_2420_3B_AnalyticMS_SR	2021/11/07	PS2
20211117_074719_100a_3B_AnalyticMS_SR	2021/11/17	PS2

9.2 Ergo

Sentinel-2 Surface Reflectance Images. Downloaded from the GEE catalogue ImageCollection: “COPERNICUS/S2_SR/”.

Image	Date
20190112T075301_20190112T081438_T35JPL	2019/01/12
20190122T075221_20190122T081410_T35JPL	2019/01/22
20190226T074859_20190226T081205_T35JPL	2019/02/26
20190328T074839_20190328T081422_T35JPL	2019/03/28
20190417T074619_20190417T081016_T35JPL	2019/04/17
20190522T074621_20190522T081148_T35JPL	2019/05/22
20190616T074619_20190616T081453_T35JPL	2019/06/16
20190711T074621_20190711T080806_T35JPL	2019/07/11
20190815T074619_20190815T081324_T35JPL	2019/08/15
20190919T074611_20190919T081148_T35JPL	2019/09/19
20191014T074859_20191014T080733_T35JPL	2019/10/14
20191128T075251_20191128T081430_T35JPL	2019/11/28
20191203T075209_20191203T080806_T35JPL	2019/12/03
20200127T075201_20200127T081349_T35JPL	2020/01/27
20200216T075011_20200216T081546_T35JPL	2020/02/16
20200307T074751_20200307T081122_T35JPL	2020/03/07
20200406T074611_20200406T080826_T35JPL	2020/04/06
20200516T074621_20200516T081446_T35JPL	2020/05/16
20200605T074621_20200605T080829_T35JPL	2020/06/05
20200725T074621_20200725T080832_T35JPL	2020/07/25
20200824T074621_20200824T081049_T35JPL	2020/08/24
20200923T074641_20200923T081054_T35JPL	2020/09/23
20201023T075001_20201023T081055_T35JPL	2020/10/23
20201107T075129_20201107T081540_T35JPL	2020/11/07
20201212T075321_20201212T081150_T35JPL	2020/12/12
20210121T075231_20210121T081059_T35JPL	2021/01/21
20210220T074941_20210220T081050_T35JPL	2021/02/20
20210307T074749_20210307T081542_T35JPL	2021/03/07
20210401T074611_20210401T081040_T35JPL	2021/04/01
20210516T074609_20210516T081219_T35JPL	2021/05/16
20210615T074609_20210615T081221_T35JPL	2021/06/15
20210720T074621_20210720T081054_T35JPL	2021/07/20
20210809T074611_20210809T080832_T35JPL	2021/08/09

20210913T074609_20210913T081216_T35JPL	2021/09/13
20211023T074959_20211023T081223_T35JPL	2021/10/23
20211102T075009_20211102T081541_T35JPL	2021/11/02

PlanetScope 4 Band Imagery (downloaded from the Planet Explorer)

Image	**Date**	**Sat. Gen.**
20190112_075008_0f43_3B_AnalyticMS_SR	2019/01/12	PS2
20190122_082614_1051_3B_AnalyticMS_SR	2019/01/22	PS2
20190228_082317_0f4d_3B_AnalyticMS_SR	2019/02/28	PS2
20190331_075246_1013_3B_AnalyticMS_SR	2019/03/31	PS2
20190414_075117_1014_3B_AnalyticMS_SR	2019/04/14	PS2
20190522_093551_34_1063_3B_AnalyticMS_SR	2019/05/22	PS2.SD
20190615_075343_1010_3B_AnalyticMS_SR	2019/06/15	PS2
20190711_093150_42_106b_3B_AnalyticMS_SR	2019/07/11	PS2.SD
20190814_075327_0f46_3B_AnalyticMS_SR	2019/08/14	PS2
20190818_093314_05_106a_3B_AnalyticMS_SR	2019/08/18	PS2.SD
20190919_075257_1013_3B_AnalyticMS_SR	2019/09/19	PS2
20191014_075436_101b_3B_AnalyticMS_SR	2019/10/14	PS2
20191128_074331_0e26_3B_AnalyticMS_SR	2019/11/28	PS2
20191130_075458_1012_3B_AnalyticMS_SR	2019/11/30	PS2
20191214_075328_1035_3B_AnalyticMS_SR	2019/12/14	PS2
20200126_075520_1013_3B_AnalyticMS_SR	2020/01/26	PS2
20200217_072402_1053_3B_AnalyticMS_SR	2020/02/17	PS2
20200307_075801_1008_3B_AnalyticMS_SR	2020/03/07	PS2
20200405_080002_1026_3B_AnalyticMS_SR	2020/04/05	PS2
20200511_080858_73_105c_3B_AnalyticMS_SR	2020/05/11	PSB.SD
20200516_072833_09_2277_3B_AnalyticMS_SR	2020/05/16	PS2
20200605_070800_0f32_3B_AnalyticMS_SR	2020/06/05	PS2
20200725_075656_1005_3B_AnalyticMS_SR	2020/07/25	PS2
20200825_075516_101f_3B_AnalyticMS_SR	2020/08/25	PSB.SD
20200923_073155_15_222b_3B_AnalyticMS_SR	2020/09/23	PSB.SD
20201023_082337_89_2424_3B_AnalyticMS_SR	2020/10/23	PS2
20201106_080330_1026_3B_AnalyticMS_SR	2020/11/06	PSB.SD
20201213_073453_56_225a_3B_AnalyticMS_SR	2020/12/13	PSB.SD
20210121_081810_92_2408_3B_AnalyticMS_SR	2021/01/21	PSB.SD
20210220_081825_98_240a_3B_AnalyticMS_SR	2021/02/20	PSB.SD

20210307_073452_89_2276_3B_AnalyticMS_SR	2021/03/07	PS2
20210401_073144_0e26_3B_AnalyticMS_SR	2021/04/01	PSB.SD
20210516_072656_18_2421_3B_AnalyticMS_SR	2021/05/16	PSB.SD
20210615_081444_75_2254_3B_AnalyticMS_SR	2021/06/15	PSB.SD
20210720_072431_33_241e_3B_AnalyticMS_SR	2021/07/20	PSB.SD
20210809_081404_53_2274_3B_AnalyticMS_SR	2021/08/09	PSB.SD
20210913_072510_17_220b_3B_AnalyticMS_SR	2021/09/13	PSB.SD
20211023_072507_56_2206_3B_AnalyticMS_SR	2021/10/23	PS2
20211102_074941_1025_3B_AnalyticMS_SR	2021/11/02	PS2

9.3 Impala

Sentinel-2 Surface Reflectance Images. Downloaded from the GEE catalogue ImageCollection: “COPERNICUS/S2_SR/”.

Image	Date
20190115T080251_20190115T082230_T35JNM	2019/01/15
20190224T075921_20190224T081537_T35JNM	2019/02/24
20190316T075651_20190316T082220_T35JNM	2019/03/16
20190430T075619_20190430T081903_T35JNM	2019/04/30
20190510T075619_20190510T082447_T35JNM	2019/05/10
20190619T075619_20190619T082215_T35JNM	2019/06/19
20190719T075619_20190719T082310_T35JNM	2019/07/19
20190803T075611_20190803T081929_T35JNM	2019/08/03
20190917T075609_20190917T082612_T35JNM	2019/09/17
20191012T075851_20191012T082507_T35JNM	2019/10/12
20191201T080301_20191201T082401_T35JNM	2019/12/01
20191216T080239_20191216T082039_T35JNM	2019/12/16
20200130T080151_20200130T082631_T35JNM	2020/01/30
20200214T075959_20200214T081817_T35JNM	2020/02/14
20200310T075731_20200310T082210_T35JNM	2020/03/10
20200424T075609_20200424T082227_T35JNM	2020/04/24
20200514T075609_20200514T082257_T35JNM	2020/05/14
20200623T075609_20200623T082242_T35JNM	2020/06/23
20200718T075611_20200718T082220_T35JNM	2020/07/18
20200812T075609_20200812T082116_T35JNM	2020/08/12
20200911T075609_20200911T082123_T35JNM	2020/09/11
20201016T075921_20201016T082108_T35JNM	2020/10/16
20201125T080251_20201125T082116_T35JNM	2020/11/25
20201230T080239_20201230T082138_T35JNM	2020/12/30
20210218T075959_20210218T082145_T35JNM	2021/02/18
20210310T075739_20210310T082145_T35JNM	2021/03/10
20210414T075601_20210414T082057_T35JNM	2021/04/14
20210529T075609_20210529T082146_T35JNM	2021/05/29
20210618T075609_20210618T082146_T35JNM	2021/06/18
20210718T075609_20210718T082148_T35JNM	2021/07/18
20210817T075609_20210817T082145_T35JNM	2021/08/17
20210921T075621_20210921T082107_T35JNM	2021/09/21
20211016T075919_20211016T082148_T35JNM	2021/10/16

20211105T080029_20211105T082147_T35JNM	2021/11/05
20211230T080331_20211230T082202_T35JNM	2021/12/30
20220124T080119_20220124T081814_T35JNM	2022/01/24

PlanetScope 4 Band Imagery (downloaded from the Planet Explorer)

Image	Date	Sat. Gen.
20190115_075342_1034_3B_AnalyticMS_SR	2019/01/15	PS2
20190224_075322_0f35_3B_AnalyticMS_SR	2019/02/24	PS2
20190316_075701_0f22_3B_AnalyticMS_SR	2019/03/16	PS2
20190430_094223_08_1063_3B_AnalyticMS_SR	2019/04/30	PS2.SD
20190510_075536_1005_3B_AnalyticMS_SR	2019/05/10	PS2
20190619_093730_91_106a_3B_AnalyticMS_SR	2019/06/19	PS2.SD
20190719_075644_1012_3B_AnalyticMS_SR	2019/07/19	PS2
20190803_075733_1009_3B_AnalyticMS_SR	2019/08/03	PS2
20190917_081407_86_1061_3B_AnalyticMS_SR	2019/09/17	PS2.SD
20191012_080046_1039_3B_AnalyticMS_SR	2019/10/12	PS2
20191201_081706_45_1061_3B_AnalyticMS_SR	2019/12/01	PS2.SD
20191216_073945_0f44_3B_AnalyticMS_SR	2019/12/16	PS2
20200130_092628_44_1069_3B_AnalyticMS_SR	2020/01/30	PS2.SD
20200214_082324_68_1058_3B_AnalyticMS_SR	2020/02/14	PS2.SD
20200310_080013_1006_3B_AnalyticMS_SR	2020/03/10	PS2
20200424_092321_25_1065_3B_AnalyticMS_SR	2020/04/24	PS2.SD
20200514_092101_64_106e_3B_AnalyticMS_SR	2020/05/14	PS2.SD
20200623_091741_24_1068_3B_AnalyticMS_SR	2020/06/23	PS2.SD
20200718_081401_54_105c_3B_AnalyticMS_SR	2020/07/18	PS2.SD
20200812_091456_98_106a_3B_AnalyticMS_SR	2020/08/12	PS2.SD
20200911_073219_82_2212_3B_AnalyticMS_SR	2020/09/11	PSB.SD
20201016_080059_1034_3B_AnalyticMS_SR	2020/10/16	PS2
20201125_090926_62_1069_3B_AnalyticMS_SR	2020/11/25	PS2.SD
20201230_080104_0f15_3B_AnalyticMS_SR	2020/12/30	PS2
20210218_082536_18_227b_3B_AnalyticMS_SR	2021/02/18	PSB.SD
20210310_082500_80_2406_3B_AnalyticMS_SRf	2021/03/10	PSB.SD
20210414_082431_46_2254_3B_AnalyticMS_SR	2021/04/14	PSB.SD
20210529_082359_04_2426_3B_AnalyticMS_SR	2021/05/29	PSB.SD
20210618_082253_58_2403_3B_AnalyticMS_SR	2021/06/18	PSB.SD
20210718_084446_71_1058_3B_AnalyticMS_SR	2021/07/18	PS2.SD

20210817_081855_11_2419_3B_AnalyticMS_SR	2021/08/17	PSB.SD
20210921_072701_77_2442_3B_AnalyticMS_SR	2021/09/21	PSB.SD
20211016_085114_73_1067_3B_AnalyticMS_SR	2021/10/16	PS2.SD
20211105_081752_31_2403_3B_AnalyticMS_SR	2021/11/05	PSB.SD
20211230_085540_71_1064_3B_AnalyticMS_SR	2021/12/30	PS2.SD
20220124_075727_1014_3B_AnalyticMS_SR	2022/01/24	PS2

10 APPENDIX-D: GOOGLE EARTH ENGINE CODE

10.1 Threshold optimisation

GitHub:

https://github.com/christphr/GEE_Tailings_Pond_Monitoring/blob/e40a40a12815aaa8be5f8b5a6a89da5424acb2d4/01_Pond_Threshold.js

Google Earth Engine:

https://code.earthengine.google.com/305e3a0c8d98112c9fd3c20940cb0da2

10.2 Transect

GitHub:

https://github.com/christphr/GEE_Tailings_Pond_Monitoring/blob/e40a40a12815aaa8be5f8b5a6a89da5424acb2d4/03_Transect.js

Google Earth Engine:

https://code.earthengine.google.com/b3e8ce852af75729f09fdc6cac20ea66

10.3 Histogram

GitHub:

https://github.com/christphr/GEE_Tailings_Pond_Monitoring/blob/e40a40a12815aaa8be5f8b5a6a89da5424acb2d4/02_Collection_Histogram.js

Google Earth Engine:

https://code.earthengine.google.com/c81cf3753af11ee424e566e7db3f7a03